HYDROGEN IN NOMINALLY ANHYDROUS CRUSTAL MINERALS

Thesis by

Elizabeth A. Johnson

In Partial Fulfillment of the Requirements for the

degree of

Doctor of Philosophy

CALIFORNIA INSTITUTE OF TECHNOLOGY

Pasadena, California

2003

(Defended May 20, 2003)

ACKNOWLEDGEMENTS

First and foremost, I thank George Rossman, my thesis advisor, for his encouragement and advice when nothing was easy (which was most of the time). Thanks also go to my thesis committee members: John Eiler, Ken Farley, and Paul Asimow. Much of the work on feldspars could not have been accomplished without the sage advice and sample collections of Hugh P. Taylor, Jr. The work on diopside from the Adirondacks was originally suggested by John Valley while on sabbatical at Caltech. John kindly invited me on a collecting trip to the Adirondacks, and he and Cory Clechenko welcomed me at UW-Madison when I stopped by. I'd like to thank M. Darby Dyar for her enthusiastic contribution to the work on OH in diopside, and for her interest in my life and work. When all the necessary journals were missing and the photocopier was jammed, it was GPS librarians Susan and Jim who came to the rescue. Thanks for finding the things that were lost right in front of my nose!

A large number of individuals generously contributed the mineral specimens that were used in this thesis. This is especially true for the material used in the survey of igneous feldspars (Chapter 3). Those who personally gave me samples include Jorge Vazquez, Kari Cooper, Julie Bryce, Cory Clechenko,

and John Valley. Thanks to G. Cleve Solomon for the preliminary work that set the stage for Chapter 3, and Cory Clechenko for data and discussions relating to the material in Chapter 7. Many editors and reviewers have improved the chapters that are modified versions of manuscripts. These include Bob Downs, Sheila Seaman and Andreas Kronenberg (Chapter 2), and Henrik Skogby (Chapter 6).

A number of people have aided me in the use of various analytical instruments. I appreciate the stories and technical expertise of Ma Chi, head of the GPS Division Analytical Facility. Herman Cho of PNNL patiently introduced me to the world of NMR spectroscopy. Sonjong Hwang of the Solid-State NMR facility in Chemical Engineering at Caltech made me into an almost independent user of NMR (laughing all the while). Liz Arredondo was always helpful in the lab, and has been a great friend and a technical guru. Many others on the third floor of Arms have made my life more amusing and interesting, including Jedley Mosenfelder, Julie Bryce, Kari Cooper, and Laura Baker.

I truly appreciate the scientific discussions I have had with many of my fellow graduate students, especially Julie O'Leary, Wang Zhengrong, Charlie Verdel, and Laura Baker. Of course, my socializing with other graduate students was hardly limited to the lab, and over the years I have befriended many wonderful

and intriguing people, of whom there are too many to list here. I'd especially like to thank Magali Billen, a friend and neighbor, as well as Sarah, Sujoy, Ronit, Emily, Yulia, Laura Wasylenki, Matt, Liu Jing, Selene, and all those "reading group" people. Greg Gerbi and Joe Akins provided sanity (or was it insanity?) in the early years.

I encountered wonderful teaching and travel opportunities at Caltech that provided an added depth to my education. Thanks to the undergraduates (and graduates) who made teaching mineralogy labs a joy. Over the past six years I have traveled to Greece, Turkey, South Africa, Switzerland, Hawaii, upstate New York, and yes, even Reno, NV. My appreciation goes to those people and funds that made these trips possible.

On a more personal level, I have to thank our cats, Masala and Tonka, for providing non-stop comic relief while I worked on my thesis at home. I appreciate the support of my family. Above all, thanks to Edwin, whose love and eternally optimistic perspective on life gave me the patience and encouragement I needed in order to complete this monumental task.

ABSTRACT

Systematic infrared and nuclear magnetic resonance investigations of common crustal minerals (feldspars, diopside, and grossular garnets) were undertaken to better understand the geologic significance of minor components of structural hydrous species within these nominally anhydrous minerals.

The absolute hydrogen concentration in three alkali feldspars and eight plagioclase samples was measured with ^{1}H nuclear magnetic resonance spectroscopy. The mid-infrared integral absorption coefficient was determined to be 15.3 ± 0.7 $ppm^{-1} \cdot cm^{-2}$, allowing quantitative analysis of OH and H_2O in feldspars with infrared spectroscopy. A survey of hydrous species in igneous feldspars found that feldspars contain structural OH (0-512 ppm H_2O), H_2O (0-1350 ppm H_2O), and NH_4^+ (0-1500 ppm NH_4^+) groups as well as fluid inclusions and alteration products. Composition and crystal structure influence the type of hydrous species that can be incorporated into feldspars, but the concentration and speciation of structural hydrogen is at least partially determined by the geologic environment. The diffusivity of H in OH-bearing plagioclase was determined at 800-1000°C (D_0=5.7±2.5×10^{-4} m^2/sec and Q=224±33 kJ/mol). A millimeter-sized volcanic feldspar phenocryst would be

expected to lose a significant proportion of its OH concentration on the timescale of a typical eruption (hours to weeks).

The structures and compositions of low albite and ussingite, $Na_2AlSi_3O_8(OH)$, are similar, making the OH in ussingite a possible analog of the structural OH in feldspars. The strong hydrogen bonding in ussingite is found to be fundamentally different from the hydrogen bonding environment of OH in feldspars. Comparison of the infrared spectra of structural isomorphs reedmergnerite, $NaBSi_3O_8$, and low albite suggest that OH is incorporated in both structures through protonation of the most underbonded oxygen site.

The concentration of structural OH in diopside was determined for four granulite facies siliceous marble samples from the Adirondacks, New York. Diopside OH concentration increases monotonically with increasing estimated water fugacity for each outcrop.

Hydrogen concentration is correlated to Ti concentration in zoned grossular skarn garnets from Birch Creek, CA. Decrease of Ti and H from garnet cores to rims may be related to the solubility of Ti in the skarn-forming fluid. Skarn garnets from an Adirondacks, NY, wollastonite ore deposit exhibit a large range of OH concentrations broadly related to rock type that are due to recrystallization and partial dehydration during a complicated geologic history.

TABLE OF CONTENTS

LIST OF ILLUSTRATIONS AND TABLES

Number *Page*

Number *Page*

Chapter 1

INTRODUCTION

Essentially all anhydrous minerals, including common rock-forming minerals such as pyroxenes, olivine, garnet, feldspars, and quartz, contain minor to trace amounts of hydrogen incorporated into their structures in the form of OH, H_2O, and NH_4^+ (Wilkins and Sabine 1973; Solomon and Rossman 1988; Bell and Rossman 1992a; Bell 1993; Rossman 1996). Although the presence of structural hydrous species in anhydrous minerals is in itself interesting, it is important to constrain the mechanisms for incorporation and retention of hydrogen in these minerals. This is a fundamental concern if we wish to use hydrous species in nominally anhydrous minerals to understand geochemical and geological processes in nature.

Many factors, including water fugacity, oxygen fugacity, crystallographic charge-coupled substitutions, and the diffusive properties of hydrogen within the mineral structure, may all play a role in determining the concentration of hydrous species eventually preserved in a mineral. This thesis addresses the problem of understanding the crystallographic and geologic processes of hydrogen retention and incorporation in nominally anhydrous crustal minerals,

in part by empirically investigating the relationship between OH concentration in minerals and the external geologic environment.

Fluid-rock interactions are important everywhere on Earth. Water affects the rates of cation and oxygen diffusion in minerals (Yund and Tullis 1980; Yund 1983; Goldsmith 1987; Goldsmith 1988), and is important in weathering, alteration, and precipitation of minerals at the Earth's surface. Mineral melting temperatures are lowered in the presence of water, and fluids are important in many aspects of volcanism (for example, the explosive or effusive nature of an eruption, and melting in the mantle wedge above a subducting slab). Structural and inclusion water within minerals cause hydrolytic weakening of rocks (Kronenberg and Wolf 1990), and influence the electrical conductivity and seismic properties of the mantle (Karato 1990; Zhang and Karato 1995). Measurements of OH concentrations in upper mantle minerals indicate a large quantity of "water" amounting to about a third of the water in the oceans is stored in the upper mantle (Ingrin and Skogby 2000), and is therefore an important part of the hydrogen budget of the Earth. These mantle minerals are brought up to the Earth's surface as xenoliths or xenocrysts in volcanics and are not likely to be in chemical equilibrium with the surrounding melt. There is some geochemical evidence to support retention of original hydrogen concentration in mantle xenolith minerals (Bell 1993), but there is also evidence that the hydrogen concentrations may be

modified during eruption, especially by reduction-oxidation reactions in iron-rich mantle minerals (Skogby and Rossman 1989; Ingrin and Skogby 2000).

The abundance of geological and geochemical information available for many exposures of continental crust, combined with the ubiquitous potential for water-rock interactions, make the crust an ideal place to learn about hydrogen in nominally anhydrous minerals. Feldspars are the most commonly occurring minerals in the Earth's crust, and are present in a variety of volcanic, plutonic, and metamorphic rocks. In addition, the textural and structural properties of feldspars are greatly affected by the presence of water (Ragland 1970; Parsons and Boyd 1971; Yund and Anderson 1974; Yund and Anderson 1978; Yund and Ackermand 1979; Yund and Tullis 1980; Farver and Yund 1990). Chapters 2, 3, 4, and 5, and Appendix 1 address the concentration, speciation, diffusivity, and crystallographic site occupancy of hydrogen in feldspars, and explore the role the geologic environment plays in determining the speciation and concentration of hydrogen in the feldspar group.

In Chapter 2, a universal absorption coefficient is determined for quantitative analysis of OH and H_2O in feldspars using infrared spectroscopy. ^{1}H MAS (magic-angle spinning) NMR spectroscopy is used to measure the H concentration in three alkali feldspars, and for the first time, eight plagioclase samples. The integral absorption coefficient for total mid-IR peak area is

found to be 15.3 ± 0.7 $ppm^{-1} \cdot cm^{-2}$ (107000 ± 5000 L/(mol $H_2O \cdot cm^2$)) for natural feldspars that contain structural OH or H_2O. Chapter 2 was published as an article in *American Mineralogist* (Johnson and Rossman 2003).

Chapter 3 is a survey of the infrared spectra of eighty-five igneous feldspars in which I determine: (1) the structural and non-structural hydrous species commonly present in plagioclase and alkali feldspars from a wide variety of geologic environments, (2) their approximate ranges in concentration, and (3) the general relationships between hydrous speciation and concentration, crystal composition, and the geologic environment. The results of this survey provide a basis for more detailed investigations of the role of water in structural and compositional transformations in feldspars. This chapter is submitted for publication in *American Mineralogist* (co-author George Rossman).

Diffusion experiments on an OH-bearing plagioclase feldspar were undertaken to better understand the thermal stability of hydrous species in feldspars, and to constrain the effect of hydrogen diffusion during eruption and cooling (Chapter 4). Hydrogen in OH-bearing plagioclase diffuses at a rate similar to that of Na (D_0 = 5.7±2.5×10^{-4} m^2/sec and Q = 224±33 kJ/mol) and the mechanism of hydrogen diffusion is likely related to the movement of Na vacancies in the crystal structure. Even though the diffusion rate for hydrogen

in OH-bearing plagioclase is much slower than hydrogen diffusion measured previously in other nominally anhydrous minerals, the timescale for complete diffusive loss of OH from a millimeter-sized feldspar is on the order of a day to a week for typical eruption temperatures. Since many volcanic feldspars contain significant amounts of structural OH (0 to 510 ppm H_2O by weight), the diffusion rate at 1 bar pressure under nitrogen gas may not accurately reflect processes of OH loss or incorporation during eruption.

The mineral ussingite, $Na_2AlSi_3O_8(OH)$, an "interrupted" tectosilicate, has a structure similar to that of low albite. Chapter 5 is an infrared and ^1H NMR study of ussingite, conducted to determine if the stoichiometric OH in ussingite is structurally analogous to the small quantities (0-0.051 wt% H_2O) of OH that are incorporated into feldspars. Infrared spectra of ussingite contain a polarized, very broad OH stretching band with an ill-defined maximum between 1500-1800 cm^{-1}, which is characteristic of very strong hydrogen bonding (O-H···O distance of 2.48-2.50 Å). ^1H NMR spectroscopy provides an independent confirmation of 5-8% Al-Si disorder in the tetrahedral sites of ussingite. The complete dissimilarity between the infrared and NMR spectra of ussingite and feldspars signifies that the bonding environment of OH in low albite and other feldspars is fundamentally different from the strong hydrogen bonding found in ussingite. This chapter has been

submitted to *Physics and Chemistry of Minerals* and is co-authored by George Rossman.

Appendix 1 compares the infrared spectra of low albite with infrared spectra of the isostructural mineral reedmergnerite, $NaBSi_3O_8$, to gain insight into the mechanism of OH incorporation in the crystal structure of low albite.

Chapters 6 and 7 investigate the systematics of the OH concentrations in other nominally anhydrous crustal minerals within specific geologic settings.

In Chapter 6, the structural OH concentration of diopside in granulite facies siliceous marble samples from the Adirondack Mountains, New York, is determined using FTIR spectroscopy. The OH concentration in diopside increases monotonically with increasing estimated water fugacity for the sample. Charge-coupled substitution with M^{3+} and Ti^{4+} in the crystal structure may have allowed retention of OH in the diopside structure during and after peak metamorphism (~750ºC, 7-8 kbar). This chapter was published as an article in *American Mineralogist*, with co-authors George R. Rossman, M. Darby Dyar (Mount Holyoke College), and John Valley (University of Wisconsin, Madison) (Johnson et al. 2002). John Valley provided the samples and initial motivation for this study, and Darby Dyar collected and analyzed the Mössbauer data.

Chapter 7 examines OH concentrations and major element chemistry of skarn garnets from two localities: a contact metamorphic aureole of the Inyo Batholith near Birch Creek, CA, and a massive wollastonite ore deposit along the Marcy Anorthosite in the Adirondack Mountains, NY. Hydrogen concentration is correlated to Ti concentration in zoned grossular skarn garnets from Birch Creek, CA. Decrease of Ti and H from garnet cores to rims may be related to the solubility of Ti in the skarn-forming fluid. Grossular-andradite garnets from the Adirondacks ore deposit exhibit a large range of OH concentrations broadly related to rock type that are due to recrystallization and partial dehydration during a complicated geologic history. Electron microprobe analyses of the Adirondacks garnets and polished samples were kindly provided by Cory Clechenko and John Valley of the University of Wisconsin, Madison.

Appendix 2 is a database of the spectroscopic data files used in this thesis. The data files are in text format (.csv or .txt) so that they may be easily imported into many graphing programs. The data are organized by chapter in an .html file, and detailed instructions and descriptions of the spectral files are included in this master page.

The two principal analytical methods used to investigate hydrous species in this thesis are Fourier-transform infrared spectroscopy and ^{1}H MAS (magic-

angle spinning) NMR (nuclear magnetic resonance) spectroscopy. The stretching modes of hydrous species absorb strongly in the mid-infrared (2000-3800 cm^{-1}) region. Infrared spectroscopy is sensitive to the speciation of hydrogen, and polarized IR spectra provide information about the orientation of hydrous species within a mineral structure. Polarized infrared microscopy allows greater spatial resolution than in conventional IR spectroscopy (200-50 μm analysis areas, compared to ≥500 μm), providing the capability to measure infrared spectra on small mineral grains and to investigate the heterogeneity of hydrogen speciation and concentration within a single large mineral grain. A new procedure for using ^{1}H NMR spectroscopy to quantify small hydrogen concentrations in solids was developed as part of the effort to calibrate the infrared absorbance of OH and H_2O in feldspars. ^{1}H MAS NMR is also utilized in more conventional ways in this thesis, to probe the local bonding environments and dynamic behavior of protons in solid-state materials. Detailed analytical descriptions are provided in each chapter.

Chapter 2

THE CONCENTRATION AND SPECIATION OF HYDROGEN IN FELDSPARS USING FTIR AND ^{1}H MAS NMR SPECTROSCOPY[1]

Abstract

A universal absorption coefficient was determined for quantitative analysis of OH and H_2O in feldspars using infrared spectroscopy. ^{1}H MAS (magic-angle spinning) NMR spectroscopy was used to determine the H concentration in three alkali feldspars, and for the first time, eight plagioclase samples. It was necessary to eliminate signal due to adsorbed water in the powdered NMR sample to accurately measure structural H concentration in samples with low H (<1000 ppm H_2O). The pegmatitic and metamorphic albites are transparent, but contain variable (40-280 ppm H_2O) concentrations of microscopic to sub-microscopic fluid inclusions. The pegmatitic albites also have sharp bands in

[1] Modified from Johnson, E.A. and Rossman, G.R. (2003) American Mineralogist, 88, 901-911.

the mid-IR similar to the OH bands found in quartz. All the other plagioclases used in the IR calibration have broad, anisotropic bands around 3200 cm^{-1} in the mid-IR and weak combination stretch-bend bands near 4550 cm^{-1} in the near-IR, indicative of structural OH. The OH vector in plagioclases is preferentially aligned parallel to the crystallographic *a*-axis. The concentration of structural OH in the plagioclases ranges from 210-510 ppm H_2O by weight. The microclines contain structural H_2O molecules (1000-1400 ppm H_2O) and the sanidine contains structural OH (170 ppm H_2O). An approximately linear trend is produced when the total integrated mid-IR absorbance is plotted versus the concentration of structural H determined from NMR (OH and H_2O) for plagioclase and alkali feldspars. The integral absorption coefficient for total mid-IR peak area is 15.3 ± 0.7 $ppm^{-1} \cdot cm^{-2}$ (107000 ± 5000 L/(mol $H_2O \cdot cm^2$)) for natural feldspars that contain structural OH or H_2O. Measurements of band areas of unpolarized IR spectra on (001) cleavage fragments provide an estimate of H concentration for alkali feldspars, but this method does not work for most plagioclase feldspars.

Introduction

Much has been done to quantify the concentration of H in many nominally anhydrous minerals (Rossman 1996), especially common mantle minerals such as olivine, garnet, and pyroxenes (Bell et al. 1995; Ingrin and Skogby

2000). However, there has been less effort to quantify the amount of H found in naturally occurring feldspars. It has been known for some time that IR spectra of feldspars show evidence of trace structural H (Wilkins and Sabine 1973; Smith and Brown 1988). Mid-IR and near-IR spectroscopic studies of feldspars (Solomon and Rossman 1979; Hofmeister and Rossman 1985a; Hofmeister and Rossman 1985b; Hofmeister and Rossman 1986) determined that plagioclase contains structural OH groups and alkali feldspars can incorporate OH, H_2O, and NH_4^+ (Solomon and Rossman 1988). The concentration of hydrous species has been determined for a few alkali feldspars using hydrogen manometry (Hofmeister and Rossman 1985a; Hofmeister and Rossman 1985b) but there has been no determination of absolute H contents for plagioclase.

Quantitative analysis of trace H in feldspars is particularly interesting because feldspars are abundant in the Earth's crust in a variety of volcanic, plutonic, and metamorphic rocks, and because textural and structural properties of feldspars are greatly affected by the presence of water. The rate of oxygen diffusion (Yund and Anderson 1974; Yund and Anderson 1978; Farver and Yund 1990) and Al and Si interdiffusion rates (Yund and Tullis 1980) in feldspars increase with increasing water pressure in hydrothermal experiments. Knowledge of the amount and speciation of H in feldspars could be used to study the interaction of water and rock in hydrothermal systems, low-

temperature alteration of feldspars, the water content of magmas, and devolatilization during eruption. The purpose of this study is to determine absorption coefficient(s) for the mid-IR absorption bands of hydrous species in feldspars so that interesting geologic problems can be addressed quantitatively with IR spectroscopy. To do this, reliable measurements of H concentration in plagioclase must be made for the first time.

Infrared spectroscopy is sensitive to the speciation of hydrogen, and polarized IR spectra provide information about the orientation of hydrous species in the feldspar structure. It is also possible to distinguish structural hydrogen from fluid inclusions or fine-grained hydrous alteration products with IR spectra.

The Beer-Lambert law is used to determine the concentration of hydrous species in a mineral from IR spectra:

$$A = \varepsilon \times c \times t, \quad (2.1)$$

where A is the total maximum band height in the region of interest, summing over measurements in the principal optic directions ($A_X + A_Y + A_Z$), c is the concentration of hydrous species expressed in moles H_2O/L mineral, t is the thickness of the polished slab (path length) in cm, and ε is the molar absorption coefficient in units of L/(mol·cm). In the modified version of the Beer-Lambert law used in this study, A is replaced by Δ, the total integrated

area of bands in the region of interest ($\Delta_X + \Delta_Y + \Delta_Z$), and *c* is expressed as moles H_2O/L mineral. In this case, the absorption coefficient becomes the integral molar absorption coefficient (*I*, L/(mol·cm^2)). When c is expressed as ppm H_2O by weight, the absorption coefficient becomes the integral specific absorption coefficient (*I'*, ppm^{-1}·cm^{-2}). The absorption coefficient for each species of hydrogen is found by determining the concentration *c* (in this case, with NMR spectroscopy) and measuring Δ from polarized IR spectra in the three principal optical directions (*X*, *Y*, and *Z*) for feldspars with different H concentrations. The slope of a best-fit line through the data is equal to the absorption coefficient for that species. We also evaluate other methods of estimating H concentrations from mid-IR spectra using the maximum band height in polarized spectra, and unpolarized band area or band height on (001) cleavage flakes.

^{1}H MAS NMR is an ideal method for determining H concentration in minerals with low Fe content (less than about 0.4 wt% FeO) because it is inherently quantitative. Quantitative NMR measurements become much more difficult at H concentrations less than about 1 wt% H_2O because the probe background overwhelms the sample signal unless the background is minimized through the use of pulse sequences or is somehow subtracted from the sample signal. Two previous studies have determined hydrogen concentrations in alkali feldspars

using NMR. Yesinowski et al. (1988) determined H concentrations for three microclines (>1000 ppm H_2O), quartz, and nepheline from ^1H MAS NMR spectra. Xia et al. (2000) calculated water concentrations for three anorthoclase megacrysts (365-915 ppm H_2O) using ^1H MAS NMR.

Paterson (1982) and more recently Libowitzky and Rossman (1997) provide calibration curves for approximating absorption coefficients according to the mean wavenumber of the OH stretching bands in glasses, water solutions, and hydrous minerals. These approximate calibrations do not hold for hydrous species in many nominally anhydrous minerals (for example, pyrope (Bell et al. 1995)) so it is necessary to individually calibrate each mineral of interest.

Sample Localities and Compositions

The compositions, localities, and geologic settings of feldspar samples used in this study are listed in Table 2.1. To fully characterize and calibrate the hydrous species in feldspar, we examined three potassium feldspars, and eight plagioclase feldspars ranging in composition from Ab_{100}-Ab_4. A variety of geological environments are also represented in our sample selection: six feldspars come from pegmatites, four are volcanic in origin, and one albite sample is metamorphic in origin. Feldspar samples used in this study were

unaltered and free of inclusions visible to the naked eye, and transparent on the scale of a centimeter or more. Samples of such exceptional quality were necessary to produce both thick polished slabs for near-IR measurements and more than 200 mg of pure material for NMR studies. Some samples (from pegmatites or metamorphic veins) had turbid or milky regions that were not used for quantitative measurements but were also examined by NMR and IR spectroscopy. Low Fe concentrations (<0.4 wt% FeO) were required to avoid line-broadening problems in the NMR spectra.

Experimental Methods

Electron microprobe analysis

Electron microprobe analyses of four feldspar samples (GRR1608, GRR1609, GRR1280 and GRR1281) were obtained on a JEOL JXA-733 electron microprobe at Caltech. An accelerating voltage of 15 kV, a beam current of 25 nA, and 10 μm beam size were used. Oxide totals were calculated using the CITZAF correction (Armstrong 1995) and fell within the range 99.5-100.5%. An average of three analyses was used to determine the compositions reported in Table 2.1.

Density determination

Feldspar densities were determined with a Roller-Smith density balance by measuring the weight of grains in air and in toluene. For each sample, the density was an average of measurements of three grains, with a resulting 2σ error of less than 1.3% relative.

Infrared spectroscopy

Polarized mid-IR spectra were measured in the three principal optical directions on doubly polished slabs of each mineral. Although measurement of six vibration directions is needed to fully characterize the anisotropy of bands in monoclinic and triclinic minerals (Dowty 1978), only three mutually perpendicular polarized spectra are needed to determine total band intensity and area for calibration purposes. We tested this theory by measuring polarized spectra in three random perpendicular directions on two cubes of anorthite sample GRR1968, as well as measuring spectra in the three principal optical directions. The total integrated band areas for the two sets of random measurements agreed with the band area determined for the principal optical directions to within ±5% relative.

Cleavage or twin planes, optical interference figures, and morphology were used to orient the mineral slabs. Care was taken to avoid taking spectra through more than one twin layer. Slab thickness were 0.3 to 9.2 mm for mid-IR spectra and 1.2 to 9.2 mm for near-IR spectra. Infrared spectra of water

and ice were obtained by creating films (150 μm to a few μm) between plates of synthetic Al_2O_3.

Infrared spectra were obtained in the main compartment of a Nicolet Magna 860 FTIR spectrometer at 4 cm^{-1} resolution using a 1000 μm or 600 μm aperture. Mid-IR spectra were obtained using a CaF_2 beamsplitter, infrared source, MCT-A detector, and $LiIO_3$ Glan-Foucault prism polarizer and were averaged over 512 scans. Near-IR spectra were averaged over 1024 scans and were obtained using a white light source and CaF_2 beamsplitter with an MCT-B, MCT-A, or InSb detector. Infrared spectra were obtained at 77 K using a homebuilt vacuum chamber in the main compartment of the FTIR spectrometer.

Total band area ($\Delta = \Delta_X + \Delta_Y + \Delta_Z$) and maximum height ($A = A_X + A_Y + A_Z$) were determined for mid-IR bands using the Omnic E.S.P. 5.2 software associated with the FTIR spectrometer (Table 2.2 and Table 2.3). For most spectra, no background correction was needed. A few spectra had sloping backgrounds that were removed by manual extrapolation underneath the bands of interest. The error on total integrated area (Δ) (Table 2.2) is due mostly to background subtraction and is estimated to be at most 10% relative, as determined in other polarized infrared studies of nominally anhydrous minerals (Bell et al. 1995). Unpolarized mid-IR spectra were also

measured on (001) cleavage fragments of feldspars used in the calibration. To eliminate the effect of internal polarization of the IR spectrometer, an average of two unpolarized spectra taken with the slab in two perpendicular orientations (with ~5-30 % difference in band area) was used for each sample.

^{1}H MAS NMR

Previous ^{1}H NMR work on nominally anhydrous minerals (Yesinowski et al. 1988; Kohn 1996; Keppler and Rauch 2000) has pointed out the difficulty of removing proton signals due to adsorption of water and organics on grain boundaries and onto the NMR probe or rotor. It is especially important to eliminate or identify such signals for minerals like feldspars that have very low hydrogen concentrations. Samples were examined under the binocular microscope for visible fluid and mineral inclusions. The minerals were broken or crushed and inclusion-free grains were picked for use in the NMR experiments.

Initially, samples were ground and loaded into NMR rotors in a dry box, without using a liquid as a grinding aid. The filled rotors were placed in a desiccator when not in use. Anhydrous synthetic corundum was prepared in the same way as the feldspar samples and was used as a blank for the NMR experiments. The initial NMR experiments were done over the course of two years, and it was found that the anhydrous corundum powder was adsorbing

water from air, making it difficult to determine how to subtract the signal due to adsorbed water from structural H signal for samples with low H (<1000 ppm H_2O).

To reduce the amount of adsorbed water on powders, the sanidine and plagioclase feldspars containing only structural OH were picked and crushed in air, and grain size was constrained to be between 45 and 149 μm by sieving. Each sample was loaded into an NMR rotor and heated at 200°C under vacuum for about 11 hours before obtaining NMR spectra. A labradorite sample (GRR2058, from Ponderosa Mine, Oregon) determined to be anhydrous from its mid-IR spectrum (maximum <1 ppm H_2O) was prepared this way, and was used to create a background spectrum for the plagioclase and sanidine samples. The powders were removed from the rotors and weighed after the NMR experiments. Sample weights ranged from 125 to 160 mg.

All NMR experiments were done at the solid-state NMR facility in the Department of Chemical Engineering at Caltech. NMR spectra were recorded on a Bruker DSX 500 MHz spectrometer using a 4 mm CP-MAS probe. Spinning speeds ranged from 6-14 kHz, but all quantitative measurements were run at 12 kHz. A 4 μs 90° – 8 μs 180° pulse depth sequence (program written by Sonjong Hwang; Cory and Ritchey 1988) was used to minimize

probe background. Spectra were averaged over 128 or 512 scans. In order to maximize the signal, saturation-recovery experiments were used to determine the relaxation time T_1 for each sample. The recycle delay time ranged from 70 to 110 seconds and was chosen to be at least five times as long as T_1. The receiver gain was identical for all samples, and spectra were recorded in analog mode. No exponential line-broadening function was applied to the spectra. For room temperature experiments, zirconia sample rotors with Kel-F caps were used. Tetrakis-(trimethylsilyl)silane (TKTMS) was used as a primary chemical shift reference. Chemical shifts (δ) are referenced to tetramethylsilane (TMS), using the relationship δ(TMS) = δ(TKTMS) + 0.247 ppm (Hayashi and Hayamizu, 1991). Variable temperature experiments were conducted between 178 K and 373 K. During the variable temperature experiments, zirconia caps were used on the rotors. Dry nitrogen from a high-pressure liquid nitrogen tank was used for cooling and spinning the samples.

Analcime from Table Mountain, near Golden, CO, (GRR1379) containing 8.15 wt% H_2O (determined by thermogravimetric analysis) was used as a hydrogen concentration standard for NMR. The total integrated area of a particular proton species was determined by measuring the area of the center peak and any spinning sidebands after the background was subtracted.

Results

IR spectroscopy

Mid-IR

Polarized spectra of feldspars in the 2800-3700 cm^{-1} range are shown in Figures 2.1 and 2.2, and band positions are listed in Table 2.2. In this region, absorbance is due to stretching of structural OH groups and the symmetric and asymmetric stretches of H_2O.

Four types of bands are observed in the mid-IR spectra of the feldspars. The mid-IR spectra of the oligoclases (GRR1280 and GRR580), andesine, and anorthite have a prominent broad band near 3200 cm^{-1} with minor bands around 3400 cm^{-1} and 3600 cm^{-1}. These bands have their maximum intensities closest to the *a*-axis (*X* in oligoclase and andesine, *Y* in anorthite). The *Y* and *Z* optical spectra reported here for the oligoclase sample GRR580 are reversed from the *Y* and *Z* polarized spectra for the same sample reported in Hofmeister and Rossman 1986. The assignment of optical directions in the present study was confirmed by obtaining the *Y* spectrum from a slab of known orientation that produced an optic axis interference figure. The mid-IR spectra of sanidine (GRR638) also contain broad bands centered at 3400 cm^{-1} and 3250 cm^{-1} with maximum absorption in *X*, and at 3060 cm^{-1} with maximum absorption in *Y*. At 77 K, the mid-IR bands in plagioclase and sanidine become slightly

narrower and shift by only a few wavenumbers compared to the room temperature spectra (e.g., for oligoclase GRR580; Hofmeister and Rossman 1986). Therefore, very little of the band intensity in the mid-IR can be due to fluid inclusion water for these feldspars.

The polarized mid-IR spectra of the microclines are characterized by four bands, two (3630 cm^{-1} and 3450 cm^{-1}) with absorbance in *X* greater than in *Z* or *Y*, and two (3575 cm^{-1} and 3285 cm^{-1}) with maximum absorbance in *Z*.

The mid-IR spectra of pegmatitic and metamorphic albites contain two distinct types of bands that are very different from those found in spectra of other plagioclases. The metamorphic albite (GRR1610) has only a broad, non-polarized asymmetric band roughly centered at 3450 cm^{-1}. The other three albites have spectra containing the broad 3450 cm^{-1} band as well as a broad asymmetric band centered at about 3050 cm^{-1} with maximum absorbance in the *Y* direction. These three albite specimens also have a dominant sharp band at 3507 cm^{-1} and other less intense sharp bands with maximum absorbance along *X*. At 77 K, the broad band at 3450 cm^{-1} shifts to about 3200 cm^{-1}, similar to the position and shift of water bands to ice bands (Figure 2.2). Multiple narrow bands appear in the 77 K spectra of the three pegmatitic albites, and other bands visible in the spectra at 298 K (e.g., the bands at 3050 cm^{-1} and 3507 cm^{-1}) shift by at most only a few wavenumbers at 77 K.

Near-IR

Near-IR spectra (5400-3900 cm^{-1}) of the feldspars in this study are shown in Figure 2.3. Bands in this region are assigned as in Stolper (1982a). Absorbance in the 4550-4560 cm^{-1} region is due to combination bend-stretch modes of Si-OH and Al-OH groups. Bands at about 5200 cm^{-1} are due to the combination of stretching and bending modes of molecular water. Absorbance at 4000 cm^{-1} is thought to be due to combination of low-energy lattice modes and stretch modes of H_2O or OH (Stolper 1982a).

Plagioclase feldspars and sanidine have bands present at 4500-4600 cm^{-1} and 4000 cm^{-1}, with no visible bands in the 5200 cm^{-1} region (Figure 2.3A). The polished slabs of plagioclase and sanidine used to obtain the near-IR spectra were 2.6 mm to 9.2 mm thick. The microclines have two polarized bands at 5125 cm^{-1} and 5230 cm^{-1} (Figure 2.3B).

An asymmetric band near 5200 cm^{-1} is present in the near-IR spectra of the pegmatitic and metamorphic albites (Figure 2.3C). This band resembles the combination stretch-bend mode for liquid water, and upon cooling to 77 K shifts to lower wavenumbers and resembles the near-IR spectrum of ice. The intensity of the band near 5200 cm^{-1} in these albites is much greater for the turbid, milky areas than in clear areas. No bands near 4500 cm^{-1} are seen in

the albite near-IR spectra, although slab thicknesses were limited to 1-2 mm for these samples because of twinning.

^{1}H MAS NMR

The ^{1}H MAS NMR spectra of feldspars in this study are shown in Figure 2.4 and band positions are listed in Table 2.2. The NMR spectra of feldspars contain bands due to structural water, adsorbed water, and organic materials. As described by Yesinowski et al. (1988), organic contaminants present in the NMR probe and possibly on the sample rotor produce a series of sharp bands near 1.5 ppm. This signal is present in the spectrum of an empty rotor (Figure 2.4A). This peak and a broad band centered at about 3.5 ppm are present in the spectrum of anhydrous labradorite (Figure 2.4A) and synthetic anhydrous corundum. The broad band at 3.5 ppm is assigned to water adsorbed onto the surface of the powdered sample because it only appears when a powder is present, and its intensity increases with increased exposure to air. Figure 2.4A shows the raw data for sample GRR1389 (andesine), and the resulting spectra for GRR1389 after subtracting the background signal. The organic bands are not identically intense in the background and sample spectra, so after the anhydrous labradorite spectrum is subtracted from the sample spectrum, some proportion of the empty rotor spectrum is also subtracted or added to minimize the residual organics signal. The resulting noise in the vicinity of 1.5 ppm adds less than 5% error to the overall area measurement.

Plagioclase feldspar spectra have broad bands at about 6 ppm and 4.8 ppm (Figure 2.4B), with low-intensity spinning sidebands. In contrast, the microcline spectra (Figure 2.4B) have a central band at 4.8 ppm surrounded by spinning sidebands, with a very sharp fluid inclusion water band superimposed on the spectrum. The bands due to structural H are outlined by the shape of a Pake doublet, which is indicative of isolated H_2O molecules within the mineral structure. The NMR spectra of these microclines are identical to the ones in Yesinowski et al. (1988).

The NMR spectra of pegmatitic and metamorphic albites (Figure 2.4B) have a very sharp band at 4.7 ppm. As the temperature is lowered this band decreases in intensity and disappears by about 250 K, returning to its original intensity at room temperature. This band was assigned to fluid inclusions by Yesinowski et al. (1988). These samples may also have a component of OH (up to a maximum of 50% OH, with an OH concentration of 40 ppm H_2O estimated from the IR spectra of GRR1609, and total fluid inclusion water calculated to be about 40 ppm from the NMR spectrum). It was not possible to deconvolve these low-intensity, broad bands from the adsorbed water signal.

The H concentrations determined by NMR in this study agree with previously determined concentrations using manometry or NMR (Table 2.2). The largest contributor to the error in concentration measurements for the plagioclase

feldspars is the uncertainty in the intensity of the adsorbed water band that is subtracted from the structural H signal. The area under this band in the anhydrous labradorite spectrum is equivalent to about 100 ppm H_2O. Although grain size was constrained to be 45 to 149 μm for these samples, the mean grain size (and thus the amount of adsorbed water) could vary within this range. The surface area per unit volume for 45 μm cubes is 3.3 times larger than for 149 μm cubes. Assuming that the 100 ppm of adsorbed water on the labradorite is adsorbed onto a sample with an average grain size distribution, the quantity of adsorbed water on the surface can have a maximum range of 50 to 150 ppm H_2O (for samples with all 149 μm and all 45 μm grains, respectively). Therefore, the error due to subtraction of adsorbed water signal from plagioclase NMR spectra is estimated to be ± 50 ppm H_2O. Additional error (estimated to be about 7% relative from repeated measurements of the analcime standard) is incurred by the use of a standard to determine absolute concentrations in NMR. Total error (± 60-90 ppm H_2O) is the sum of the adsorbed water subtraction error and the standardization error for OH-bearing feldspars, and is the standardization error for the microclines.

The data from this study suggest that there are two distinct ranges of H concentration in feldspars. Feldspars containing structural OH have lower H concentrations than those containing structural H_2O. It is possible, however,

that the gap in concentration between OH- and H_2O- containing feldspars may be spanned by samples we have not examined here. For example, Xia et al. (2000) report H concentrations of 365-915 ppm H_2O in anorthoclase from Cenozoic alkalic basalts.

Calculation of absorption coefficients

The total mid-IR band areas (2900-3600 cm^{-1}) and H concentrations from NMR are listed in Table 2.2 and plotted in Figure 2.5A. The pegmatitic and metamorphic albites are not included in the determination of absorption coefficients, because of the difficulty of separating structural H signal (when present) from heterogeneous fluid inclusion signal in the IR and NMR. All of the data, regardless of hydrous species, follow a single trend. Therefore, only one line is fit to the data (constrained to pass through the origin), producing a single set of absorption coefficients (I and I') for all feldspars with structural hydrogen. The specific integral absorption coefficient I' is 15.3 ± 0.7 $ppm^{-1}\cdot cm^{-2}$ and the molar integral absorption coefficient I is 107000 ± 5000 $L/(mol\ H_2O\cdot cm^2)$. The error on the absorption coefficient translates into about 4.5% error for the H concentration determined using this calibration.

The total maximum polarized IR band height, the maximum band height with ~E||*a*, and the unpolarized band area on (001) are also plotted versus H concentration in Figures 2.5B-D. The graphs involving maximum band

heights (Figure 2.5B and 2.5C) show evidence for two trends: one trend for feldspars containing structural H_2O and a less steep trend for feldspars containing OH. The difference in band shape between OH-bearing and H_2O-bearing feldspars is probably responsible for this phenomenon. The H_2O-bearing microclines have complex spectra with multiple bands having nearly the same maximum intensity, whereas the spectra of OH-bearing feldspars have one broad, dominant band. If more data were available, it might be possible to fit two separate lines to the data in either of these graphs, but it is more accurate to measure band areas on the polarized spectra.

The simplest measurement to make is either the band area (Figure 2.5D) or band height of unpolarized IR spectra on (001) cleavage fragments. No reasonable trend is seen in the unpolarized band height data. For the unpolarized band areas, a line with slope of 6.7 $ppm^{-1} \cdot cm^{-2}$ can be fit through the potassium feldspar and oligoclase GRR1280 data points, but the rest of the plagioclase fall off of this trend. This may be due to the rotation of the optical axes as a function of composition along the plagioclase series. Measurement of unpolarized spectra is the quickest way to get a rough estimate of a feldspar's hydrogen content, but for quantitative determination of H concentration it is necessary to measure band areas in polarized spectra of any three perpendicular directions.

Discussion

Hydrous species and orientation from IR

From the IR data, we conclude that plagioclase and sanidine contain structural OH, consistent with Hofmeister and Rossman (1985a) and Hofmeister and Rossman (1986). The OH-stretch bands for these minerals are very broad, implying that a range of O-H···O distances is involved. The OH bands are only a few wavenumbers narrower at 77 K than at room temperature, suggesting the width of the bands is due to multiple OH sites rather than dynamic disordering.

The IR spectra of hydrogen feldspar, $HAlSi_3O_8$, synthesized by Müller (1988) show some similarities to the IR spectra of OH in plagioclase and sanidine. Hydrogen feldspar has a set of broad OH bands in the 2700-3500 cm^{-1} region that are similar in location and polarity (with maximum intensity in E||*a*) to OH bands in natural feldspars. The preferred orientation of OH along the crystallographic *a*-axis may be related to the position of oxygen atoms surrounding the M site (e.g., $O_A(2)$, Behrens and Müller 1995) that are most receptive to forming OH bonds. The H-feldspar therefore has the potential to provide a useful analogy to the location and nature of OH in natural feldspars,

although further studies are needed to determine the location of OH in the H-feldspar structure.

Our conclusion that the sanidine contains OH is consistent with the interpretation of Hofmeister and Rossman (1985b) but not with Beran (1986), who concludes that sanidine (also from Volkesfeld, Germany) contains H_2O molecules. Although the near-IR OH band is very weak, the lack of absorption in the 5200 cm^{-1} region means that no more than 5% of the hydrogen can be incorporated as H_2O molecules.

As in the previous studies of microclines (Solomon and Rossman 1979; Hofmeister and Rossman 1985a; Hofmeister and Rossman 1985b; Kronenberg et al. 1996), we find that there are two types of structural water molecules (from the two stretch-bend combination modes and four H_2O stretch bands). Based on the polarization of near-IR and mid-IR bands, Solomon and Rossman (1979) assigned the two types of water to lie in a plane parallel to (001), with H-H vectors not aligned with each other. The H_2O molecules are assigned to the K site by Hofmeister and Rossman (1985b) and Kronenberg et al. (1996) using hydrogen-bonding and site size considerations.

The isotropic nature of the broad band in the mid-IR around 3450 cm^{-1} and the low-temperature mid-IR and near-IR spectra of end-member albites clearly indicate that fluid inclusions are present. The transparent areas of the albites

were examined under 500× and 1000× magnification on a petrographic microscope to evaluate the dimensions of the fluid inclusions in each sample. All four albites contain heterogeneous patches of inclusions, as well as areas where no inclusions are visible under 1000× magnification (the fluid inclusions are either not present or are <1 μm in diameter in these areas). The Amelia albite (GRR1605) contains abundant, euhedral, rod-shaped inclusions 2-3 μm in diameter and ranging from a few micrometers to greater than 20 μm in length. The Brazilian albites, GRR1608 and GRR1609, contain layers of pancake-shaped inclusions perpendicular to (010), a few micrometers thick but up to 80 μm in length and width. They also contain regions of inclusions with maximum dimensions of a few μm. The large sample thickness (about 1 mm) and aperture size (at least 600 μm) needed to obtain good IR spectra of the pegmatitic albites means that these microscopic fluid inclusions cannot realistically be avoided (at least 100 inclusions per 1000 μm area), and are likely responsible for the fluid inclusion band seen in the IR spectra of these samples. The metamorphic albite, GRR1610, contains tiny fibers of actinolite (the OH bands of actinolite can be seen in the 3600-3700 cm^{-1} region in Figure 2.1C), but no fluid inclusions are visible at 1000× magnification, suggesting that submicroscopic inclusions are responsible for the IR spectra of liquid water in this sample.

The interpretation of the narrow bands in the albite mid-IR is less straightforward because of the lack of corresponding bands in the near-IR. Quartz is a tectosilicate that also has IR spectra with broad bands due to fluid inclusions (Aines and Rossman 1984) and very narrow (< 25 cm^{-1}) bands due to structural OH. The sharp bands in quartz are due to OH associated with alkali ions and aluminum (Kats 1962; Aines and Rossman 1984). Downs et al. (1994, 1996) determined that the O_{CO} atom is uniquely underbonded in the low albite structure and is therefore a potential bonding site for hydrogen that is not present in other feldspars. This may explain why the sharp OH bands in the low albite spectra are so different from the OH spectra of other feldspars.

We see no evidence in the IR spectra for the presence of the ammonium ion, NH_4^+, in any of the samples studied here, although it is known that NH_4^+ can be incorporated in minor amounts (Solomon and Rossman 1988) or can completely substitute into the large cation site in feldspar forming the mineral buddingtonite.

Quantitative H measurements

This study shows that ^1H MAS NMR can be used to quantitatively measure low H concentrations in minerals. Care must be taken to distinguish signal due to adsorbed water or organics from structural H. The most consistent way to subtract these signals is to remove as much adsorbed water as possible from

the powders and to use the spectrum of an anhydrous powder as a baseline. The broad NMR bands of plagioclase may represent a worst-case scenario in terms of background subtraction. There is likely less error involved in H concentration measurements for minerals with sharper ^{1}H MAS NMR bands.

For quantitative H concentration determinations, it is necessary to measure the total integrated absorbance in three mutually perpendicular polarized infrared spectra. An estimate of H concentration for alkali feldspars can be made using band areas of unpolarized spectra on cleavage fragments, but this method does not work for plagioclase-series feldspars (excluding oligoclase GRR1281).

Paterson (1982) and Libowitzky and Rossman (1997) estimate absorption coefficients according to the mean stretch frequency of hydrous species in the mid-IR (about 3200 cm^{-1} for OH in plagioclase; about 3500 cm^{-1} for OH and H_2O in potassium feldspars). Therefore, it is expected that the feldspar data would lie along two linear trends in Figure 2.5A: one for OH in plagioclase, and another with a shallower slope for OH and H_2O in potassium feldspars. The Paterson (1982) calibration predicts a molar integral absorption coefficient of 174000 L/(mol $H_2O \cdot cm^2$) for 3200 cm^{-1} and 84000 L/(mol $H_2O \cdot cm^2$) for 3500 cm^{-1}. The Libowitzky and Rossman (1997) calibration predicts a molar integral absorption coefficient of 136370 L/(mol $H_2O \cdot cm^2$) for 3200 cm^{-1} and 62390 L/(mol $H_2O \cdot cm^2$) for 3500 cm^{-1}. None of these

absorption coefficient estimates match the slope of the data. This confirms the need to calibrate the IR bands individually for specific mineral groups. A single slope and thus a single absorption coefficient (107000 ± 5000 L/(mol $H_2O \cdot cm^2$)) for all hydrous species in all typical feldspars is therefore unexpected but convenient, because this calibration can be used for any feldspar containing structural OH and H_2O. The structural H concentration can now be determined with IR spectroscopy on polished slabs of material, eliminating the need to make a powder of the material for NMR work.

Table 2.1. Compositions and localities of feldspar samples.

Sample Number	Mineral name	Composition*	Fe content (wt% oxide)	References	Locality and geological environment	References
GRR1605	Albite (cleavelandite)	$Ab_{98.3}An_{0.0}Or_{1.7}$	0.03 Fe_2O_3 0.02 FeO	Kracek and Neuvonen 1952	Amelia, VA; pegmatite	Sinkankas 1968; Pegau 1929
GRR1608	Albite (cleavelandite)	$Ab_{99.6}An_{0.2}Or_{0.2}$	<0.01 Fe_2O_3	this work	Governador Valadaras, Minas Gerais, Brazil; pegmatite	Proctor 1984
GRR1609	Albite (cleavelandite)	$Ab_{98.8}An_{0.5}Or_{0.7}$	<0.01 Fe_2O_3	this work	Pederiniera Mine, São Jose da Safira, Minas Gerais, Brazil; pegmatite	Proctor 1984
GRR1610	Albite	$Ab_{99.3}An_{0.5}Or_{0.2}$	not determined	Pohl et al. 1982	New Melones Dam, Calaveras County, CA; gash veins in metamorphic rock	Pohl et al. 1982
GRR1280	Oligoclase	$Ab_{67}An_{25}Or_{8}$	not determined	this work	Black Rock Pass, Nevada; basalt	
Harvard Min. Mus.81228 GRR580	Oligoclase	$Ab_{82.0}An_{16.4}Or_{1.6}$	0.04 FeO	Hofmeister and Rossman 1986	South Carolina; pegmatite	Kracek and Neuvonen 1952
GRR1389 (CIT13759)	Andesine	$Ab_{66}An_{30}Or_{3}$	0.11 Fe_2O_3 0.03 FeO	Hofmeister and Rossman 1985a	Halloran Springs, CA; Cima volcanics, basalt	Wise 1982; Colville and Novak 1991; Farmer et al. 1995
GRR1968	Anorthite	$Ab_{4.0}An_{93.8}$	0.37 FeO	Kimata et al. 1995	Miyake Island, Japan; tholeiite	Kimata et al. 1995
GRR968	Microcline	$Ab_{6}Or_{94}$	0.003 FeO	Hofmeister and Rossman 1985a	Elizabeth R Mine, Pala, CA; pegmatite	Foord et al. 1991
GRR1281	Microcline	$Ab_{8.3}An_{0.0}Or_{91.7}$	<0.01 Fe_2O_3	this work	White Queen Mine, Pala, CA; pegmatite	Foord et al. 1991
GRR638	Sanidine	$Ab_{14.2}An_{0.0}Or_{85.8}$	0.12 Fe_2O_3	Hofmeister and Rossman 1985a	Volkesfeld, Eifel, Germany; leucitic-phonolitic pumice	Wondratschek 1985

* Ab = $NaAlSi_3O_8$; An = $CaAl_2Si_2O_8$; Or = $KAlSi_3O_8$

Table 2.2. Hydrogen speciation and concentration, mid-IR and NMR data for feldspars.

Sample Number	Mineral name	Proton speciation	IR band position (cm^{-1})	Total IR band area (cm^{-2})*	Total IR peak height (cm^{-1})†	IR peak height ~E‖a (cm^{-1})	IR unpolarized band area (001) (cm^{-2})
I. Samples used to determine absorption coefficient.							
GRR968	Microcline, Elizabeth R Mine, CA	H_2O	3290, 3450, 3575, 3630	13061	56.5	25.2	6768
GRR1281	Microcline, White Queen Mine, CA	H_2O	3280, 3450, 3575, 3626	23232	81.3	42.9	8799
GRR638	Sanidine, Eifel, Germany	OH	3390-3412, 3250, 3061	2075	5.19	2.58	778
GRR1280	Oligoclase, Black Rock Pass, NV	OH	3100-3200, 3425	3979	8.56	5.54	1105
GRR580 (H.M.M.81228)	Oligoclase, SC	OH	3167-3189, 3450, 3600	1931	3.74	2.38	444
GRR1389 (CIT13759)	Andesine, Halloran Springs, CA	OH	3169, 3219, 3350, 3580	4908	9.45	5.68	657
GRR1968	Anorthite, Miyake Island, Japan	OH	3160-3215, 3550	1688	3.58	2.68	465
I. Samples not used to determine absorption coefficient.							
GRR1605	Albite, Amelia, VA	fluid inclusions	3450	-	-		
		OH	2995, 3344, 3367, 3400, 3429, 3466, 3489, 3506, 3514, 3562, 3599, 3626‖	-	-		
		total		789	-		
GRR1608	Albite, Governador Valadaras	fluid inclusions	3450	-	-		
		OH	2999, 3236, 3296, 3340, 3405, 3435, 3471, 3506, 3516, 3564, 3599, 3626‖	-	-		
		total		2600	-		
GRR1609	Albite, Sao Jose da Safira	fluid inclusions	3450	-	-		
		OH	2995, 3124, 3220, 3241, 3294, 3342, 3345, 3431, 3467, 3491, 3506, 3516, 3562, 3599, 3626‖	631#	1.4#		
		total		992	-		
GRR1610	Albite, Calaveras, CA	fluid inclusions	3450	659	-		

*Area of polarized bands ($\Delta_X+\Delta_Y+\Delta_Z$) in 2600-3900 cm^{-1} region.

† Sum of maximum band height ($A_X+A_Y+A_Z$) in 2600-3900 cm^{-1} region.

‡ Determined by manometry (Hofmeister and Rossman 1985a and 1985b).

§ Determined by ^{1}H MAS NMR (Yesinowski et al. 1988).

|| Band position determined from 77 K spectra.

Area estimated from X and Y spectra only.

Table 2.2. Continued.

Sample Number	NMR ^{1}H δ (TMS)	NMR [H] (ppm H_2O wt.)	[H] previous work (ppm H_2O wt.)	Density (g/cm^3) ± 2σ	NMR [H] (mol H_2O/L mineral)
I. Samples used to determine absorption coefficient.					
GRR968	4.7	1000	1000‡, 1100§	2.556 ± 0.017	0.142
GRR1281	4.7	1350	1300‡, 1500‡, 1400§	2.585 ± 0.018	0.194
GRR638	4.7	170	170‡	2.563 ± 0.009	0.024
GRR1280	6.0, 4.7	230		2.641 ± 0.025	0.034
GRR580 (H.M.M.81228)	6.0, 4.7	290		2.653 ± 0.019	0.043
GRR1389 (CIT13759)	4.0, 6.0	510		2.661 ± 0.017	0.075
GRR1968	4.7, 6.0	210		2.768 ± 0.036	0.032
I. Samples not used to determine absorption coefficient.					
GRR1605	4.7	~280			
	-				
GRR1608	4.7	~50			
	-				
GRR1609	4.7	~40			
	-				
GRR1610	4.7	~140			

Table 2.3. Polarized band areas and heights of feldspar mid-IR spectra.

Sample Number	Mineral name	Proton speciation	IR band position (cm^{-1})	Total IR band area (cm^{-2})*	IR band area Δ_X (cm^{-2})‡	IR band area Δ_Y (cm^{-2})‡	IR band area Δ_Z (cm^{-2})‡	Total IR peak height (cm^{-1})†	IR peak height A_X (cm^{-1})‡	IR peak height A_Y (cm^{-1})‡	IR peak height A_Z (cm^{-1})‡
GRR968	Microcline, Elizabeth R Mine, CA	H_2O	3290, 3450, 3575, 3630	13061	8010	2791	2260	56.5	25.2	8.2	23.1
GRR1281	Microcline, White Queen Mine, CA	H_2O	3280, 3450, 3575, 3626	23232	12764	3583	6885	81.3	42.9	9.5	28.9
GRR638	Sanidine, Eifel, Germany	OH	3390-3412, 3250, 3061	2075	903	487	685	5.19	2.58	0.97	1.64
GRR1280	Oligoclase, Black Rock Pass, NV	OH	3100-3200, 3425	3979	2496	1290	193	8.56	5.54	2.60	0.42
GRR580 (H.M.M. 81228)	Oligoclase, SC	OH	3167-3189, 3450, 3600	1931	1219	521	191	3.74	2.38	1.03	0.33
GRR1389 (CIT13759)	Andesine, Halloran Springs, CA	OH	3169, 3219, 3350, 3580	4908	2836	1298	774	9.45	5.68	2.32	1.45
GRR1968	Anorthite, Miyake Island, Japan	OH	3160-3215, 3550	1688	221	1166	301	3.58	0.41	2.68	0.49

* Area of polarized bands ($\Delta_X+\Delta_Y+\Delta_Z$) in 2600-3900 cm^{-1} region.

† Sum of maximum band height ($A_X+A_Y+A_Z$) in 2600-3900 cm^{-1} region.

Figure 2.1. Polarized mid-IR spectra of feldspars at 298 K, normalized to 1 mm sample thickness. Spectra are shifted vertically for comparison. (a) Spectra of sanidine and plagioclase with An ≥ 25. (b) Spectra of microclines. (c) Spectra of pegmatitic and metamorphic albites.

Figure 2.1A.

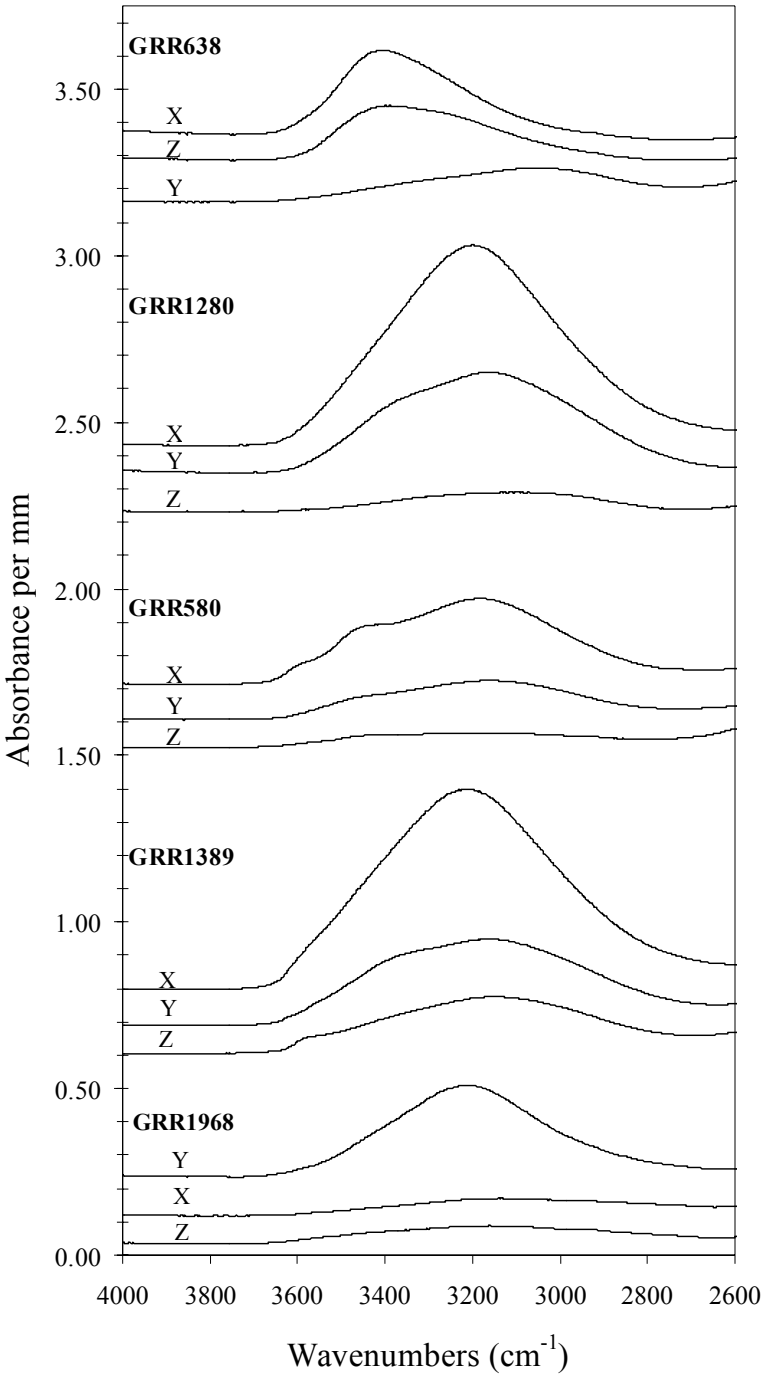
GRR638
X
Z
Y
GRR1280
X
Y
Z
GRR580
X
Y
Z
GRR1389
X
Y
Z
GRR1968
Y
X
Z
3.50
3.00
2.50
2.00
1.50
1.00
0.50
0.00
Absorbance per mm
4000
3800
3600
3400
3200
3000
2800
2600
Wavenumbers (cm-1)

Figure 2.1B.

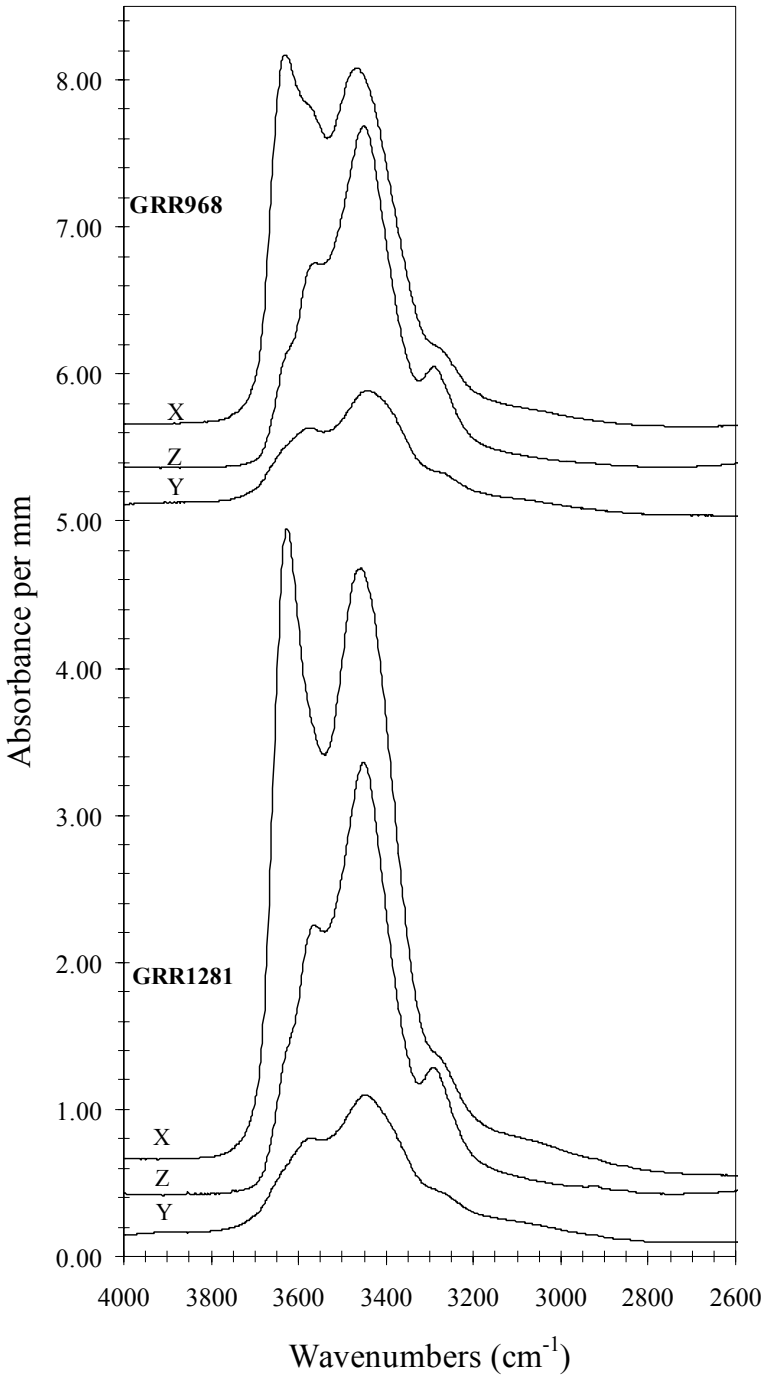
8.00
7.00
6.00
5.00
4.00
3.00
2.00
1.00
0.00
GRR968
X
Z
Y
GRR1281
X
Z
Y
Absorbance per mm
4000
3800
3600
3400
3200
3000
2800
2600
Wavenumbers (cm-1)

Figure 2.1C.

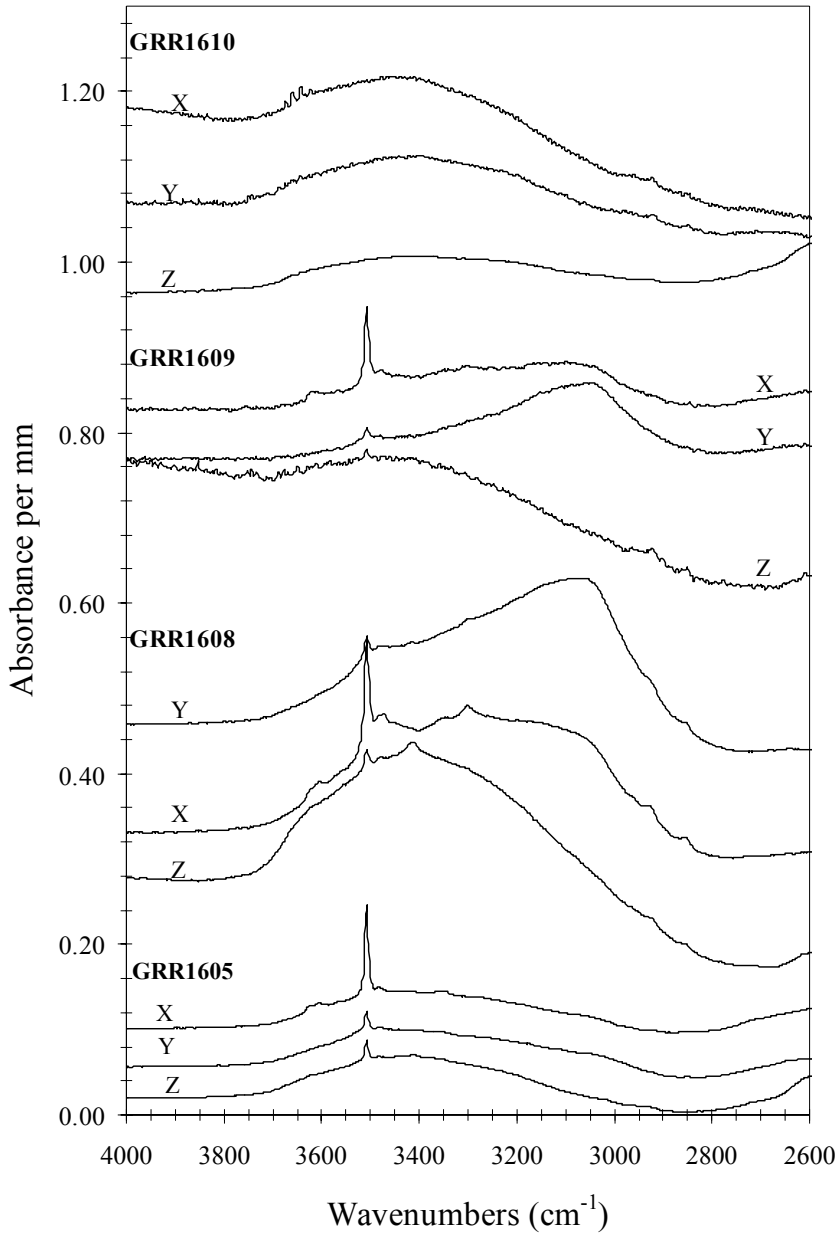
GRR1610
X
Y
Z
GRR1609
X
Y
Z
GRR1608
Y
X
Z
GRR1605
X
Y
Z
1.20
1.00
0.80
0.60
0.40
0.20
0.00
Absorbance per mm
4000
3800
3600
3400
3200
3000
2800
2600
Wavenumbers (cm-1)

Figure 2.2. Mid-IR spectra of pegmatitic albites, water, and ice at 298 K and 77 K. The feldspar spectra are normalized to 1 mm thickness, and the water and ice bands are scaled to approximately 0.15 μm thickness. Spectra are shifted vertically for comparison.

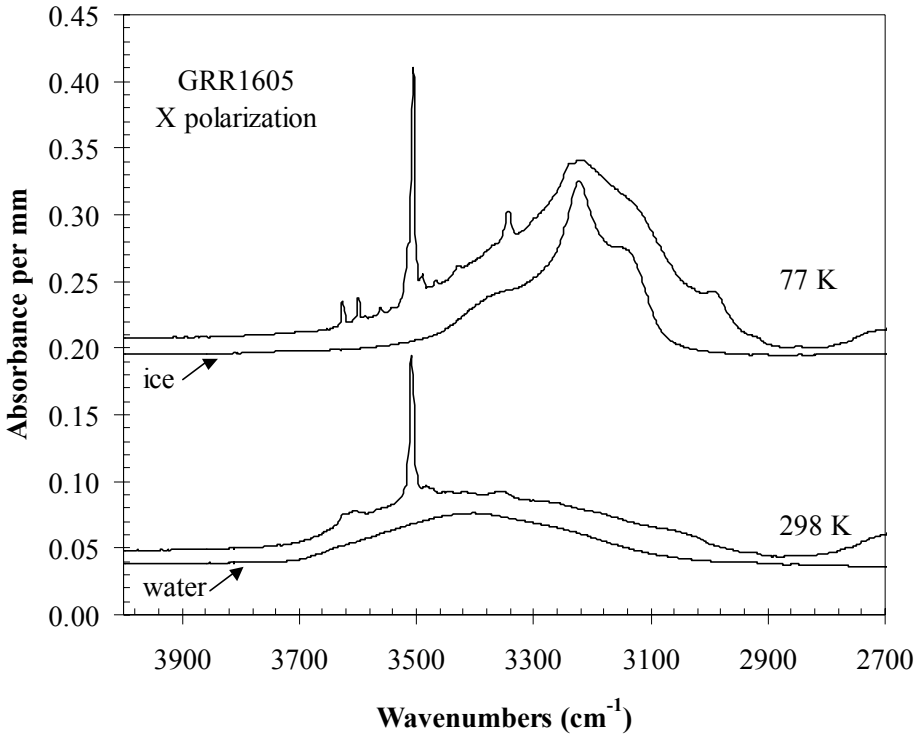

Figure 2.2 continued.

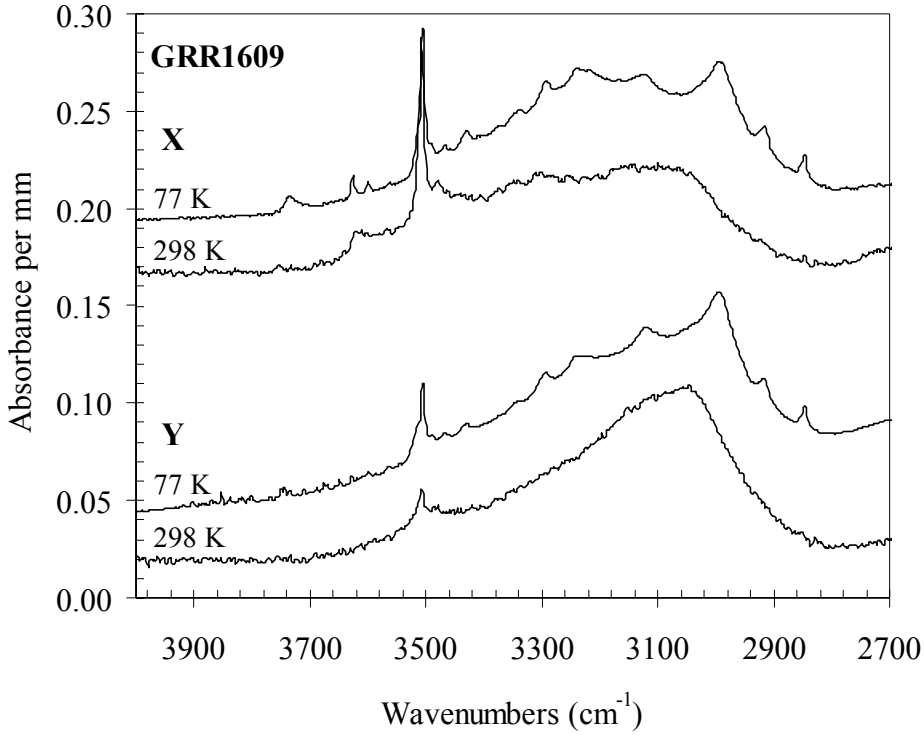

Figure 2.3. Near-IR spectra of feldspars, water, and ice. (a) Unpolarized spectra of plagioclase (298 K) and sanidine (77 K). (b) Polarized spectra of microcline. (c) Unpolarized spectra of a pegmatitic albite and water and ice at 298 K and 77 K. All feldspar spectra are normalized to 1 cm sample thickness, and water and ice spectra are scaled to 25 μm thickness from 150 μm. Spectra are shifted vertically for comparison.

Figure 2.3A.

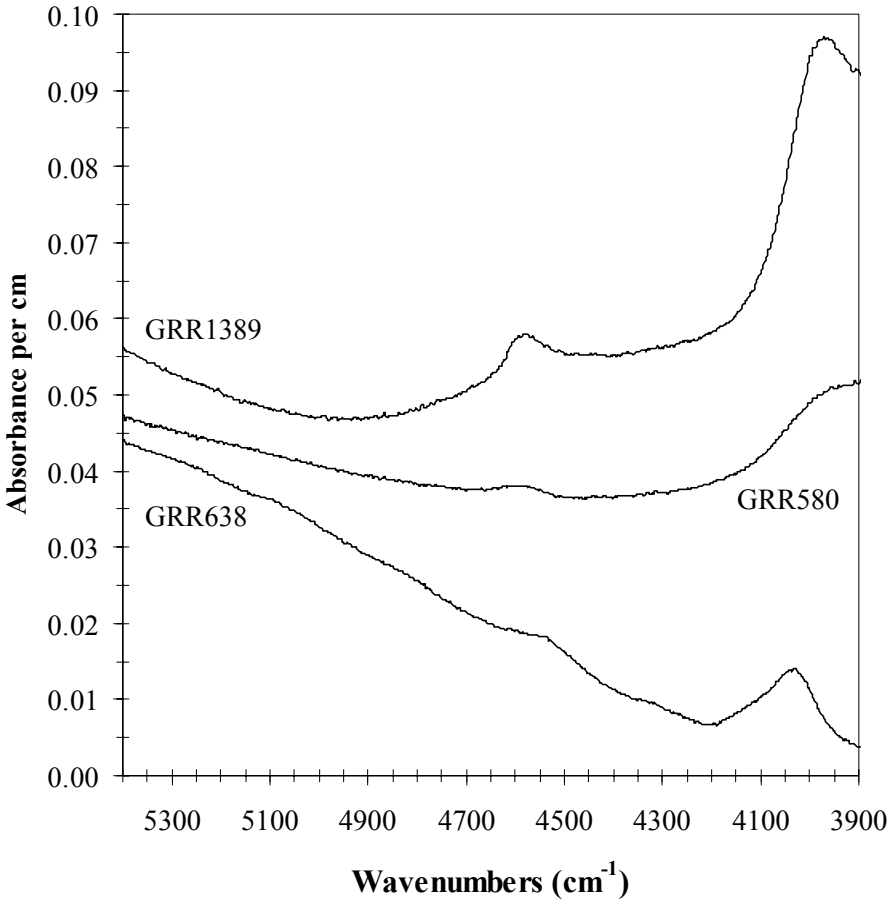

Figure 2.3B.

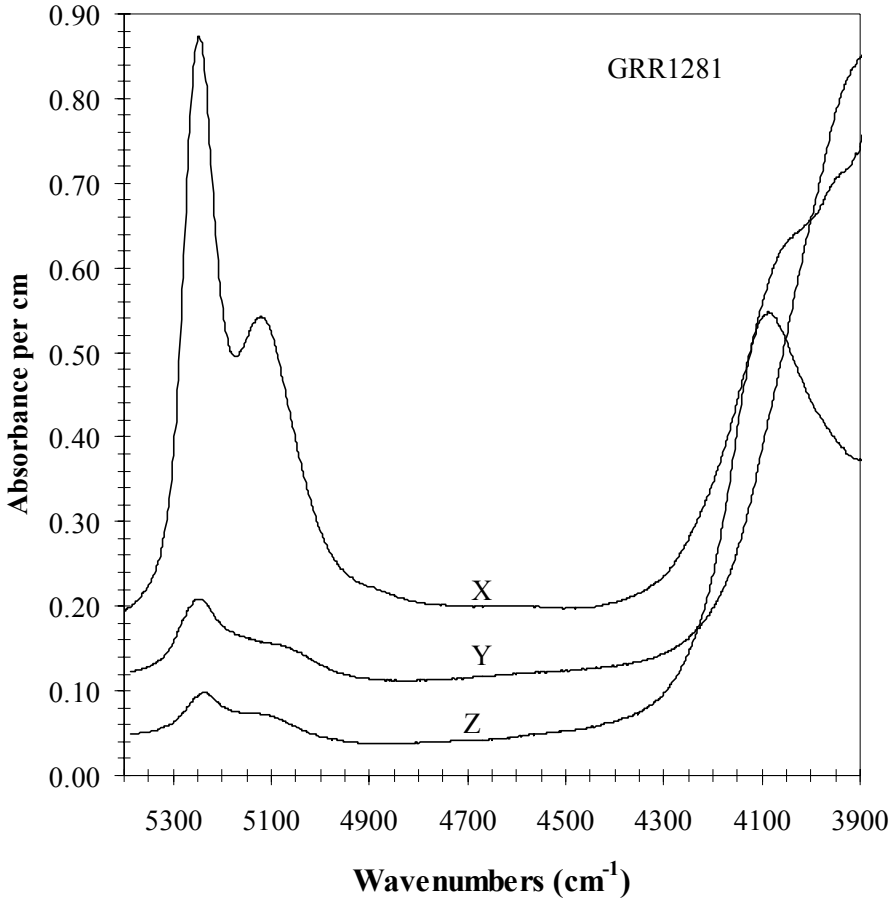
GRR1281
X
Y
Z
Absorbance per cm
0.90
0.80
0.70
0.60
0.50
0.40
0.30
0.20
0.10
0.00
5300
5100
4900
4700
4500
4300
4100
3900
Wavenumbers (cm-1)

Figure 2.3C.

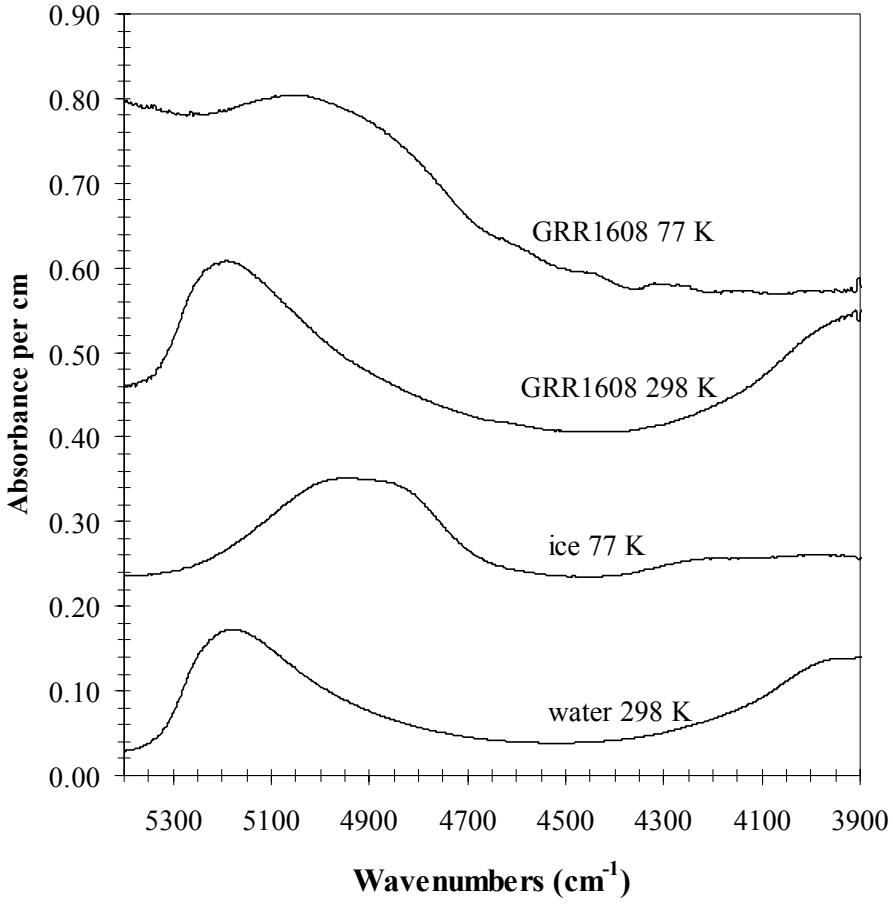
0.90
0.80
0.70
0.60
0.50
0.40
0.30
0.20
0.10
0.00
Absorbance per cm
GRR1608 77 K
GRR1608 298 K
ice 77 K
water 298 K
5300
5100
4900
4700
4500
4300
4100
3900
Wavenumbers (cm-1)

Figure 2.4. ^{1}H MAS NMR spectra. (a) Raw data and spectrum with background subtracted for GRR1389, spectrum of anhydrous labradorite, and spectrum of an empty rotor. The narrow band at 1.5 ppm is due to organic material. (b) Spectra of feldspars. Subtraction of background was done for samples containing only structural OH.

Figure 2.4A.

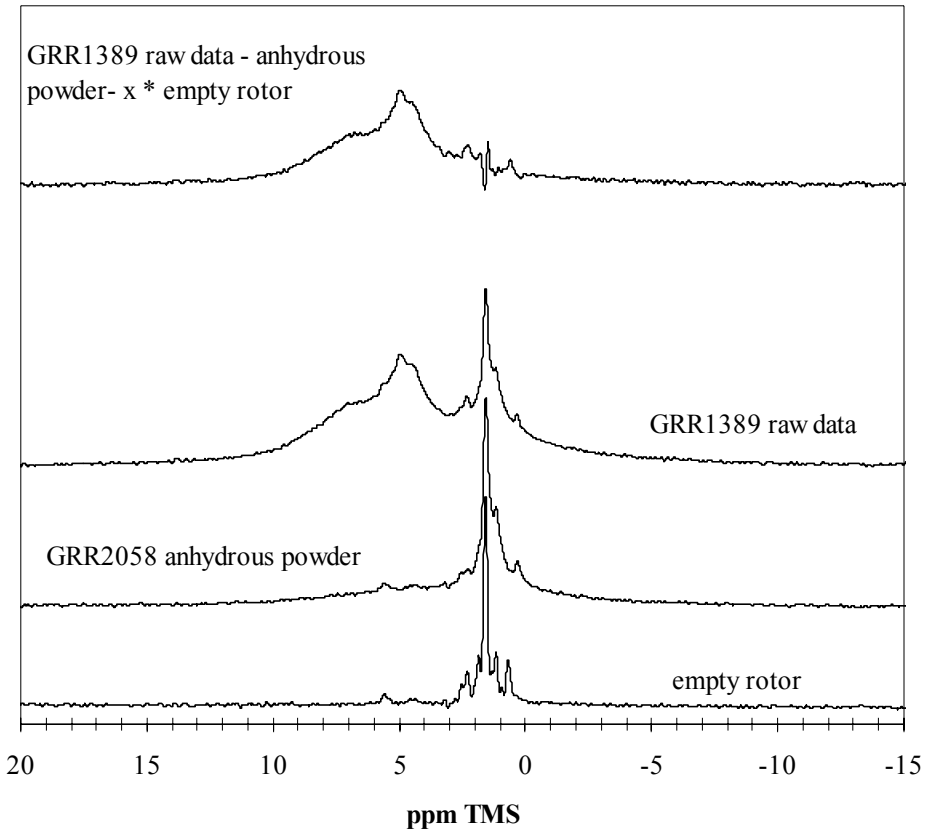

Figure 2.4B.

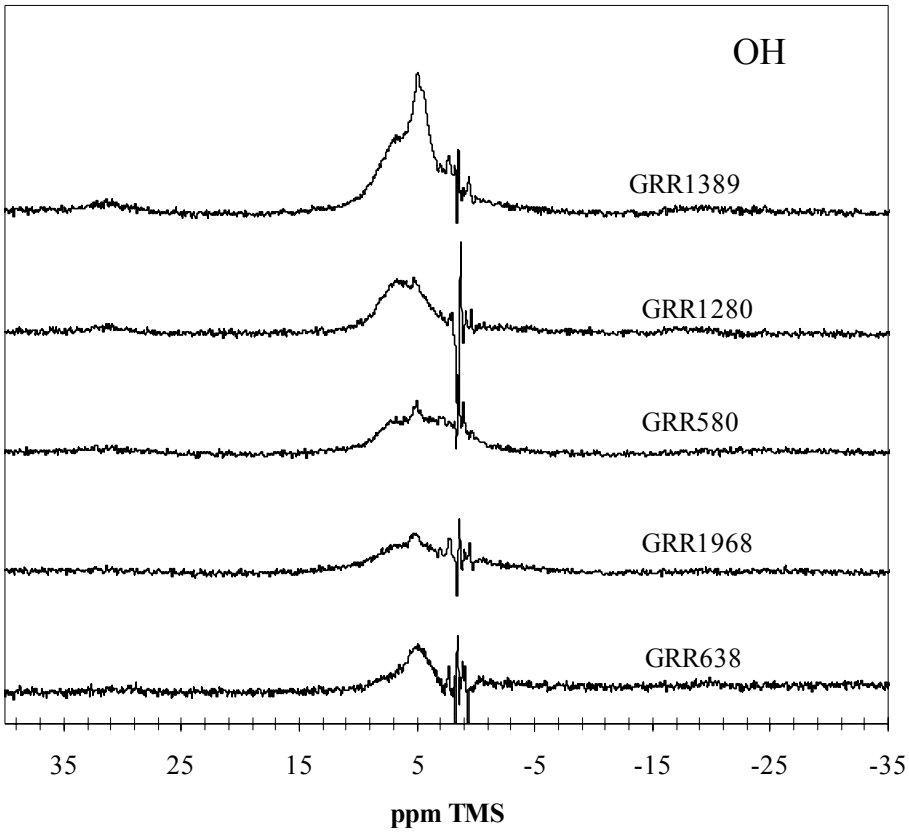
OH
GRR1389
GRR1280
GRR580
GRR1968
GRR638
35
25
15
5
-5
-15
-25
-35
ppm TMS

Figure 2.4B continued.

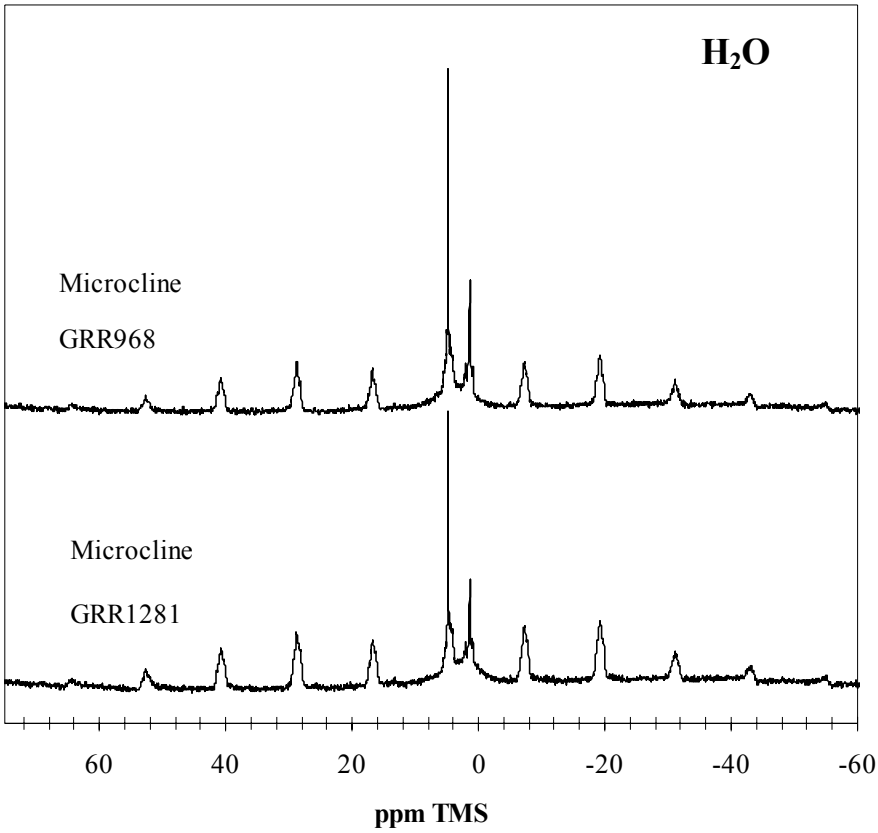

Figure 2.4B continued.

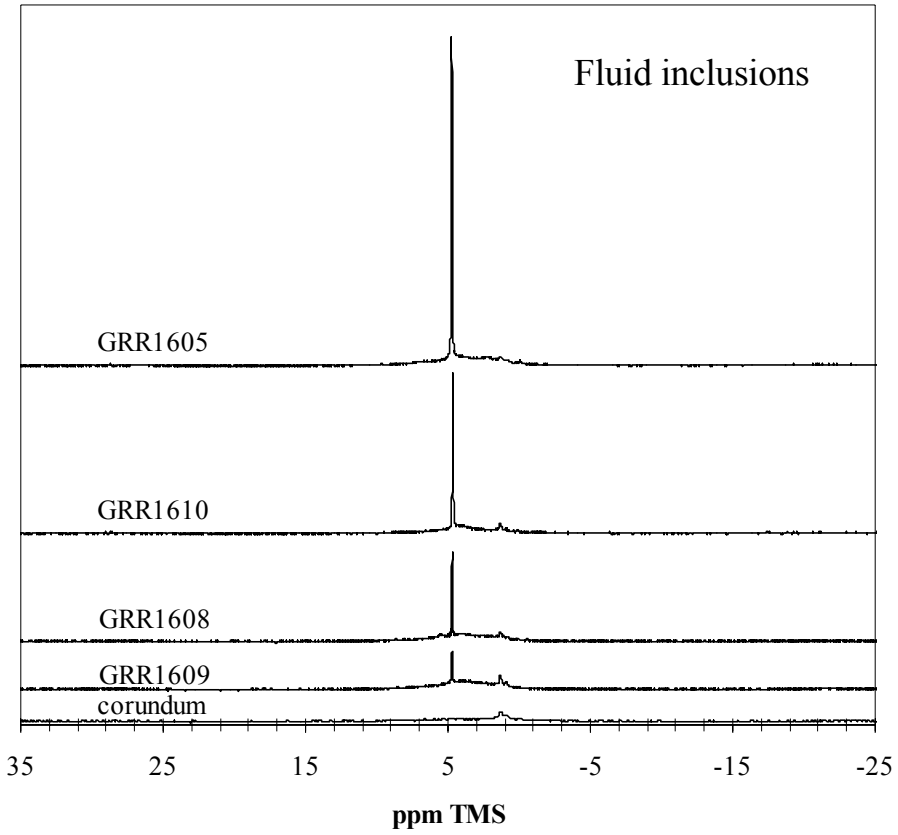

Figure 2.5. (a) Total polarized integrated band area in the mid-IR per cm thickness versus the concentration of H (in ppm H_2O by weight) determined from NMR for feldspars containing structural hydrogen. The slope of the best-fit line through the data is the absorption coefficient (I'). (b) Total polarized maximum band height (c) maximum band height E||*a* and (d) unpolarized band area on (001) cleavage flake versus H concentration.

Figure 2.5A.

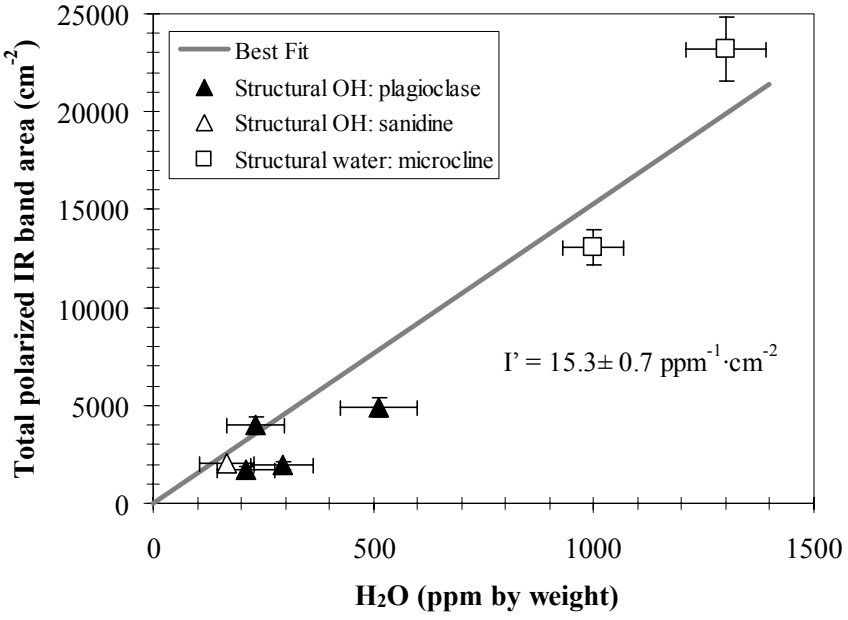

Figure 2.5B.

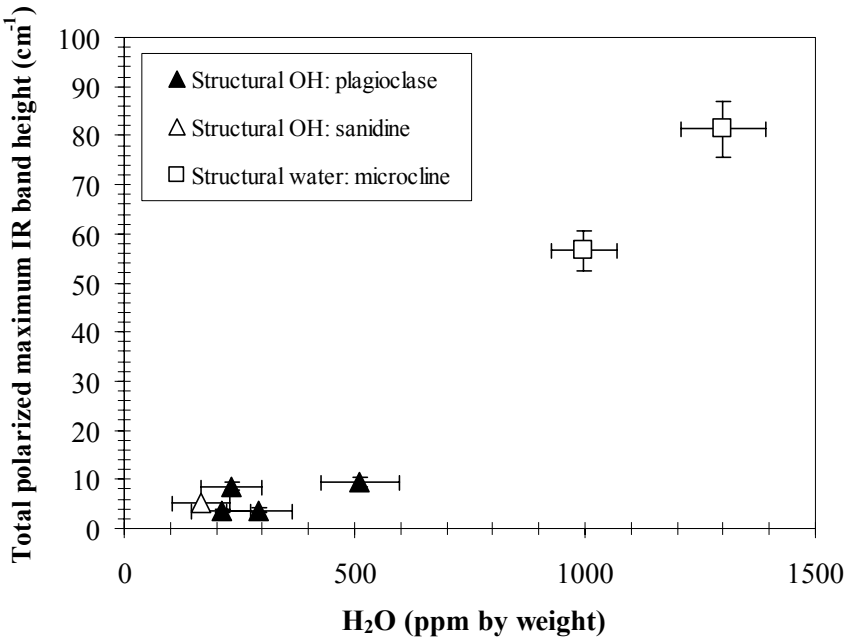

Figure 2.5C.

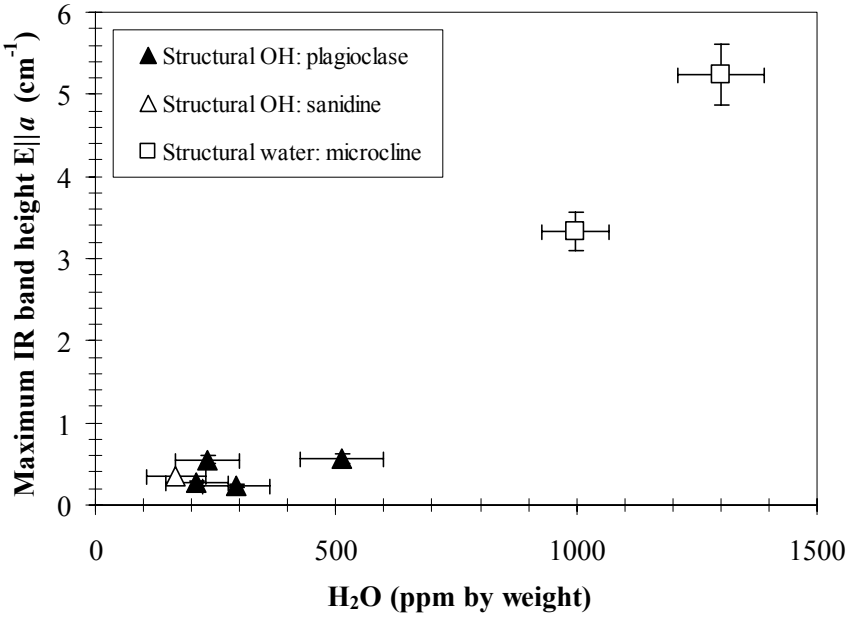

Figure 2.5D.

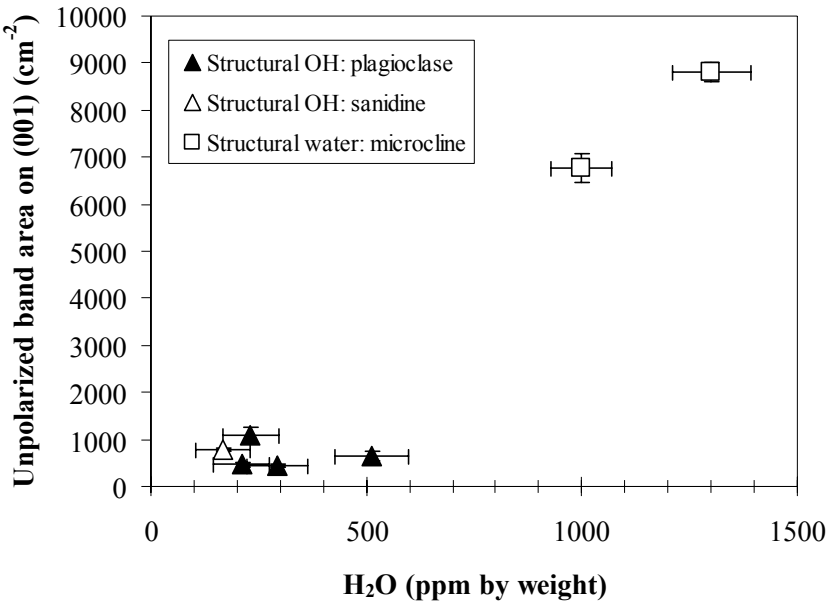
Unpolarized band area on (001) (cm-2)
10000
9000
8000
7000
6000
5000
4000
3000
2000
1000
0
Structural OH: plagioclase
Structural OH: sanidine
Structural water: microcline
0
500
1000
1500
H2O (ppm by weight)

Chapter 3

A SURVEY OF HYDROUS SPECIES AND CONCENTRATIONS IN IGNEOUS FELDSPARS[2]

Abstract

The hydrous components in 85 feldspars from various igneous environments spanning the range of naturally occurring compositions were examined with infrared spectroscopy. The feldspars contain structural OH (0-512 ppm H_2O), H_2O (0-1350 ppm H_2O), and NH_4^+ (0-1500 ppm NH_4^+) groups as well as fluid inclusions and alteration products. Although composition and structure do influence the type of hydrous species that can be incorporated into a particular feldspar mineral, the concentration of these species is not controlled by major element composition. Coarse perthitic microclines have a heterogeneous distribution of hydrous species, and contain H_2O or NH_4^+ in K-rich lamellae and fluid inclusions in Na-rich areas. The structural OH in plagioclase

[2]Submitted to American Mineralogist.

feldspars is not associated with twin boundaries or exsolution lamellae. All of the possible structural hydrous species are found in pegmatite feldspars, whereas volcanic feldspars contain only structural OH. The variation in OH concentration within a given feldspar composition suggests that fluids in the geologic environment play a role in determining the hydrogen concentration of each sample. The vast majority of plutonic feldspars have undergone partial or total equilibration with meteoric fluids during low-temperature (400-150°C) hydrothermal exchange, obliterating any structural hydrogen and creating substantial concentrations of fluid inclusions (up to 4000 ppm H_2O) in the exchanged regions. The amount of water stored as fluid inclusions within feldspars in the upper crust (1×10^{19} kg) is small compared to the 1.35×10^{21} kg of water in the oceans, but is roughly equivalent to the reservoir of water stored in hydrous minerals in the upper crust.

Introduction

There have been a number of surveys of hydrous species and their concentrations in anhydrous minerals, including garnets, pyroxenes, and olivine (Aines and Rossman 1984; Miller et al. 1987; Skogby et al. 1990). Much effort has gone into understanding the concentration and behavior of

hydrous species in mantle minerals (Bell 1992; Bell and Rossman 1992a; Bell and Rossman 1992b; Bell 1993; Ingrin and Skogby 2000). However, there has been no systematic survey of trace hydrogen in feldspar group minerals, even though the feldspars are the most abundant minerals in the Earth's crust, and the textural and structural properties of feldspars are affected by the presence of water.

The occurrence of hydrogen-bearing species in feldspars has not been thoroughly explored, although many infrared studies report the presence of structural OH, H_2O, and NH_4^+ (Wilkins and Sabine 1973; Hofmeister and Rossman 1985a; Hofmeister and Rossman 1985b; Hofmeister and Rossman 1986; Smith and Brown 1988; Solomon and Rossman 1988; Kronenberg et al. 1996; Johnson and Rossman 2003). Infrared spectroscopy is particularly sensitive to the speciation of hydrogen, but determination of an absorption coefficient relating hydrogen concentration to infrared band height or area is necessary to determine absolute concentrations of these hydrous species. Recently, the infrared absorption coefficient for OH and H_2O in feldspars was determined for plagioclase and microcline using NMR spectroscopy (Johnson and Rossman 2003). The absorption coefficient for NH_4^+ in microcline has also been estimated (Solomon and Rossman 1988). These calibrations make it possible to efficiently determine both the hydrogen speciation and concentration for a large number of feldspars.

A clearer picture of the nature of hydrous components in feldspars is crucial because many of the physical, textural and chemical features of feldspars are profoundly affected by fluid-mineral interactions and by the hydrous species themselves. It has been hypothesized that thermal and compositional transformations of the aluminosilicate structure in feldspars could be catalyzed by the presence of H_2O if H^+ and OH^- acted to break tetrahedral bonds (Donnay et al. 1960). Laboratory studies have shown that this may indeed be the case, because the rate of Al-Si disordering in ordered feldspar structures increases with water pressure (Yund and Tullis 1980; Goldsmith 1986; Goldsmith 1987; Goldsmith 1988). The rate of oxygen self-diffusion in feldspars shows a strong positive correlation with H_2O pressure in experimental hydrothermal systems (Farver and Yund 1990). This phenomenon has been explained by the rapid diffusion of water molecules in the feldspar (Zhang et al. 1991a).

Furthermore, plutonic alkali feldspars have a higher degree of Al-Si ordering, and have developed coarsened exsolution lamellae, where fluids were available during their cooling history (Ragland 1970; Parsons and Boyd 1971; Parsons 1978). It has been suggested that local textural heterogeneity within a single perthite is due to local fluid conditions (Yund and Ackermand 1979). Hydrous components also greatly modify the susceptibility of feldspars to the effects of ionizing radiation (Hofmeister and Rossman 1985a; Hofmeister and

Rossman 1985b; Hofmeister and Rossman 1986) and influence their mechanical strength (Tullis and Yund 1980).

In this paper we report the results of a broad survey of the infrared spectra of igneous feldspars in which we determine (1) the structural and non-structural hydrous species commonly present in plagioclases and alkali feldspars from a wide variety of geologic environments, (2) their approximate ranges in concentration, and (3) the general relationships between hydrous speciation and concentration, crystal composition, and the geologic environment. The results of this survey provide a basis for more detailed investigations of the role of water in structural and compositional transformations in feldspars.

Methods

Feldspar samples

Infrared spectra were obtained on 85 feldspars. Table 3.1 describes the approximate compositions, localities, and petrogenesis of feldspars used in our survey. These samples have experienced a diverse set of crystallization and subsolidus conditions in environments which include mafic to silicic volcanic flows, mafic to silicic plutons (both epizonal and deeper), and pegmatites and veins. Compositions span the range of those typical for naturally occurring feldspars and include potassium feldspars of various structural states.

Elemental analyses of selected feldspars were obtained at Caltech on a JEOL JXA-733 electron microprobe at 15 keV and 25 nA, using a 10 μm beam size. Oxide totals were calculated using the CITZAF correction software (Armstrong 1995). Major-element analyses for other feldspars were obtained at 20 kV accelerating voltage using an Oxford Instruments INCA EDS analysis system on a LEO 1550 VP field emission SEM.

Spectroscopic measurements

Polarized mid-infrared (MIR) transmission spectra were obtained in the range 2600 cm^{-1} to 4000 cm^{-1} for all of the samples, and where sample quality permitted, polarized near-infrared (NIR) spectra were taken between 4000 cm^{-1} and 7500 cm^{-1}, usually on separate, thicker pieces of the same specimen. The absorption intensity of bands resulting from NIR OH overtone or combination-type vibrations is about 100 times smaller than those for fundamental IR OH stretching vibrations. Therefore, samples with negligible amounts of hydrous components or with low transmission characteristics were unsuitable for NIR investigation. For all feldspars that contained structurally bound hydrous species, three mutually perpendicular spectra were taken to determine the total band area or band intensity. For samples containing fluid inclusions, melt inclusions, or alteration products, the band intensities of unpolarized spectra were used to determine hydrogen concentration.

Infrared spectra were taken with a Nicolet Magna 860 FTIR spectrometer at 4 cm^{-1} resolution and were averaged over 256 scans. Mid-IR spectra were obtained using a CaF_2 beamsplitter, infrared source, MCT-A detector, and $LiIO_3$ Glan-Foucault prism polarizer or a wire grid on CaF_2 polarizer. Near-IR spectra were obtained using a visible light source and CaF_2 beamsplitter with an MCT-B or MCT-A detector. For large homogeneous crystals or to obtain average spectra on heterogeneous materials, spectra were taken in the main compartment of the spectrometer using a 1000 μm or 600 μm circular aperture. A Spectra-Tech Continuμm® microscope accessory was used to evaluate heterogeneity in large samples and to measure spectra on smaller samples with a square aperture 100-150 μm on a side. Low-temperature infrared spectra were obtained at 77 K using a homebuilt vacuum chamber in the main compartment of the FTIR spectrometer.

The polished sample slabs ranged in thickness from 0.20 mm to 1 cm. In some cases where it proved difficult to remove phenocrysts from their rock matrices, rock slabs were cut and polished parallel to the feldspar cleavage surfaces to expose the sample.

Determination of structural hydrous species

The hydrous species encountered as structural components in feldspar in previous studies are H_2O, OH, and NH_4^+. These species can be distinguished

from one another by their characteristic stretching frequencies in the mid-IR and overtones in the near-IR. Molecular water has three fundamental vibrations. The symmetric and asymmetric OH stretching vibrations are found in the 3000 cm^{-1} to 3700 cm^{-1} region. Their exact frequencies depend upon the hydrogen bonding distances between the OH in the water and surrounding oxygens in the enclosing crystalline framework (Nakamoto et al. 1955). The asymmetric stretch is usually higher in frequency than the symmetric stretch by about 100 cm^{-1}, although distortion of the water molecule due to hydrogen bonding interactions with the crystal structure can increase this energy difference. The third vibrational frequency for molecular water is caused by symmetric bending, and occurs at around 1625 cm^{-1}. In infrared spectra of feldspars, this band is obscured by the much more intense absorption from the aluminosilicate framework. In contrast to molecular water, an OH group has only one fundamental stretching vibration that occurs in the same energy region as the H_2O stretch frequencies. H_2O and OH groups can be distinguished from each other based on bend + stretch combination bands in the near-IR. Molecular water exhibits a bend + stretch absorption at ~5240 cm^{-1} which arises from the combination of the 1625 cm^{-1} and the asymmetric stretch at approximately 3620 cm^{-1}. Hydroxyl does not have an IR-allowed bending mode, but it does have a librational bend when it is bonded to Si or Al. This frequency is generally found around 1000 cm^{-1} in silicate minerals

and glasses (Stolper 1982a), and the combination librational bend + stretch band is at about 4540 cm^{-1}. Bands at 5200 cm^{-1} and 4540 cm^{-1} are used to distinguish between H_2O and OH, respectively.

The IR-active NH_4^+ stretching frequencies are degenerate but typically split into numerous bands in the 2800-3350 cm^{-1} range. The ammonium ion in buddingtonite ($(NH_4^+)AlSi_3O_8$) has at least three stretch + bend overtones from 4400-5000 cm^{-1} (Solomon and Rossman 1988).

Structural species in feldspars are expected to be anisotropic because of the low symmetry of the feldspar structures (monoclinic and triclinic). On the other hand, non-structural species such as fluid inclusions, melt inclusions, and alteration are isotropic in nature (unless alteration minerals are somehow preferentially aligned along crystallographic directions), and can be distinguished from structural species with polarized infrared measurements.

Determination of absolute hydrogen concentration

The Beer-Lambert law provides the quantitative relationship between the concentration of hydrous species and the intensity of their absorption peaks:

$$c = \frac{18.02 \times A}{t \times \rho \times \varepsilon} \times 10^6, \quad (3.1)$$

where c is the concentration of the hydrous species in ppm H_2O by weight, 18.02 is the molecular weight of H_2O, A is the height of the absorption band, t is the thickness of the sample in cm, ρ is the density of the sample in g/L, and ε is the molar absorption coefficient in L/mol·cm. The height of the absorption band was determined after correction for background absorbance. Whenever possible, a linear correction using the slope of the spectrum on both sides of the OH stretch region was used. At low concentrations of hydrous species, the background was not linear due to absorption by silicate overtone modes, and in these cases a smoothly curving background was interpolated under the absorption bands.

The value of the molar absorption coefficient depends on the speciation of hydrogen and the phase in which it is hosted. For melt inclusions, we used an ε of 67 ± 7 L/mol·cm determined for hydrous components in glasses (Stolper 1982a). For fluid inclusions, we used value of ε of 115 ± 6 L/mol·cm from Clunie et al. (1966), determined for water and a 1 M potassium chromate solution at 2.93 μm. This molar absorption coefficient is slightly higher but similar to the value of ε (81 L/mol·cm) reported in Thompson (1965). To determine the concentration of NH_4^+, we used the calibration estimated by Solomon and Rossman (1988) for buddingtonite. In this case, the molar absorption coefficient ε is 162 L/mol·cm and is used with a value of A equal to

the height of the 3220 cm^{-1} band in the *E*||*X*' polarization direction in (001). The molecular weight of NH_4^+ (18.04 g/mol) replaces the molecular weight of water in Equation 3.1.

Selection of an appropriate absorption coefficient for the amount of hydrogen found in hydrous alteration products of feldspars was more difficult. We measured the absorption intensity of the OH band at 3620 cm^{-1} for illite in a KBr pellet taken from a spectrum used in Potter and Rossman (1977). The illite contains 6.70 wt% H_2O, and 0.50 mg of the illite was used in a 200 mg KBr pellet. From this data, the ε for OH in hydrous alteration products is estimated as about 120 L/mol·cm. This value is within the range of reasonable ε estimates for bands in this region, but absolute concentrations determined using this absorption coefficient may vary from true concentrations by as much as a factor of 2-3 considering the uncertainty in orientation of the fine-grained materials within the KBr pellet and the feldspars themselves, as well as the likely possibility that alteration products other than illite (such as epidote) are present.

A modified form of the Beer-Lambert law was used to determine the concentration of structural OH and H_2O in feldspars:

$$\Delta = I \times c \times t, \quad (3.2)$$

where Δ is the total integrated area of bands in the region of interest ($\Delta_X + \Delta_Y + \Delta_Z$; *X*, *Y*, and *Z* are the principal optical directions), and *c* is expressed as moles H_2O/L mineral. In this case, the absorption coefficient becomes the integral molar absorption coefficient (*I*, L/(mol·cm^2)). When *c* is expressed as ppm H_2O by weight, the absorption coefficient becomes the integral specific absorption coefficient (*I'*, ppm^{-1}·cm^{-2}). For OH and H_2O in natural alkali and potassium feldspars, the specific integral absorption coefficient *I'* is 15.3 ± 0.7 ppm^{-1}·cm^{-2} and the molar integral absorption coefficient *I* is 107000 ± 5000 L/(mol H_2O·cm^2) (Johnson and Rossman 2003).

A discussion of the importance of measuring polarized IR spectra in anisotropic minerals is given in Dowty (1978). Although measurement of six vibration directions is needed to fully characterize the anisotropy of bands in monoclinic and triclinic minerals, only three mutually perpendicular polarized spectra are needed to determine total band intensity and area for concentration determinations. Polarized measurements with the electric vector vibrating parallel to the three principal optical directions are preferred (*E*||*X*, *E*||*Y*, *E*||*Z*; *X*, *Y*, and *Z* are the principal optical directions); however, Johnson and Rossman (2003) showed experimentally that any three mutually perpendicular spectra will give the same integrated band area within ± 5% relative error. The difficulty of orienting polished slabs perpendicular to principal optic axes

for triclinic feldspars made it necessary to use this simplified approach for most of the OH- and H_2O-bearing feldspars in this study. In many cases, at least two of the polarized spectra are taken parallel to the projection of principal optical directions onto a cleavage plane, because often one polished slab was created with faces parallel to the {001} or {010} cleavages. These spectra are labeled as *E||X'*, *E||Y'*, and *E||Z'*. The orientation of the principle optical directions rotates with respect to the crystallographic directions as a function of plagioclase composition, and in some cases a spectrum is labeled with the closest crystallographic direction (E||**a'**) so that spectra from samples of different compositions can be compared.

For feldspar samples containing more than one hydrous species, it was necessary to deconvolve the signal due to each species in order to determine their respective concentrations. For feldspars with heterogeneous distributions of hydrous species, it was possible to take spectra in more than one area of the grain to maximize signal from one species while minimizing the effect seen by the other. In other cases, it was necessary to estimate the relative proportion of species by measurement of maximum band intensity. The fluid inclusion component was estimated in some cases by observing the spectrum at 77 K, in which the liquid water bands shift to lower-frequency ice bands. A few samples contained both H_2O and OH structural groups. The broad bands

overlapped to such an extent that the signals were not deconvolved for these feldspars.

Results and Discussion

Characterization of structural and non-structural hydrous species

Assignment of the hydrous species and band types for each feldspar sample are given in Table 3.1, and Figure 3.1 provides examples of each type of hydrous species found in feldspars in this survey. Definitions of the various band types, including polarization, band positions, and approximate MIR band widths, are outlined in Table 3.2.

Characteristics of the mid-IR (2600-3700 cm^{-1}) and near-IR (4000-5300 cm^{-1}) regions of the feldspar spectrum have been previously reported for a number of feldspar compositions (Hofmeister and Rossman 1985a; Hofmeister and Rossman 1985b; Hofmeister and Rossman 1986; Solomon and Rossman 1988; Kronenberg et al. 1996; Johnson and Rossman 2003). The features used to classify each spectral type are (1) the position and number of MIR and NIR absorption bands, as discussed for different hydrous species in the methods section; (2) degree of anisotropy of absorption bands; and (3) behavior of the

spectra at low temperatures (77 K). Infrared bands in feldspars are categorized as follows:

Structural hydrous species

Type I OH

Anisotropic, narrow bands are found at 3500-3600 cm^{-1} with a much broader band also present at 3100 cm^{-1} (Figure 3.1a). At 77 K, additional sharp bands are visible, and these are presumably also due to OH. Fluid inclusions are often associated with this type of OH, and manifest themselves as broad isotropic bands at about 3450 cm^{-1} that shift to ice bands at 77 K (Johnson and Rossman 2003). The narrow OH bands are only found in spectra of low albite.

Type IIa OH

These bands are very broad and are centered at about 3100, 3400, and 3600 cm^{-1}. The maximum intensity of these bands is always closely aligned with the **a** crystallographic axis (Figure 3.1b). Alkali feldspars and plagioclase other than low albite contain this type of OH.

Type IIb OH

This category of infrared bands is similar to Type IIa OH bands, but in this case the band at 3050 cm^{-1} is most intense in the *Y* (**b**) direction, with the other

OH bands around 3400 cm^{-1} most intense in *X*. This type of OH band is apparently restricted to spectra of sanidine.

Type I H_2O

This type of structurally bound water molecule is represented by a pair of antisymmetric + symmetric stretches (Figure 3.1c; 3620 cm^{-1} most intense in *X*; 3550 cm^{-1} most intense in *Z*).

Type II H_2O

As seen in Figure 3.1c, the antisymmetric and symmetric stretches of type II H_2O are found at lower energies than those for type I, but have maximum intensities in the same orientations. Types I and II H_2O in feldspar were originally defined by Aines and Rossman (1985), who found that type II H_2O is lost by 400°C when heated in air; type I is not fully removed until 660°C. Both types of structural H_2O are found in orthoclase, microcline, and anorthoclase.

NH_4^+

The polarized spectra of structurally bound ammonium are shown in Figure 3.1d. The degenerate ammonium stretching frequencies are split by the low symmetry of the irregular cation site, and appear as multiple, fairly narrow bands from 3067 to 3328 cm^{-1} (Solomon and Rossman 1988). The ammonium

ion is found in microcline and hyalophane ($(K,Ba)Al(Si,Al)_3O_8$) feldspar (Beran et al. 1992; Solomon and Rossman 1988).

Non-structural fluid inclusions and alteration products

Even though they are not structurally bound species, some types of inclusions are so abundant in certain feldspars that they are included here for completeness.

Fluid inclusions

The bands due to fluid inclusions are characteristically broad and isotropic, with a main peak at 3440 cm^{-1} and a shoulder at 3270 cm^{-1} (Figure 3.1e). For most fluid inclusions, these bands shift to 3200-3100 cm^{-1} when the sample is cooled to 77 K (Johnson and Rossman 2003).

Melt inclusions

A few volcanic feldspars have an asymmetric, isotropic band with maximum intensity around 3550 cm^{-1} (Figure 3.1f). This type of spectrum is typical for OH and H_2O in silicate glasses (Stolper 1982a).

Various alteration products

Feldspars are commonly altered to "sericite" (fine-grained mica) and clays. Plagioclase can also be altered to epidote group minerals and albite as well as sericite ("saussurite") (Nesse 1991). Infrared spectra of moderately to extremely turbid feldspars characteristically contain bands due to fluid

inclusions as well as higher-energy, narrow bands from 3500-3700 cm^{-1} that resemble MIR bands of illite and other clay minerals (Figure 3.1g; e.g., Potter and Rossman (1977); Shoval et al. (2002)). Spectra from an anorthite containing visible patches of epidote alteration are shown in Figure 3.1h. A few feldspars in this survey also contain apparently primary mineral inclusions, (some of which, such amphiboles, contain OH) incorporated during the crystallization of the igneous rock, that contribute to the absorbance in the OH region.

Possible crystallographic sites for structurally bound hydrous species

Although infrared spectroscopy does not determine the location of the actual site in which the absorbing species resides, some information on the size of the site and on the orientation of the absorbing species within the site can be obtained. Crystallographically-oriented species may reside in the large, irregular cation site (M-site), in tetrahedral nodes where local charge imbalance requires a hydroxyl, in lattice defects, and in channel-like cavities which traverse the crankshaft structure along the *a*-axis. One of the big mysteries in the study of nominally anhydrous minerals is knowledge of the exact crystallographic or defect locations of trace hydrous species.

Many other workers have discussed possible lattice sites for hydrous species in feldspars, including Wilkins and Sabine (1973); Solomon and Rossman

(1988); Kronenberg et al. (1996); and Johnson and Rossman (2003). The results of these studies are summarized here.

The most compelling argument for the location of a hydrous species in a feldspar is that for ammonium (Solomon and Rossman 1988). Buddingtonite ($(NH_4^+)AlSi_3O_8$) is a feldspar mineral that contains stoichiometric NH_4^+ in the large cation site, and its mid-IR and near-IR spectra are essentially identical to those for NH_4^+-bearing microcline (Solomon and Rossman 1988). Thus, it is reasonable to conclude that NH_4^+ is located in the M-site of the feldspar structure.

The assignment of structural H_2O to crystallographic sites is complicated by the fact that there are apparently two types of structural water in feldspars. These two types of water have different thermal stabilities (type II water is only stable to 400°C; type I water is stable to about 660°C) (Aines and Rossman 1985). Types I and II H_2O also have different hydrogen bonding environments, since the asymmetric stretch frequency of type I is 180 cm^{-1} higher than that of type II. Using the correlation between stretching frequency and hydrogen bonding distance (Nakamoto et al. 1955), type I H_2O has O-H···O distances of 3.00-3.05 Å, and type II H_2O has O-H···O distances of 2.80-2.85 Å. The difference between the asymmetric and symmetric stretches is 70 cm^{-1} for type I and 160 cm^{-1} for type II H_2O, reflecting a difference in the

degree of distortion of the symmetry of the molecule (Lutz 1988). Both types of H_2O lie in a plane approximately parallel to (001) (Solomon and Rossman 1979).

It is possible that H_2O molecules could be accommodated in alkali feldspars via coupled substitutions involving divalent cations in the M sites, such as $Ca^{2+} + H_2O = 2K^+$ (Kronenberg et al. 1996). Another possibility is that H_2O molecules are accommodated within the crankshaft-like chains that run parallel to the **a** axis. The fact that two water sites exist may in fact imply that both of these choices are valid.

The sharp bands of OH type I in low albite may be related to protonation of the underbonded bridging oxygen between ordered Al and Si tetrahedral sites (Downs et al. 1994). The possible locations of type II OH are unresolved at this time (see Johnson and Rossman (2003) for a discussion of possible sites).

The question of H_3O^+

The H_3O^+ ion (oxonium or hydronium ion) has four fundamental bands in the infrared: there are two bending modes at about 1130 cm^{-1} and 1670 cm^{-1} (Bethell and Sheppard 1953), and two sets of broad stretching modes in the 2500-2600 cm^{-1} and 3150-3250 cm^{-1} regions (Ferriso and Hornig 1955). Although the OH type II stretching bands fall within the range of the highest-frequency stretching modes of oxonium, there is other evidence regarding the

presence or absence of H_3O^+ in feldspars. The possible oxonium stretching mode in the 2600 cm^{-1} region and the bending modes are overwhelmed by vibrational overtones of the aluminosilicate structure in feldspars. A bend-stretch combination mode for oxonium would be expected around 4800-5000 cm^{-1}, but no such combination mode is present in any of the NIR spectra of feldspars in this or previous (Johnson and Rossman 2003) studies. Finally, the ^1H NMR (nuclear magnetic resonance) spectrum of $H_3O^+ClO_4^-$, a standard example of an oxonium compound, has a chemical shift of 10.7 ppm, and the NMR band assigned to H_3O^+ for the hydronium-bearing mineral alunite has a chemical shift of 11.4 ppm (Ripmeester et al. 1986). In contrast, "OH-bearing" feldspars have ^1H NMR chemical shifts of 5-7 ppm, typical of other materials containing OH groups. This is the strongest evidence against the presence of H_3O^+ in feldspars. Nonetheless, it is possible that oxonium could be incorporated into feldspars. Such a process could be important during weathering, when aqueous solutions interact with feldspars to effect incongruent dissolution. The oxonium feldspar may be an intermediate phase during the surface reactions that lead to alteration of feldspar to hydrated aluminosilicates (Busenberg and Clemency 1976).

Ranges of hydrous speciation and concentration in igneous rocks

Figure 3.2 presents a summary of the hydrogen species and concentrations found in three categories of igneous rocks: pegmatites and veins, volcanic

phenocrysts, and plutonic rocks (all of the data in Table 3.1 except for the "unknown/other" category, and excluding primary mineral inclusions). There are important differences in hydrous species and concentrations between feldspars of different geologic origins.

Pegmatite feldspars contain the widest variety of hydrous species. Structural H_2O and NH_4^+ (up to 1350-1500 ppm) are found in microcline and orthoclase, and plagioclase from pegmatites contains up to 300 ppm structural OH. Fluid inclusions are common in the low albite crystals found in pegmatites, and some altered pegmatite minerals contain fine-grained clay and epidote. On the other hand, volcanic feldspars always incorporate structural OH groups (up to 510 ppm), or minor amounts of OH and water in melt inclusions. Only one plutonic feldspar (KG-109 from the Skaergaard intrusion) has infrared bands that are indicative of structural OH groups. All other feldspars from plutons contain fluid inclusions (up to 4300 ppm, or 0.43 wt% H_2O) and alteration products. Due to the uncertainty in the absorption coefficient used to determine the concentration of alteration products, absolute values could be off by as much as a factor of three. However, it is clear that alteration products and fluid inclusions are found at higher concentrations than structurally bound hydrous species in natural feldspars, and are predominantly found in plutonic feldspars.

The maximum structural OH concentration of feldspars in this study (512 ppm) is lower than the maximum amount of structural H_2O (1350 ppm). The overall maximum concentration of hydrous species is greater for pegmatite feldspars than for volcanic phenocrysts. Intuitively, it would be expected that feldspars from pegmatites would contain higher water concentrations than those from volcanic rocks, since the pegmatite specimens likely crystallized from volatile-enriched (up to 11 wt% H_2O) late-stage melts or from a combination of melt and fluids (Jahns and Burnham 1969). However, the maximum OH concentration observed in pegmatitic plagioclases is actually lower than the maximum concentration of OH observed in volcanic phenocrysts, so the higher H_2O in some K-rich feldspars from pegmatites should be interpreted with caution. There is a maximum of 1500 ppm NH_4^+ in microcline and hyalophane, although only three samples in this study contain ammonium.

For any given rock type and hydrous species, a range of hydrogen concentrations from zero to some maximum value exists in nature. In the following sections, the data from Table 3.1 and Figure 3.2 will be explored in greater detail, focusing on hydrous speciation in pegmatite feldspars, compositional effects in volcanic feldspars, and alteration effects for plutonic feldspars.

Pegmatite feldspars and partitioning of hydrous species

Figure 3.3a shows the mid-IR spectra taken on a polished slab of perthitic microcline from a pegmatite at the southern end of the Pikes Peak batholith in Colorado (CIT19237). The perthitic texture is easily visible in hand sample; the K-rich bands are 0.5-2 mm across, transparent, and colorless, and the Na-rich areas are 0.5 to 1 mm across, turbid, and pink. The infrared spectra indicate that the distribution of hydrous species is also heterogeneous. The K-rich areas contain 450 ppm of structural NH_4^+, whereas the Na-rich areas contain only fluid inclusions (about 670 ppm H_2O).

Spectra taken from intergrown microcline and albite (cleavelandite) from a topaz-bearing pegmatite from Myanmar (GRR2066) are shown in Figure 3.3b. These minerals presumably formed nearly simultaneously and so should record the same fluid conditions. The microcline is perthitic on the scale of hundreds of micrometers, and the K-rich transparent areas contain structural H_2O while the turbid white Na-rich areas contain only fluid inclusions. In contrast, the single crystals of low albite contain type I OH and fluid inclusions. The partitioning of hydrous species is clearly different in the Na-rich and K-rich areas of microcline. There is also apparently a difference in the ability to incorporate type I OH between single crystals of low albite and the Na-rich perthitic regions of microcline. The Na-rich and K-rich areas of the perthite contain roughly the same concentration of hydrogen (200 and 140

ppm H_2O), but the cleavelandite crystal contains more than twice that amount (520 ppm H_2O as fluid inclusions).

It is noteworthy that the microcline with the coarser perthite texture contains a higher concentration of hydrogen that the microcline with the finer perthite texture. This is consistent with evidence that hydrous fluids aid in the inversion and exsolution of alkali feldspars (Ragland 1970; Parsons 1978). It is not clear why the single crystal of low albite from sample GRR2066 contains type I OH and fluid inclusions, while the Na-rich areas of the corresponding perthite does not contain any structural species. This could be due to the different formation mechanisms of these coexisting feldspars, since one was formed by crystallization from a hydrous melt while the other formed during subsolidus exsolution and subsequent recrystallization. Slight compositional and structural differences between these feldspars could also affect hydrous speciation.

The fact that coexisting potassium and sodium feldspars contain such different structural and non-structural hydrous species strongly suggests that there are structural controls on the partitioning of hydrous species between feldspars of different compositions and different structural states. However, the geologic environment also can influence hydrous speciation, since the microcline from Colorado contains NH_4^+, but the microcline from Myanmar contains structural

H_2O. These two minerals may have interacted with different proportions of primary magmatic fluid and fluids derived from local geologic units during coarsening of the perthite texture.

Multiple structural species within a single feldspar

For a few samples in this study, there is evidence of both structural H_2O and type II OH incorporation into a single, pristine (unaltered) feldspar. Figure 3.3c shows the spectra from a moonstone from the Mogok Stone Tract in Myanmar (GRR2065). Single megacrystals of moonstone, some more than 20 cm in diameter, are hosted within marble. This area has a complex geologic history; there is evidence for intrusive activity, skarn formation, and metasomatism by fluids (George Harlow, personal communication). Four bands that correspond to the positions and anisotropy of the bands due to H_2O types I and II are seen in the spectra of this feldspar. Additionally, there is at least one other broad, anisotropic band at 3100 cm^{-1} with maximum absorbance in E||*Y*, that resembles a type IIb OH band. This interpretation is supported by the near-IR spectra that shows an OH combination mode at 4600 cm^{-1} and H_2O combination modes at 5250 and 5150 cm^{-1}.

In silicate glasses, the ratio of molecular water to hydroxyl groups increases with increasing total water content (Stolper 1982a; Stolper 1982b). This is not the case with feldspars, where structure rather than absolute concentration

seems to mandate hydrous speciation. A feldspar with about 150 ppm H_2O may contain type II OH (GRR25), or only structural H_2O (GRR2066).

Composition and OH concentration in volcanic phenocrysts

The data in Figure 3.2 and Table 3.1 show that all volcanic feldspar phenocrysts incorporate hydrogen as structural OH groups (except for a few that contain non-structural melt inclusions). This group of feldspars can be used to test for possible effects of compositional control on absolute hydrogen concentration. The OH concentrations of volcanic feldspars are plotted as a function of feldspar composition in Figures 3.4a and 3.4b. There is not a distinctive relationship between feldspar composition and OH concentration, but the maximum OH concentration is greater for Na-rich plagioclase than for Ca-rich plagioclase, and the maximum OH concentration is greater for Na-rich alkali feldspars than K-rich alkali feldspars. However, it is not possible to completely divorce feldspar composition from paragenesis (for example, in this survey all plagioclase with compositions ~An_{60} were found in basalts). The plagioclase containing the highest amount of OH (GRR1389; 510 ppm H_2O) is derived from a MORB (mid-ocean ridge basalt)-like source under the eastern Mojave desert that experienced little or no crustal contamination (Farmer et al. 1995). Other feldspars with approximately the same composition (An_{30}) contain lower OH concentrations, down to essentially no

OH in the structure. It is possible that feldspar OH concentrations at least partially record magmatic fluid conditions or high-temperature conditions.

Variation in relative OH band intensities in volcanic feldspars

The variability in relative intensities of observed OH bands (type IIa and IIb) in volcanic (and pegmatite) feldspars is shown in Figure 3.5. Figures 3.5a and 3.5b are the mid-IR spectra of oligoclase from a pegmatite (GRR580) and from a basalt flow (GRR1280). The spectra of the pegmatite sample have more intense OH bands at 3450 cm^{-1} and 3600 cm^{-1} compared to the spectra of the volcanic oligoclase. Two basaltic labradorite phenocrysts (Figures 3.5c and 3.5d) also show variable relative intensities of OH bands in the mid-IR. The labradorite from Rabbit Hills, Oregon, is a deep red color and contains native copper schiller and nanometer-scale copper blebs that exsolved during cooling (Hofmeister and Rossman 1985c). The most intense OH band is at 3350 cm^{-1} for this sample. In contrast, the OH band at 3200 cm^{-1} is slightly more intense than the band at 3350 cm^{-1} in the labradorite from Crater Elegante (GRR25). Finally, sanidines have OH bands that are different from those found in plagioclase or anorthoclase (type IIb OH, a band at 3050 cm^{-1} with maximum intensity in *Y* and another band at 3400 cm^{-1} with maximum intensity in *X*). The spectra taken on a sanidine from a leucite-phonolite pumice (GRR638) are featureless at 3600 cm^{-1} whereas a transparent sanidine

from Yellowstone Plateau (JV1) has an anisotropic OH band at that energy (Figures 3.5e and 3.5f).

The energy of the predominant OH band in feldspars does not vary as a function of composition (Johnson and Rossman 2003). Rather, variations in relative band intensities among a set of four OH bands are seen for phenocrysts within a given feldspar composition. The differences in relative band intensity could be due to differences in trace element concentrations in phenocrysts from different localities (for example, the different OH band patterns in Cu-rich and Cu-poor labradorites). Another possible explanation involves the complex subsolidus behavior of feldspars, especially plagioclase feldspars that form "intermediate" structures of alternating domains of albite-like and anorthite-like structures ~30 Å across (Nakajima et al. 1977). Slower cooling rates and ordering of Al and Si within the aluminosilicate framework could increase the number of distinct bonding environments for OH, producing multiple bands in the mid-IR region. This may explain why the pegmatite oligoclase has a number of distinguishable OH bands while the volcanic oligoclase has one predominant OH band.

Twins and lamellae

We have shown that coarse perthitic microclines have heterogeneous distributions of hydrous species, perhaps because of the mineral-fluid

interactions that resulted in coarsening of the exsolution textures. It is important to establish the possible effects of macroscopic and microscopic twinning and exsolution on measured hydrogen contents for feldspars with other structures and compositions.

Whenever possible, when making infrared measurements to determine the hydrogen concentrations and species for Table 3.1, we avoided passing the IR beam through any macroscopic or microscopic twins or lamellae (either perpendicular or parallel to the lamellae or twin plane). Even so, it is likely that some of the feldspar samples have submicroscopic exsolution textures and that these textures could affect hydrogen content. We tested the possibility that hydrous species are heterogeneously distributed in a peristerite (GRR1280) containing Na-rich lamellae about 50 μm thick, with spacing between lamellae of about a millimeter. Mid-IR spectra were taken perpendicular to (010), in one case with the beam passing through four lamellae, and in the other case with the beam passing through no Na-rich lamellae. The normalized OH band areas ($X+Y$ = 3851 cm^{-2} through four lamellae; $X+Y$ = 3786 cm^{-2} through no lamellae) are identical within measurement error (about a 1.7 % difference in area). The OH band shapes and positions are identical. Therefore, exsolution had no effect on the distribution and species of hydrogen within this sample.

The same procedure was performed on a twinned plagioclase, GRR25. There was no difference in band shape or band area whether the infrared beam was passed through three twin boundaries or no twin boundaries. The structural OH in feldspars is therefore not concentrated within twin boundaries. However, we did find one "veiled" twin layer in sample GRR1604 that contained fluid inclusions trapped within the boundary. We did not find fluid inclusions in any other twin boundary in this sample, or in any other sample in the feldspar survey. In general, however, we feel that it is good practice to avoid twin boundaries whenever possible, especially since spectra taken through multiple twins with different crystallographic orientations do not produce useful structural information or quantitative determination of hydrogen concentration, as do polarized infrared measurements.

Plutonic feldspars and alteration

A polished slab of feldspar from the Southern Idaho Batholith (RH 68) is shown in Figure 3.6a. In this picture, turbid regions appear as dark gray areas and transparent regions are lighter in color. The turbid areas are concentrated along the grain boundary and fractures within the grain. The mid-IR spectra of turbid, clear, and partially turbid areas show there is an increased degree of alteration and fluid inclusions in turbid areas as opposed to the optically clear areas.

Figure 3.6b shows IR spectra of two feldspars from granitic plutons in the Southern Idaho Batholith. The feldspar from sample RB 68 has a $\delta^{18}O$ of +10.1 ‰, which is within the range of feldspar $\delta^{18}O$ values from granites in this region that have not undergone significant hydrothermal exchange with meteoric fluids. This feldspar contains minor amounts of fluid inclusions (about 120 ppm H_2O). Sample RB 163 has a reported $\delta^{18}O$ of –5.8 ‰, and has undergone extensive interaction with meteoric fluids at temperatures of 150 to 400°C (Criss and Taylor 1983). The mid-IR spectrum of this sample shows that it contains a large amount of fluid inclusions (over 0.2 wt%, or 2000 ppm H_2O).

We also examined a suite of feldspars from the epizonal Fry Mountains Pluton. These samples were chosen to include a range of $\delta^{18}O$ whole rock values, and therefore represent varying degrees of hydrothermal exchange between meteoric fluids and the pluton during cooling (Solomon and Taylor 1991). The concentration of fluid inclusions in these feldspars generally increases with decreasing $\delta^{18}O$ of the whole rock, a proxy for the degree of hydrothermal exchange (Figure 3.6c). Thus, fluid inclusion concentrations in plutonic feldspars are related to the process of oxygen isotope exchange between the feldspar and meteoric fluids.

The nature of the relationship between these fluid inclusions and oxygen isotope exchange can be explained by hydrothermal exchange experiments performed on single crystals of albite (O'Neil and Taylor 1967). The albite was partially exchanged with a KCl solution at 700°C, producing an exchanged zone of K-feldspar along the outer rim and in fractures that was full of fluid inclusions, in sharp contrast to the unexchanged core which was free of inclusions. There was a sharp but irregular boundary, filled with inclusions, between the exchanged feldspar and the remnant core. This boundary represents a fluid front that progressed through the sample, dissolving and reprecipitating the feldspar and facilitating equilibrium oxygen isotope exchange between the fluid and feldspar (O'Neil and Taylor 1967). This explains the correlation observed between fluid inclusions (trapped during this exchange process) and the $\delta^{18}O$ of the feldspar. The fluid inclusions are a minor proportion of the total mass of the mineral, up to about 0.4 wt%, and are not responsible for the overall oxygen isotopic ratio of the feldspar itself.

Figure 3.5d shows the behavior of the fluid inclusions that are produced by hydrothermal exchange as a function of temperature. Upon cooling to liquid nitrogen temperature, the liquid water bands slightly narrow and shift by only a few wavenumbers. In contrast, Figure 3.5e shows the low-temperature behavior of distilled water; the water is converted to ice at 77 K and the mid-IR stretch frequencies change shape and position. Infrared spectra of fluid

inclusions in low albite that are ~1-100 μm across show a similar water-to-ice transition (Johnson and Rossman 2003). The numerous micropores (~0.1 μm in length) that have been observed in electron microscope images of turbid alkali feldspars (e.g., David (1990); David et al. (1995)) could contain the hydrothermally-incorporated fluids. Perhaps these fluid inclusions are too small to behave like liquid water at low temperatures, and cannot freeze to ice. The fluid inclusions could also be a briny liquid or a mix of liquid and mineral precipitates.

A single igneous intrusive feldspar in this survey had polarized IR bands resembling those for structural OH. This sample is from a gabbro in the Upper Border Group of the Skaergaard mafic layered intrusion (KG-109) (Taylor and Forester 1979). The plagioclase has a $\delta^{18}O$ of +3.6 ‰, and a $\Delta^{18}O_{plagioclase\text{-}pyroxene}$ of –0.4 ‰, suggesting significant hydrothermal exchange. The area of the feldspar containing structural OH was transparent, but there were also turbid areas containing fluid inclusions and alteration within the same grain, implying that some regions of the feldspar exchanged with hydrothermal fluids while other areas did not experience exchange.

The consequence of feldspar recrystallization during exchange with hydrothermal fluids is that whatever primary structural species were originally hosted in the feldspar become obliterated and overprinted by fluid inclusions

and alteration. Finding primary, structural OH and H_2O in plutonic feldspars is likely to be uncommon, since meteoric-hydrothermal exchange is so prevalent in plutonic systems on Earth.

Conclusions

This survey provides insight into a number of systematic behaviors regarding the speciation and concentration of hydrous species in igneous feldspars.

Feldspars may contain structural OH, H_2O, and NH_4^+. There is no convincing evidence for the occurrence of H_3O^+ in feldspars. These structurally bound species are found primarily within unaltered, transparent volcanic phenocrysts and pegmatite minerals. The speciation of hydrogen is at least partially controlled by the feldspar structure. Microcline and hyalophane are the only feldspars that were found to contain NH_4^+; incorporation of structural H_2O is limited to the microcline and anorthoclase in this study. OH is the only structural species found in sanidine and plagioclase. The absolute concentrations of these structural hydrous species are low (maxima 510 ppm OH, 1350 ppm H_2O, and 1500 ppm NH_4^+).

We have a limited knowledge of where these hydrous species are located in the feldspar structures. It is likely that NH_4^+ and H_2O substitute into the large

cation site (M-site). Structural H_2O may also be found within channels in the aluminosilicate framework. Low albite may incorporate hydrogen at the underbonded Al-Si bridging oxygen, whereas intermediate plagioclase and alkali feldspars have complicated OH spectra that may reflect involvement of OH with submicroscopic ordering domains or with trace element composition. Hydrous species are not concentrated along twin boundaries or within exsolution lamellae in plagioclase feldspars. Macroscopically perthitic microclines do have a partitioning of structural species into K-rich areas and fluid inclusions into Na-rich areas that is likely due to hydrothermal or meteoric fluid-related textural coarsening.

All volcanic feldspars contain OH as the structurally incorporated hydrous species. The variation of OH concentrations among feldspar samples of similar composition and paragenesis is the most convincing evidence in this study that the OH concentrations record magmatic fluid conditions or other high-temperature fluid events.

This study has shown that plutonic feldspars predominantly contain fluid inclusions and fine-grained alteration produced during exchange with meteoric-hydrothermal fluids. Any trace of the structural hydrous species that were incorporated into the feldspar at higher temperatures is erased during the exchange process that forms the fluid inclusions. The amount of fluid

inclusion water found in plutonic feldspars ranges from zero to over 4000 ppm H_2O (0-0.4 wt%).

Feldspars are the most abundant group of minerals in the continental crust (Brown 1983). Using an average water content of 2000 ppm for a typical plutonic feldspar, and assuming that the mass of the continental crust is 2.44×10^{22} kg, the upper crust constitutes about 30% of the entire crust, and feldspars make up two-thirds of the upper crust (McLennan and Taylor 1999), there is a maximum of about 1×10^{19} kg of water stored within fluid inclusions in the upper continental crust. This amount of water is small compared to the 1.35×10^{21} kg of water in the oceans (Garrels and Mackenzie 1971) and the maximum water mass of 4×10^{20} kg stored in the upper mantle within nominally anhydrous minerals (using the estimate of Ingrin and Skogby (2000) of 600 ppm as the water concentration of the mantle). The amount of water contained within fluid inclusions in feldspars in the upper crust is, however, roughly equivalent to the water stored in the hydrous minerals in the upper crust (about 6×10^{19} kg, assuming an upper crust mineral composition from McLennan and Taylor (1999) and an average of 4, 10, and 2 wt% H_2O for micas, chlorite, and amphibole, respectively).

This survey establishes the need for further studies on the relationship between hydrous components in feldspars and crystallographic and geologic processes.

For example, it is possible that useful information about water content of melts or loss of volatiles during magma cooling might be obtained from OH concentrations in volcanic feldspars. The relationship between the OH concentration of volcanic phenocrysts and variables such as the water content of a melt and cooling rate should be explored more thoroughly in specific volcanic systems. Experimental constraints on the diffusivity of hydrogen in volcanic feldspars would provide important constraints on the retention of OH during eruption. The involvement of meteoric fluids in textural transformations of perthites and fluid inclusions in plutonic feldspars could be further confirmed by investigating the heterogeneity of oxygen isotope values within a single partially exchanged feldspar or perthite. Finally, it may be possible to provide further constraints on the structural mechanisms by which water affects the Al-Si interdiffusion in feldspars with combined infrared and X-ray diffraction studies.

Table 3.1. Feldspar sample localities, geological settings, hydrous species and concentrations, and infrared band areas and heights.

Composition	Ab	An	Or	Sample Number	Location	Hydrous Species*	Total Band Area (cm^{-2})	Band Height (cm^{-1})	[H] (ppm H_2O or NH_4^+)	References
Pegmatites										
microcline	6	0	94	968	Elizabeth R Mine, Pala, CA	H_2O I			1000	
						H_2O II				1,2
microcline	8.3	0	91.7	1281	White Queen Mine, Pala, CA	H_2O I			1350	
						H_2O II				2
microcline				1533	Ingersoll Mine, SD	NH_4^+		12.6	540	3
microcline				2066	Sakan-Gyi, Myanmar	H_2O I	2072		140	
						H_2O II				
						fi		3.2	200	
microcline	4	0	96	CIT19237	near Cañon City, CO	fi		11.2	670	
						NH_4^+		10.6	450	
microcline	3	0	97	CIT19249	High Plateau Pegmatite, NM	fi		14.6	880	
orthoclase	10	0	90	146	Itrongay, Madagascar	OH IIa 3600	61.1		4	4
orthoclase				1275	Ampandandrava, Madagascar	OH IIa 3600	73.2		5	
orthoclase (adularia)	9		90	1618	Kristallina, Switzerland	H_2O I	1221		80	
						H_2O II				
						OH IIa				5
orthoclase				CIT10774	Goodsprings, Nevada	alteration		33.8	1950	
						fi		22.4	1350	

Table 3.1 continued.

Composition	Ab	An	Or	Sample Number	Location	Hydrous Species*	Total Band Area (cm^{-2})	Band Height (cm^{-1})	[H] (ppm H_2O or NH_4^+)	References
Pegmatites										
sanidine	5	0	95	2063	Madagascar	OH IIa	22.3		1	
albite	93	6	1	680	Kenya	OH IIa †	2930		190	6
albite	98.8	0.4	0.8	901	Blue Lady Mine, San Diego Co., CA	fi		4.1	250	6
						OH I		0.7	unknown	
albite	91	9	1	904	Kenya	OH IIa	3772		250	
albite	98.3	0	1.7	1605	Amelia, VA	fi		0.7	40	7,2
						OH I			unknown	
albite	99.6	0.2	0.2	1608	Governador Valadaras, Brazil	OH I			unknown	2
						fi		1.9	110	
albite	98.8	0.5	0.7	1609	Pederiniera, Brazil	OH I			unknown	2
						fi		0.6	40	
albite	99.3	0.5	0.2	1610	Metamorphic gash vein, New Melones, CA	fi		0.2	10	8,2
albite	98	1	1	2066	Sakan-Gyi, Myanmar	fi		8.6	520	
						OH I		1.2	unknown	
oligoclase	82	16	2	580	South Carolina	OH IIa			290	6,2
oligoclase	75	21	4	681	Hawk Mine, Bakersville, Mitchell Co., NC	OH IIa	320		20	
anorthite				HPT	Duke Island, AK, plagioclase-hornblende pegmatite	alteration		24.3	1400	9
						fi		9.5	570	
hyalophane				1532	Zagrlski Potok pegmatites, Yugoslavia	NH_4^+ ‡			1500	10

Table 3.1 continued.

Composition	Ab	An	Or	Sample Number	Location	Hydrous Species*	Total Band Area (cm^{-2})	Band Height (cm^{-1})	[H] (ppm H_2O or NH_4^+)	References
Volcanic										
sanidine	14	0	86	638	Eifel, Germany	OH IIb			170	4,2
sanidine	33	2	65§	JB1	Bishop Tuff, CA	OH IIb	1426		90	
sanidine	37	2	61§	JV1	2nd cycle, Yellowstone Plateau Volcanic Field	OH IIb	218		10	
anorthoclase	71	6	23§	1554	Mt. Franklin, Daylesford, Victoria, Australia	OH IIa	3649		240	
anorthoclase	70	6	24	1276a	Aikins Quarry, Cima Volcanic Field, San Bernardino Co., CA	OH IIa	4921		320	
anorthoclase	72	5	23	1277	Cone 32, McBride Province, Queensland, Australia	OH IIa	4129		270	
oligoclase	67	24	9	1280	Black Rock Pass, NV	OH IIa			230	2
andesine	62	34	2	1276b	Aikins Quarry, Cima Volcanic Field, San Bernardino Co., CA	OH IIa	3812		250	
andesine	66	30	3	1389	Halloran Springs, CA basaltic tuff	OH IIa			510	4,2
andesine	64	31	5	1604	Cima cinder cones, San Bernardino, CA	OH IIa	60.2		4	
labradorite				15	Lake County, OR	OH IIa	1.6		0	
labradorite	37	61	2	25	Crater Elegante, Pinacate Ridge, Sonora, Mexico	OH IIa	1905		130	
labradorite	33	67	0§	145	Lake View, Lake Co., OR	nd	0		0	
labradorite	38	61	1§	289	Clear Lake Mine, Lake View, Lake Co., OR	OH IIa	279		20	

Table 3.1 continued.

Composition	Ab	An	Or	Sample Number	Location	Hydrous Species*	Total Band Area (cm^{-2})	Band Height (cm^{-1})	[H] (ppm H_2O or NH_4^+)	References
Volcanic										
labradorite				1613	Rabbit Hills, Plush, Lake Co., OR	OH IIa	329		20	
labradorite		67		1615	Ponderosa Mine, Harney, OR	OH IIa	68.7		4	11
labradorite	38	60	2§	1679	Cinder cone 15 mi W of Spencer, ID	OH IIa	1221		80	
labradorite	35	64	1§	1920	Chihuahua, Mexico	nd	0		0	
labradorite	36	63	1§	1606	Casas Grandes, Chihuahua, Mexico	OH IIa	701		50	
labradorite	32	67	1§	144	Flagstaff, Coconino Co, AZ	OH IIa	13.9		1	
bytownite	22	77	1	1884	Pacaya Volcano, Guatemala	OH IIa	1756		120	
anorthite	5	95.0	0	1597	Great Sitkin Island, Aleutian Islands, AK	OH IIa	2759		180	12
anorthite	4	93.8	2.2	1968	Miyake Island, Japan	OH IIa			210	13,2
anorthite				M-1	Iceland	mi		0.5	60	
plagioclase				97KC02	Kilauea 1974 summit eruption, HI	mi		0.4	50	
plagioclase				URA5	Marianas basalt	OH IIa	377		30	
feldspar				ARG4b	Marianas basalt	mi		0.1	10	

Table 3.1 continued.

Composition	Ab	An	Or	Sample Number	Location	Hydrous Species*	Total Band Area (cm^{-2})	Band Height (cm^{-1})	[H] (ppm H_2O or NH_4^+)	References
Plutonic										
alkali feldspar				B45 HPT	Bushveld Granite	fi		11.6	700	
						alteration		6.3	360	
alkali feldspar				HPT	Port Coldwell Syenite Complex. Ontario, Canada	fi		21.6	1300	
						alteration		10.5	600	
oligoclase				S-12 HPT	Stillwater Complex, Montana	inclusions		36.2	2090	
andesine	75	22	3	CIT19224	Kragerø, Norway	fi		22.8	1370	
						alteration		17.5	1000	
andesine				1550	Sannidal, Norway	fi		4.8	290	
						alteration		6.1	350	
labradorite	6	94	0	CIT19234	Labrador, Canada	fi		1.1	70	
						alteration		0.1	6	
bytownite	24	76	0	CIT19232	Crystal Bay, MN	inclusions		1.3	80	
anorthite	7	93	0	CIT19230	Grass Valley, CA	fi		6.1	370	
						alteration		5.9	340	
plagioclase				CIT19231	Oslo, Norway	fi		5.3	320	
						alteration		5.3	310	
plagioclase				B46c HPT	Bushveld Complex, plagioclase-rich layer	fi		33.1	1990	
						alteration		59.3	3430	

Table 3.1 continued.

Composition	Ab	An	Or	Sample Number	Location	Hydrous Species*	Total Band Area (cm^{-2})	Band Height (cm^{-1})	[H] (ppm H_2O or NH_4^+)	References
Plutonic										
plagioclase				81-205 HPT	Samail Ophiolite cumulate gabbro	alteration		23.3	1350	14
plagioclase				D81-75 HPT	Plagiogranite, Samail Ophiolite, $\delta^{18}O_{wr}$= +6.2	fi		13.8	830	14
						alteration		7.3	420	
plagioclase				81-SR3	Marcy Anorthosite, NY	nd		0.0	0	15
plagioclase				83-AUS-11	Marcy Anorthosite, NY	nd		0.0	0	15
plagioclase				RT3#1	Marcy Anorthosite, NY	inclusions		4.6	260	15
feldspar				GCS026 (PUP11)	Kitt Peak Granodiorite, AZ	fi		6.3	380	16
feldspar	4	96	0§	PI 210 HPT	Percy Island, AK	alteration		67.7	3900	
feldspar	0	30	70§	Sky-9 HPT	Loch Ainort epigranite, Isle of Skye, $\delta^{18}O_{feldspar}$= -0.5	fi		6.0	360	20

Table 3.1 continued.

Composition	Ab	An	Or	Sample Number	Location	Hydrous Species*	Total Band Area (cm^{-2})	Band Height (cm^{-1})	[H] (ppm H_2O or NH_4^+)	References
Plutonic Series: Fry Mountains Pluton										
plagioclase				GCS349	Biotite-hornblende granodiorite, Fry Mountains Pluton, Rodman Mountains, San Bernardino Co., CA $\delta^{18}O_{wr}$= +8.9	fi		13.5	810	17
plagioclase				GCS348	Biotite monzogranite, Fry Mountains Pluton, Rodman Mountains, San Bernardino Co., CA $\delta^{18}O_{wr}$= +6.7	fi		25.1	1510	17
orthoclase				GCS284	Biotite-hornblende granodiorite, Fry Mountains Pluton, Rodman Mountains, San Bernardino Co., CA $\delta^{18}O_{wr}$= +4.8	fi		38.5	2320	17
plagioclase				GCS283	Biotite monzogranite, Fry Mountains Pluton, Rodman Mountains, San Bernardino Co., CA $\delta^{18}O_{wr}$= +3	fi		22.8	1380	17
plagioclase				GCS280	Biotite monzogranite, Fry Mountains Pluton, Rodman Mountains, San Bernardino Co., CA $\delta^{18}O_{wr}$= +0.5	fi		70.8	4270	17

Table 3.1 continued.

Composition	Ab	An	Or	Sample Number	Location	Hydrous Species*	Total Band Area (cm^{-2})	Band Height (cm^{-1})	[H] (ppm H_2O or NH_4^+)	References
Plutonic Series: Skaergaard Intrusion										
plagioclase				KG-109 HPT	Skaergaard Intrusion, Upper Border Group gabbro $\delta^{18}O_{plag}$= +3.6	OH IIa		1257.1	80	18
						alteration		2.1	120	
plagioclase				SK-15 HPT	Skaergaard Intrusion, Upper Zone, ferrodiorite, $\delta^{18}O_{plag}$= +4.5	fi		6.8	400	18
						alteration		65.6	3790	
plagioclase				KG-236 HPT	Skaergaard Intrusion, Upper Border Group gabbro $\delta^{18}O_{plag}$= -1.4	fi		17.9	1080	18
						alteration		11.5	670	
Plutonic Series: Southern Idaho Batholith										
feldspar	10	0	90§	RH 68 HPT	Southern Idaho Batholith $\delta^{18}O_{feldspar}$= +10.1	fi		2.0	120	19
alkali feldspar				RB 163 HPT	Southern Idaho Batholith $\delta^{18}O_{feldspar}$= -5.8	fi		35.9	2160	19

Table 3.1 continued.

Composition	Ab	An	Or	Sample Number	Location	Hydrous Species*	Total Band Area (cm^{-2})	Band Height (cm^{-1})	[H] (ppm H_2O or NH_4^+)	References
Unknown/Other Paragenesis										
microcline				752	Ceylon	OH IIa	458		30	
						H2O I				
orthoclase	8	0	92	1414	Four Metals Breccia Pipe, AZ, hydrothermal deposit	fi		16.3	980	
orthoclase	6	0	94	2064	Myanmar	OH IIb	3393		220	
orthoclase	10	0	90§	1278	unknown	OH IIb	279		20	
albite				67	Mozambique	alteration		3.4	200	
anorthoclase	35	2	63	2065	Ohn-bin, Mogok, Myanmar; moonstone in marble- intrusive?	H_2O I	307		20	
						H_2O II				
						OH IIa				
plagioclase				1085	Madagascar	OH IIa	127		8	
						inclusions		0.04	2	

1. Hofmeister and Rossman 1985b; 2. Johnson and Rossman 2003; 3. Solomon and Rossman 1988; 4. Hofmeister and Rossman 1985a; 5. Kronenberg et al. 1996; 6. Hofmeister and Rossman 1986; 7. Kracek and Neuvonen 1952; 8. Pohl et al. 1982; 9. Irvine 1967; 10. Beran et al. 1992; 11. Hofmeister and Rossman 1985c; 12. Shannon et al. 1992; 13. Kimata et al. 1995; 14. Stakes and Taylor 1992; 15. Morrison and Valley 1988; 16. Solomon 1991; 17. Solomon and Taylor 1991; 18. Taylor and Forester 1979; 19. Criss 1981; 20. Taylor and Forester 1971.

Note: nd = species not determined; fi = fluid inclusions; mi = melt inclusions; alteration = infrared bands for typical alteration products of feldspars (clays, epidote) and textural evidence supporting this interpretation; inclusions = mineral inclusions interpreted to be primary magmatic; wr = whole rock value; HPT = from the collection of Hugh P. Taylor, Jr.; CIT = from the Caltech collection (other samples labelled numerically are from the collection of George R. Rossman).

* See Table 2 for explanation.

† Estimated from two extinction directions.

‡ Bands shifted from non-Ba-rich feldspars.

§ Composition determined with SEM using EDS.

Table 3.2. Characteristic mid-IR bands used to determine hydrogen speciation and concentration.

Band Type	Band Position (cm^{-1})	Approximate Band FWHM (cm^{-1})	Orientation of Maximum Band Intensity†	Position of Corresponding NIR Band (cm^{-1})	Mid-IR Absorption Coefficient‡	Reference
OH Type I	3506, 3050 *	20, 200	X, Y	not determined	unknown	1
OH Type IIa	3050-3200, 3350-3450, 3575-3610	330-500	*a′*	~4450-4600	10700±5000 L/mol·cm^2	1
OH Type IIb	3400, 3060	300, 500	X, Y	~4550	10700±5000 L/mol·cm^2	1
H_2O Type I	3620, 3550	100	X, Z	5250	10700±5000 L/mol·cm^2	1,2
H_2O Type II	3440, 3280	125	X, Z	5120	10700±5000 L/mol·cm^2	1,2
NH_4^+	3328, 3220, 3067	50-130	Z', X', X'	4990, 4753, 4440	162 L/mol·cm	3
Fluid inclusion water	3450, 3270 shoulder	360-440	isotropic	5200	115±6 L/mol·cm	4
Melt inclusions	3530-3570	asymmetric; 420	isotropic	5230, 4500	67±7 L/mol·cm	5
Fine-grained alteration-clays	3620-3700	100		4430-4530	120 L/mol·cm	6

1. Johnson and Rossman 2003; 2. Aines and Rossman 1985; 3. Solomon and Rossman 1988; 4. Clunie et al. 1966; 5. Stolper 1982a; 6. Potter and Rossman 1977

* Most prominent bands in spectrum; others seen at 77 K.

† Refers to principal optical direction (*X*,*Y*,*Z*), projection of optical direction onto (001) (*X′*, *Y′*, *Z′*), or the optical direction closest to the *a* crystallographic axis (*a′*).

‡ See experimental methods section for useage of mid-IR absorption coefficients.

Figure 3.1. Representative spectra of structural and non-structural hydrous species in feldspars. *X*', *Y*', and *Z*' are the projections of the principal optical directions on the {001} or {010} cleavages.

Figure 3.1A.

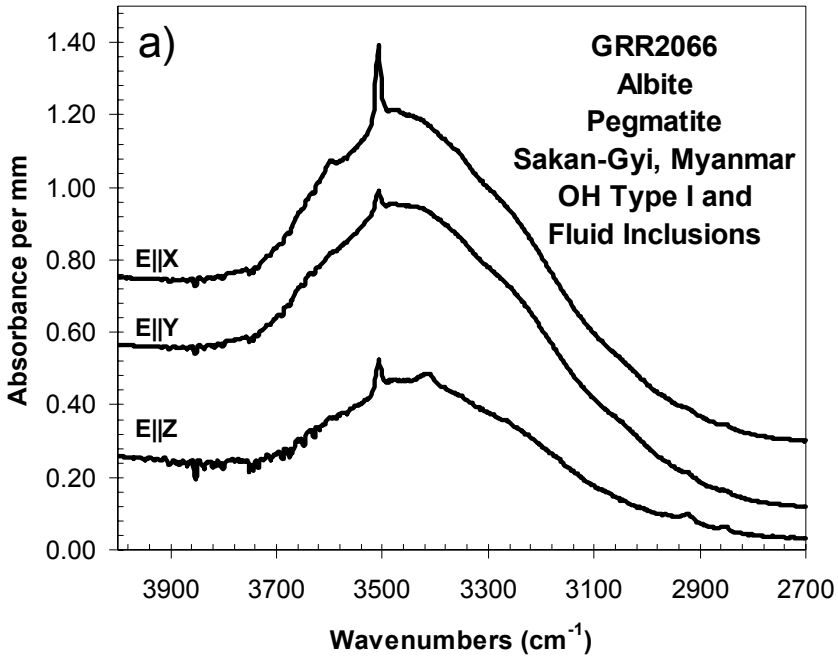

Figure 3.1B.

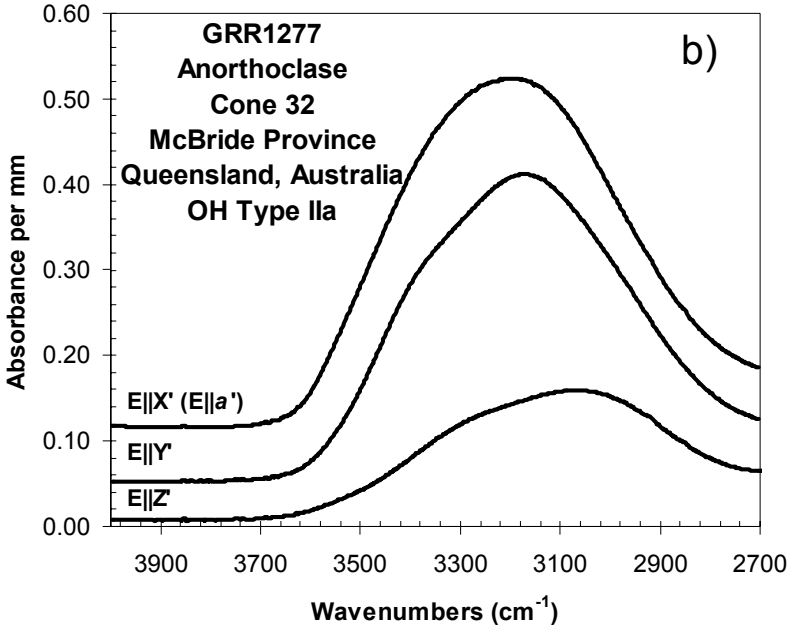

Figure 3.1C.

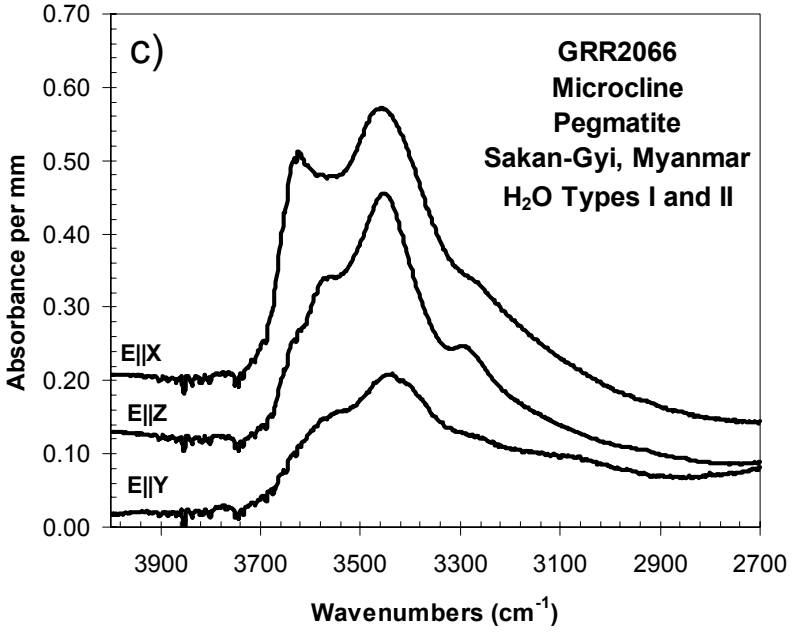

Figure 3.1D.

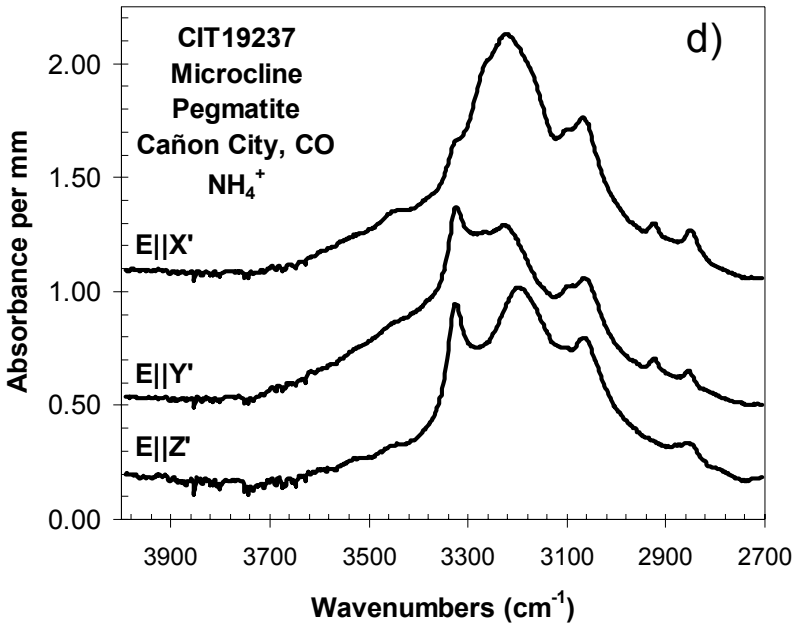

Figure 3.1E.

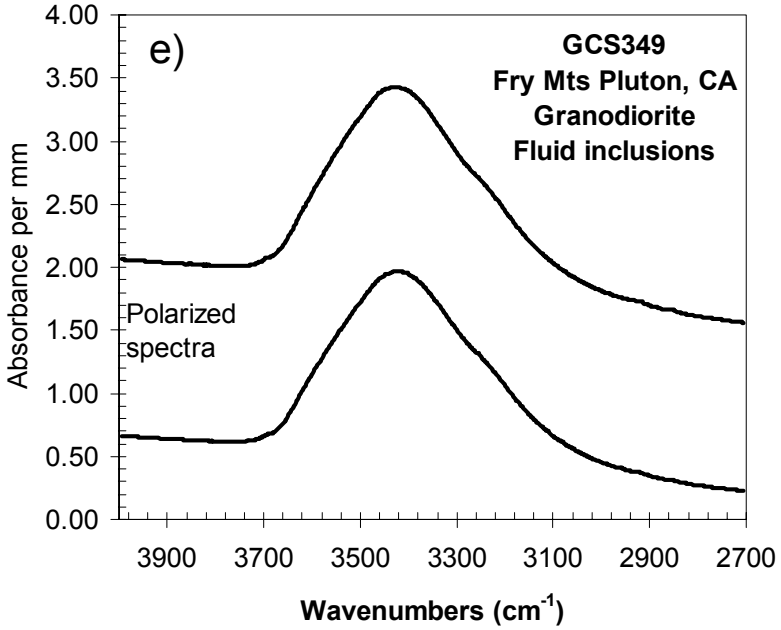

Figure 3.1F.

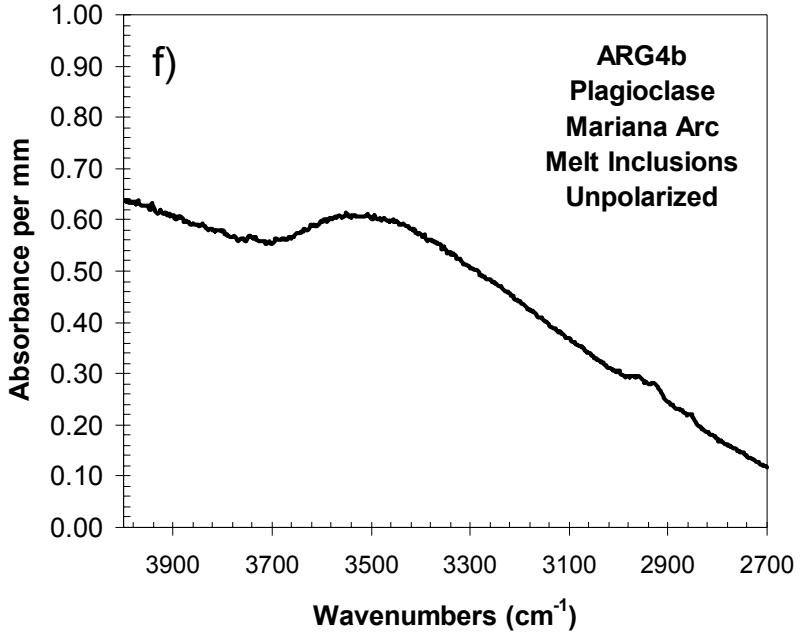

Figure 3.1G.

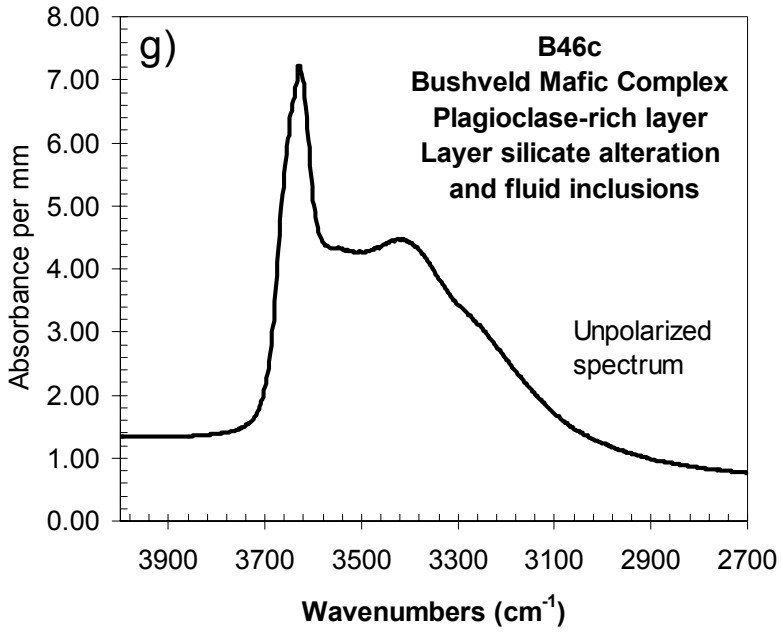

Figure 3.1H.

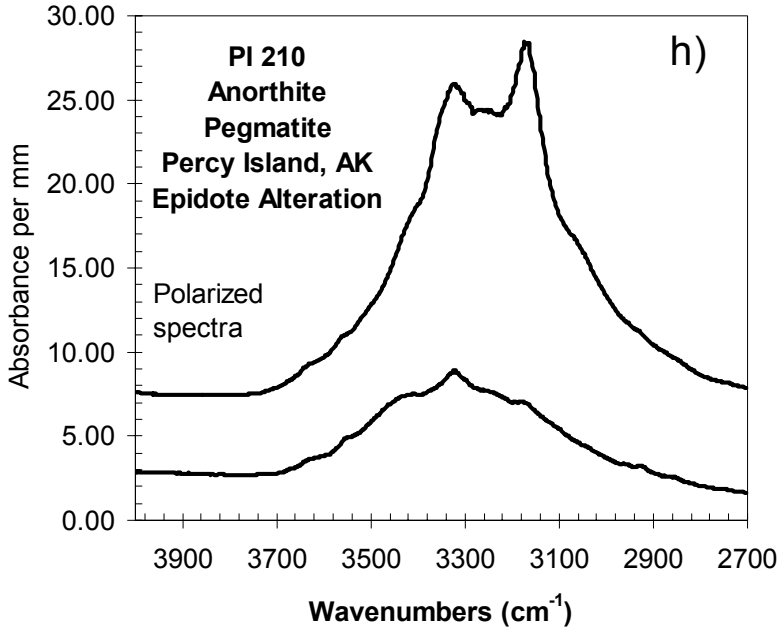
30.00
25.00
20.00
15.00
10.00
5.00
0.00
Absorbance per mm
PI 210
Anorthite
Pegmatite
Percy Island, AK
Epidote Alteration
h)
Polarized
spectra
3900
3700
3500
3300
3100
2900
2700
Wavenumbers (cm-1)

Figure 3.2. The hydrogen concentrations of igneous feldspars organized by rock type and hydrous species.

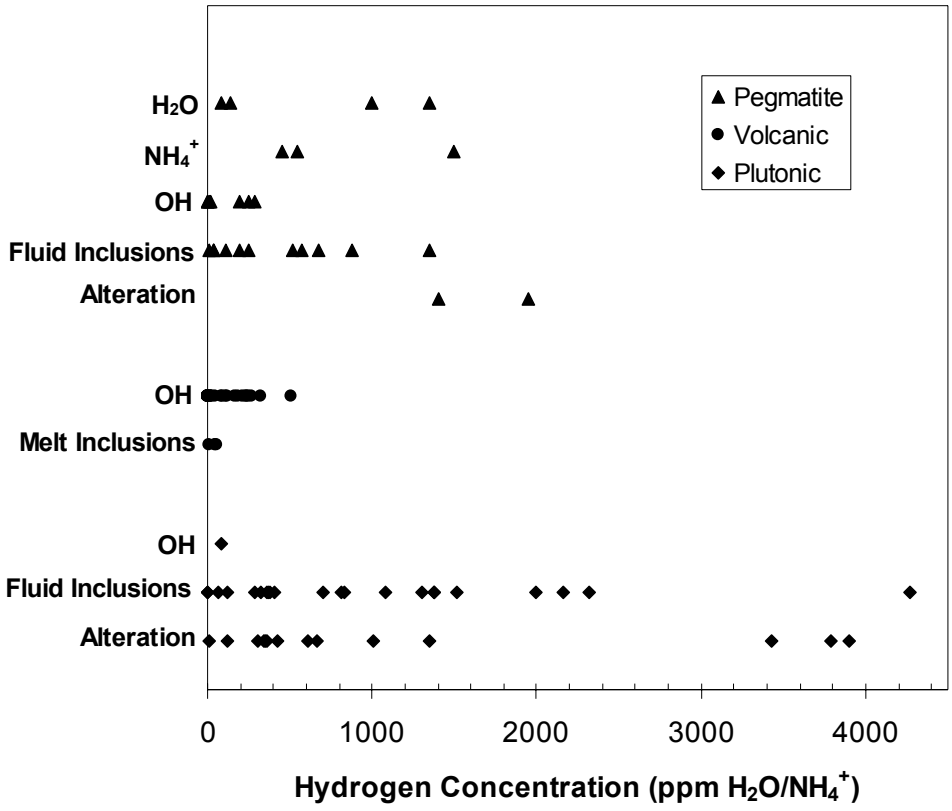

Figure 3.3. Mid-infrared spectra of a) the heterogeneously distributed hydrous species in a perthite; b) microcline perthite and albite intergrowth; and c) anorthoclase containing both structural OH and H_2O. d) Near-infrared spectrum of the anorthoclase.

Figure 3.3A.

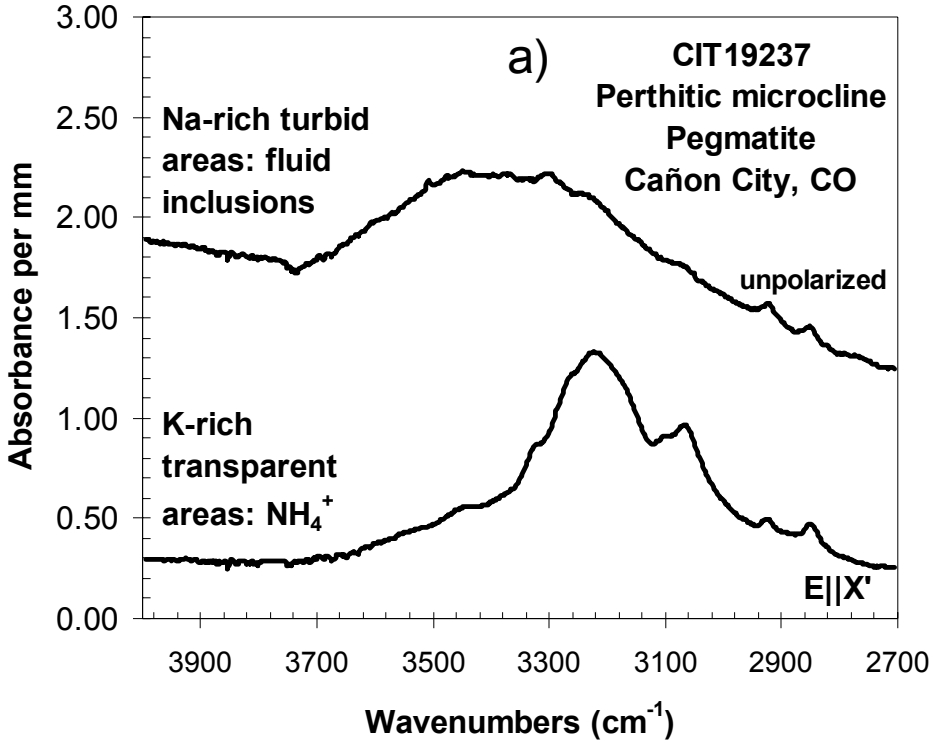

Figure 3.3B.

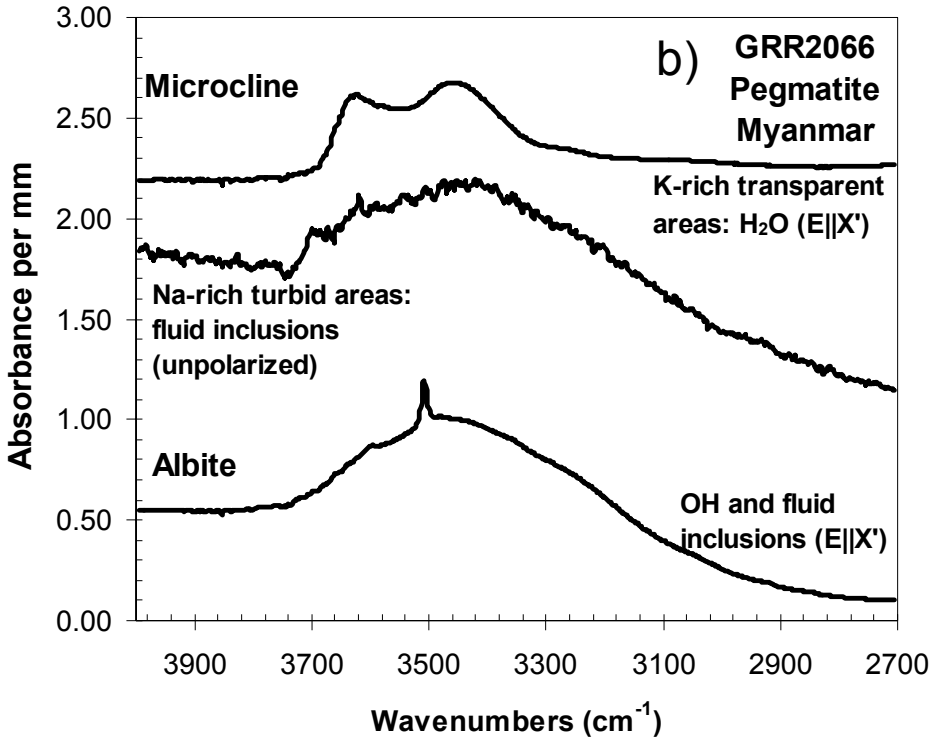
b)
GRR2066
Pegmatite
Myanmar
Microcline
K-rich transparent
areas: H2O (E||X')
Na-rich turbid areas:
fluid inclusions
(unpolarized)
Albite
OH and fluid
inclusions (E||X')
Absorbance per mm
3.00
2.50
2.00
1.50
1.00
0.50
0.00
3900
3700
3500
3300
3100
2900
2700
Wavenumbers (cm-1)

Figure 3.3C.

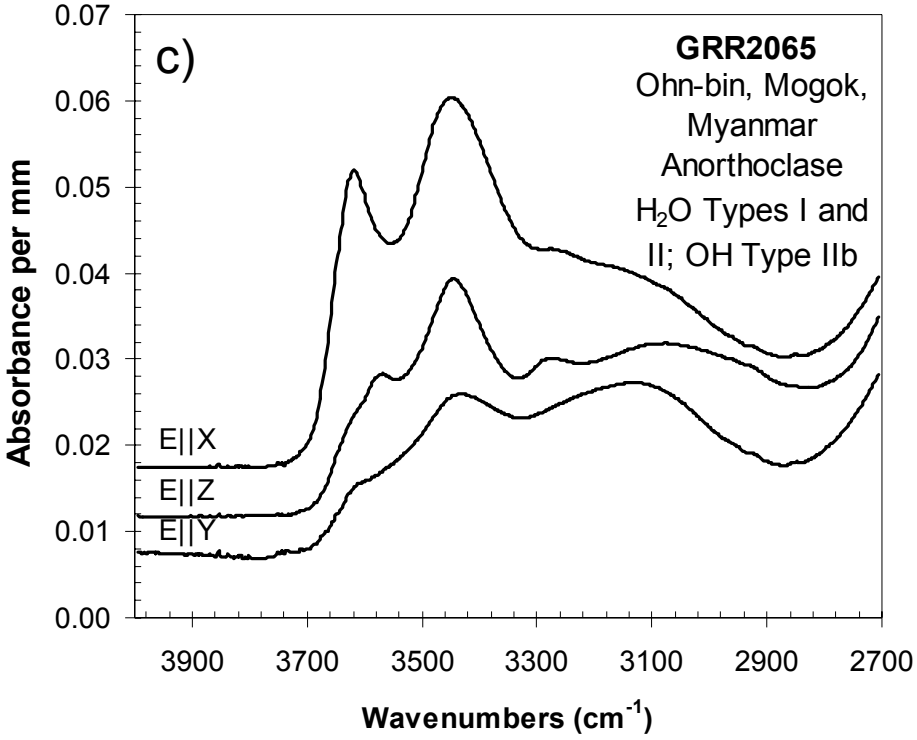
c)
GRR2065
Ohn-bin, Mogok, Myanmar
Anorthoclase
H2O Types I and II; OH Type IIb
E||X
E||Z
E||Y
Absorbance per mm
0.07
0.06
0.05
0.04
0.03
0.02
0.01
0.00
3900
3700
3500
3300
3100
2900
2700
Wavenumbers (cm-1)

Figure 3.3D.

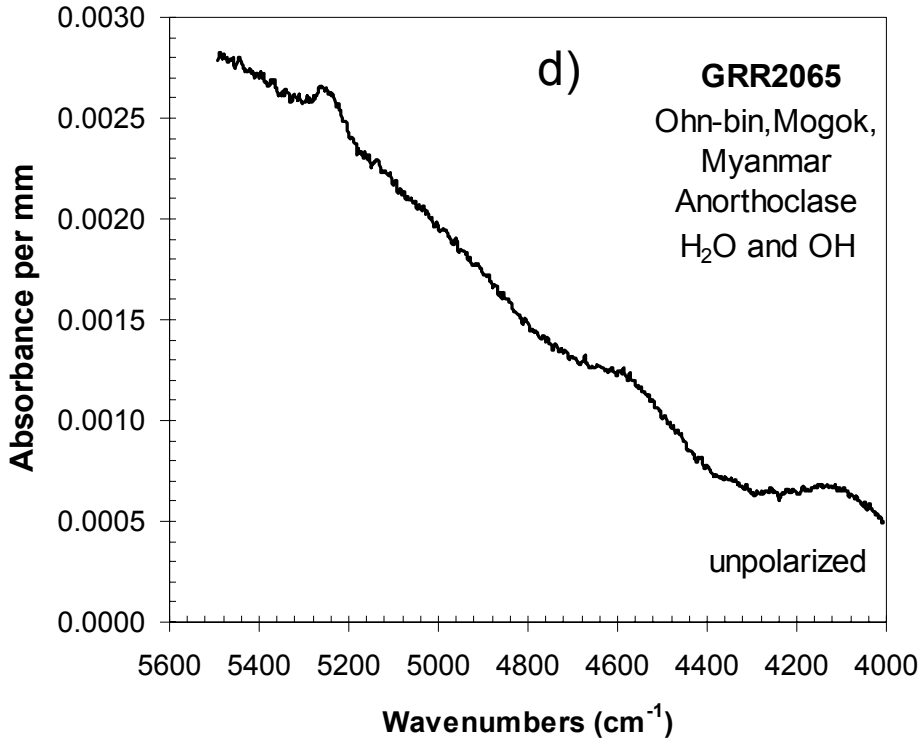
d)
GRR2065
Ohn-bin,Mogok,
Myanmar
Anorthoclase
H_2O and OH
unpolarized
Absorbance per mm
0.0030
0.0025
0.0020
0.0015
0.0010
0.0005
0.0000
5600 5400 5200 5000 4800 4600 4400 4200 4000
Wavenumbers (cm^{-1})

Figure 3.4. The OH concentration of volcanic feldspars as a function of major element composition.

Figure 3.4A.

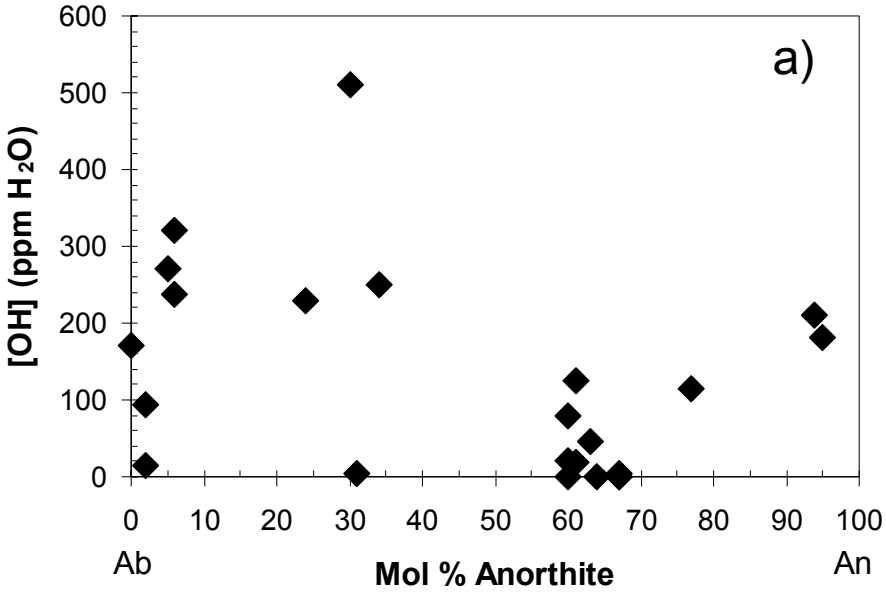

Figure 3.4B.

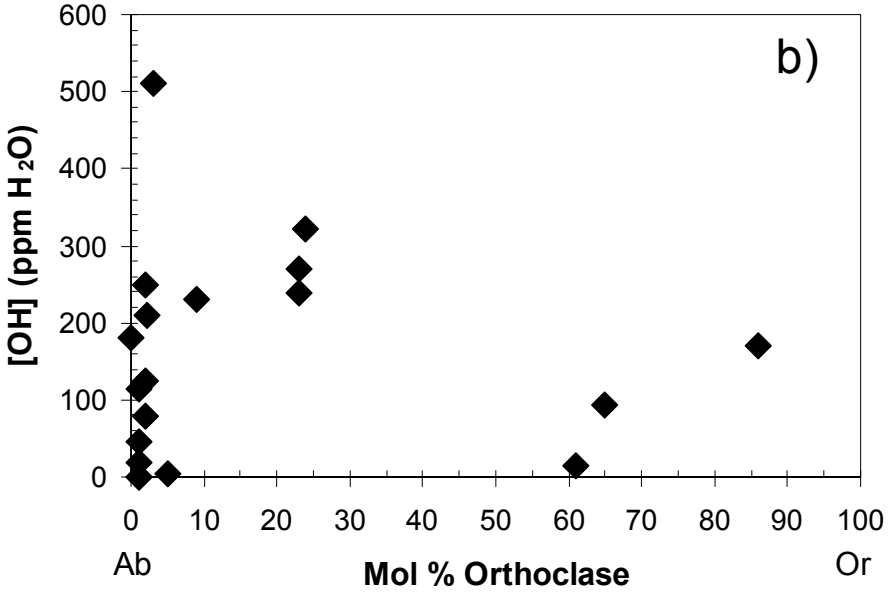

Figure 3.5. Spectra of type II OH bands found in volcanic and pegmatite feldspars. a) and b) oligoclase; c) and d) labradorite; e) and f) sanidine.

Figure 3.5A.

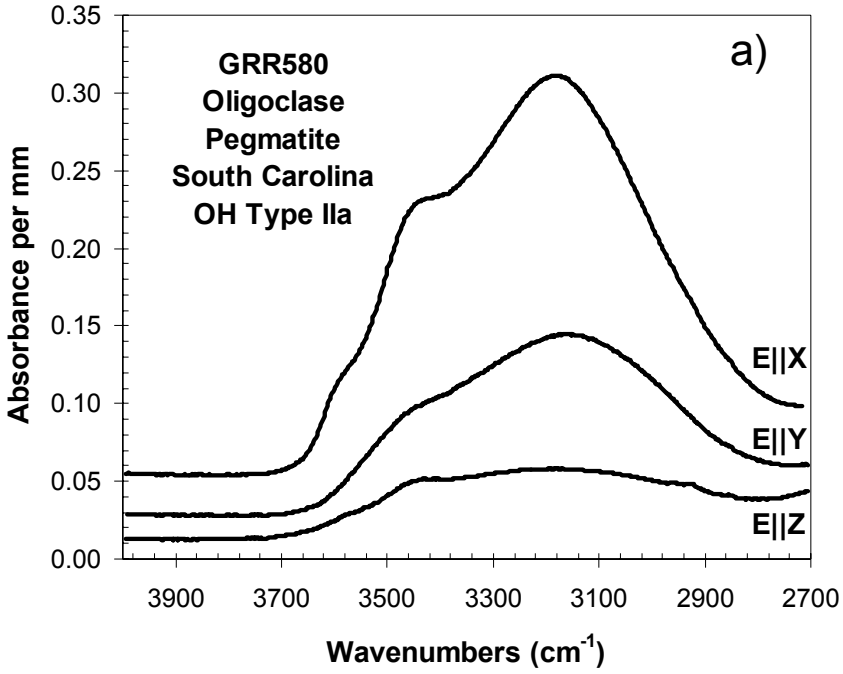

Figure 3.5B.

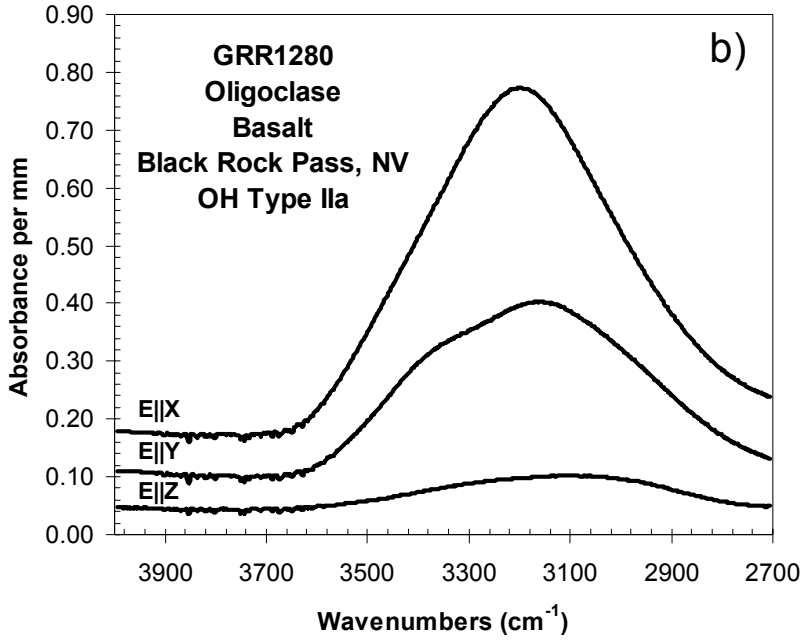

Figure 3.5C.

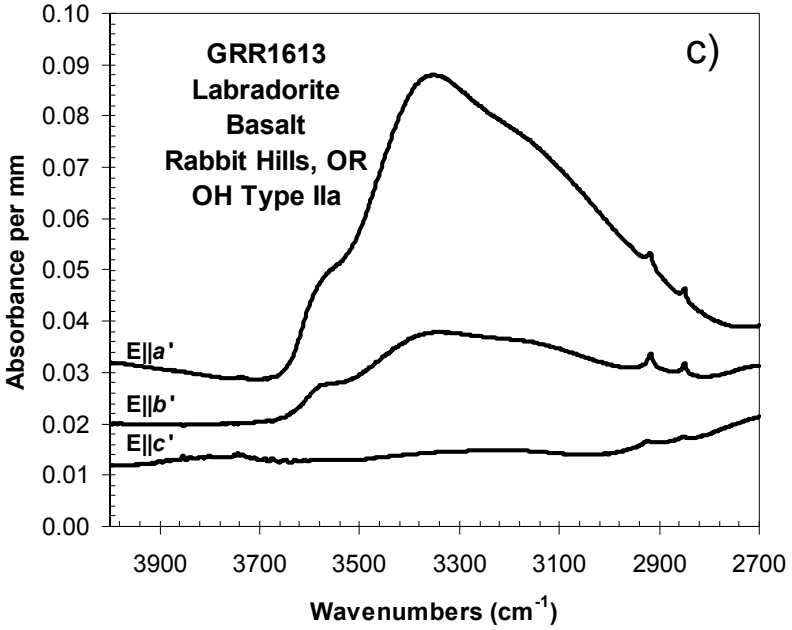

Figure 3.5D.

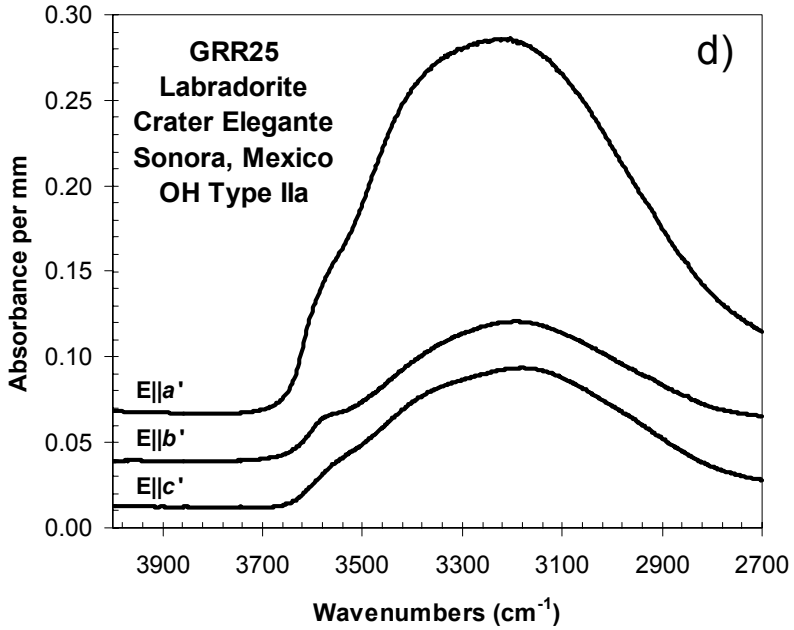

Figure 3.5E.

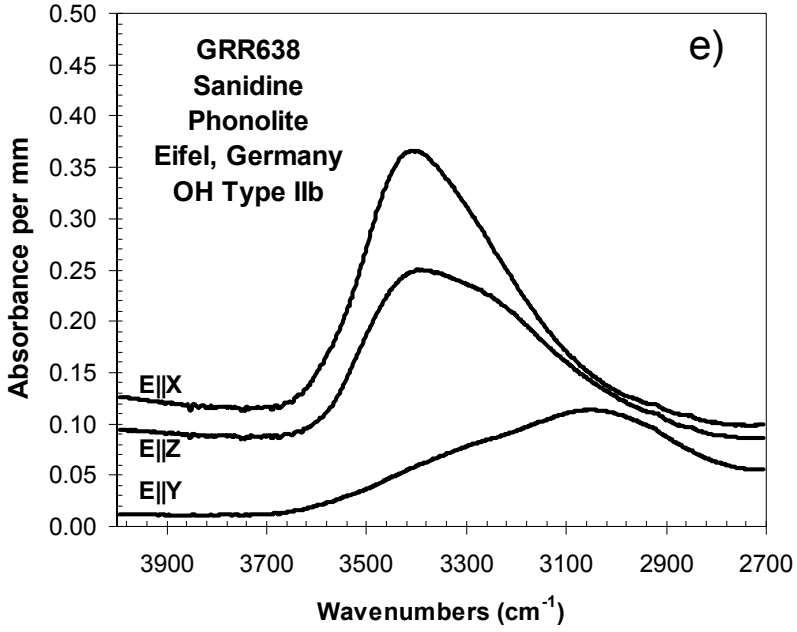

Figure 3.5F.

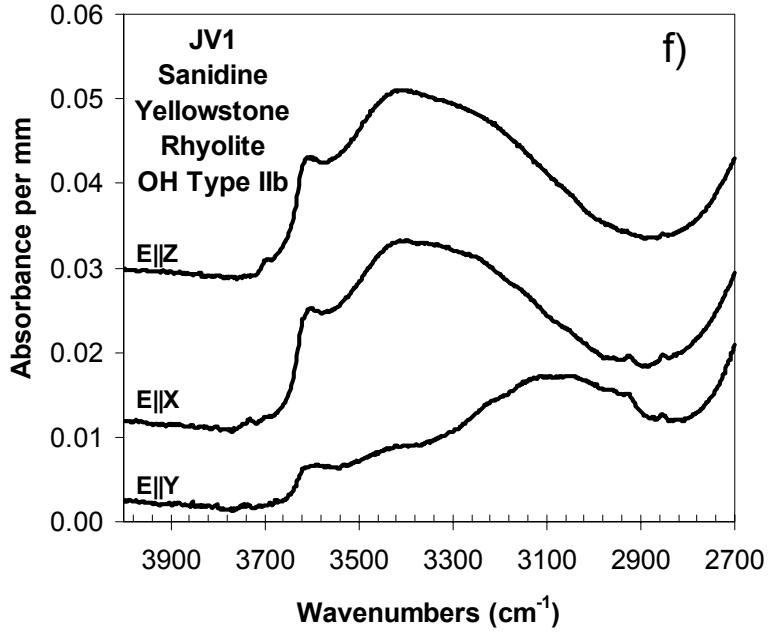

Figure 3.6. a) The infrared spectra of turbid, intermediate, and clear areas in a feldspar that has undergone partial hydrothermal exchange. b) Infrared spectra of fluid inclusions in feldspars from the Southern Idaho Batholith that have undergone minor ($\delta^{18}O = +10.1‰$) and extensive ($\delta^{18}O = -5.8‰$) hydrothermal exchange with meteoric fluids. c) Fluid inclusion concentration of feldspars versus whole rock $\delta^{18}O$ for samples from the Fry Mountains Pluton, CA. d) and e) Infrared spectra of "fluid inclusions" in plutonic feldspars and water/ice at 298 K and 77 K.

Figure 3.6A.

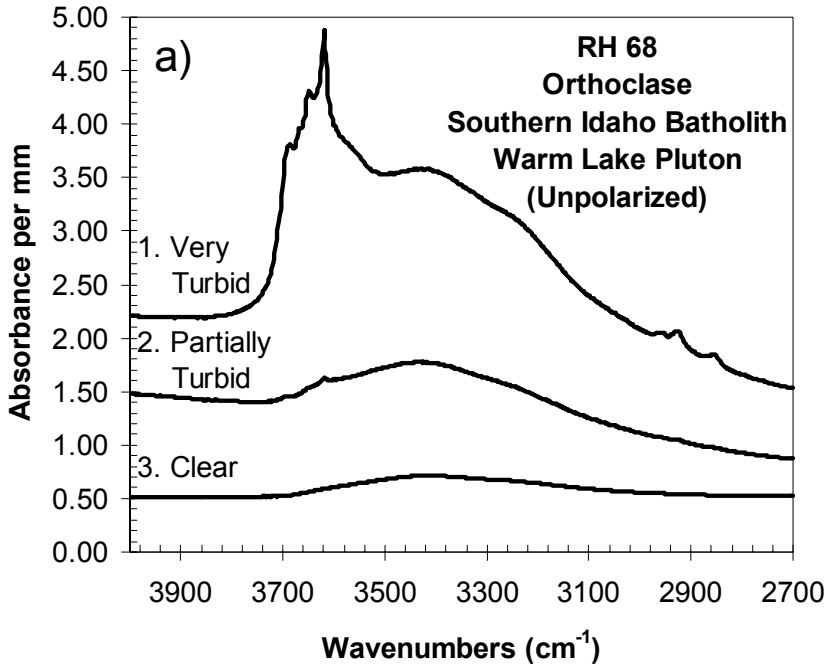
a)
RH 68
Orthoclase
Southern Idaho Batholith
Warm Lake Pluton
(Unpolarized)
1. Very Turbid
2. Partially Turbid
3. Clear
Absorbance per mm
5.00
4.50
4.00
3.50
3.00
2.50
2.00
1.50
1.00
0.50
0.00
3900
3700
3500
3300
3100
2900
2700
Wavenumbers (cm-1)

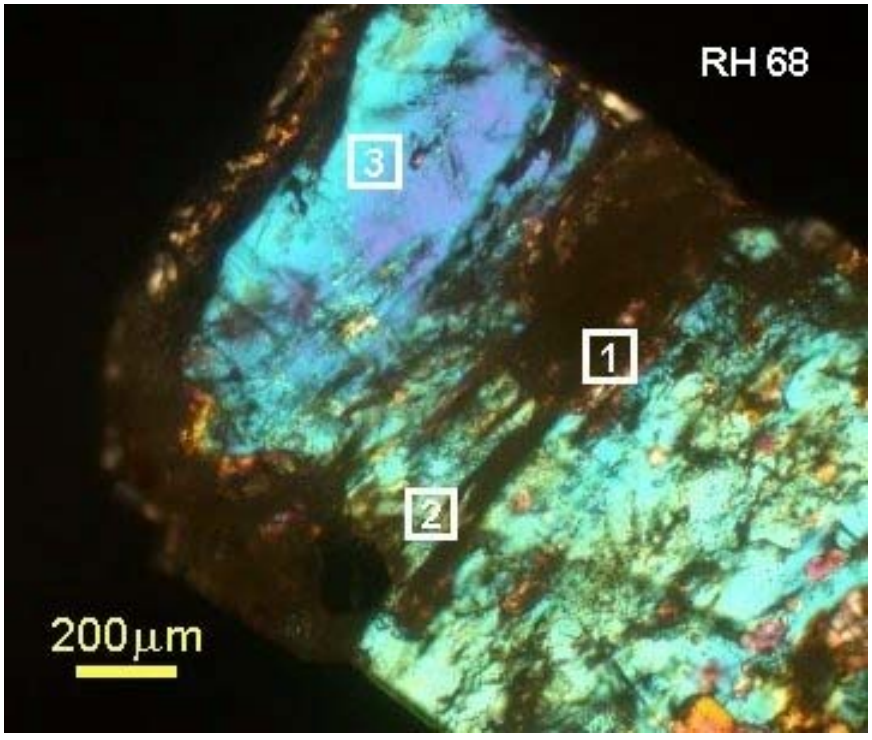
RH 68
3
1
2
200μm

Figure 3.6B.

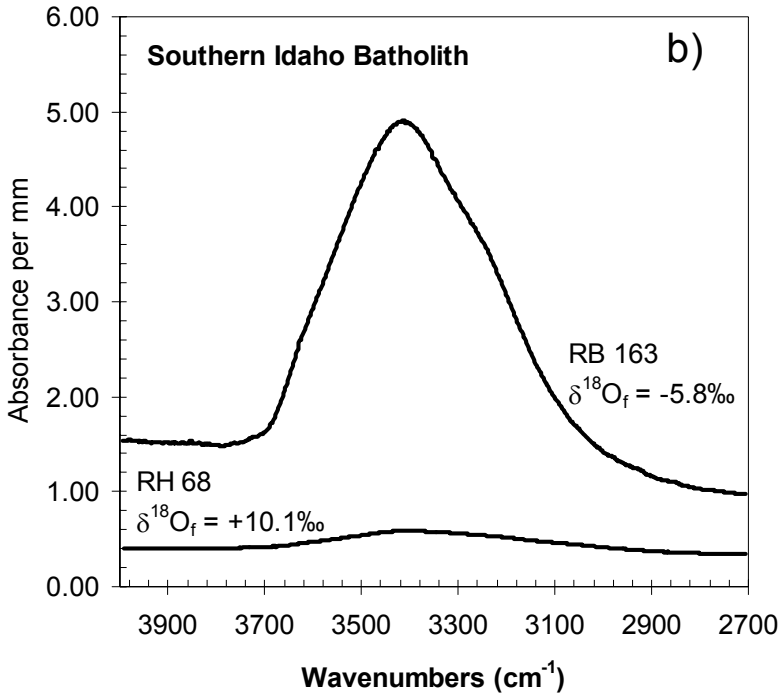

Figure 3.6C.

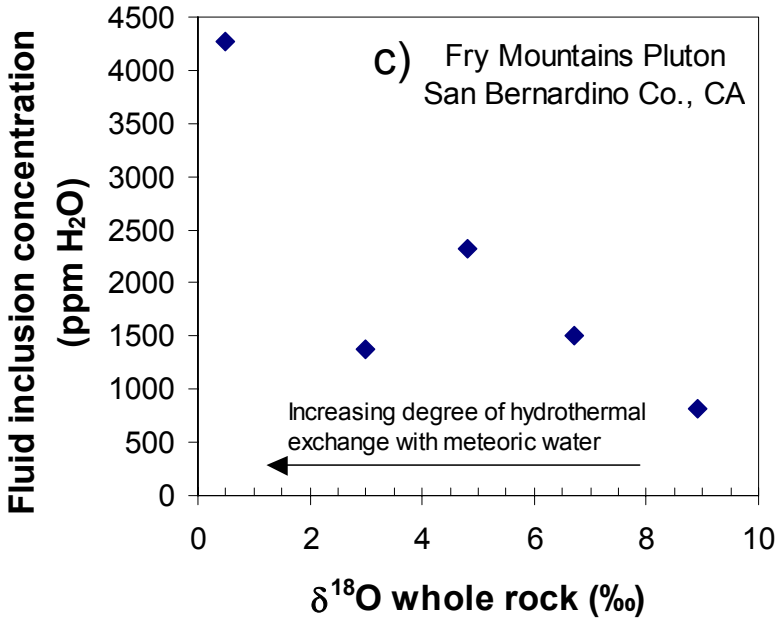

Figure 3.6D.

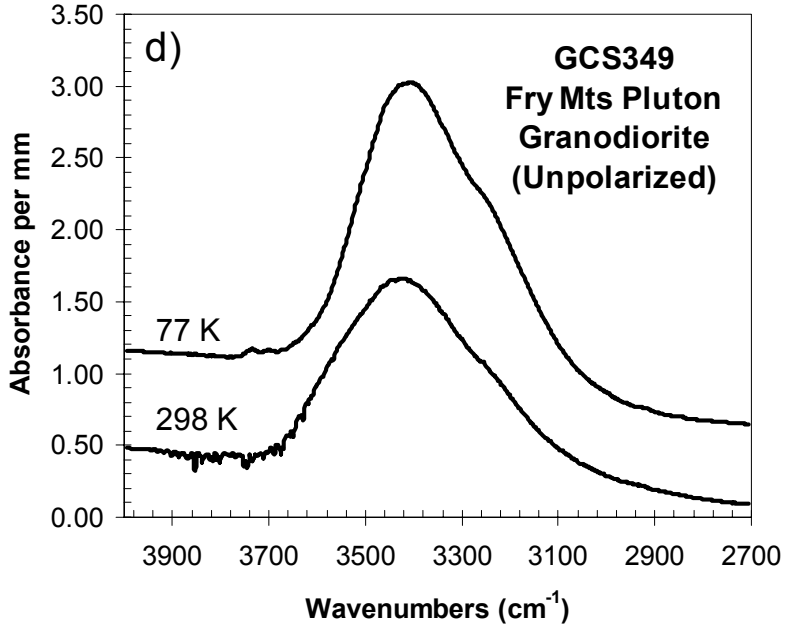

Figure 3.6E.

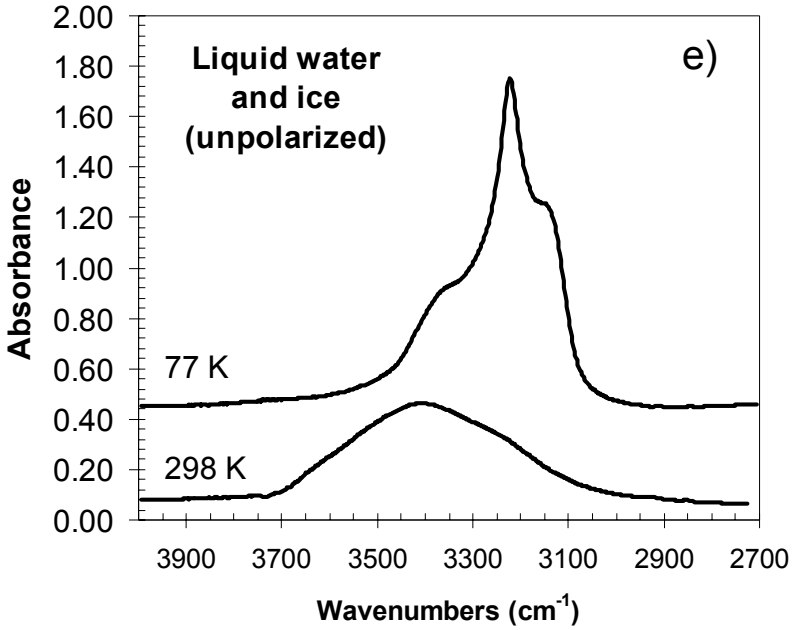

Chapter 4

DIFFUSION OF HYDROGEN IN OH-BEARING PLAGIOCLASE

Introduction

It is important to understand the diffusion behavior of hydrogen in nominally anhydrous minerals in order to interpret the geologic significance of absolute hydrogen concentrations preserved in these minerals. In contrast to pegmatite feldspars that may contain a wide array of hydrous species (OH, H_2O, NH_4^+), all volcanic feldspars incorporate structural hydrogen only in the form of OH groups (Chapter 3). A wide range of OH concentration (0-510 ppm H_2O) is observed in natural volcanic feldspar phenocrysts, even among feldspars from the same general rock type (i.e., basalt or rhyolite) and feldspars of the same major-element composition (Chapter 3). The OH concentrations in volcanic feldspars could reflect many factors, including crystallographic structure, melt composition, changes in oxygen fugacity, trace element composition, and the presence of volatiles during and after eruption. Hydrogen diffusion experiments on an OH-bearing plagioclase feldspar were undertaken to better

understand the thermal stability of hydrous species in feldspars, and to constrain the effect of hydrogen diffusion during eruption and cooling.

Previous work on hydrogen diffusion in feldspars focused only on alkali feldspars from pegmatites that contain structural H_2O groups. Microcline often contains two types of structurally bound water molecules (Type I and Type II; Aines and Rossman 1985; Hofmeister and Rossman 1985b; Johnson and Rossman 2003 and Chapter 3). High-temperature infrared spectroscopy of microcline during step-heating experiments showed that type II H_2O is lost by 400°C and type I is not fully removed until 660°C (Aines and Rossman 1985). A third type of unknown hydrous species formed irreversibly during this process.

In a separate study, the diffusivity of hydrogen was determined at 500-900°C in a K-feldspar containing about 180 ppm H_2O by weight (Kronenberg et al. 1996). The diffusion coefficient D was determined at each experimental temperature by measuring loss (or gain during hydrothermal experiments) of mid-infrared band absorbance of the OH stretch frequencies of H_2O, essentially the same technique used in the present study. Hydrogen diffusion is very rapid in H_2O-bearing adularia ($D = 2.2\times10^{-11}$ m^2/s at 900°C) (Kronenberg et al. 1996).

Sample Description

The plagioclase feldspar used in this study (andesine sample GRR1389/CIT 13759) is from a basaltic tuff near Halloran Springs, CA, at the western edge of the Cima volcanic field (Wise 1982). The major element composition of this sample is $Ab_{66}An_{30}Or_3$, and the andesine contains small amounts of ferric and ferrous iron (0.11 wt% Fe_2O_3 and 0.03 wt% FeO; Hofmeister and Rossman 1985a). The OH concentration of this feldspar was determined to be 510 ppm H_2O with ^1H MAS NMR spectroscopy, and its mid-IR and near-IR spectra are also described in Chapter 2 and Johnson and Rossman (2003). The sample is a very large (>2 cm), transparent, colorless crystal with a few macroscopic fractures partially to completely transecting the crystal and a few mineral or melt inclusions that only occur immediately adjacent to the rim of the crystal. The OH concentration is completely homogeneous within measurement error using infrared spectroscopic data. The Fe concentration (0.05 mol Fe/L andesine) is approximately three times lower than the H concentration (0.15 mol H/L andesine).

The high quality and high OH concentration of this sample makes it an ideal candidate for hydrogen diffusion studies. Polished slabs free of inclusions or fractures, several millimeters wide and 0.15 to 0.78 mm thick were prepared in two different crystallographic orientations to evaluate the extent of anisotropic

hydrogen diffusion in the feldspar. Several polished slabs were prepared approximately parallel to the {010} cleavage, and others were prepared approximately parallel to the {001} cleavage. Diffusion properties were determined along the thin direction of each slab, so in the (010) slab, diffusion was determined along ~[010]*, and for the ~(001) slab, diffusion was determined $\perp$ ~[010]*.

Methods

Polarized infrared spectra were obtained in the main compartment of a Nicolet Magna 860 FTIR spectrometer at 4 cm^{-1} resolution, using a CaF_2 beamsplitter, MCT-A detector, and a $LiIO_3$ Glan-Foucalt prism polarizer. Each spectrum was obtained using a 1000 μm circular aperture in the center of the polished slab, and was averaged over 256 scans.

The polished slabs of plagioclase were heated in a silica glass tube furnace under nitrogen gas. The variation in temperature was less than 3°C across the area in the center of the furnace where the samples were placed during heating. At least one ~(010) and one ~(001) polished slab were included in the heating experiments at each temperature (1000°C, 900°C, and 800°C). The duration of a particular heating run was timed from insertion of the ceramic boat

containing the samples into the center of the tube until removal of the boat from the furnace. After each heating run, infrared spectra were obtained in the center of the slab and the remaining OH concentration was calculated. This study is concerned with changes in the OH concentration during heating rather than absolute OH concentration, so the total OH concentration at each time step (including the initial OH concentration before heating) is represented simply by the sum of the areas of the mid-IR OH absorption bands (2700-3600 cm^{-1}) in the two polarized spectra obtained on each slab. For ~(010), these are the *X* and *Y* principal optical directions. For the (001) slab, spectra were obtained with E||*X* and E||Z.

Calculation of Diffusion Coefficients

A one-dimensional model of diffusion in an infinite plane sheet with an initial uniform distribution of hydrogen is assumed, with surfaces that are kept at constant and equal concentrations. The appropriate diffusion equation for this situation is Equation 4.18 of Crank (1970):

$$\frac{M_t}{M_\infty} = 1 - \sum_{n=0}^{\infty} \frac{8}{(2n+1)^2 \pi^2} e^{-D(2n+1)^2 \pi^2 t / 4L^2}, \quad (4.1)$$

where M_t is the amount of diffusing substance that has left the sheet after time *t*, M_∞ is the amount of diffusing substance that has left the sheet after infinite time, 2*L* is the thickness of the sheet, and *D* is the diffusion coefficient.

For the purposes of these diffusion experiments, the infinite plane sheet is approximated with a polished slab of plagioclase with a thickness much less than its width. Thus, 2*L* in Equation 4.1 corresponds to the thickness of a particular polished slab. The time *t* is the cumulative duration of heating at a particular temperature. The quantity M_t is determined from the amount of OH band area lost after time *t* (100 – the % of the original band area at time *t*) since the infrared spectra measure the integrated OH concentration through the thickness of the slab. The total loss of OH is determined from heating experiments at very long times. Here, it is assumed that M_∞ is 100%, and that all OH is eventually lost from the feldspar, since this is closely approached in the 1000°C experiments. From a series of measurements of *t* and M_t, the diffusion coefficient *D* can be determined for a particular temperature.

Results

The shape and position of the OH absorbance bands remained constant during the step heating experiments (Figure 4.1). Each polarization direction within a single slab experienced the same rate of loss of OH band area during dehydration.

Determination of diffusion coefficients

The data obtained from the series of experiments are shown as $\frac{M_t}{M_\infty}$ versus $\sqrt{t}/L$ at 1000°C, 900°C, and 800°C in Figures 4.2, 4.3, and 4.4. For a given temperature, the hydrogen loss data from slabs of different thicknesses representing the two different crystallographic diffusion directions follow a single trend. Since the normalized data from slabs of varying thicknesses are essentially indistinguishable, the thickness of the slab ($2L$) is the correct characteristic length scale of diffusion, and smaller domains within the crystal are not responsible for the measured diffusion properties. Diffusion data from the two crystallographic directions can be fit with a single diffusion coefficient, thus diffusion of hydrogen in the feldspar is isotropic within error.

The diffusion coefficient D was determined at each temperature using Equation 4.1, assuming total loss of hydrogen from the slab at large values of time ($M_\infty = 0$). At 1000°C, D is equal to $4.2 \pm 1.1 \times 10^{-13}$ m^2/s; at 900°C D is $4.3 \pm 1.2 \times 10^{-14}$ m^2/s; and at 800°C D is $1.0 \pm 0.6 \times 10^{-14}$ m^2/s. Equation 4.1 (Equation 4.18 of Crank (1970)) is plotted on each graph, using the corresponding diffusion coefficient obtained from minimizing the sum of the squares of the data. The errors on the calculated diffusion coefficients were estimated from the maximum error on the measurement of the OH band areas, which is taken to be ± 5% of the maximum band area (determined from the range of $X+Y$ OH band areas measured before heating).

For the experiments at 1000°C, only the data points with $\frac{M_t}{M_\infty}$ less than or equal to 0.5 were used to determine the diffusion coefficient, since the data at larger values do not fit the curve expected from Equation 4.1. In this case, D is an apparent diffusivity at short times. This type of deviation (the sample loses OH more slowly than is expected at high values of time) is seen for OH diffusion in glasses and in pyrope garnet (Zhang et al. 1991a; Zhang et al. 1991b; Wang et al. 1996), and occurs when diffusion is dependent on the concentration of the hydrous component. It is not clear why this behavior is observed only at 1000°C and is not present in the experiments at 900°C in this study.

Calculation of D_o and activation energy

The temperature dependence of D was determined from a least-squares fit of the diffusion data using the relationship:

$$D = D_0 \exp\left(-\frac{Q}{RT}\right), \qquad (4.2)$$

where the diffusion coefficient D and the pre-exponential term D_0 are in units of m^2/s, Q is the activation energy in kJ/mol, R is the gas constant (8.31441×10^{-3} kJ/(K·mol)), and T is temperature in Kelvins. A least-squares fit of the linear form of Equation 4.2 was used to calculate a D_0 of $5.7 \pm 2.5 \times 10^{-4}$ m^2/sec and an activation energy Q of 224±33 kJ/mol.

Discussion

Diffusion behavior of cations and oxygen in feldspars

The hydrogen diffusion data for andesine are plotted along with diffusion data for other cations and oxygen in Figure 4.5. In feldspars, hydrogen diffuses more rapidly than most other cations, but the diffusion data for hydrogen are comparable to self-diffusion for Na. The diffusion of alkali atoms (Na and K) in feldspars occurs via a vacancy mechanism involving Frenkel defects (a

cation vacancy and a compensating cation interstitial) (Petrovic 1972a). The activation energy Q for Na diffusion in feldspars is 176-239 kJ/mol (Yund 1983), and the Q for hydrogen diffusion in OH-bearing plagioclase falls within this range. The diffusion of hydrogen in plagioclase is isotropic, and the diffusion coefficient for Na is either isotropic or only slightly anisotropic (Petrovic 1972a; Yund 1983). The crystallographic location of OH in intermediate plagioclase feldspars is not known, but polarized infrared spectra of OH bands in plagioclase and synthetic hydrogen feldspar ($HAlSi_3O_8$) indicate that O atoms surrounding the large cation (M) site may form hydroxyl groups (Müller 1988; Johnson and Rossman 2003). Therefore, the activation energy, isotropic diffusivity, and possible location of H within the Na site all point to a hydrogen diffusion mechanism involving movement of Na vacancies and H interstitials. Note that alkali diffusion is not affected by the presence of water (Yund 1983), although the rate of oxygen self-diffusion and degree of Al-Si disordering are dependent on water pressure (Yund and Anderson 1978; Goldsmith 1987; Goldsmith 1988).

Diffusion of hydrogen in nominally anhydrous minerals

The diffusion data for hydrogen in plagioclase and other nominally anhydrous minerals are plotted in Figure 4.6. The measured rates of hydrogen diffusion in nominally anhydrous minerals are generally an order of magnitude faster than the rate of hydrogen diffusion in OH-bearing plagioclase. In relatively

Fe-rich nominally anhydrous minerals such as diopside, olivine, and pyrope, the experimentally determined rate of diffusion involves a mechanism of protons moving in concert with rapidly diffusiong electrons (e.g., Woods et al. 2000). In olivine, two rates of hydrogen diffusion are observed: rapid diffusion involving electrons (as shown in Figure 4.6), and slower diffusion, similar to that of hydrogen in plagioclase, involving hydrogen and point defects such as metal vacancies (Kohlstedt and Mackwell 1998). Since the andesine in this study contains only a small amount of Fe compared to the amount of OH present in the structure, metastable rapid diffusion is not observed for the feldspar.

The rate of hydrogen diffusion in OH-bearing plagioclase is much slower than diffusion of hydrogen in H_2O-bearing K-feldspar. The OH concentration of the andesine (510 ppm H_2O) is a little more than twice the concentration of structural H_2O in the K-feldspar (180 ppm H_2O) used in Kronenberg et al. (1996), so the number of hydrous defects in each feldspar structure is roughly equivalent. Hydrogen in the H_2O-bearing K-feldspar may diffuse as proton interstitials, as in β-quartz (Kats et al. 1962), or as mobile H_2O defects, as in glasses (Zhang et al. 1991a; Zhang et al. 1991b). It is possible that the diffusing species of hydrogen is different for OH-bearing and H_2O-bearing feldspars, and that this is the reason for the different rates of hydrogen diffusion. It is interesting that molecular H_2O is the dominant diffusing

species in glasses with a wide range of water concentrations, even in those with low water contents containing mostly OH groups (Zhang et al. 1991a; Zhang et al. 1991b). Further modeling of the hydrogen diffusion data at 1000°C from this study may elucidate whether concentration-dependent diffusion occurs in OH-bearing plagioclase.

Geological implications

The degree of hydrogen retention expected for volcanic feldspar phenocrysts during cooling from magmatic temperatures can be estimated using the diffusion data from this study and Equation 6.20 of Crank (1970) for diffusion in a solid sphere. The percent of initial OH concentration remaining in a spherical feldspar grain, assuming total loss of hydrogen from the mineral at large values of time, is plotted as function of time in Figure 4.7. This graph is only an approximate representation of the diffusion behavior at 1000°C and underestimates the retention of OH at long times for that temperature. Most of the original OH concentration is lost from a 1 mm feldspar grain after hours to weeks at 800-1000°C. This is on the same order of magnitude as the timescale of a typical eruptive event, and diffusion of OH during and immediately post-eruption may greatly affect the final OH concentration preserved in a feldspar phenocryst. A feldspar that is brought to the surface and cools quickly would likely retain a significant portion of the original OH concentration, while one that takes longer to get to the surface and cool will lose a greater proportion of

its OH concentration. The initial OH concentration is still an important factor in determining the final OH concentration, however, since a phenocryst with high initial OH content that cools more slowly may still retain a significant OH concentration.

It is assumed here that the total loss of hydrogen from the plagioclase observed at 1000°C when heated under nitrogen gas at 1 bar is directly applicable to feldspar phenocrysts exposed to a dynamic system involving melt and volatiles during and after an eruptive event. Depending on the partitioning behavior of OH into the feldspar, In a water-rich system, the concentration of OH in a feldspar phenocryst in equilibrium with the environment may be greater than zero, and less hydrogen may be lost or uptake of OH into the feldspar structure could occur. Determining the effective grain size of a natural feldspar is another potential complication. Millimeter-size phenocrysts are not uncommon in many volcanic rocks, but plagioclase feldspars are often twinned, and the effect of twins on diffusion behavior was not tested here.

Conclusions

Hydrogen in OH-bearing plagioclase diffuses at a rate similar to that of Na (D_0 = 5.7±2.5×10^{-4} m^2/sec and Q = 224±33 kJ/mol) and the mechanism of

hydrogen diffusion is likely related to the movement of Na vacancies in the crystal structure. Even though the diffusion rate for hydrogen in OH-bearing plagioclase is much slower than hydrogen diffusion measured previously in other nominally anhydrous minerals, the timescale for complete diffusive loss of OH from a millimeter-sized feldspar is on the order of a day to a week for typical eruption temperatures. Since many volcanic feldspars contain significant amounts of structural OH (Chapter 3), the total loss of OH concentration at 1 bar pressure under nitrogen gas may not accurately reflect the potentially volatile-rich environment of a phenocryst during eruption.

Table 4.1. Infrared band areas for time series of heating experiments under nitrogen gas at 1000°C, 900°C, and 800°C.

1000°C														
Slab || (010)	**0.499 mm thick**	**Cumulative heating duration**	**seconds**	**0**	**3600**	**10800**	**21600**	**36000**	**52200**	**70200**	**99000**	**142200**	**216000**	**432480**	**863280**
			hours	**0**	**1**	**3**	**6**	**10**	**14.5**	**19.5**	**27.5**	**39.5**	**60**	**120.13**	**239.8**
		Polarized IR band areas*	X	132.7	107.7	91.3	85.2	66.9	52.7	47.6	36.6	30.3	20.6	11.7	7.5
			Y	27.3	23.8	17.8	16.1	12.9	9	7.1	5.6	4.7	2.9	1.6	0.6
			X + Y	160	131.5	109.1	101.3	79.8	61.7	54.7	42.2	35	23.5	13.3	8.1
		% of initial band area†		**100**	**82**	**68**	**63**	**50**	**39**	**34**	**26**	**22**	**15**	**8**	**5**
		M_t/M_∞		**0.00**	**0.18**	**0.32**	**0.37**	**0.50**	**0.61**	**0.66**	**0.74**	**0.78**	**0.85**	**0.92**	**0.95**
Slab || (010)	**0.311 mm thick**	**Cumulative heating duration**	**seconds**	**0**	**3600**	**10800**	**21600**	**36000**	**52200**	**70200**	**99000**	**142200**	**216000**	**432480**	**863280**
			hours	**0**	**1**	**3**	**6**	**10**	**14.5**	**19.5**	**27.5**	**39.5**	**60**	**120.13**	**239.8**
		Polarized IR band areas*	X	90.8	55.9	42.7	38.9	28.8	23.8	19.2	14.5	12.7	9.9	5.6	4.1
			Y	18.2	11.3	9.7	6.3	4.5	3.4	3.3	2.1	2.4	1.5	1.1	0.6
			X + Y	109	67.2	52.4	45.2	33.3	27.2	22.5	16.6	15.1	11.4	6.7	4.7
		% initial band area		**100**	**62**	**48**	**41**	**31**	**25**	**21**	**15**	**14**	**10**	**6**	**4**
		M_t/M_∞		**0.00**	**0.38**	**0.52**	**0.59**	**0.69**	**0.75**	**0.79**	**0.85**	**0.86**	**0.90**	**0.94**	**0.96**
Slab ⊥ (010)	**0.787 mm thick**	**Cumulative heating duration**	**seconds**	**0**	**3600**	**10800**	**21600**	**36000**	**52200**	**70200**	**99000**	**142200**	**216000**	**432480**	**863280**
			hours	**0**	**1**	**3**	**6**	**10**	**14.5**	**19.5**	**27.5**	**39.5**	**60**	**120.13**	**239.8**
		Polarized IR band areas*	X	221	188.4	174.9	164.7	150.5	130.4	116.9	97.6	82	62.3	43	27.9
			Z	130.9	104.7	96.5	89.4	81.7	74.1	64.8	52.7	42.3	31.8	20	13.4
			X + Z	351.9	293.1	271.4	254.1	232.2	204.5	181.7	150.3	124.3	94.1	63	41.3
		% initial band area		**100**	**83**	**77**	**72**	**66**	**58**	**52**	**43**	**35**	**27**	**18**	**12**
		M_t/M_∞		**0.00**	**0.17**	**0.23**	**0.28**	**0.34**	**0.42**	**0.48**	**0.57**	**0.65**	**0.73**	**0.82**	**0.88**

Table 4.1 continued.

900°C

Slab || (010)	**0.521 mm thick**	**Cumulative heating duration**	**seconds**	**0**	**3600**	**7200**	**15000**	**25800**	**47400**	**101400**	**162900**	**216000**	**288000**	**374700**	**471900**	**644700**
			hours	**0**	**1**	**2**	**4.17**	**7.17**	**13.17**	**28.17**	**45.25**	**60**	**80**	**104.08**	**131.08**	**179.08**
		Polarized IR	X	146.8	134.5	132.5	128.1	126.8	117.6	107.1	96.9	89.7	78.5	70.4	58.2	39
		band areas*	Y	28.5	25.3	22.8	22.3	22.2	20.8	17.9	17.8	16.7	13.9	12.5	10.4	7.1
			X + Y	175.3	159.8	155.3	150.4	149	138.4	125	114.7	106.4	92.4	82.9	68.6	46.1
		% initial band area		**100**	**91**	**89**	**86**	**85**	**79**	**71**	**65**	**61**	**53**	**47**	**39**	**26**
		M_t/M_∞		**0.00**	**0.09**	**0.11**	**0.14**	**0.15**	**0.21**	**0.29**	**0.35**	**0.39**	**0.47**	**0.53**	**0.61**	**0.74**
Slab ⊥ (010)	**0.644 mm thick**	**Cumulative heating duration**	**seconds**	**0**	**3600**	**7200**	**15000**	**25800**	**47400**	**101400**	**162900**	**216000**	**288000**	**374700**	**471900**	**644700**
			hours	**0**	**1**	**2**	**4.17**	**7.17**	**13.17**	**28.17**	**45.25**	**60**	**80**	**104.08**	**131.08**	**179.08**
		Polarized IR	X	178.4	174.4	164.9	163	159.2	154.4	143.1	137.3	127.1	116.2	110.4	94.2	63.7
		band areas*	Z	105	95.2	97.9	94.8	93.6	86.9	82.2	74.9	73.7	67.5	58.5	52.1	38.7
			X + Z	283.4	269.6	262.8	257.8	252.8	241.3	225.3	212.2	200.8	183.7	168.9	146.3	102.4
		% initial band area		**100**	**95**	**93**	**91**	**89**	**85**	**79**	**75**	**71**	**65**	**60**	**52**	**36**
		M_t/M_∞		**0.00**	**0.05**	**0.07**	**0.09**	**0.11**	**0.15**	**0.21**	**0.25**	**0.29**	**0.35**	**0.40**	**0.48**	**0.64**
Slab ⊥ (010)	**0.153 mm thick**	**Cumulative heating duration**	**seconds**	**0**	**3600**											
			hours	**0**	**1**											
		Polarized IR	X	44.7	35											
		band areas*	Z	26	18.2											
			X + Z	70.7	53.2											
		% initial band area		**100**	**75**											
		M_t/M_∞		**0.00**	**0.25**											

Table 4.1 continued.

800°C

Slab || (010)	**0.300 mm thick**	**Cumulative heating duration**	**seconds**	**0**	**7320**	**34020**			
			hours	**0**	**2.03**	**9.45**			
		Polarized IR band areas*	X	84.7	80.3	69.8			
			Y	16.8	15.1	12.9			
			X + Y	101.5	95.4	82.7			
		% initial band area		**100**	**94**	**81**			
		M_t/M_∞		**0.00**	**0.06**	**0.19**			
Slab ⊥ (010)	**0.625 mm thick**	**Cumulative heating duration**	**seconds**	**0**	**7320**	**34020**	**108720**	**195120**	**281100**
			hours	**0**	**2.03**	**9.45**	**30.2**	**54.2**	**78.08**
		Polarized IR band areas*	X	184.4	172.3	166.4	162.2	148.2	151.7
			Z	100.9	105.4	99.5	95.9	88.8	87.4
			X + Z	285.3	277.7	265.9	258.1	237	239.1
		% initial band area		**100**	**97**	**93**	**90**	**83**	**84**
		M_t/M_∞		**0.00**	**0.03**	**0.07**	**0.10**	**0.17**	**0.16**

* X, Y, and Z are the principle optical directions.

†M_t/M_∞ = [100-(% initial band area)]/100

Figure 4.1. Mid-IR OH absorption bands in the *X* polarization direction on the polished slab perpendicular to (010) (approximately parallel to (001)) before and after heating at 1000°C. The OH band shapes and positions do not change during the dehydration experiments.

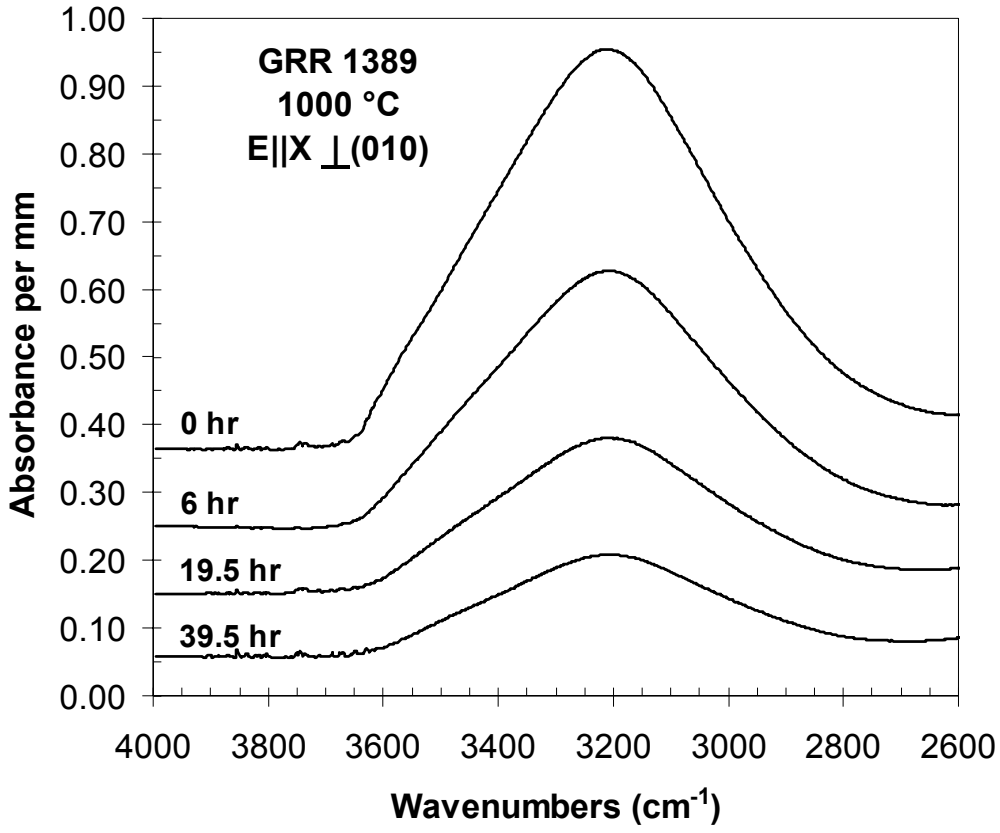

Figures 4.2-4.4. Time series of OH band area measurements plotted as total fraction of OH band area lost ($\frac{M_t}{M_\infty}$) versus the square root of time (t) in seconds divided by half the thickness of the polished slab ($2L$). Error bars reflect the uncertainties in measuring total OH band area from the IR spectra. The solid line is Equation 4.18 of Crank (1970) (Equation 4.1 in this chapter) plotted using the best-fit diffusion coefficient for each temperature assuming an infinite slab of thickness $2L$ and total loss of OH at large t.

Figure 4.2. 800°C.

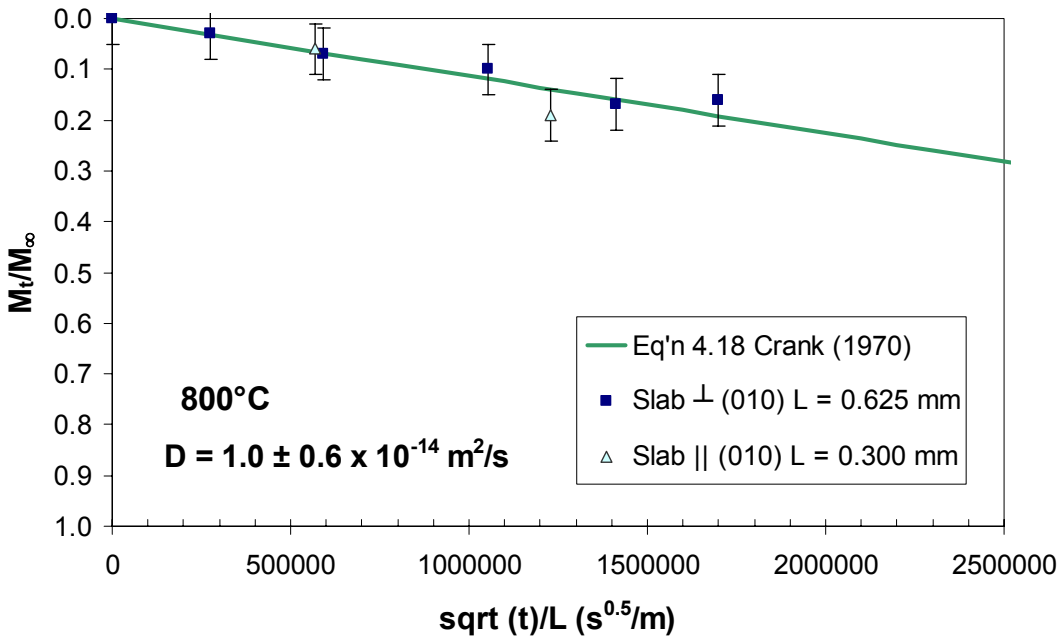

Figure 4.3. 900°C.

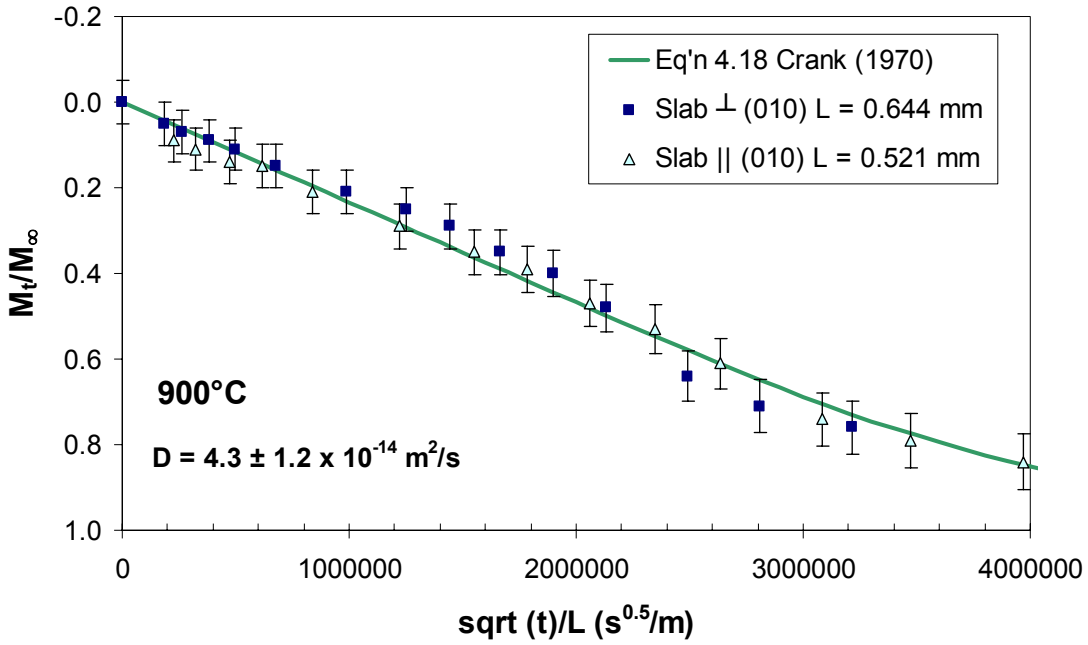

Figure 4.4. 1000°C.

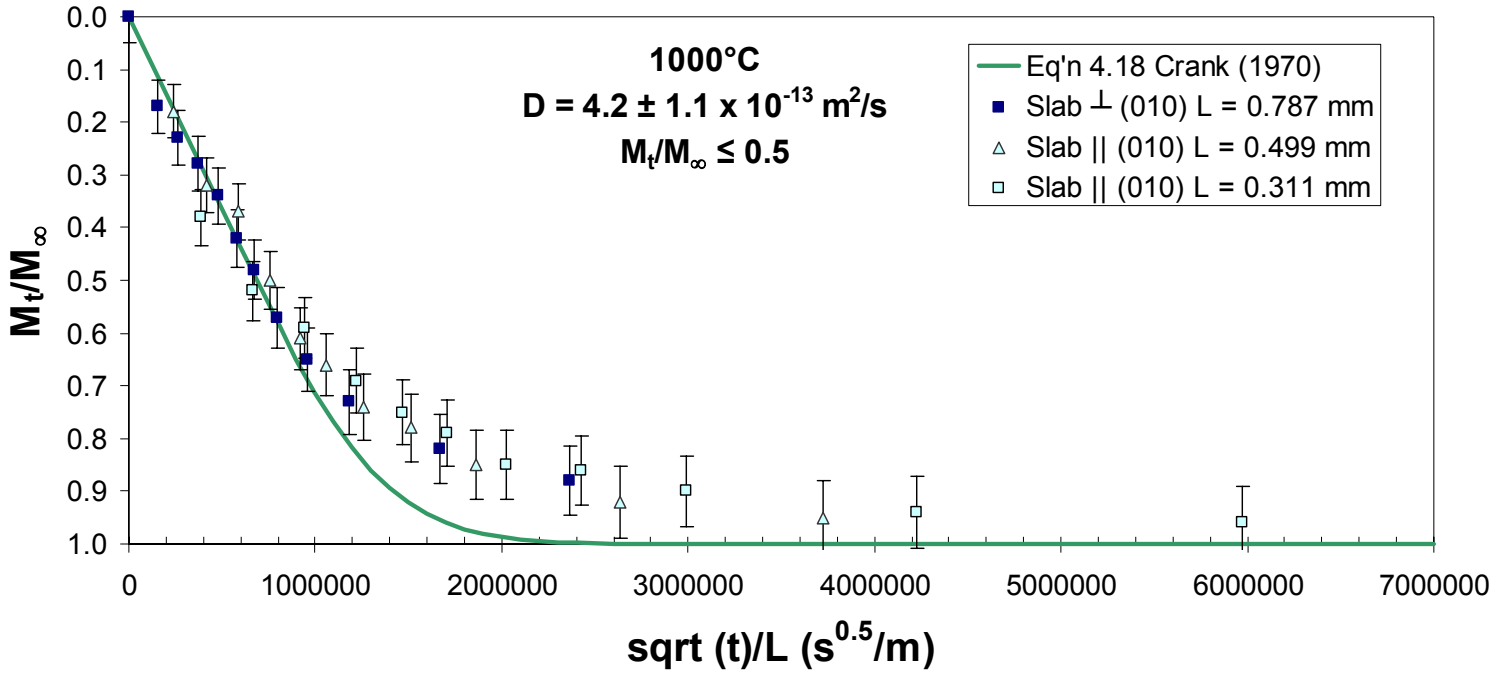

Figure 4.5. Diffusivities of cations and oxygen in feldspar as a function of temperature. The hydrogen diffusion data for andesine is from this study. References to other data are: (P 1972) = Petrovic (1972b); (B 1971) = Bailey (1971); (B 1990) = Behrens et al. (1990); (MK 1974) = Muehlenbachs and Kushiro (1974); and (G 1978) = Giletti et al. (1978).

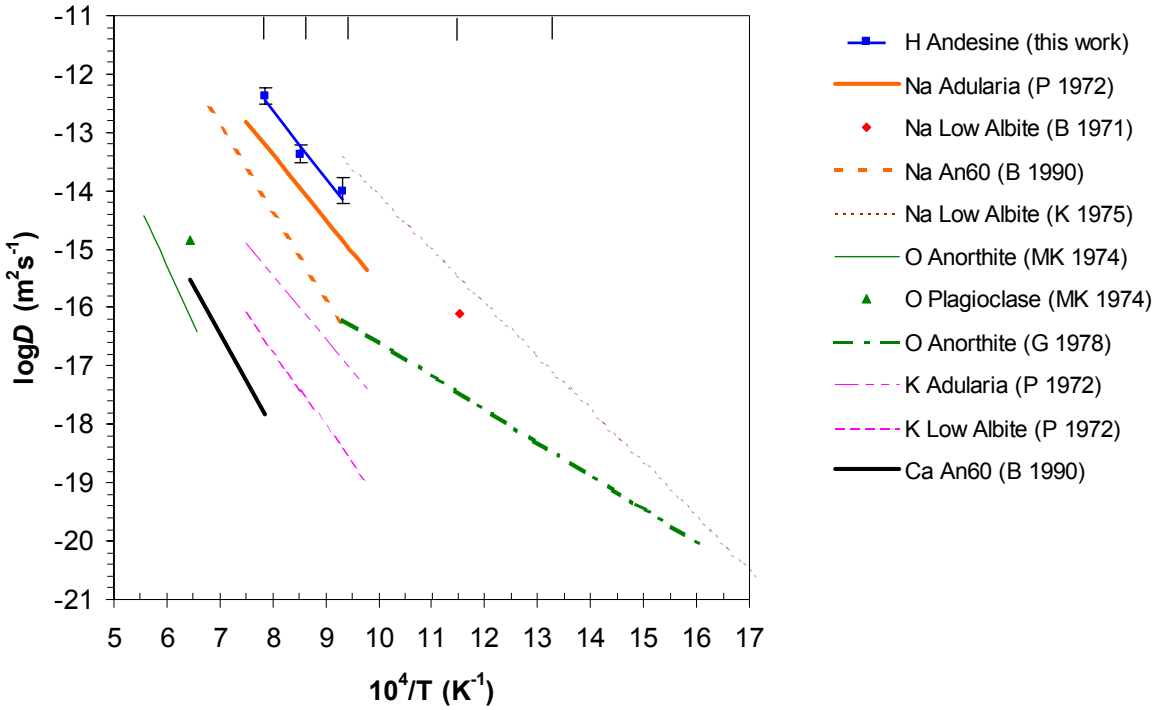

Figure 4.6. Diffusivities of hydrogen in nominally anhydrous minerals as a function of temperature. The hydrogen diffusion data for andesine is from this study. References to other data are: (K 1996) = Kronenberg et al. (1996); (K 1962) = Kats et al. (1962); (W 2000) = Woods et al. (2000); (HI 1999) = Hercule and Ingrin (1999); (MK 1990) = Mackwell and Kohlstedt (1990); and (W 1996) = Wang et al. (1996).

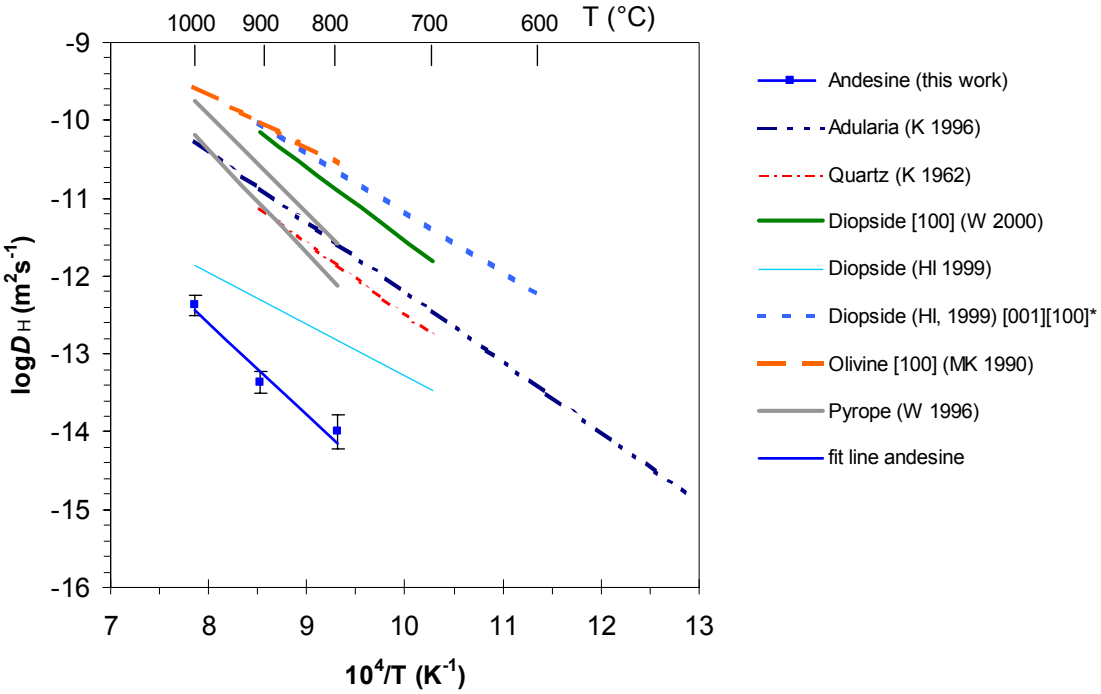

Figure 4.7. Percent of initial OH concentration remaining in spherical feldspar grains 1 mm and 0.5 mm in diameter as a function of time (assuming total loss of OH at large values of time) at a) 800°C, b) 900°C, and c) 1000°C using diffusion data from this study.

Figure 4.7A.

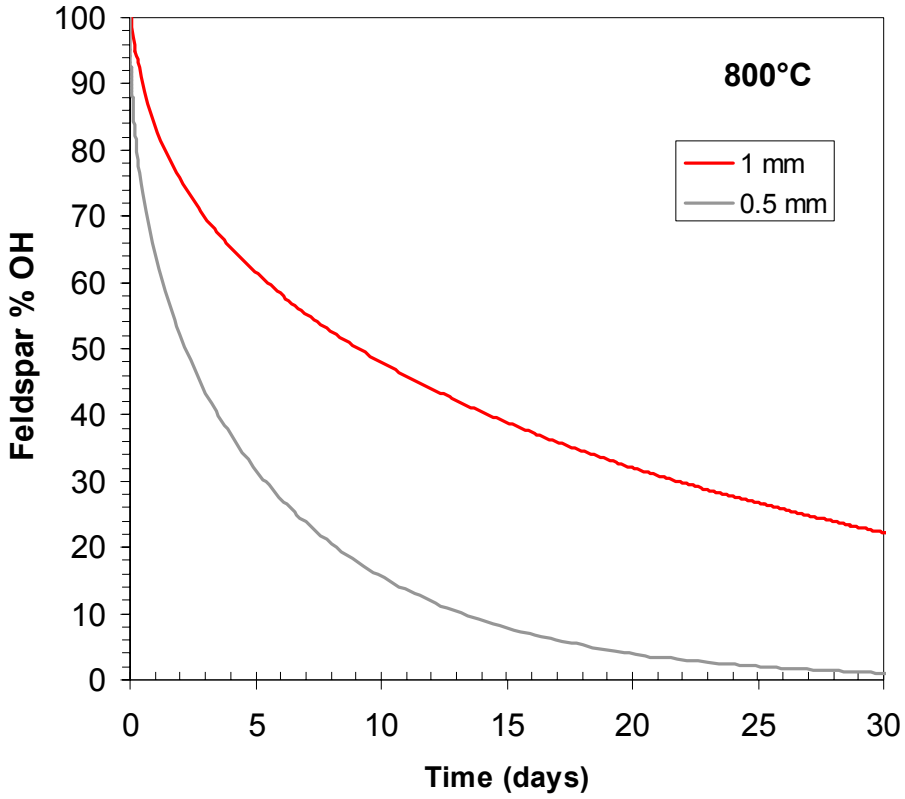

Figure 4.7B.

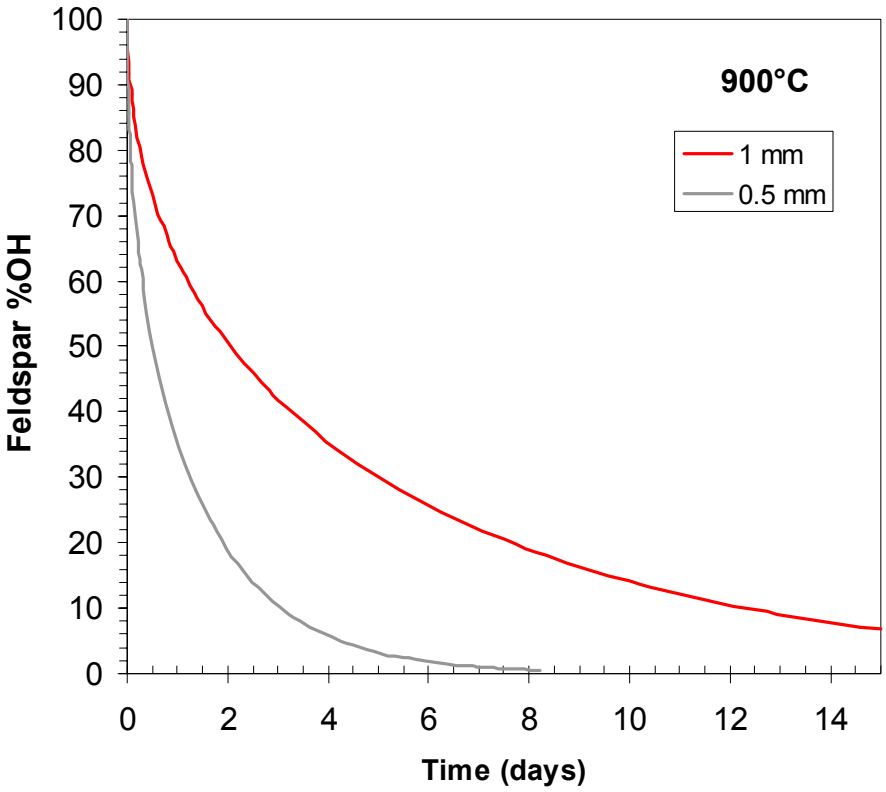
900°C
1 mm
0.5 mm
Feldspar %OH
Time (days)
0
10
20
30
40
50
60
70
80
90
100
0
2
4
6
8
10
12
14

Figure 4.7C.

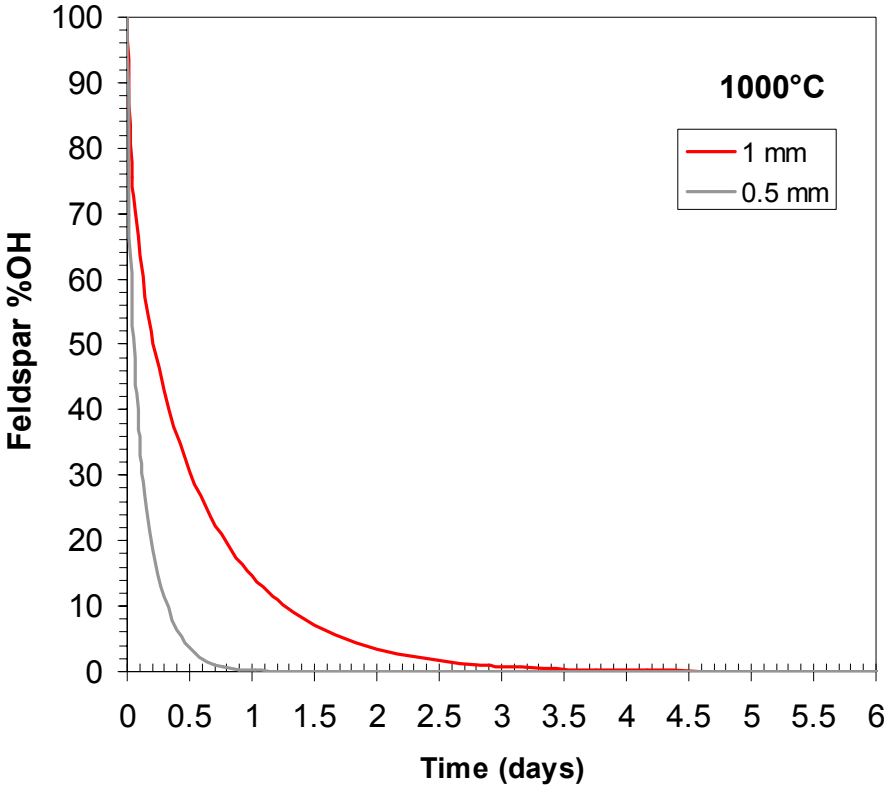
100
90
80
70
60
50
40
30
20
10
0
Feldspar %OH
0
0.5
1
1.5
2
2.5
3
3.5
4
4.5
5
5.5
6
Time (days)
1000°C
1 mm
0.5 mm

C h a p t e r 5

AN INFRARED AND ^{1}H MAS NMR INVESTIGATION OF STRONG HYDROGEN BONDING IN USSINGITE, $Na_2AlSi_3O_8(OH)$[3]

Abstract

The mineral ussingite, $Na_2AlSi_3O_8(OH)$, an "interrupted" tectosilicate, has strong hydrogen bonding between OH and the other non-bridging oxygen in the structure. Infrared spectra contain a strongly polarized, very broad OH stretching band with an ill-defined maximum between 1500-1800 cm^{-1}, and a possible OH librational bend at 1295 cm^{-1}. The IR spectra confirm the orientation of the OH vector within the triclinic unit cell as determined from X-ray refinement (Rossi et al. 1974). There are three distinct bands in the ^{1}H NMR spectrum of ussingite: a predominant band at 13.5 ppm (TMS) representing 90% of the structural hydrogen, a second band at 15.9 ppm

---

[3] Submitted to Physics and Chemistry of Minerals.

corresponding to 8% of the protons, and a third band at 11.0 ppm accounting for the remaining 2% of structural hydrogen. From the correlation between hydrogen bond length and ^{1}H NMR chemical shift (Sternberg and Brunner 1994), the predominant hydrogen bond length was calculated to be 1.49 Å, in comparison to the hydrogen bond length determined from X-ray refinement (1.54 Å). The population of protons at 15.9 ppm is consistent with 5-8% Al-Si disorder. Although the ussingite crystal structure and composition are similar to those of low albite, the bonding environment of OH in low albite and other feldspars, as characterized through IR and ^{1}H NMR, is fundamentally different from the strong hydrogen bonding found in ussingite.

Introduction

Ussingite, $Na_2AlSi_3O_8(OH)$, is a very rare mineral first identified by Böggild (1914) that occurs in extremely basic, silica-poor sodalite syenites ("hyperagpaitic" rocks) (Sørenson 1997). Ussingite formed as a late-stage hydrothermal pegmatite mineral in the Ilímaussaq intrusive complex in southwest Greenland (Engell et al. 1971) and the Lovozero and Khibina complexes of the Kola peninsula (Ilyukhin and Semenov 1959). It is also found in sodalite xenoliths in the Mont Saint-Hilaire, Canada, alkalic gabbro-syenite complex (Mandarino and Anderson 1989).

The crystallographic structure of ussingite was determined by Rossi et al. (1974). Ussingite has an "interrupted" aluminosilicate framework structure, in which seven of the nine oxygens are bridging oxygens linking the Al and Si tetrahedra in 4-, 6-, and 8-fold rings. The remaining two oxygens (O(2) and O(8)) are non-bridging and participate in hydrogen bonding (Figure 5.1). The O(8)-H, O(2)-H, and O(2)-O(8) distances were determined from structural refinement of the X-ray data to be 0.97 Å, 1.54 Å, and 2.507 Å, respectively. The hydrogen bonding in ussingite is characterized as strong, since the O(2)-O(8) distance is significantly shorter than the sum of the van der Waals radii of two oxygen atoms (about 3.0 Å) (Emsley 1981). As is typical for strongly hydrogen bonded systems, the O(2)-H-O(8) angle is nearly linear (171°) (Rossi et al. 1974).

The Al in ussingite is almost completely ordered into the T(1) tetrahedron, one of four tetrahedral sites in the structure (Rossi et al. 1974). However, Ribbe (1974) found a better agreement between observed and calculated T-O distances for ussingite when 5% of the Al was transferred from T(1) to T(3). Ussingite is triclinic, but it exhibits a pseudo-monoclinic symmetry (Rossi et al. 1974). The complete Al-Si ordering and the asymmetric nature of the O-H···O bonding are the causes of the triclinic symmetry.

Previous workers have investigated some of the physical properties, the crystallographic structure, and chemistry of ussingite. A ^{29}Si nuclear magnetic resonance (NMR) and ^{29}Si-^{1}H cross-polarization (CP) NMR study confirmed the assignment of Si to three tetrahedral sites and provided additional constraints on Si-H distances in the ussingite structure (Oglesby and Stebbins 2000). Thermal gravimetric analysis showed that ussingite is dehydrated over a temperature range of 500 to 650° C (Ilyukhin and Semenov 1959). Several sets of chemical analyses report that ussingite largely contains stoichiometric Na, Al, Si, and H (Böggild 1914), with some samples containing minor amounts of K, Ca, Fe, Mn, S, and Cl (Ilyukhin and Semenov 1959; Povarennykh et al. 1970).

However, the OH in ussingite has not previously been characterized with IR or ^{1}H NMR spectroscopy. Both of these techniques can provide important constraints on the nature of hydrogen bonding. Correlations have been established between hydrogen bond length and ^{1}H NMR chemical shift (Jeffrey and Yeon 1986; Sternberg and Brunner 1994), as well as between the IR OH stretch frequency and O-H$\cdots$O distance (Nakamoto et al. 1955; Libowitzky 1999) for minerals and solid hydrates. The crystallographic orientation of the OH vector can be determined with single-crystal polarized IR spectroscopy. Magic-angle spinning (MAS) NMR reduces the band width

of the proton signal in solids, so that it is possible to resolve proton populations that experience slightly different hydrogen bonding environments.

As discussed in Ribbe (1974) and Rossi et al. (1974), there are striking similarities between the structures of low albite and ussingite. Both structures have complete or nearly complete Al-Si ordering in tetrahedra that form 4-, 6-, and 8-fold rings, and in both structures the Na atoms are irregularly coordinated (with coordination numbers of 5 and 6 in ussingite, and 5 in low albite) (Rossi et al. 1974; Downs et al. 1996). In fact, an equation derived from structural data of sodic plagioclases used to quantitatively describe the variation in T-O bond lengths in these minerals produces excellent estimates of the Al-O, Si-O, and Si-(OH) bond distances in ussingite (Ribbe 1974).

There are two main purposes for conducting this study. The first is to determine if the stoichiometric OH observed in ussingite (2.98 wt% H_2O) can be used as a structural model for the small quantities (0-0.051 wt% H_2O) of structural OH that are incorporated into low albite as well as other plagioclase feldspars, sanidine, and anorthoclase (Hofmeister and Rossman 1985a; Hofmeister and Rossman 1985b; Hofmeister and Rossman 1986; Johnson and Rossman 2003). The mechanism for how OH is incorporated into the feldspar structures is unknown, so a comparison of the IR and ^{1}H NMR spectra of OH in feldspars (Johnson and Rossman 2003) and the OH in ussingite will provide

important constraints on the possible bonding environments of OH in feldspars. The second reason for this study is that there have been few IR investigations of strong and very strong hydrogen bonding in minerals, such as serandite and pectolite (Hammer et al. 1998), and mozartite (Nyfeler et al. 1997). A complete study of the IR spectra of ussingite will increase knowledge of the characteristics (energy, band shape, polarization, and symmetry) of strong hydrogen bonds in minerals.

Methods

The ussingite used in this study is from the Ilímaussaq complex, Greenland (sample GRR1967). It occurs in a white, transparent to translucent granular aggregate. Single crystals are less than 100 μm to several millimeters across. Mineral identification was confirmed with powder X-ray diffraction.

Oriented, polished slabs of single crystals were prepared for infrared spectroscopic measurements using cleavage and twin planes. Because of the granular nature of the sample, no crystal faces were visible. Three cleavages, $c\{001\}$, $m\{110\}$ and $M\{1\bar{1}0\}$, were originally reported for ussingite (Böggild 1914). In the present study the triclinic unit cell of Rossi et al. (1974) was used, and in these coordinates the cleavages are $c\{100\}$, $m\{01\bar{1}\}$, and $M\{1\bar{1}\bar{1}\}$.

A polished slab was prepared parallel to the {100} cleavage to obtain polarized IR spectra with E||*b* and E||*c*. The *b* and *c* axes are nearly perpendicular to each other (α = 90°45') (Rossi et al. 1974), and the angle between the normal to (010) and the principal optical direction Y is 5-6° (Böggild 1914), which, in addition to cleavage planes, made it possible to locate the *b* and *c* axes within the polished slab. Twinning occurs parallel to {010}, and grains lying on this surface produce a slightly off-center flash figure. The principal optical direction Z (the acute bisectrix) is about 33° from the vector normal to (100) in the {010} plane (Böggild 1914). Thus, it was possible to obtain a polarized spectrum with E||*a* on a polished slab parallel to (010). It was necessary to fabricate polished slabs that were as thin as possible since ussingite has a relatively high OH concentration (2.98 wt% H_2O), and because the OH bands overlap the very intense silicate modes. Slabs were prepared with Al_2O_3 and diamond films. The grain was mounted on a circular thin section slide with Crystalbond® thermal adhesive, and after preparation, the adhesive was dissolved in acetone to produce an unsupported, slightly wedge-shaped slab for IR work. The thickness of the portion of each slab used to obtain IR spectra was determined using the birefringence colors obtained under crossed polars (refractive indices α = 1.504, β = 1.508, γ = 1.545) (Böggild 1914). The final polished slabs were 17 μm thick (010) and 15 μm thick (100).

Polarized infrared spectra were obtained in the 400-5000 cm^{-1} region using a Spectra-Tech Continuμm® microscope accessory with a Nicolet Magna 860 FTIR spectrometer at 4 cm^{-1} resolution, an extended-range KBr beamsplitter, Au wire grid on AgBr polarizer, and MCT-B detector. Each spectrum was averaged over 512 scans, using a 50-100 μm square aperture.

^{1}H MAS NMR spectra were recorded on a Bruker DSX 500 MHz spectrometer and a Bruker Avance 200 MHz spectrometer at the solid-state NMR facility in the Department of Chemical Engineering at Caltech. A 4 μs 90° – 8 μs 180° pulse depth sequence (program written by Sonjong Hwang; Cory and Ritchey (1988)) was used to minimize probe background for most spectra. Tetrakis-(trimethylsilyl)silane (TKTMS) was used as a primary chemical shift (δ) reference, but final spectra are referenced to tetramethylsilane (TMS), using the relationship δ(TMS) = δ(TKTMS) + 0.247 ppm (Hayashi and Hayamizu 1991). Saturation-recovery experiments were used to determine a spin-lattice relaxation time T_1 of about 100 seconds for ussingite. Variable temperature experiments were conducted between 178 K and 373 K. Dry nitrogen from a high-pressure liquid nitrogen tank was used for cooling and spinning the samples.

Results

The polarized infrared spectra of ussingite are shown in Figure 5.2. In each spectrum, the absorption bands of the silicate modes (1200-600 cm^{-1}) are off scale (absorbance is greater than 2.0). The E||*b* spectrum is characterized by a flat background in the 3500-1300 cm^{-1} region, with a small, broad absorbance band at about 1700 cm^{-1} and a sharper, more intense band at 1295 cm^{-1}. The E||*c* spectrum lacks the 1295 cm^{-1} band, but has a very broad and intense band that begins at around 3000 cm^{-1} and continues under the silicate modes to less than 800 cm^{-1}. This broad band is interrupted by features at 2500 cm^{-1}, 2200 cm^{-1}, and 1300 cm^{-1} that resemble notches or inverse bands that cut into the absorption. It is difficult to determine the exact energy of the maximum absorbance of this band due to its breadth and due to the interference of the silicate modes and inverse bands. However, the maximum absorbance likely occurs between 1500 and 1800 cm^{-1}, since the intensity of this broad band in the minimum at 850 cm^{-1} is roughly equivalent to that at 3000 cm^{-1}, after subtraction of estimated absorbance due to the silicate modes. Finally, the spectrum taken with E||*a* also contains this very broad band, although it is not as intense and lacks the prominent notches seen in E||*c*. The narrow band at 1298 cm^{-1} is most intense in the E||*a* spectrum.

There are three distinct bands present in the ^{1}H MAS NMR spectra of ussingite. The NMR spectra taken at 6 kHz and 12 kHz magic angle spinning speeds are shown in Figure 5.3A. Spinning sidebands occur at intervals of the spinning speed on either side of the primary bands. There is one predominant band in the spectrum at δ = 13.9 ppm, which (along with its spinning sidebands) accounts for 90% of the total band area and ^{1}H in the crystal structure. The other two primary bands are at δ = 15.9 ppm and δ = 11.0 ppm, and represent about 8% and 2% of total structural hydrogen, respectively. The band at 4 ppm is due to adsorbed water on the sample and materials in the NMR probe. The center bands of ^{1}H MAS spectra obtained using different magnetic field strengths and pulse sequences are presented in Figure 5.3B. The three distinct ^{1}H bands are present in the spectra regardless of field strength (200 and 500 MHz) and pulse sequence (a depth sequence versus a single pulse), although the fine structure of the band at 15.9 ppm is apparently an artifact caused by the depth pulse sequence since it is not present in the single pulse experiment. The shapes, positions, and proportions of all three bands in the ussingite ^{1}H NMR spectrum remain constant over a range of temperatures (178-373 K).

Discussion

IR spectroscopy

The energy of maximum absorption and width of the very broad band in the E||*c* and E||*a* IR spectra in Figure 5.2 are characteristic of OH bands in other silicate minerals that have strong or very strong hydrogen bonding. For example, pectolite, $NaCa_2[Si_3O_8(OH)]$ and serandite, $NaMn_2[Si_3O_8(OH)]$, have O-H···O distances of 2.45 to 2.48 Å, and have OH stretch bands that are centered at approximately 1000 cm^{-1} and span a region from greater than 3000 cm^{-1} to less than 600 cm^{-1} (Hammer et al. 1998). Similarly, the IR spectrum of mozartite, $CaMn^{3+}O[SiO_3OH]$, has an extremely broad OH stretch band with a maximum at 1300-1700 cm^{-1}, and a corresponding O-H···O distance of 2.501 Å (Nyfeler et al. 1997). The unusual notches or inverse absorbance features that interrupt the OH stretch band in the ussingite spectra are also present in the IR spectra of mozartite, pectolite, and serandite (Nyfeler et al. 1997; Hammer et al. 1998). These features are called Fermi (or Fano) resonances, and are caused by the interaction of the broad OH stretch with the OH bending librations (Hadži and Bratos, 1976; Emsley 1981; Struzhkin et al. 1997). The unusual structure of the most intense region of the OH band (a central maximum with weaker submaxima) is also seen in hydrogen-bonded complexes of ethers with hydrogen halides and is likely due to sum and

difference modes of the OH stretch and a low energy stretching mode in the structure (Hadži and Bratos, 1976).

The broad OH stretch band is very strongly polarized. This very strong polarization of the OH stretching frequency is consistent with the strong directionality of the OH vector in the triclinic symmetry of ussingite. The E||*c* spectrum has very strong OH absorption (Figure 5.2), whereas the E||*b* spectrum has little or no OH stretch absorption, consistent with the alignment of the OH vector in the crystal structure (Figure 5.1). In the (010) plane, the OH vector is aligned with the principal optical direction *Z*, which is not aligned with the crystallographic axes. This is the reason for the intermediate OH stretch absorption in the E||*a* spectrum.

It is known that the OH stretching frequency is related to the degree of hydrogen bonding for many materials. More specifically, the OH stretching frequency decreases with increasing degree of hydrogen bonding, due to a combination of a decrease in the bond strength (and force constant) of the hydroxyl group and an increase in vibrational anharmonicity (Lutz 1988). A number of experimental studies have quantified the relationship between hydrogen bonding and IR frequency in organic and inorganic compounds, including minerals, and discuss the deviations from this correlation due to the effects of non-linear and bifurcated geometries and proton dynamics (e.g.,

Nakamoto et al. (1955); Libowitzky (1999)). The precise energy of the maximum OH stretch band intensity of ussingite is not tightly constrained, but occurs between 1500 and 1800 cm^{-1}. Using the correlation between OH stretching frequency and O-H···O distance given in Libowitzky (1999), the O-H···O distance in ussingite is calculated to be 2.48-2.50 Å. This agrees well with the O(2)-O(8) distance of 2.507 Å determined by least-squares refinement (Rossi et al. 1974).

The band at 1295 cm^{-1} in the E||*a* and E||*b* spectra of ussingite may be an OH librational bending mode or a silicate mode. There are three reasons for concluding that this band is an OH bending mode. The OH bending mode is expected to be infrared active in a direction perpendicular to the OH vector, and the 1295 cm^{-1} band is absent in the E||*c* spectrum but present in the E||*b* and E||*a* spectra. Other minerals with strongly hydrogen bonded OH groups also have OH bending modes at energies higher than the fundamental silicate modes (serandite at 1386 cm^{-1}, pectolite at 1396 cm^{-1}; Hammer et al. (1998)). Finally, the highest energy Fermi resonance occurs at 2525 cm^{-1}, which is approximately twice the frequency of the 1295 cm^{-1} mode. The origin of the other two Fermi resonances is unknown.

^{1}H MAS NMR spectroscopy

The ^{1}H NMR chemical shift is largely determined by O-H bond polarization, which is dominated by hydrogen bonding to the neighboring oxygen (Sternberg and Brunner 1994). Short hydrogen bonding distances increase bond polarization and thus also increase the proton chemical shift relative to protons that experience weak hydrogen bonding. Since ussingite has only one hydrogen site with a single hydrogen bonding distance ($H^{\cdots}O$), only one band is expected in the ^{1}H NMR data, and in fact most of the protons (90%) constitute a single band at 13.9 ppm. Using the correlation between inverse hydrogen bond length $rH^{\cdots}O^{-1}$ and isotropic chemical shift δ determined by Sternberg and Brunner (1994), the band at 13.9 ppm corresponds to an $H^{\cdots}O$ bond length of 1.49 Å. This distance is slightly shorter but within 5% of the $H^{\cdots}O$ distance determined from X-ray refinement (1.54 Å) (Rossi et al. 1974).

There are two additional NMR bands (about 10% of the protons) that are not accounted for with this model. The Al in ussingite was originally determined to be completely ordered in the T(1) site, with Si filling the remaining three tetrahedral sites, including the T(4) site attached to the O(8) hydroxyl-forming oxygen and the T(3) site coordinated by the O(2) hydrogen-bonding oxygen (Rossi et al. 1974). However, Ribbe (1974) found that the mean T(1)-O distance in ussingite was significantly shorter (0.01-0.013 Å) than the mean Al-O distance in low albite. Ribbe (1974) concluded that about 5% of the Al was in the T(3) site rather than the T(1) site. Since Al-O bonds are longer than

the Si-O bonds, in a local bonding environment where Al is substituted for the Si in the T(3) site, the increased T(3)-O bond length would result in a shorter hydrogen bond length and a higher ^{1}H NMR chemical shift value. The relative underbonding of the O(2) attached to Al rather than Si would also be expected to increase hydrogen bonding. To quantify this expected shift in δ, the difference between the mean Al-O bond distance for the T(1) site (1.734 Å) and the Si-O(2) bond distance for the T(3) site (1.584 Å) (Rossi et al. 1974) was calculated to be 0.15 Å. Shortening the H···O distance by this amount results in a hydrogen bond length of 1.39 Å and a predicted chemical shift of 16.0 ppm. This value of δ agrees well with the observed δ = 15.9 ppm of the band in the ussingite ^{1}H NMR spectrum corresponding to 8% of the total hydrogen concentration. The ^{1}H NMR spectrum therefore provides an independent confirmation of minor amounts of Al-Si disorder between T(1) and T(3) in ussingite.

The band at δ = 11.0 ppm represents about 2% of the total hydrogen atoms, or about 0.06 wt% H_2O. The H···O bond distance calculated for this value of δ is 1.64 Å. The origin of this band is unknown, but it is possible that local distortion of the crystal structure due to the substitution of Ca^{2+} for 2 Na^{+}, for example, could result in longer hydrogen bonding distances and lower the chemical shift value. Alternatively, small amounts of other mineral impurities

in the ussingite sample could be responsible for this ^{1}H NMR band, although an investigation of the sample with optical microscopy and Raman spectroscopy revealed only alteration products, likely zeolites, forming distinct coatings on the outside surface of the hand sample.

The lack of temperature dependence of the band positions and shapes in the ^{1}H NMR spectrum and the long spin-lattice relaxation time (100 seconds) means there is little or no dynamic chemical motion involving the protons in ussingite.

Criteria for strong hydrogen bonding

The criteria for classifying hydrogen bonds as strong or weak are summarized in Emsley (1981), and include considerations of bond length, O-H···O bond symmetry, infrared OH and OD stretch modes, NMR chemical shift, and bond energy. As mentioned above, the O-H···O distance (as determined by X-ray refinement and now IR spectroscopy) in ussingite characterizes it as a material with strong hydrogen bonding. The large downfield ^{1}H NMR chemical shift and broad IR OH stretching band with a maximum of 1500-1800 cm^{-1} are also consistent with the definition of strong hydrogen bonding.

Strong hydrogen bonds tend to be linear, i.e., the O-H···O angle is about 180° (Emsley 1981), and indeed this angle is 171° in ussingite (Rossi et al. 1974). For strong hydrogen bonds, it has been suggested that the hydrogen is

symmetrically centered between oxygens (Emsley 1981), but the data in this study point to an asymmetric bonding environment. The H···O distance constrained by ^{1}H NMR data is significantly longer than half of the O-H···O distance determined with IR spectroscopy. Of the criteria for strong hydrogen bonding examined in this study, this is the only one that ussingite does not meet. There are many recently reported examples of minerals with strong hydrogen bonding exhibiting asymmetric O-H···O bonding (Beran and Libowitzky 1999), so it is concluded that ussingite is well characterized as a material with strong hydrogen bonding.

Comparison of OH in ussingite to OH in feldspars

The nature of OH in low albite or other plagioclase feldspars is apparently very different from that of the OH in ussingite, despite similarities of their respective crystal structures. This can be seen in the polarized IR spectra of low albite, andesine, and ussingite in Figure 5.4. The silicate modes in the thick feldspar samples are off scale below 2300 cm^{-1}, but it is still possible to observe the differences between the feldspar and ussingite spectra in the 3000-3700 cm^{-1} region. Low albite is characterized by very sharp OH bands around 3500 cm^{-1}, a broad underlying fluid inclusion band at about 3450 cm^{-1}, and a broad OH band around 3050 cm^{-1} (Johnson and Rossman 2003). Andesine (and other plagioclase and alkali feldspars) have broader OH bands in the 3000-3500 cm^{-1} region, and no Fermi resonances are visible in the spectrum.

The OH in feldspars is therefore not strongly hydrogen bonded as is the case in ussingite. This is supported by the small ^{1}H NMR chemical shift of OH in feldspars (4-6 ppm) (Johnson and Rossman 2003) as compared to the δ for ussingite (11-15.9 ppm).

Implications of strong hydrogen bonding for H isotope partitioning

For weakly hydrogen bonded systems, the ratio of the OH stretch frequency to the OD stretch frequency (in a deuterated sample), νOH/νOD, is approximately equal to 1.36, but in conditions of strong hydrogen bonding this ratio changes. Specifically, the νOH/νOD ratio reaches a minimum of ~1 at an O-H···O distance of about 2.50 Å (Emsley 1981), which is the value for the O(8)-O(2) distance in ussingite. This phenomenon is caused by the large anharmonicity of the hydroxyl due to strong hydrogen bonding (Hadži and Bratos, 1976), which affects the zero point energy of the system. Ussingite and other strongly hydrogen bonded minerals would therefore be expected to have very low δD values. The δD values of four pectolite samples from rodingites in serpentinized ultramafic rocks range from –281 to –420 ‰ (Wenner 1979). Preliminary isotopic measurements by Julie O'Leary at Caltech (unpublished data) have found that the δD of the ussingite sample used in this study is –170 ‰. Thus, minerals with strong hydrogen bonding might be expected to have some of the lightest δD values of minerals on Earth.

Conclusions

Ussingite is a mineral with characteristically strong hydrogen bonding, as constrained by H···O (1.49 Å) and O-H···O (2.48-2.50 Å) distances determined from the ^{1}H NMR and IR data in this study. The polarized IR spectra of ussingite contain a characteristically broad OH band with a maximum at 1500-1800 cm^{-1}, and confirm the hydrogen bond length and orientation of OH vector in the crystal structure as determined by X-ray refinement (Rossi et al. 1974). The O-H···O bond is asymmetrical, even in the strong hydrogen bonding environment. Most of the hydrogen in ussingite experiences a single hydrogen bonding environment with a hydrogen bond distance of about 1.49 Å and an ^{1}H MAS NMR chemical shift δ = 13.9 ppm, but disordering of several percent Al into the tetrahedral site adjoining the oxygen participating in hydrogen bonding causes a population of hydrogen (~8 %) to experience stronger hydrogen bonding (δ = 15.9 ppm). A third, smaller hydrogen population (~2 %) experiences weaker hydrogen bonding than the majority of the protons in the structure (δ = 11.0 ppm), and could be due to charge coupled substitutions in the structure, or possibly other minerals in an impure mineral sample.

Figure 5.1.

The crystal structure of ussingite projected onto (100).

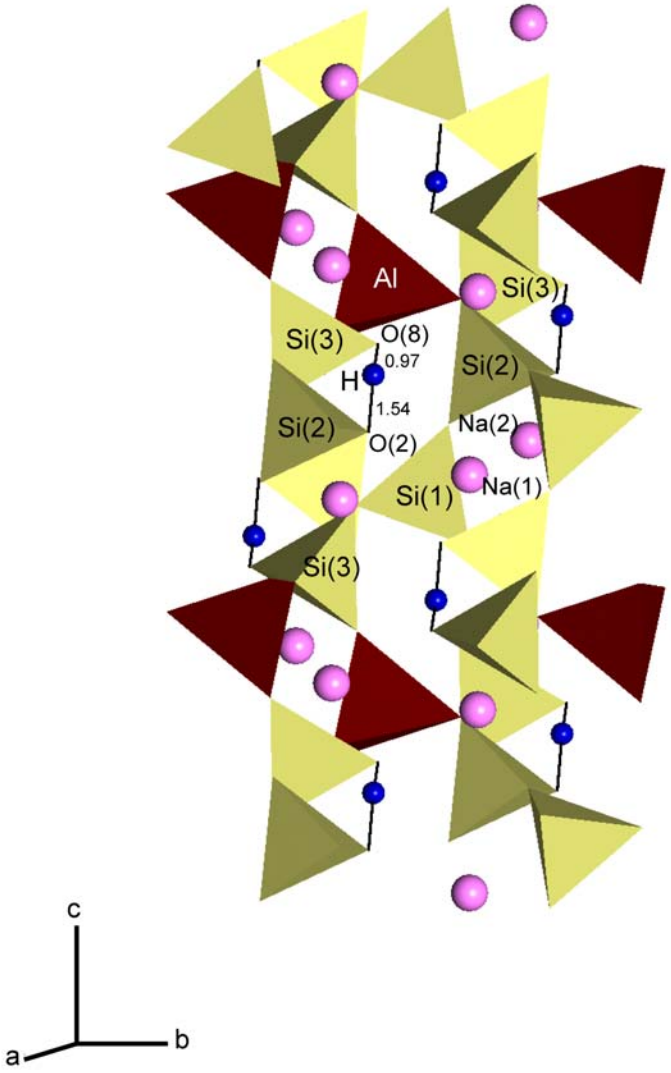

Figure 5.2.

Polarized single-crystal infrared spectra of ussingite. The asterisks mark the "inverse" Fermi resonances superimposed on the broad OH band (3000-800 cm^{-1}).

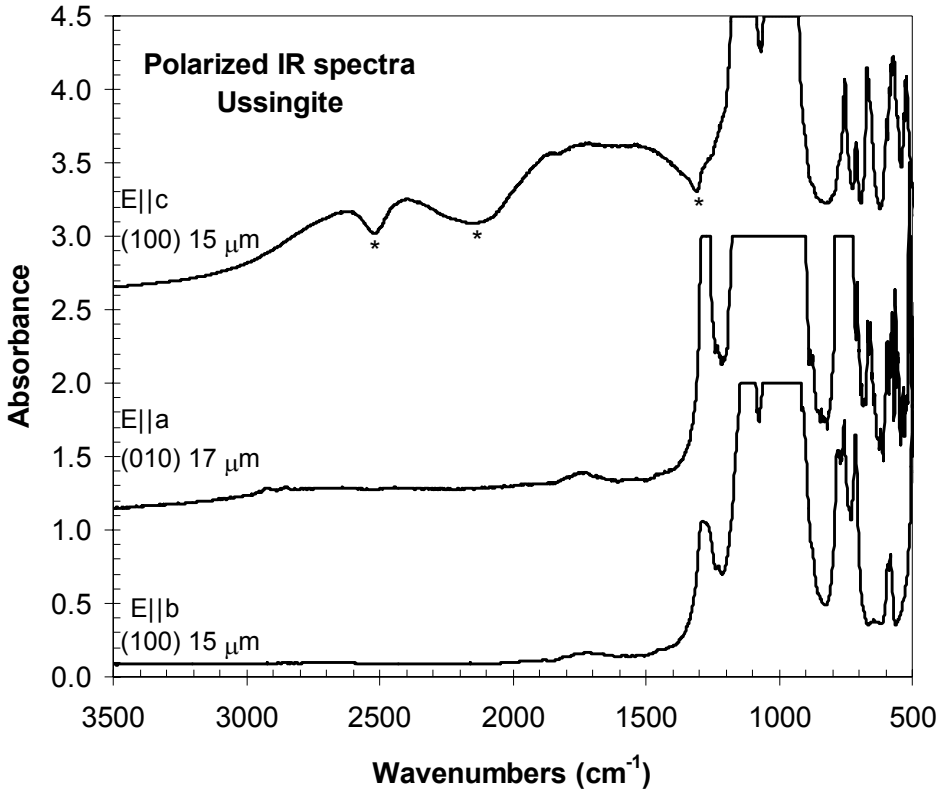

Figure 5.3.

^{1}H MAS NMR spectra of ussingite. A. Spectra obtained on a 500 MHz magnet at 6 kHz and 12 kHz magic-angle spinning speeds, showing the main bands and spinning sidebands (marked with asterisks). The band at 4 ppm is due to adsorbed water and probe materials. B. Expanded view of the three center bands of ussingite spectra taken on a 500 MHz magnet using a depth pulse sequence and a 200 MHz magnet using a single pulse.

Figure 5.3A.

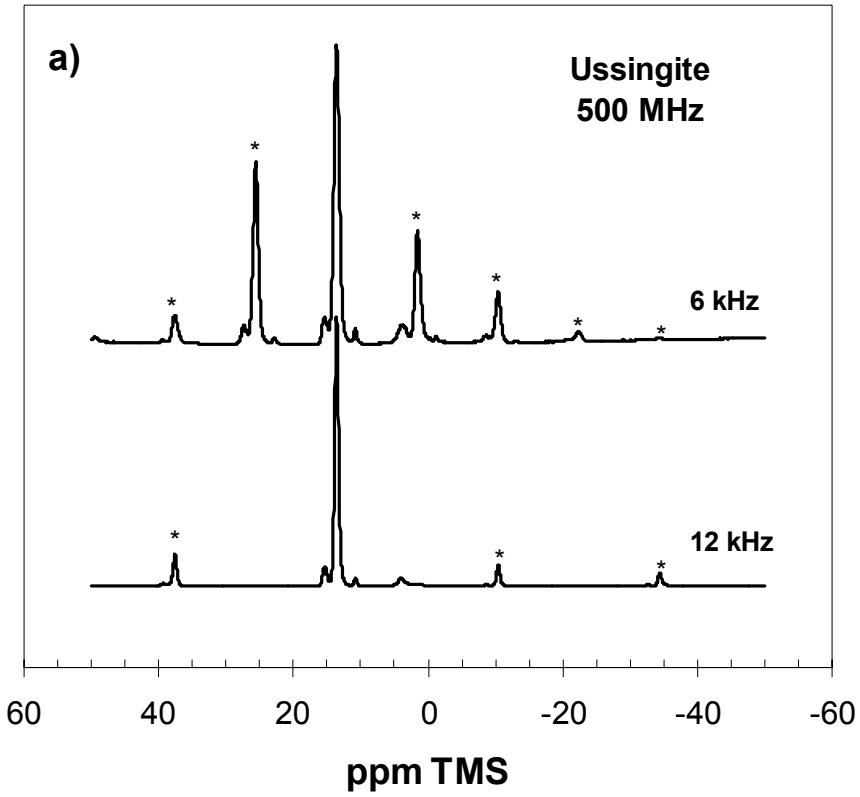

Figure 5.3B.

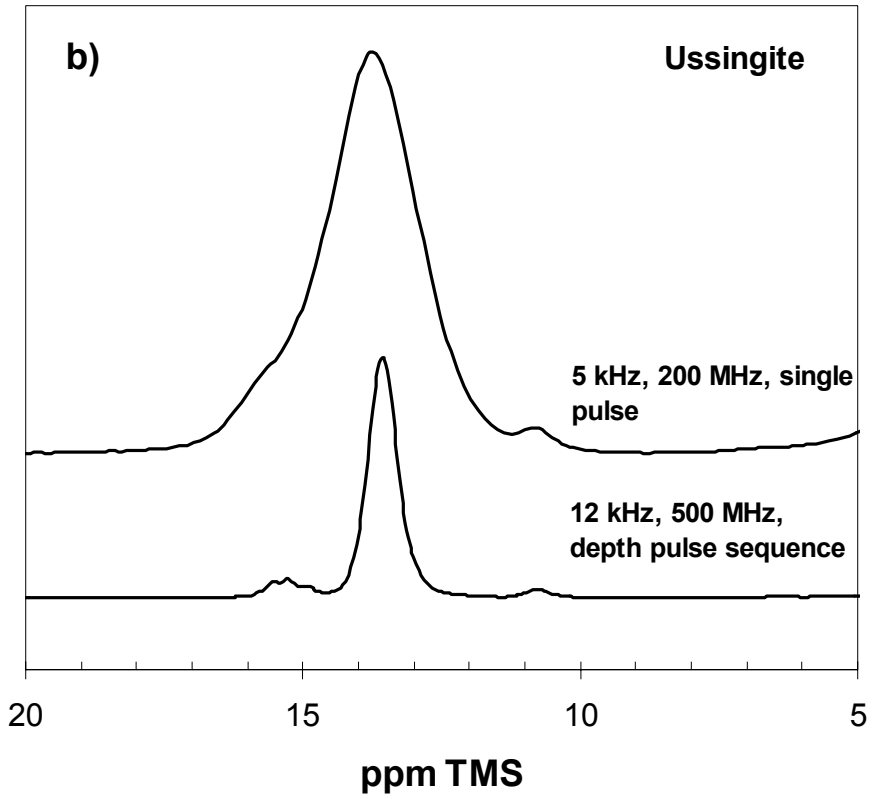
b)
Ussingite
5 kHz, 200 MHz, single pulse
12 kHz, 500 MHz, depth pulse sequence
20
15
10
5
ppm TMS

Figure 5.4.

Comparison of the polarized IR spectra of low albite, andesine, and ussingite, showing the difference in hydrogen bonding environments between feldspars and ussingite.

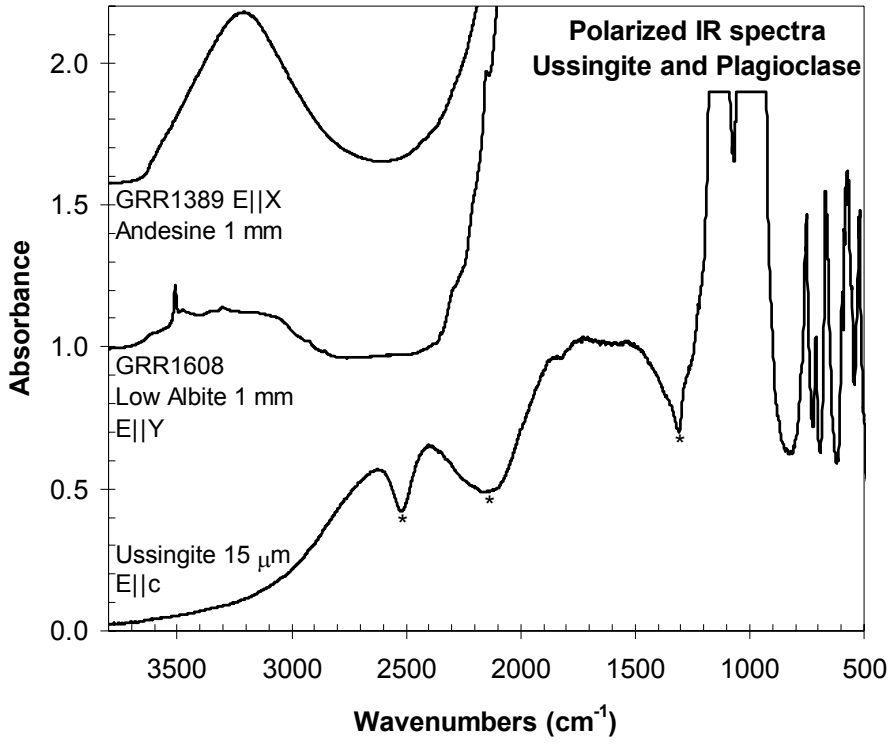

Chapter 6

CORRELATION BETWEEN OH CONCENTRATION AND OXYGEN ISOTOPE DIFFUSION RATE IN DIOPSIDES FROM THE ADIRONDACK MOUNTAINS, NEW YORK[4]

Abstract

The concentration of structural OH in diopside was determined for four granulite facies siliceous marble samples from the Adirondack Mountains, New York, using FTIR spectroscopy. Single-crystal polarized IR spectra were measured on (100) and (010) sections of diopside. The relative intensities of four OH bands in the 3700-3200 cm^{-1} region vary among the samples, with the 3645 cm^{-1} band dominating the spectra of diopside from a xenolith at Cascade Slide. Total OH content in the diopsides ranges from 55 to 138 ppm H_2O by weight. The OH concentration in diopside increases monotonically with increasing f_{H_2O} for the sample, as estimated using oxygen isotope systematics for these samples from Edwards and Valley (1998). There is no significant

[4] Modified from E.A. Johnson et al. (2002) American Mineralogist. 87, 899-908.

variation in OH content within a single diopside grain or among diopside grains from the same hand sample. Charge-coupled substitution with M^{3+} and Ti^{4+} in the crystal structure may have allowed retention of OH in the diopside structure during and after peak metamorphism (~750ºC, 7-8 kbar). The Cascade Slide diopsides have an Fe^{3+}/Fe^{2+} of 0.98, compared to Fe^{3+}/Fe^{2+} (0 to 0.05) for the other samples, implying that some loss of hydrogen through oxidation of Fe was possible in this sample. This is the first study we know of which shows that the OH content in anhydrous minerals from natural samples affects the rate of oxygen isotope diffusion.

Introduction

Studies of the concentration of OH in pyroxenes throughout the world (e.g., Skogby et al. 1990) show a large range (0.12 to 0.001 wt% OH; 60300 to 500 ppm H_2O) in OH concentration that is broadly related to rock type. Nominally anhydrous minerals (NAMs) from the mantle, especially clinopyroxenes, have high OH concentrations (up to 1300 ppm H_2O, 400-600 ppm for diopside), suggesting there is a significant reservoir of water in the mantle (Bell 1993; Ingrin and Skogby 2000). Calculations of water content of melt in equilibrium with mantle xenocrysts (Bell 1993), and initial calculations of the total amount of hydrous species stored in the mantle (200 to 550 ppm H_2O; Bell and

Rossman 1992a) assume that the OH in mantle xenoliths was not incorporated or removed during the journey to the surface. Subsequent estimates of mantle OH concentration (300 to 600 ppm H_2O; Ingrin and Skogby 2000) have factored in estimates of possible loss of H from NAMs due to redox reactions. There is little evidence that OH concentration in NAMs from the mantle is strictly preserved. Bell (1993) found that OH concentration in garnet and clinopyroxene xenocrysts from the Monastery kimberlite in South Africa was correlated with the Mg# (100Mg/(Mg+Fe)) and Ca# (100Ca/(Ca+Mg)) of these minerals, respectively, and pyroxene OH content was found to be correlated with major element trends in the mantle wedge below Mexico and Washington State (Peslier et al. 2000). Even less is known about the preservation and concentration of hydrous species in NAMs in the lower crust. The lower crustal contribution to the hydrogen budget of the Earth is unknown. To prove that estimates of water content of the mantle and lower crust are correct, it is important to establish that the OH concentration of NAMs is directly related to high-temperature fluid conditions.

We know of no previous work to determine if OH concentration in NAMs is correlated to oxygen isotope systematics, which provides information about fluids in hydrothermal systems and during peak and post-metamorphism. Linking the concentration of hydrogen species in an anhydrous mineral to the amount of water in a particular geological system through oxygen isotope data

would be further proof that incorporation of hydrous components into NAMs is influenced by geological conditions. Additionally, it would be useful to separate the effect of water activity from the potentially important effects that crystal chemistry and oxygen fugacity (Peslier et al. 2000) could exert on OH concentration in the clinopyroxene structure. An ideal region for study is one with large areas of outcrop exposed, and where previous work has established the regional geological context, including peak pressures and temperatures, post-metamorphic cooling rate, oxygen fugacity, and water activity.

Locality

One such well-studied area is the Adirondack Mountains, NY, at the southeastern tip of the Grenville Province. The Adirondacks Highlands underwent granulite-facies metamorphism ~1 Ga ago at maximum temperatures of 725 to 800°C and maximum pressures of 7-8 kbar (Bohlen et al. 1985). There was low-*P*, high-*T* metamorphism due to intrusion of the Marcy anorthosite ~100 Ma before granulite facies metamorphism (McLelland et al. 1996, Valley and O'Neil 1982; Valley and O'Neil 1984). In this work we consider only the effects of cooling from the last (granulite-facies) metamorphism. Water activities calculated for fluid-buffered mineral assemblages in the region are low ($a_{H_2O} \approx 0$ to 0.2) and locally variable (Lamb and Valley 1988; Valley et al. 1990). The oxygen fugacity during

metamorphism of most Adirondacks rocks ranged from log f_{O_2} = +1 to –2 relative to QMF (Valley et al. 1990). The post-metamorphic cooling rate for the Adirondack Highlands was about 4ºC/Ma (Mezger et al. 1991).

Previous Work

Edwards and Valley (1998) studied diopside from calc-silicate rocks in the Adirondacks (see description of samples below). At ~750°C, the rate of oxygen diffusion in calcite is many orders of magnitude faster than oxygen diffusion in diopside for either "wet" (Farver 1989; Farver 1994) or "dry" (Ryerson and McKeegan 1994; Anderson 1969) systems. If oxygen isotope exchange in diopside during cooling is due only to volume diffusion, then small diopside grains will exchange a greater proportion of their oxygen with the surrounding calcite than large diopside grains. Edwards and Valley (1998) measured the $\delta^{18}O$ of sieved size fractions (from 0.075 mm to 3 mm) of diopside from each outcrop. They found that the small diopside grains were pulled down in $\delta^{18}O$ (towards the value in low temperature equilibrium with calcite) relative to the large grains such that the difference in $\delta^{18}O$ between the smallest and largest diopside ($\Delta^{18}O_{(large\text{-}small)}$) is always ≥ 0. The magnitude of $\Delta^{18}O_{(large\text{-}small)}$ ranged from 1.4 permil to within measurement error (about 0.1 permil). Experiments have shown that the rate of oxygen diffusion in diopside is a function of the water pressure (Farver 1989; Ryerson and McKeegan

1994; Pacaud et al. 1999). Using the Fast Grain Boundary Diffusion model (Eiler et al. 1992; Eiler et al. 1993; Eiler et al. 1994; Kohn and Valley 1998), Edwards and Valley (1998) calculated $\Delta^{18}O_{(large\text{-}small)}$ for each sample using experimental diffusion coefficients for diopside determined under "wet" (1 kbar H_2O; Farver 1989) and under "dry" (1 bar CO_2; Ryerson and McKeegan 1994) conditions. Samples used in the current study had $\Delta^{18}O_{(large\text{-}small)}$ ranging between "wet" and "dry" conditions. Edwards and Valley (1998) pointed out that a water fugacity of 1 kbar in a 7-8 kbar terrane yields a similar maximum water activity as that estimated for fluid-buffered assemblages in the Adirondacks. They suggested that heterogeneous a_{H_2O} during cooling caused the variation in oxygen isotope diffusion rate and the variation in $\Delta^{18}O_{(large\text{-}small)}$ between samples. According to the "wet" diffusion models, the closure temperature for the smallest diopside grains in all of the samples was >500°C. The "dry" models showed no oxygen isotopic exchange even at peak metamorphic temperatures. The models were relatively insensitive to changes in cooling rate and peak temperature. A more recent investigation of oxygen isotope diffusion in diopside (Ingrin et al. 2001) confirms that "dry" diffusivity of oxygen in diopside parallel to *c* is about 10 times slower than the "wet" diffusivity reported in Farver (1989).

This study investigates the possibility that diopside grains from Edwards and Valley (1998) retain OH in their crystal structure from peak and high-*T* (>500°C) post-metamorphism fluid conditions, using FTIR (fourier transform infrared) spectroscopy to determine OH content of diopsides from each sample. We characterize the crystal composition and Fe^{3+}/Fe^{2+} to investigate if the OH content of the diopside in these samples is due to water activity during peak and post-peak high-temperature metamorphism or if OH concentration is determined by other processes.

Methods

Samples

In this study, diopsides from four of six outcrop localities used in Edwards and Valley (1998) were analyzed. These four samples are all from the Adirondack Highlands (see Fig. 1 in Edwards and Valley (1998); three (Samples 4=95AK24, 6=95AK6, and 7=95AK8f) are from marble metasediment layers, and one (95ADK1A, Sample 1) is from a marble xenolith in the Mount Marcy anorthosite massif at the Cascade Slide. Diopside grains from each sample were separated from the rock by dissolving several kilograms of marble in dilute HCl.

Grains from the largest grain-size fraction of diopsides from each sample (1.5 to 3 mm in diameter) were used in this study so that polished slabs for FTIR

spectroscopy were thick enough (~0.5 mm) to measure the low concentrations of OH in the diopside. Large grains also made it possible to take IR spectra on more than one spot in each diopside grain to test for OH zoning. For Mössbauer analysis, cleaned, pure diopside separates (about 100 mg) for each sample were made by crushing and hand-picking grain fragments under a binocular microscope.

Orientation of samples for spectroscopy

Polarized spectra were measured in the three principal optical directions (**X**, **Y**, and **Z**) for each sample to determine OH content and characterize optical spectra. This was done by making two polished slabs: one parallel to the (010) plane (for **X** and **Z**) and one parallel to (100) (for **Y**). For each sample, whole grains relatively free of inclusions were chosen so that possible variations in OH within a single grain could be investigated.

Although some faces, particularly {110}, were developed on some crystals, the grains were generally rounded, making orientation by morphology difficult. Instead, orientation was done using optical figures and a modified spindle stage. Once the crystal was oriented, it was transferred to a brass plug for polishing to a 1 μm finish using Al_2O_3 and diamond films. Each grain produced one oriented slab, so two diopside crystals from each sample were oriented to make (100) and (010) slabs.

Orientation was confirmed by comparing polarized IR reflectance spectra (Figure 6.1) in the **X**, **Y**, and **Z** directions to the same spectra taken on chromian diopside from Russia, which was previously oriented using single-crystal X-ray diffraction (Shannon et al. 1992). The reflectance spectra were collected using the experimental setup for the transmission spectra (below).

Other diopside grains were also made into slabs without being oriented. Spectra from these grains were used to estimate maximum difference in OH concentration between diopsides in a single sample and natural variation of OH within a single diopside.

FTIR spectroscopy

FTIR spectra were taken using a Nicolet Magna 860 FTIR spectrometer with a Spectra-Tech Continuμm® microscope accessory, KBr beamsplitter, Au wire grid on AgBr polarizer, and MCT-A detector. An aperture size of 50-100 μm was used, and care was taken to avoid taking spectra through any fractures and inclusions. Each spectrum was collected at 4 cm^{-1} resolution and was averaged from 256 scans.

Calculation of OH concentration

The OH concentration in each sample was determined using an integral form of the Beer-Lambert law, $c = A / (I' \times t)$, where c is the concentration of OH

expressed as ppm H_2O by weight, A is the total integrated peak area in the region 3200-3650 cm^{-1} ($A = A_X + A_Y + A_Z$), I' is the specific integral absorption coefficient in units of $1/(ppm \bullet cm^2)$ calculated to be 7.09±0.32 for clinopyroxenes by Bell et al. (1995), and t is the normalized path length (thickness of the polished slab) in cm. Actual slab thickness ranged from 0.2 to 0.6 mm. Although the background for some of the polarized FTIR spectra was nearly flat in the OH region, other samples had sloping backgrounds due to absorption by Fe^{2+} in the M(2) site. The baseline for each polarized spectrum could be adequately modeled as a linear continuation of the background under the OH peaks in the 3200-3650 cm^{-1} region.

The analytical error in the OH concentration is calculated to be ±12% relative, ±7-18 ppm absolute. This is determined by the error in the calibration of I' and the error of the mean of OH concentrations calculated from multiple measurements on one spot of one diopside. The I' value taken from Bell et al. (1995) was calculated for augite with a mean OH absorption of about 3550 cm^{-1}, which is about the same as the mean OH absorption for diopside in three of the samples. The OH concentration calculated for diopside from 95ADK1A, with a mean OH absorption of about 3645 cm^{-1}, could be underestimated at most by 30%. Error due to measurement of slab thickness (±0.002 mm, determined using an electronic micrometer) was insignificant compared to the other sources of error. The error involved in measuring the

peak area of a single spectrum ten times using the Omnic E.S.P. 5.2 software program associated with the FTIR spectrometer is 1.47% relative using the method of Bell et al. (1995). No single diopside grain from either the oriented or non-oriented crystals showed any significant zoning in OH content from core to rim or with proximity to fractures or inclusions in the grain. This was true even for grains that showed major-element zoning. All spots on a single diopside had OH contents within or almost within analytical error of each other (maximum 30 ppm range). Thus, natural variation within each sample was about the same as analytical error, and OH concentrations calculated from FTIR spectra on oriented diopside slabs are representative of the OH concentration of diopsides in each sample as a whole.

Optical spectra

Polarized optical absorption spectra were obtained on 100 μm spots in the 400-1700 nm range, using a home-built spectrometer consisting of a highly modified NicPlan infrared microscope with a calcite polarizer and Si and InGaAs diode-array detectors. Diopside slabs were immersed in mineral oil to reduce interference fringes caused by cracks in the diopside grains.

Efforts to calculate Fe^{3+}/Fe^{2+} from optical data were thwarted by a lack of suitable calibrations for Fe^{3+} and Fe^{2+} bands and the low intensity of the bands.

Without further calibration the optical spectra are qualitative indicators of the oxidation state of Fe for the samples in this study.

Electron microprobe analysis

Microprobe analyses were obtained at Caltech on a JEOL JXA-733 electron microprobe at 15 keV and 25 nA, using a 10 μm beam size and synthetic diopside (Sample Y6) as a standard. Oxide totals were calculated using the CITZAF correction (Armstrong 1995) and fell within the range of 99.5% - 100.4% after recalculation including Fe_2O_3. Four spots on each diopside were analyzed along a transect from core to rim, to investigate compositional heterogeneity of grains in each sample.

Mössbauer analysis

Samples were prepared for Mössbauer analysis by mixing with sugar under acetone to avoid preferred orientation before being placed in the sample holder for the spectrometer, which is a Plexiglas ring 3/8" in diameter. Samples were held in place with cellophane tape. We estimate that polarization and absorber texture effects add <±2-3% error to our results. Spectra were acquired at room temperature using the WEB Research Co. constant acceleration Mössbauer spectrometer in the Mineral Spectroscopy Laboratory at Mount Holyoke College under the supervision of M.D.D. A source of ~25 mCi ^{57}Co in Rh

was used. Mirror image spectra were folded to obtain a flat background. Isomer shifts are referenced to the center of metallic Fe.

Data were fit using quadrupole splitting distributions (QSD) with the software package WMOSS by WEB Research Company. QSD fitting has been shown to be superior to the Lorentzian-based approach in mica spectra in which there are poorly resolved quadrupole pairs (Rancourt 1994a; Rancourt 1994b; Rancourt et al. 1994b). Such is the case for the diopsides in this study.

The best models for the spectra included two Fe^{2+} octahedral sites (or possibly one Fe^{2+} site with two components), and two Fe^{3+} sites (or one with up to two components). Quadrupole splitting, linewidth, and isomer shift values (Δ_0, σ_Δ, δ_1, and δ_0) were allowed to vary independently in all models. Peak width (Lorentzian FWHM, or γ) was held constant, constrained to vary as a group, and then released. Lorentzian peak height (h_+/h_-) was either constrained to be equal to 1, or allowed to vary independently. Multiple fits were made for each spectrum to test the variation in $\%Fe^{3+}$ as a function of fit model, and the differences among widely varying fit strategies were less than +/-4%. This illustrates the non-uniqueness of the populations as determined by Mössbauer spectroscopy, a fact that is an intrinsic limitation of non-linear least-squares minimization methods (c.f. Rancourt et al. 1994a). In order to have a single value of total $\%Fe^{3+}$ it was necessary to pick a single "preferred" fit for each

sample based upon chi-squared values. Effects of differential recoilless emission (f) of Fe^{2+} and Fe^{3+} in the different sites must be considered in order to determine "true" Fe^{3+}/Fe^{2+}. Work by DeGrave and VanAlboom (1991) and Eeckhout et al. (2000) has quantified the temperature dependence of the hyperfine parameters of clinopyroxenes, and the former study tabulates values of f for ferridiopside and diopside. Since the amount of Fe^{3+} in most of the samples studied here is small, any changes in f due to composition are lost in the noise of the estimated ± 2-3% absolute error on our data. We use f values from DeGrave and VanAlboom (1991) of 0.708 for Fe^{2+} and 0.862 for Fe^{3+} to correct the final $\%Fe^{3+}$ results.

Results

FTIR spectroscopy

Peak Positions.

Four distinct OH vibrational peaks are seen in the FTIR spectra of the diopsides (Figure 6.2): 3645 cm^{-1}, 3530 cm^{-1}, 3450 cm^{-1}, and 3350 cm^{-1}. These peak positions and their pleochroism (**X** = **Y**, **Z** ≈0 for 3645 cm^{-1}; **Z** > **X** = **Y** for the other three peaks) are similar to those found in other diopside samples (Skogby et al. 1990). None of the samples show sharp bands near 3675 cm^{-1} (talc-like or amphibole-like peaks) that are indicative of amphibole lamellae or disordered pyribole layers (Ingrin et al. 1989; Skogby et al. 1990).

Unlike spectra from the other three samples, the spectra from sample 95ADK1A contain only one major OH peak at 3645 cm^{-1}. Skogby and Rossman (1989) found a correlation between the height of this peak and Si deficiency in the tetrahedral site for Fe-rich diopside and augite. This peak and the one at 3450-3460 cm^{-1}, when present in the clinopyroxenes and esseneite, were found to increase in intensity after heating in H_2 gas at 700°C and to decrease in intensity and disappear when heated in air. The reduction-oxidation reaction,

$$Fe^{3+} + O^{2-} + {}^1/_2H_2 = Fe^{2+} + OH^- \quad (6.1)$$

known to occur in amphiboles and micas (Addison et al. 1962; Vedder and Wilkins 1969), is thought to be responsible for the structural incorporation of the OH in diopside that gives rise to vibrational frequencies of ~3640 cm^{-1} and perhaps 3450 cm^{-1} (Skogby and Rossman 1989).

During hydrothermal experiments at 600 – 800°C and P_{H_2O} = 1-2 kbar (Skogby and Rossman 1989), the diopside OH peaks at ~3640 cm^{-1} and 3450 cm^{-1} increased in intensity at the expense of the other two (3350 cm^{-1} and 3530 cm^{-1}) OH peaks, with no net loss or gain of OH in the samples. Oxygen fugacity was not buffered during these experiments. The temperature and water pressure conditions of these experiments are similar to the temperature

(~750°C) and partial pressure of water ($a_{H_2O} \approx$ 0.1-0.2) at peak metamorphism in the Adirondacks (Valley et al. 1990). According to the results of Skogby and Rossman (1989), the 3645 cm^{-1} and 3450 cm^{-1} bands in the Adirondack diopsides would be expected to increase in intensity during peak and post-peak high-temperature metamorphism. These OH bands are referred to as "hydrothermal" bands in the subsequent discussion.

Skogby et al. (1990) suggested that the other OH peaks (3350 and 3530 cm^{-1}) were related to doubly charged cations in the clinopyroxene structure (Mg^{2+} and Fe^{2+}, respectively). These and other compositional correlations are investigated below.

OH concentration

Table 6.1 lists the total OH content of diopside from each sample, as well as estimated OH concentration contributed by each of the four OH bands, calculated from integrated peak areas in the 3200 – 3700 cm^{-1} region. Even though the 3645 cm^{-1} peak height in 95ADK1A is much greater than any of the peak heights in sample 95AK8f in the **Y** direction (Figure 6.2B), the sum of the integrated peak areas in all three optical directions is almost equal for these two samples.

The total OH content of the diopside from each sample is plotted versus f_{H_2O}, as estimated using the oxygen isotope data of Edwards and Valley (1998), in Figure 6.3. To convert the measured $\Delta^{18}O_{(large\text{-}small)}$ to an estimated water fugacity in kbar, the difference between it and the calculated $\Delta^{18}O_{(large\text{-}small)}$ for dry diffusion (P_{CO_2} = 1 bar) is divided by the difference in $\Delta^{18}O_{(large\text{-}small)}$ between wet (P_{H_2O} = 1 kbar) and dry diffusion, then multiplied by the water fugacity of the wet experiments (1 kbar). This calculation assumes that the diffusion rate of oxygen in diopside changes linearly with water pressure. There is some evidence that this relationship is true in NAMs, for example, in quartz (Farver and Yund 1991; McConnell 1995). The OH content in diopside contributed by the "hydrothermal" peaks at 3645 cm^{-1} and 3450 cm^{-1} is plotted on the same graph.

The total OH content of the diopside increases with increasing calculated water fugacity (Figure 6.3). The diopside with the greatest OH content (sample 95ADK1A) is from the Cascade Slide Xenolith (a geological environment different from the other three samples) and has the single-band OH spectra. If this diopside is excluded from the total OH data set, the remaining three points define a straight line. The OH content from "hydrothermal" bands increases linearly with increasing f_{H_2O}.

Microprobe analysis

The results of electron microprobe analysis are listed in Table 6.2. Each analysis on a diopside grain was individually converted from unnormalized wt% oxides to moles of cations and normalized to four cations, including H. Fe^{3+} and Fe^{2+} concentrations were taken from Mössbauer results. Site occupancies were assigned according to the method of Robinson (1980), except that Mn was preferentially assigned to the M(1) site over excess Fe^{2+} for sample 95AK24. The four recalculated analyses from each grain were then averaged together to produce a representative analysis for the whole sample. Only sample 95AK8f was continuously zoned from core to rim with respect to most major and trace elements, producing a large uncertainty in the average composition of that sample.

To investigate any possible correlation between OH content and diopside composition, the total OH content, OH from "hydrothermal" peaks, and OH contributed from each individual OH band were plotted versus each major and trace element component. Results are shown in Figure 6.4 for elements previously associated with OH incorporation in clinopyroxene, as well as discernable trends for any other element. Element abundances are plotted in mol element/L diopside assuming a density of 3300 g/L for diopside for both H and microprobe analyses.

The element that is most closely correlated to total H content is Ti. There is almost a one-to-one molar ratio between these elements; all other elements measured have concentrations orders of magnitude greater than hydrogen in the diopsides. The OH concentration due to the 3450 cm^{-1} band increases with greater Na content. Total OH increasing with total Al content is also seen. The total content of M^{3+} cations is correlated with the total OH, which was also observed by Skogby et al. (1990). However, no correlation is found between Mg concentration and the peak area of the 3350 cm^{-1} band as reported in Skogby et al. (1990). Variations in Ti and M^{3+} content within sample 95AK8f do not result in any discernable zonation of OH concentration.

Optical spectroscopy

Polarized optical spectra in the **X** direction are shown in Figure 6.5. The high-frequency oscillations in the spectra are interference fringes caused by cracks in the samples. Site occupancies cannot be quantitatively determined from these spectra because of the uncertainty in molar absorption coefficients, but they do show a qualitative difference in the oxidation state of iron between diopside samples. The sharp peak at 450 nm indicates all or most of the Fe^{3+} is in the tetrahedral site (Rossman 1980). If all or most of the Fe^{3+} was in the M(1) site, a sharp peak at about 435 nm would be expected. The 450 nm band is most intense for sample 95ADK1A, from the Cascade Slide, and is very weak or nonexistent in the spectra of the other diopsides, even though

95ADK1A contains the second lowest amount of total Fe of the four samples. Not all of the iron in 95ADK1A is ferric, however, because a band at 1050 nm due to Fe^{2+} in the M(2) site is also present in the **Y** spectrum. The other samples have bands centered at 1050 nm (Fe^{2+} in the M(2) site) and perhaps weak bands at 950 and 1150 nm (Fe^{2+} in the M(1) site).

Mössbauer spectroscopy

Mössbauer spectra and peak fits for 95ADK1A and 95AK8f are shown in Figure 6.6. Samples 95AK24 and 95AK6 have Mössbauer spectra similar to 95AK8f. The resulting $\%Fe^{3+}$ and $\%Fe^{2+}$ for each sample are tabulated in Table 6.3. The spectrum of sample 95ADK1A is markedly different from the other three spectra because of its larger $\%Fe^{3+}$. For this sample, two Fe^{3+} doublets were fitted, both with isomer shifts (δ) typical of octahedral coordination (e.g., Bakhtin and Manapov 1976a; Bakhtin and Manapov 1976b). It is possible that sample 95ADK1A may contain Fe^{3+} in the tetrahedral rather than M(1) or M(2) sites because one Fe^{3+} component has a quadrupole splitting ($\Delta = 1.461$) that is characteristic of tetrahedral Fe^{3+} (e.g., Hafner and Huckenholz 1971), even though δ for this component (thought to be more diagnostic than Δ) is in the range of values for Fe^{3+} in the M(1) site.

The assignment of the Fe^{2+} components for all samples is not clear-cut for the Mössbauer data. In this study, the two Fe^{2+} populations have $\Delta = 2.18$ and

1.84 mm/s. These two doublets do not have sufficiently different parameters to justify assigning them to two different sites. It is more likely that the two doublets represent Fe^{2+} in the same site, with different populations of next nearest neighbors. Attempts were made to obtain fits employing additional Fe^{2+} QSDs and/or forcing one of the QSDs to have the hyperfine parameters that would be characteristic of the other site (i.e., with Δ = 3.00 mm/s), but these did not converge. Doublets with δ =1.16 mm/s and Δ = 3.00 mm/s would have peaks at –0.32 and 2.63 mm/s, and it is obvious from visual inspection of the spectra that these peaks are not present. Therefore there is no evidence from the Mössbauer data that Fe^{2+} is present in two dramatically different sites. This issue clearly merits further study employing comparisons of X-ray diffraction data with Mössbauer results, and is outside the scope of the present work.

Despite the problems with identifying unique site occupancies for Fe^{2+} and Fe^{3+} using microprobe, optical, and Mössbauer data, the Fe^{3+}/Fe^{2+} ratio for diopside from each sample is fairly well constrained using the Mössbauer results. A plot of OH concentration vs. Fe^{3+} using $\%Fe^{3+}$ from the Mössbauer data is shown in Figure 6.4. The 3645 cm^{-1} OH peak area is correlated to the amount of Fe^{3+}.

Discussion

Figure 6.3 shows that the OH content in the diopsides increases with increasing $\Delta^{18}O_{(large\text{-}small)}$, so a first order inference is that OH in the diopside is related to the f_{H_2O} of these rocks. There are other factors underlying this conclusion, in addition to assuming that there is a linear relationship between $\Delta^{18}O_{(large\text{-}small)}$ and f_{H_2O}.

During cooling f_{H_2O} could change, so the f_{H_2O} estimated in this study is an exchange integrated average over a portion of the history of the rocks. The maximum f_{H_2O} estimated from the oxygen isotope data from these samples (for 95ADK1A) is just under 1 kbar, and f_{H_2O} is approximately equal to P_{H_2O} at the peak metamorphic pressure of 7-8 kbar (Wood and Fraser 1976). There is evidence that the Adirondacks underwent isobaric cooling (Bohlen et al. 1985), so the total pressure (P_{total}) at temperatures above 500ºC was fairly constant. Since a_{H_2O} is approximately equal to f_{H_2O} / P_{total} in this case, we calculate an a_{H_2O} of less than 0.14 for all of these samples. This is in the range of peak metamorphic water activities ($a_{H_2O} \approx 0$ to 0.2) found in fluid-buffered rocks from the Adirondacks (Lamb and Valley, 1988). Therefore, the

experimental data show that f_{H_2O} did not increase upon cooling for these rocks.

The total OH concentration of the diopsides does not linearly increase with f_{H_2O} (Figure 6.3). It is not possible to say whether this is because of scatter in the data, or because of a non-linear relationship between OH concentration and f_{H_2O}. A third possibility is that local redox conditions affected the oxidation state of Fe in diopsides from the different localities, and therefore the OH concentrations. The microprobe and Mössbauer analyses of the diopsides suggest M^{3+} and Ti^{4+} have a role in charge-balancing OH in the diopside structure. Ti^{4+} is almost 1:1 molar with total H concentration, but is not correlated with any individual absorption bands. The Fe^{3+} concentration is positively correlated to the 3645 cm^{-1} band, although the absolute concentration of Fe^{3+} is larger than the OH concentration. Since OH in the diopside structure increases the oxygen isotope diffusion rate, and a_{H_2O} was low during peak metamorphism and cooling, hydrogen was first incorporated into the diopside structure before peak metamorphism. Although Ingrin et al. (2001) showed that oxygen isotope diffusion rates in diopside are insensitive to f_{O_2} over eight to nine orders of magnitude, a change in redox conditions before or during peak granulite facies metamorphism could have reduced the hydrogen concentration in the Cascade Slide diopsides through reaction (1).

The maximum hydrogen loss for that sample is determined to be about 1270 ppm H_2O, assuming that all Fe was Fe^{2+} initially.

Conclusions

We have shown that OH concentration in diopside records f_{H_2O} during peak metamorphism and high-*T* cooling (from about 750 to 500ºC) in the Adirondack Highlands. Even if the relationship between OH and oxygen isotope data is complicated by variations in f_{O_2}, it is still possible to gain useful information about the metamorphic fluid history from the OH concentration of pyroxenes and presumably other nominally anhydrous minerals (NAMs). The hydrogen is incorporated into the crystal structure through charge-coupled substitution with M^{3+} and M^{4+} cations, making the absolute concentration of OH in the diopside difficult for decreasing temperature and pressure to change. This study shows it is reasonable to use OH concentration measurements in pyroxenes and other NAMs to learn about the high temperature fluid history of other metamorphic and igneous systems, although an understanding of the pressure, temperature, and f_{O_2} of the system is needed.

Table 6.1. Total OH concentration in diopsides determined by IR spectroscopy and contributions from each of four bands.*

	Calculated OH concentration (ppm H_2O wt.)				
Sample	3645 cm^{-1}	3530 cm^{-1}	3450 cm^{-1}	3350 cm^{-1}	Total OH
95ADK1A	125	13	0	0	138
95AK8f	18	48	48	19	134
95AK24	16	21	27	17	81
95AK6	10	15	19	11	55

*OH concentrations calculated using the specific integral absorption coefficient for clinopyroxenes from Bell et al. (1995). Analytical errors are about ±15% relative to OH concentration.

Table 6.2. Formula proportions from the electron microprobe analyses of diopside.*

Site	Element	95ADK1A 1	95ADK1A 2	95ADK1A 3	95ADK1A 4	95ADK1A Avg.	95AK8f 1	95AK8f 2	95AK8f 3	95AK8f 4	95AK8f Avg.
T	Si	1.9180	1.9118	1.9082	1.9124	1.9126	1.9277	1.9331	1.9494	1.9644	1.9437
	Al (IV)	0.0820	0.0881	0.0918	0.0876	0.0874	0.0723	0.0669	0.0506	0.0356	0.0563
	Fe^{3+} †	0.0000	0.0000	0.0000	0.0000	0.0000	0.0000	0.0000	0.0000	0.0000	0.0000
	Total T	2.0000	2.0000	2.0000	2.0000	2.0000	2.0000	2.0000	2.0000	2.0000	2.0000
M(1)	Al (VI)	0.0058	0.0000	0.0037	0.0052	0.0037	0.0710	0.0687	0.0552	0.0417	0.0592
	Fe^{3+} †	0.0285	0.0277	0.0308	0.0271	0.0285	0.0040	0.0037	0.0031	0.0028	0.0034
	Ti	0.0043	0.0041	0.0036	0.0039	0.0040	0.0048	0.0055	0.0045	0.0025	0.0043
	Cr	0.0001	0.0000	0.0000	0.0000	0.0000	0.0000	0.0000	0.0000	0.0004	0.0001
	Mg	0.9223	0.9302	0.9158	0.9264	0.9237	0.8223	0.8369	0.8614	0.8828	0.8509
	Fe^{2+} †	0.0294	0.0285	0.0317	0.0279	0.0294	0.0811	0.0745	0.0620	0.0567	0.0686
	Mn	0.0024	0.0027	0.0019	0.0007	0.0020	0.0036	0.0043	0.0038	0.0025	0.0036
	Total M(1)	0.9928	0.9932	0.9876	0.9913	0.9912	0.9868	0.9936	0.9901	0.9894	0.9900
M(2)	Ca	1.0007	1.0012	1.0067	1.0022	1.0027	0.9866	0.9802	0.9880	0.9917	0.9866
	Na	0.0000	0.0005	0.0000	0.0008	0.0003	0.0221	0.0212	0.0178	0.0146	0.0189
	K	0.0010	0.0007	0.0012	0.0006	0.0009	0.0008	0.0010	0.0010	0.0006	0.0008
	Mn	0.0000	0.0000	0.0000	0.0000	0.0000	0.0000	0.0000	0.0000	0.0000	0.0000
	Fe^{2+} †	0.0000	0.0000	0.0000	0.0000	0.0000	0.0000	0.0000	0.0000	0.0000	0.0000
	Total M(2)	1.0017	1.0023	1.0078	1.0036	1.0039	1.0096	1.0024	1.0067	1.0069	1.0064
	H*	0.00334	0.00334	0.00334	0.00334	0.00334	0.00326	0.00326	0.00325	0.00325	0.00325

* Each analysis is normalized to four cations, including H. Analyses are from core to rim (labeled 1 to 4)

† Fe^{3+}/Fe^{2+} is determined from Mössbauer data.

Table 6.2 continued.

Site	Element	95AK24 1	95AK24 2	95AK24 3	95AK24 4	95AK24 Avg.	95AK6 1	95AK6 2	95AK6 3	95AK6 4	95AK6 Avg.
T	Si	1.9571	1.9553	1.9511	1.9558	1.9548	1.9689	1.9629	1.9621	1.9650	1.9647
	Al (IV)	0.0429	0.0447	0.0489	0.0442	0.0452	0.0311	0.0371	0.0379	0.0350	0.0353
	Fe^{3+} †	0.0000	0.0000	0.0000	0.0000	0.0000	0.0000	0.0000	0.0000	0.0000	0.0000
	Total T	2.0000	2.0000	2.0000	2.0000	2.0000	2.0000	2.0000	2.0000	2.0000	2.0000
M(1)	Al (VI)	0.0126	0.0124	0.0075	0.0118	0.0111	0.0092	0.0064	0.0047	0.0030	0.0058
	Fe^{3+} †	0.0053	0.0054	0.0055	0.0054	0.0054	0.0000	0.0000	0.0000	0.0000	0.0000
	Ti	0.0030	0.0027	0.0020	0.0027	0.0026	0.0007	0.0015	0.0000	0.0005	0.0007
	Cr	0.0001	0.0000	0.0000	0.0005	0.0002	0.0004	0.0003	0.0004	0.0000	0.0003
	Mg	0.8495	0.8485	0.8435	0.8440	0.8464	0.9394	0.9424	0.9445	0.9516	0.9445
	Fe^{2+} †	0.1222	0.1232	0.1350	0.1281	0.1271	0.0386	0.0396	0.0415	0.0338	0.0384
	Mn	0.0073	0.0077	0.0066	0.0075	0.0073	0.0007	0.0013	0.0007	0.0013	0.0010
	Total M(1)	1.0000	1.0000	1.0000	1.0000	1.0000	0.9891	0.9915	0.9919	0.9902	0.9907
M(2)	Ca	0.9742	0.9720	0.9816	0.9791	0.9767	0.9993	0.9975	0.9956	0.9982	0.9977
	Na	0.0085	0.0091	0.0105	0.0090	0.0093	0.0078	0.0083	0.0083	0.0075	0.0080
	K	0.0007	0.0009	0.0006	0.0009	0.0008	0.0006	0.0007	0.0014	0.0015	0.0011
	Mn	0.0000	0.0000	0.0000	0.0000	0.0000	0.0000	0.0000	0.0000	0.0000	0.0000
	Fe^{2+} †	0.0120	0.0144	0.0048	0.0076	0.0097	0.0000	0.0000	0.0000	0.0000	0.0000
	Total M(2)	0.9954	0.9964	0.9974	0.9966	0.9965	1.0078	1.0065	1.0053	1.0072	1.0067
	H*	0.00198	0.00198	0.00198	0.00198	0.00198	0.00133	0.00133	0.00133	0.00133	0.00133

Table 6.3. Mössbauer parameters and corrected areas* for two Fe^{2+} and two Fe^{3+} components.

	Sample	95ADK1A	95AK8f	95AK24	95AK6
	χ^2	0.588	0.988	0.475	0.497
$^{[M]}Fe^{2+}$	Δ_0	1.929	2.231	2.023	1.980
	δ	1.169	1.173	1.160	1.156
	γ	0.396	0.486	0.403	0.408
	Raw Area	0.399	0.252	0.727	0.820
$^{[M]}Fe^{2+}$	Δ_0	1.608	1.869	1.803	1.713
	δ	1.141	1.176	1.171	1.183
	γ	0.226	0.334	0.270	0.294
	Raw Area	0.063	0.771	0.335	0.315
$^{[M]}Fe^{3+}$	Δ_0	0.889	0.893	1.022	
	δ	0.346	0.364	0.352	
	γ	0.500	0.500	0.331	
	Raw Area	0.434	0.062	0.051	
$^{[M]}Fe^{3+}$	Δ_0	1.461			
	δ	0.422			
	γ	0.500			
	Raw Area	0.115			
$^{[M]}Fe^{2+}$	Corrected Area*	43.7	23.5	65.9	72.2
$^{[M]}Fe^{2+}$	Corrected Area*	6.9	71.8	30.3	27.8
$^{[M]}Fe^{3+}$	Corrected Area*	39.0	4.7	3.8	0.0
$^{[M]}Fe^{3+}$	Corrected Area*	10.3	0.0	0.0	0.0
$\sum\%Fe^{3+}$		49.4	4.7	3.8	0.0

* Areas corrected using differential recoilless emission (f) values given in text.

Figure 6.1. Polarized IR reflectance spectra of diopside slabs from sample 95AK6 and the Cr diopside orientation standard (from Shannon et al. 1992). Spectra are shifted vertically for comparison.

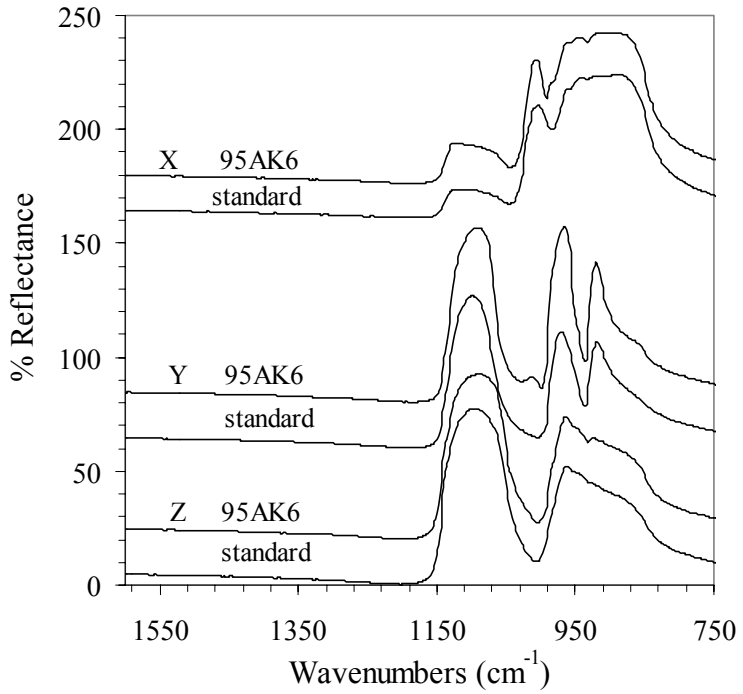

Figure 6.2. (a) Polarized FTIR spectra of diopsides, normalized to 1 mm thickness. Spectra are offset for clarity, and the absorbance scale is different for each sample to show details of spectra. (b) The **Y** polarized spectra for all samples, on the same absorbance scale for comparison. OH concentration in the samples increases from bottom to top.

Figure 6.2A.

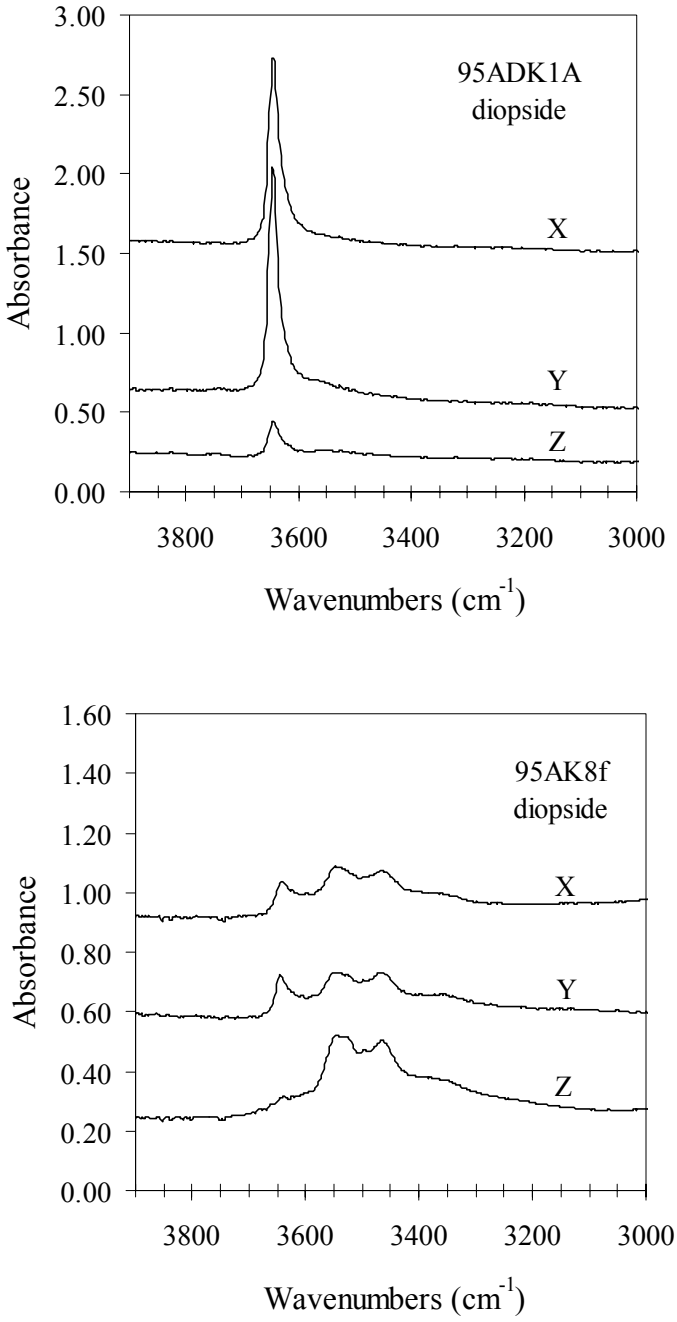
95ADK1A
diopside
X
Y
Z
Absorbance
3.00
2.50
2.00
1.50
1.00
0.50
0.00
3800
3600
3400
3200
3000
Wavenumbers (cm-1)
95AK8f
diopside
X
Y
Z
Absorbance
1.60
1.40
1.20
1.00
0.80
0.60
0.40
0.20
0.00
3800
3600
3400
3200
3000
Wavenumbers (cm-1)

Figure 6.2A continued.

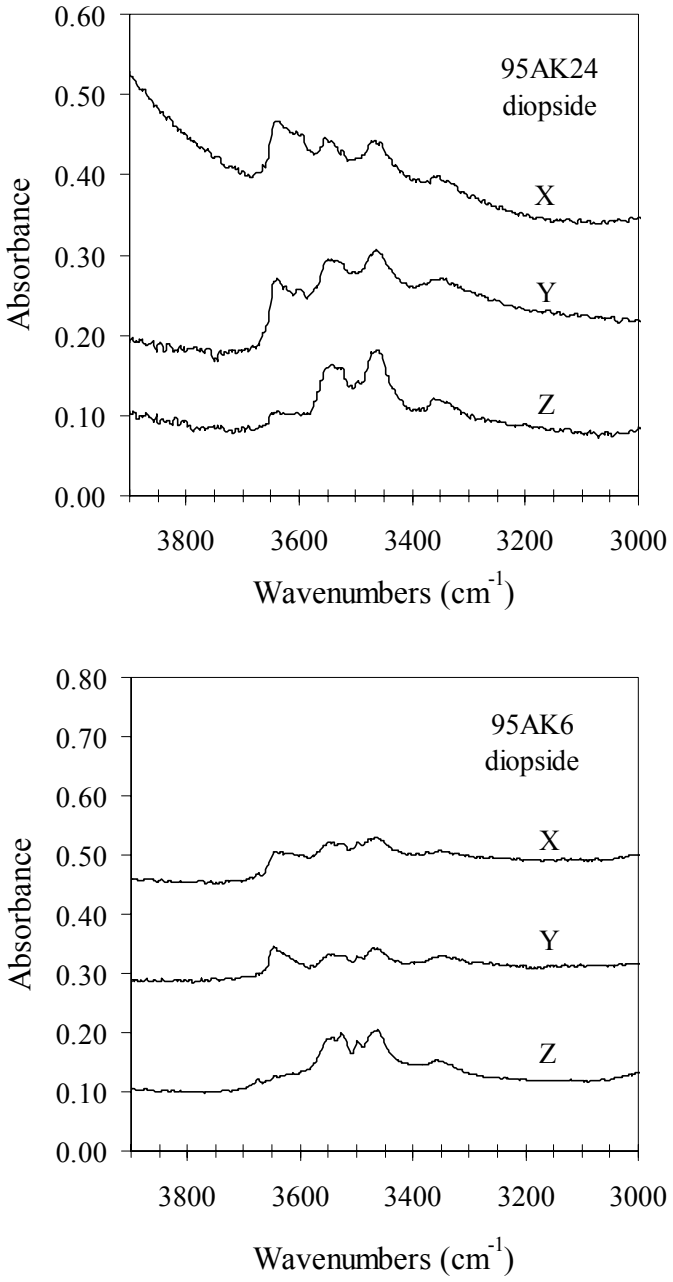

Figure 6.2B.

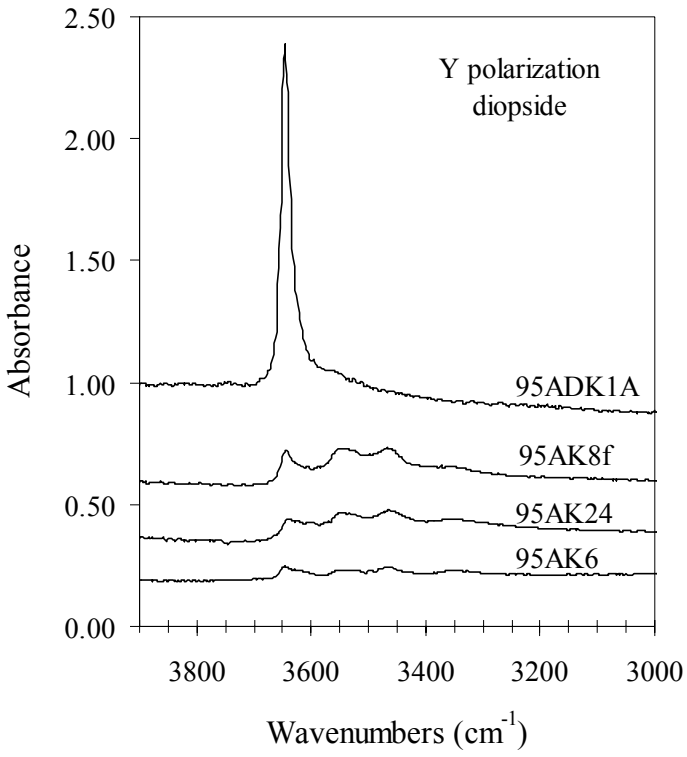
2.50
2.00
1.50
1.00
0.50
0.00
Absorbance
Y polarization
diopside
95ADK1A
95AK8f
95AK24
95AK6
3800
3600
3400
3200
3000
Wavenumbers (cm-1)

Figure 6.3. Total OH content of diopside samples from IR spectroscopy vs. water fugacity, as predicted from oxygen isotope measurements (Edwards and Valley 1998). OH from bands that increase in intensity during hydrothermal experiments (Skogby and Rossman 1989) are also plotted (as open symbols).

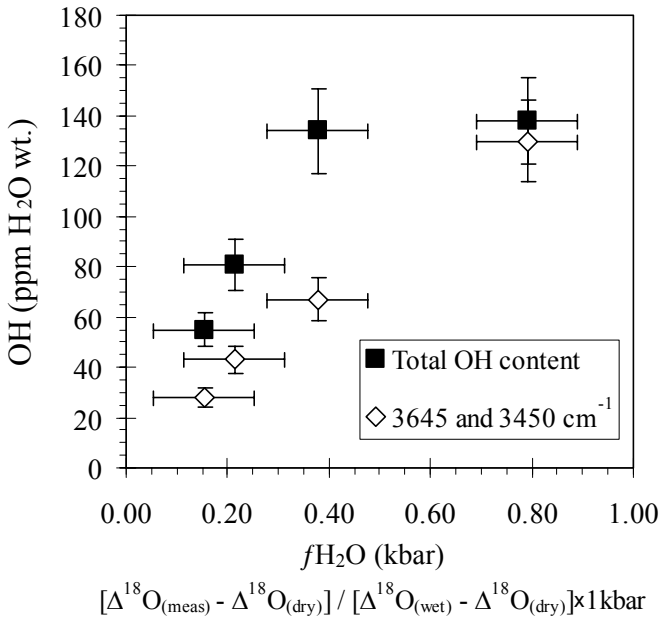

Figure 6.4. Concentration of hydrogen versus average concentration of total (a) Fe^{3+} (b) Al (c) Ti (d) Na, and (e) M^{3+}. Fe^{3+} concentration is determined from the Mössbauer data; all others are from microprobe analysis. In addition to total OH concentration, hydrogen concentrations due to individual peaks (3645 and 3450 cm^{-1}) are also shown if a discernable trend can be seen. For elements other then H, the error shown is the standard deviation of the average of four analyses for each sample.

Figure 6.4A.

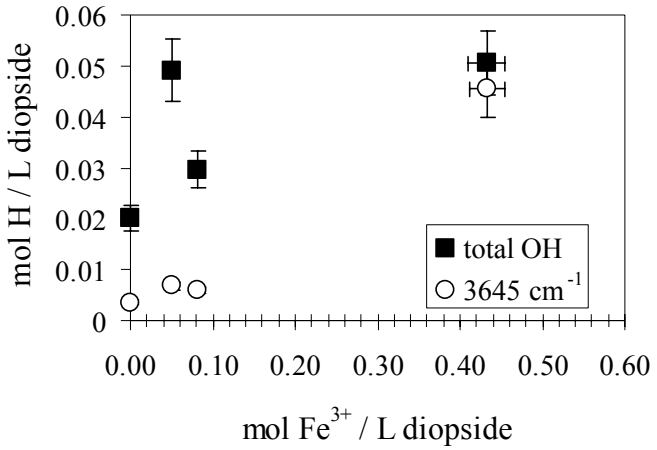

Figure 6.4B.

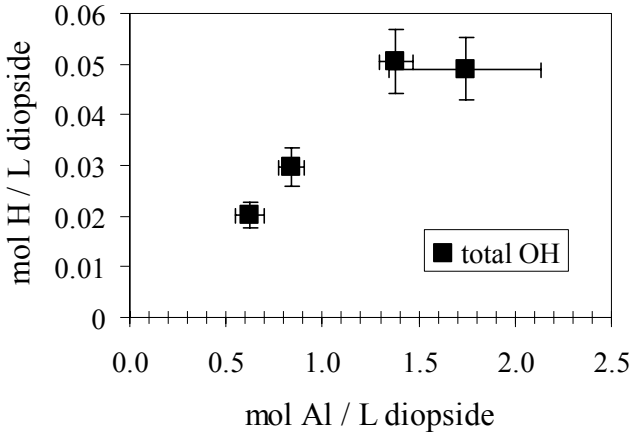

Figure 6.4C.

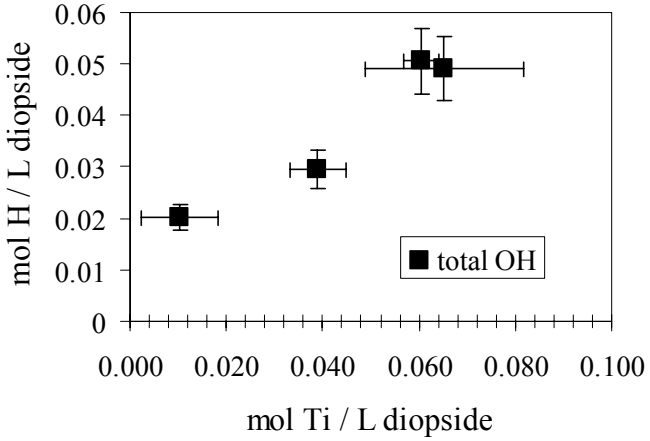

Figure 6.4D.

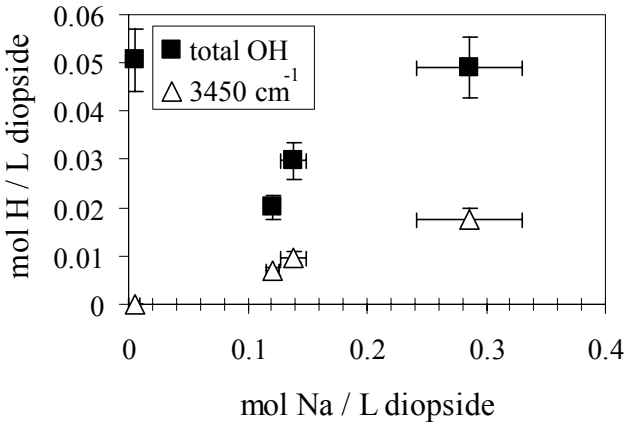

Figure 6.4E.

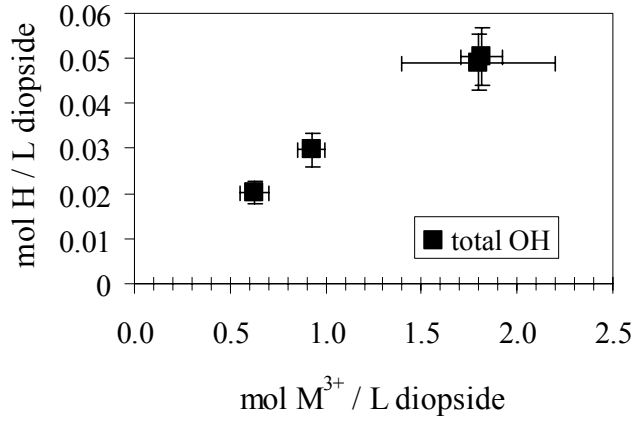

Figure 6.5. Optical absorption spectra of diopsides in the **X** polarization direction. Spectra are offset vertically for clarity (in order of increasing OH content) and are normalized to 1 mm thickness.

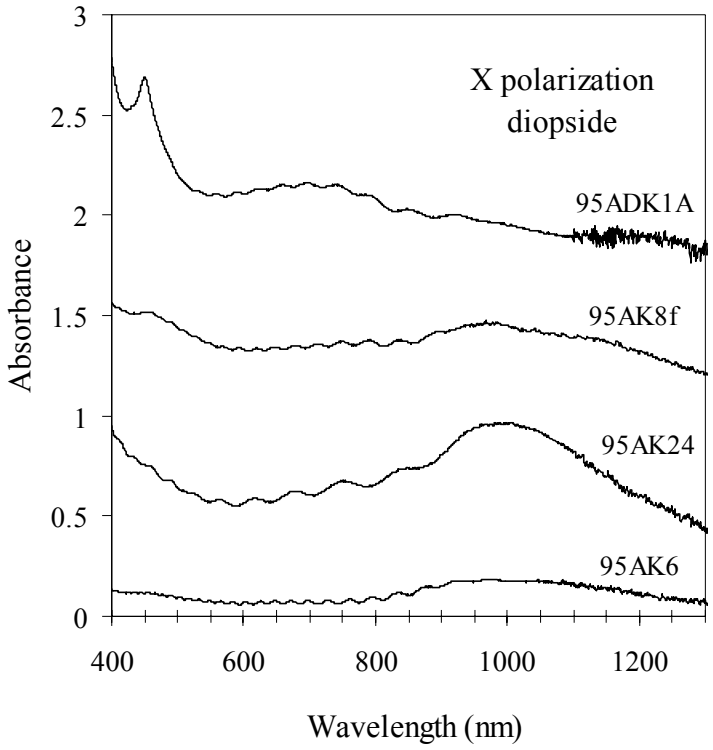

Figure 6.6. Representative Mössbauer spectra and quadrupole splitting distribution (QSD) fits (solid lines) for Fe in diopside. Isomer shifts are reported relative to metallic Fe. Each spectrum was fit with two Fe^{2+} components (with δ about 1.1 to 1.2) and up to two Fe^{3+} components (with δ about 0.3 to 0.4).

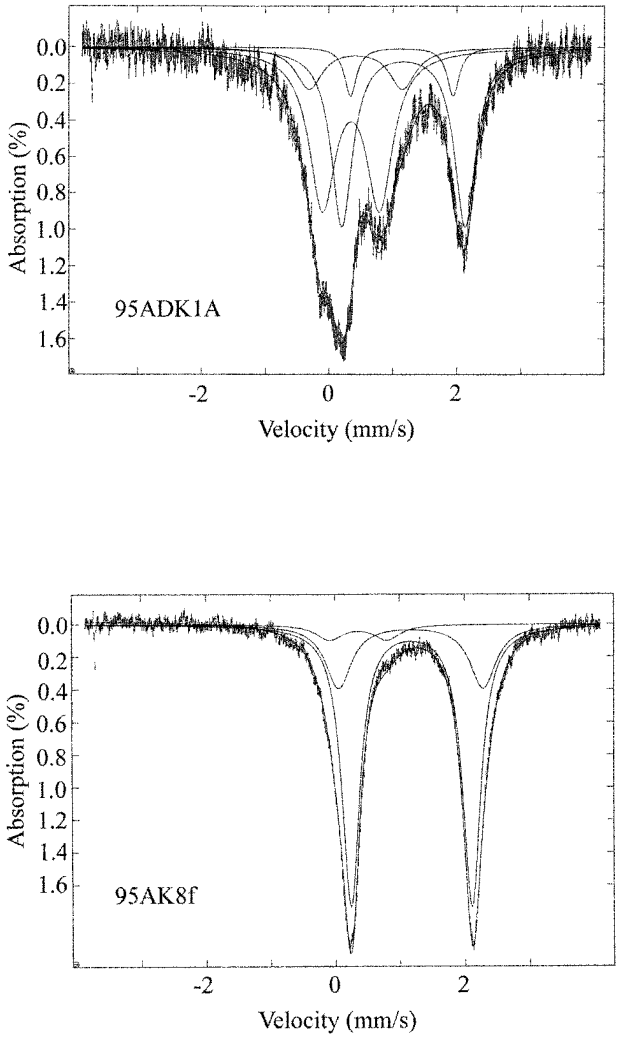

Chapter 7

OH CONCENTRATIONS OF GROSSULAR-ANDRADITE SKARN GARNETS FROM BIRCH CREEK, CALIFORNIA, AND THE ADIRONDACK MOUNTAINS, NEW YORK

Introduction

This study investigates the OH concentrations and major element chemistry of grossular-andradite garnets from the contact metamorphic aureole of the Inyo batholith near Birch Creek, California, and from a massive garnetite and wollastonite skarn along the contact of the Marcy Anorthosite, Adirondack Mountains, New York. Skarns are formed from the interaction of magmatic or meteoric hydrothermal fluids with carbonate-rich sediments. The concentrations of hydrous species within nominally anhydrous minerals such as garnet might therefore record local fluid history or spatial distributions of fluid flow.

Grossular-andradite garnets are often found in skarn assemblages. Many garnets are zoned with respect to oxygen isotope ratios, major elements, and trace elements (e.g., Taylor and O'Neil 1977; Jamtveit and Hervig 1994;

Crowe et al. 2001; Skelton et al. 2002; Clechenko and Valley in press). These zonation patterns have been interpreted to record multiple pulses of fluid flow, or the variability of fluid composition (meteoric versus magmatic fluids) over time. Single crystals of garnet might contain additional information about fluid history in the form of variable or zoned OH concentrations.

The incorporation mechanisms of structural OH in grossular garnets have been extensively studied but are not completely understood. Neutron diffraction and NMR studies of synthetic hydrogarnet $Ca_3Al_2(O_4H_4)_3$, have determined that four hydroxyl groups replace each SiO_4 tetrahedron in this structure (Lager et al. 1987; Lager et al. 1989; Cho and Rossman 1993). In natural grossular garnets with lower concentrations of OH (0.2 to 0.3 wt% H_2O), clusters of two OH groups as well as $(OH)_4$ are present within the structure (Cho and Rossman 1993). The OH absorption patterns of grossular garnets containing $\leq$ 1 wt% H_2O are more complex than the OH spectra of hydrogarnets, and seven classes of OH band in grossular have been established (Rossman and Aines 1991). Charge-coupled substitution of OH and transition metal atoms may be an important factor in the incorporation and retention of OH in garnets, and could explain the complexity of garnet OH bands. OH concentration has not been correlated with minor or trace element composition in grossular-andradite garnets (Rossman and Aines 1991).

Few studies have examined OH concentrations in natural garnets (Aines and Rossman 1984; Rossman and Aines 1991; Bell and Rossman 1992; Amthauer and Rossman 1998; Arredondo et al. 2001). Rossman and Aines (1991) found a large range of OH concentrations in grossular-hydrogrossular garnets (12.8 wt% to less than 0.005 wt% H_2O). Core-to-rim zonation of OH concentrations has been observed in several grossular garnets (Rossman and Aines 1991). In the only systematic study of garnet OH concentrations within a particular geologic setting, Arredondo et al. (2001) found that the OH concentrations of spessartine-almandine garnets record the progressive increase in water activity during evolution of granitic pegmatites.

Sample Localities

Birch Creek, CA

The first suite of grossular-andradite garnets in this study is from a contact metamorphic zone between lower Cambrian sedimentary rocks and the granitic intrusives of the Inyo batholith, located at the foot of Birch Creek on the northwest side of Deep Springs Valley, Inyo County, California. Geologic maps of the area and detailed lithologic descriptions are given in Nash (1962) and Shieh and Taylor (1969). An initial contact metamorphic aureole of marble, hornfels, and schist, approximately 793 meters in width, was formed

when the Beer Creek quartz monzonite and a foliated hornblende granodiorite were intruded into limestones and quartzitic and pelitic clastic rocks in the early to middle Jurassic (150-170 Ma; McKee and Nash 1967). In the Cretaceous (76-93 Ma; McKee and Nash 1967), further intrusions of granite and alaskite were emplaced along the margin of the granodiorite and as dikes and sills in the surrounding country rock. This later stage of intrusion produced an irregular epidote-grossular-calcite skarn less than 10 m wide in its largest dimension.

The grossular samples in this study are primarily from these irregular skarns (unit Kes of Nash (1962)). The skarn hand sample used in this study is BC-2B from Shieh and Taylor (1969). Although Shieh and Taylor (1969) report $\delta^{18}O$ values only for the matrix calcite in this sample, the rock is dominated by grossular and epidote. The grossular and epidote are found both as fine-grained granular masses with calcite, and as large (up to 1 cm across), subhedral to euhedral crystals. The euhedral grossular garnets display growth banding parallel to crystal faces. Some color variation between bands is visible (pale orange-red to intense orange-red in thick section). The growth bands are often separated by thin layers of fine-grained calcite and epidote. One additional grossular garnet is from a coarse grossularite hornfels (Єgh unit from Nash (1962) approximately 30 meters from the intrusive contact. The hand sample from this unit (BC-11 from the thesis collection of Y. N.

Shieh) contains subhedral to euhedral porphyroblasts of grossular up to 2 cm in diameter in a matrix of calcite.

Oak Hill and Willsboro wollastonite deposits, Adirondacks, NY

In contrast to the small scale of the Birch Creek metamorphic aureole, the skarn belt along the northeast edge of the Marcy Anorthosite is hundreds of meters thick and extends for tens of kilometers (Valley and O'Neil 1982). The wollastonite skarn in this unit is mined commercially, and many of the samples in this study are from drill cores provided by NYCO, the company that runs the Willsboro and Oak Hill mines (see Valley (1985) for a geologic map and the location of Willsboro). The geology of this region is complex and at least two different metamorphic histories have been proposed (Valley and O'Neil 1982; Valley 1985; Alcock and Muller 1999). Generally, it is agreed that the Adirondacks underwent a polymetamorphic history (Valley 1985; McLelland et al. 1996) during the Grenville orogeny (1350-1000 Ma). Emplacement of a suite of igneous intrusions (including the Marcy Anorthosite at about 1155±5 Ma; Clechenko et al. 2002; Hamilton et al. 2002) occurred at 1180-1130 Ma (McLelland et al. 1996). The anorthosite massif was intruded at shallow depths (<10 km) causing skarn formation involving large volumes of meteoric water (Valley and O'Neil 1982). The region subsequently underwent fluid-absent (Lamb and Valley 1988; Valley et al. 1990) granulite facies metamorphism at 700-800°C and 7-8 kbar between

1090 and about 1010 Ma (Bohlen et al. 1985; Valley et al. 1990; McLelland et al. 1996; Clechenko et al. 2002).

The wollastonite skarn is composed almost entirely of coarse-grained wollastonite, grossular-andradite garnet, and clinopyroxene. The relative proportions of these minerals are variable on the scale of a hand sample. Much of the ore deposit is predominantly wollastonite with about 40% modal garnet and pyroxene (Clechenko and Valley, in press), but there are bands ~1 cm to 1 meter thick that are predominantly composed of grossular and/or pyroxene. The wollastonite ore is intruded by a finger of anorthosite at Oak Hill. Near the contact with the major body of anorthosite at Oak Hill here is a massive garnetite layer almost completely composed of grossular-andradite garnet, with minor pods of plagioclase, quartz, clinopyroxene, and occasional titanite (Clechenko and Valley, in press). Within the massive garnetite, "boudins" of large (1-3 cm), euhedral, compositionally and geochemically zoned garnets formed during the initial hydrothermal event were preserved during granulite facies metamorphism (Clechenko and Valley, in press), although much of the garnetite is extensively fractured or recrystallized into a granular matrix of mm-sized grains. These large, euhedral garnets contain oscillatory zoning of $\delta^{18}O$ and Fe^{3+}/Al that is consistent with spatially and temporally varying proportions of magmatic and meteoric fluids during crystal growth in the hydrothermal system (Clechenko and Valley, in press).

Grossular-andradite garnets from two drill cores, Willsboro core #81-15 and Oak Hill core #98-16, are examined to evaluate the effect of the hydrothermal event and subsequent granulite facies metamorphism on garnet OH concentrations. The drill cores extend from the top of the skarn exposure to the main contact with the Marcy Anorthosite, providing a cross-section of the deposit, although folding and faulting within the ore deposit may obscure some of the original contact relationships. The spatial variations and range of OH concentrations in the large zoned garnets and neighboring granular and fractured garnets within the Willsboro Mine garnetite (94ADK11 and 94ADK12) are also investigated.

Methods

IR spectroscopy

Doubly polished thick sections (0.29 to 0.07 mm) of zoned garnets from Birch Creek, CA, and the Willsboro, NY, garnetites were created roughly perpendicular to crystal faces. The thickness of each section was measured at each point where an infrared spectra was obtained. The zoned Birch Creek garnets were subsequently reattached to glass slides, repolished with 0.3 μm diamond grit, and analyzed for major element composition on the same spots where the infrared spectra were obtained.

Polished slabs of garnets from the Oak Hill and Willsboro wollastonite transects were obtained from the University of Wisconsin, Madison. Many of the garnets were repolished at Caltech, and in some cases OH spectra on multiple spots of the same grain were measured before and after repolishing to evaluate the heterogeneity of OH within a given sample. Electron microprobe analyses of these garnets were obtained by Cory Clechenko at the University of Wisconsin, Madison, on separate garnets from the same core sample.

Some birefringent garnets exhibit strong anisotropy of structural OH bands (Rossman and Aines 1986). Several polarized spectra were taken on slightly birefringent garnets from the Adirondacks as well as on the garnets from the Birch Creek skarn. All the garnets tested in the present study had isotropic OH bands, as expected for cubic symmetry of garnet.

Infrared spectra were obtained on a Nicolet Magna 860 FTIR spectrometer with a Spectra-Tech Continuμm® microscope accessory at 4 cm^{-1} resolution using a 100 μm square aperture, KBr beamsplitter, and MCT-A detector. Spectra were averaged over 256 scans. Integrated OH band area (3500-3700 cm^{-1}) was determined using a linear background. OH concentrations were calculated using the relationship:

$$H_2O \text{ wt\%} = 0.0000786 \times \Delta, \quad (7.1)$$

from Rossman and Aines (1991) for grossular-hydrogrossular garnets, where Δ is the integrated OH absorbance per centimeter thickness near 3600 cm^{-1}. This calibration was based largely on hydrogrossular garnets, which have OH bands that are broader and less complex than those observed for low-OH grossular garnets like the ones in this study. Thus, the OH concentrations determined for the low-OH grossular garnets in this study may be systematically offset from the true values if the absorptivity of the complex OH bands is not exactly the same as the hydrogrossular OH bands. This systematic error is not likely to be large and does not affect the relative differences in OH concentrations that are important in the current study.

Electron microprobe analysis

Electron microprobe analyses of the Birch Creek skarn samples were obtained on a JEOL JXA-733 electron microprobe at Caltech, using an accelerating voltage of 15 keV, beam current of 25 nA, and 10 μm spot size. Oxide totals were calculated using the CITZAF correction (Armstrong 1995) and fell within the range 99.5-100.5%. All Fe is reported as Fe_2O_3.

Elemental analyses of the Adirondacks drill core samples were obtained at the University of Wisconsin, Madison, by Cory Clechenko and John Valley, using a Cameca SX-51 electron microprobe with an accelerating voltage of 15 keV and a beam current of 20 nA. Oxide totals were determined with the

Armstrong-Love/Scott correction of Armstrong (1988). Analyses were normalized to 8 cations, and the ratio of Fe^{2+}/Fe^{3+} was determined by charge balance with 12 oxygens, assuming no OH.

Results

Birch Creek, CA

The OH concentrations and major element chemistry of the Birch Creek garnets are reported in Tables 7.1 and 7.2. Figures 7.1, 7.2, and 7.3 show the variation in OH, Ti, and Fe^{3+} concentration as a function of distance from the center of the garnet for the skarn samples (BC2B1, BC2B3, and BC2B4). In all three garnets, the OH concentration decreases from a maximum of 0.43-0.47 wt% H_2O in the core to 0.14-0.20 wt% H_2O at the rim. Sample BC-11 from the coarse grossularite hornfels contains 0.18 wt% H_2O. No general spatial trends are seen for the other elements analyzed. Fe and Mn concentration is higher in the darker red growth bands that occur throughout the garnets.

Representative OH spectra of the Birch Creek grossular-andradites are shown in Figure 7.4. The most intense OH band occurs at about 3645 cm^{-1}, with prominent bands at 3600 cm^{-1}, 3568 cm^{-1}, and 3548 cm^{-1}. This OH band pattern is characteristic of class 2 grossular garnets (Rossman and Aines 1991), typically found in calcite veins or pods.

Plots of OH concentration versus major element composition of the garnets show no compelling correlations between garnet chemistry and OH concentration except in the case of Ti (Figure 7.5). The ratio of H to Ti in the Birch Creek garnets is roughly 3 to 1, using the infrared calibration of Rossman and Aines (1991).

Willsboro Mine garnetite: zoned garnets

Sample 94ADK12 contains a number of fractured, euhedral grossular-andradite crystals surrounding a paleocavity filled with calcite, quartz, and plagioclase, but is primarily composed of coarsely granular (1 mm crystals) garnetite. Infrared spectra were obtained on multiple spots in the zoned garnets and on multiple garnets from the granular area (Table 7.3). No spatial information about OH concentrations within the zoned garnets was obtained since the friable thick sections crumbled to pieces during preparation. The zoned garnets have a larger range in OH concentration (0.078-0.153 wt% H_2O) than the garnets from the granular garnetite (0.104-0.143 wt% H_2O). The average OH concentration of these two populations is almost identical (0.120 and 0.129 wt% H_2O, respectively).

Sample 94ADK11 also contains euhedral, zoned garnets surrounding calcite. In one region of the thick section, the garnets are fractured more extensively than in the rest of the section (Figure 7.7). There is a smoothly varying

zonation of OH concentration from the rim to the core of the visibly zoned garnet. The reddish, more Fe^{3+}-rich bands in the zoned garnet contain moderate OH concentrations (0.13-0.14 wt% H_2O). The total range of OH concentrations in the zoned garnet is 0.094 to 0.161 wt% H_2O, whereas (unlike 94ADK12) the concentration of OH in the fractured area is at the lower end of this range (0.10-0.12 wt% H_2O).

Willsboro and Oak Hill drill core samples

Representative mid-IR OH absorption patterns for grossular-andradite garnets from the Adirondacks wollastonite ore deposit are presented in Figure 7.8. Unlike the grossular garnets from Birch Creek, CA, the most intense OH band is found at 3600 cm^{-1} (class 7 OH bands; Rossman and Aines 1991). The relative OH band intensities are similar for all grossular garnets in this region regardless of OH concentration.

The OH concentrations and major element chemistry of garnets from the Willsboro and Oak Hill drill cores are given in Tables 7.5 and 7.6. Garnet OH concentrations are plotted as a function of rock type and core depth in Figures 7.9 and 7.10. The contact between ore rocks and the main body of anorthosite occurs at the bottom of each drill core. The distribution of garnet OH concentrations is correlated to rock type rather than distance from the main anorthosite contact. The garnets within the garnetite and garnetite layers have

higher average OH concentrations (0.1 to 0.17 wt% H_2O) than the grossular garnets in the wollastonite ore. The total range of OH concentrations fall between 0.05 and 0.17 wt% H_2O. The OH concentrations of the wollastonite ore garnets span the total range of OH values, but the vast majority of grossulars from the wollastonite ore have OH concentrations below 0.1 wt% H_2O. The range of OH concentration within a single millimeter-sized garnet can be as large as 0.03 wt% H_2O.

In the Willsboro transect, two almandine garnets from a band of anorthosite within the wollastonite ore were also analyzed. These garnets formed during granulite facies metamorphism (Valley 1985) and are essentially devoid of OH.

Garnet OH concentrations are plotted versus Fe^{2+}, Fe^{3+}, Ti, and Mn in Figures 7.11 and 7.12. There are no correlations between OH concentration and major element composition for the grossular garnets from the garnetite and garnetite layers. The clearest compositional trends are for the grossular garnets from the Oak Hill wollastonite ore rocks. For these samples, OH concentration decreases with increasing Fe^{3+}, and is greater for samples with low Mn and Ti concentrations.

Discussion

Birch Creek, CA

The correlation between H and Ti concentration in the Birch Creek skarn garnets may be related to crystal chemical constraints on H incorporation. If there is a charge-coupled substitution of Ti and H into the garnet structure, it must involve three H for every Ti incorporated into the structure. Ti^{4+} substitutes into the octahedral (Y) site in garnet, replacing a M^{3+} cation, in this case Fe^{3+} or Al^{3+}. This creates an excess charge that must be balanced locally. Substituting three hydrogen atoms as hydroxyl groups into an adjacent tetrahedral site would satisfy this charge imbalance in the equation: $3H^{+} + Ti^{4+} = Si^{4+} + M^{3+}$. However, there is no evidence for clusters of three OH groups in the few hydrous garnet samples that have been investigated with NMR or neutron diffraction techniques- only clusters of two OH and four OH groups are observed (Lager et al. 1987; Lager et al. 1989; Cho and Rossman 1993).

The positive correlation between H and Ti in these garnets is not seen in all grossular garnets. Most grossular garnets contain very low Ti concentrations (less than 0.04 Ti per formula unit garnet; Rossman and Aines 1991) as compared to the Birch Creek garnets (most analyses have greater than 0.04 Ti per formula unit). The complex OH band patterns may eventually aid our

understanding of this and other charge-coupled substitutions involving hydrogen that might occur in grossular garnets.

Even allowing for the uncertainty of the mechanism of H and Ti incorporation within the Birch Creek garnets, there is a steady decrease in Ti from core to rim that requires explanation. Oscillatory zoning in Fe and Mn within skarn garnets is typically interpreted as recording differences in fluid composition (Taylor and O'Neil 1977), or a time series of local pulses of magmatic and meteoric fluids (Jamtveit and Hervig 1994; Crowe et al. 2001; Clechenko and Valley, in press). It is likely that the Birch Creek Skarn was dominated by magmatic fluids due to the small scale of the intrusive tongue responsible for skarn formation. There is some oscillatory behavior of Fe in these garnets, so there could have been multiple pulses of fluid in this system. However, it seems unlikely that the steady decrease in Ti concentration is due to infiltration of pulses of compositionally variable fluids.

The concentration of Ti in natural water is generally low (ppm to ppb levels) (Van Baalen 1993). Many factors could influence the solubility of Ti, including fluid composition, pH, and temperature and pressure. Of these variables, pressure and temperature have the greatest effect on Ti solubility (Van Baalen 1993), with temperature having a greater influence than pressure, as long as the fluid behaves as a liquid and not as vapor. The temperature of

skarn formation is not known, but the intrusive contact temperature for the Beer Creek pluton was approximately 550°C (Shieh and Taylor 1969). At this temperature, Ti solubility in the fluid (log [Ti] ~ -3.3) would be about two orders of magnitude greater than the solubility at 23°C (Van Baalen 1993).

The small skarn at Birch Creek likely formed during infiltration of magmatic fluid from the late-stage intrusive dike into the surrounding country rock. The simplest explanation for the decrease of Ti from core to rim of the garnets is a decrease in temperature during growth of the grossular (and epidote). The initial fluid would be hot and would contain relatively high concentrations of Ti. The garnet and epidote would incorporate the Ti as they formed (typical epidote contains tenths of a weight percent TiO_2; Deer et al. 1992). As the dike and skarn system cooled off, even if a fracture system allowed variable fluids to enter locally, the infiltrating fluids were cooler and contained less Ti.

The garnet from the grossular hornfels sample BC-11 has an OH concentration that is at the lower end of the range of OH concentrations found in the skarn garnets. This is consistent with the lack of epidote in this rock unit, and with this sample being farther away from the initial metamorphic contact.

Zoned garnetite garnets, Willsboro Mine

In sample 94ADK11, gradients in OH concentration are preserved on the scale of less than a millimeter within the zoned garnet. Variations in $\delta^{18}O$ and

major element chemistry are also seen on a similar scale in zoned garnets from Willsboro (Clechenko and Valley, in press). In order for these compositional variations to be preserved during granulite facies metamorphism, the characteristic length of diffusion must be smaller than the zone thickness. Assuming granulite facies metamorphism lasted 50 Ma at a temperature of 750°C, Clechenko and Valley (in press) estimate the characteristic length scale of Mg and Fe^{2+} diffusion to be ~0.5 mm, and the characteristic length of diffusion for oxygen isotope diffusion was calculated to be 0.002 mm, both smaller than the millimeter-wide zoning in the Willsboro garnets. From the limited data available for hydrogen diffusion in garnets (i.e., pyrope; Wang et al. 1996), the millimeter-scale zonation of OH would be obliterated within a few years. The fact that OH zoning remains means that hydrogen diffusion in grossular garnet is different from that in pyrope, or that one or more charge balance effects stabilized the OH during metamorphism.

The Willsoboro zoned garnets in this study were analyzed for $\delta^{18}O$ and major element composition zoning in Clechenko and Valley (in press). Fe-rich bands are high in $\delta^{18}O$ and are interpreted to form during infiltration of magmatic fluids, while zones with low $\delta^{18}O$ and low Fe^{3+}/Al are thought to have formed during infiltration of meteoric fluids (Clechenko and Valley, in press). It is not clear whether OH concentrations should be expected to be

their greatest in areas of the garnets crystallized during infiltration of magmatic or meteoric fluids, since there are no buffering assemblages for silica activity or water activity. Therefore, it can only be stated that OH concentrations are moderately high in bands associated with magmatic fluids, but the lowest and highest OH concentrations are found in bands associated with meteoric fluids.

The relationship between the ranges in OH concentration in 94ADK11 and 94ADK12 is not clear. The fractured area of 94ADK11 may not have been as extensively recrystallized as the granular areas of 94ADK12, and may simply correspond to the deformed rim of a zoned garnet. The granular garnets in 94ADK12 may better represent any homogenization of OH concentration that took place during granulite facies metamorphism.

Willsboro and Oak Hill drill core samples

There are a number of possible scenarios for explaining why the grossulars in the garnetite and garnetite layers have higher OH concentrations than the grossulars from the wollastonite ore, and why only the wollastonite ore garnets show any correlation between OH concentration and major element chemistry. One possibility is that the garnetite garnets formed with initial OH concentrations greater than those of the wollastonite garnets during the initial hydrothermal phase, and these concentrations were preserved during granulite

facies metamorphism. It is difficult to explain why correlation of OH with major element chemistry is seen only in the wollastonite garnets using this model. Alternatively, all or most of the grossular garnets could have formed with high OH concentrations (0.1 to 0.15 wt% H_2O) during the initial hydrothermal event. Subsequently, some garnets were recrystallized more extensively than others during the granulite facies event. Because of the relative strength of the garnetite layers as compared to the wollastonite ore, most garnetite garnets at least partially preserved OH concentrations, while the grossular garnets in the wollastonite ore were more easily recrystallized and the resulting garnets had lower generally lower OH concentrations, depending on the local environment. The relative modal abundance of minerals in the surrounding rock (wollastonite, grossular, and pyroxene) could also have played a role in changes in garnet OH concentration and major element chemistry during this process. Fluorine-bearing garnets (up to 0.7 wt%) that formed post metamorphism in quartz-absent rocks have been found in calc-silicate rocks from the Adirondacks (Valley et al. 1983). It is possible that small quantities of fluorine could be present in the garnets used in this study, further complicating the interpretation of volatile history through garnet OH concentrations.

Conclusions

The Birch Creek skarn was formed in a fairly simple geologic context. In all the zoned garnets analyzed from this location, there is a simple trend of decreasing OH concentration during growth of the garnet. The H concentration is correlated to Ti concentration, but is not related to concentrations of other major elements, particularly Fe. The H and Ti may participate in charge-coupled substitution into the garnet crystal structure. After initial infiltration of magmatic fluid into the carbonate sediments, the system cooled and Ti solubility in the fluid dropped. The garnet cores incorporated higher Ti and H concentrations than the later growth bands.

In contrast, the garnets from the Adirondacks experienced a spatially and temporally complicated fluid and metamorphic history, and this is reflected in the wide range of OH concentrations present in the garnets, with a lack of clear chemical or geological correlations. Even in single zoned garnets with some corresponding oxygen isotope and chemical data available, it is not possible to provide a unique explanation of variations in OH concentration.

The range of OH concentrations for all of the garnetite and garnetite layers in both drill cores is similar to the range found within a single hand sample, or even within a single zoned garnet within the Willsboro garnetites. The Birch Creek garnets have high OH concentrations compared to the garnets from the

Adirondacks wollastonite deposits, even though the extent of the hydrothermal system in the Adirondacks was much larger than the localized Birch Creek skarn.

The difficulties in interpretation of OH concentrations preserved within nominally anhydrous minerals encountered here would likely extend to any other geologic system that is spatially heterogeneous or that has experienced a complex sequence of geologic events.

Table 7.1. Mid-IR band areas and OH concentrations of grossular-andradite garnets from Birch Creek, CA.

Sample	Spot	Band area per cm thickness 3450-3700 cm^{-1}	[OH]* wt% H_2O
BC2B1	1	4583	0.360
	3	4206	0.331
	4	5047	0.397
	5	3733	0.293
	9	3662	0.288
	10	3113	0.245
	11	3434	0.270
	12	2558	0.201
	13	3768	0.296
	14	5061	0.398
	15	5280	0.415
	16	4677	0.368
	17	5851	0.460
	18	4752	0.374
	19	3390	0.266
BC2B3	1	1931	0.152
	2	3455	0.272
	3	2868	0.225
	4	3569	0.281
	5	3494	0.275
	6	3439	0.270
	7	3783	0.297
	8	5521	0.434
	9	4583	0.360
	10	4246	0.334
	11	5227	0.411
	12	5965	0.469
	13	4646	0.365
	14	3552	0.279
	15	3945	0.310
	16	3640	0.286
	17	3451	0.271

*Concentrations determined using grossular-hydrogrossular calibration of Rossman and Aines (1991).

Table 7.1 continued.

Sample	Spot	Band area per cm thickness 3450-3700 cm^{-1}	[OH]* wt% H_2O
BC2B4	1	1835	0.144
	2	2194	0.172
	3	3401	0.267
	4	3580	0.281
	5	3785	0.298
	6	3753	0.295
	7	3489	0.274
	8	3647	0.287
	9	5000	0.393
	10	5514	0.433
	11	3978	0.313
	12	5360	0.421
	13	4882	0.384
	14	4641	0.365
	15	4246	0.334
BC-11	1	2314	0.182

*Concentrations determined using grossular-hydrogrossular calibration of Rossman and Aines (1991).

Table 7.2. Formula proportions from electron microprobe and IR analysis of Birch Creek, CA, grossular-andradite garnets.

Sample	Spot	Ca	Mg	Mn	Fe^{3+}	Ti	Cr	Al	Si	OH
BC2B1	1a	3.03	0.005	0.028	0.91	0.059	0.002	1.06	3.00	0.194
	1b	2.98	0.005	0.032	0.97	0.061	0.000	1.07	3.00	0.194
	3	2.96	0.006	0.051	0.76	0.048	0.000	1.27	3.00	0.176
	4	2.97	0.004	0.043	0.84	0.040	0.000	1.21	3.00	0.213
	5	2.92	0.006	0.079	0.81	0.048	0.001	1.24	3.00	0.156
	9	2.95	0.007	0.046	0.85	0.049	0.000	1.20	3.00	0.153
	10	2.95	0.006	0.049	0.84	0.046	0.000	1.21	3.00	0.130
	11	2.97	0.006	0.044	0.86	0.053	0.001	1.17	3.00	0.144
	12	2.93	0.005	0.064	1.19	0.036	0.001	0.90	3.00	0.109
	13	2.96	0.007	0.049	0.85	0.054	0.000	1.19	3.00	0.158
	14	2.80	0.004	0.169	1.06	0.079	0.001	1.03	3.00	0.218
	15	2.91	0.007	0.103	0.87	0.071	0.002	1.18	3.00	0.223
	16	2.96	0.009	0.036	0.94	0.079	0.000	1.07	3.00	0.197
	17	2.84	0.007	0.159	0.85	0.062	0.001	1.24	3.00	0.249
	18a	2.88	0.012	0.121	0.82	0.071	0.000	1.23	3.00	0.200
	18b	2.88	0.013	0.117	0.80	0.070	0.000	1.23	3.00	0.200
	19	2.97	0.007	0.054	0.71	0.070	0.000	1.32	3.00	0.142
BC2B3	2	2.95	0.004	0.048	0.86	0.046	0.000	1.17	3.00	0.144
	3	2.90	0.006	0.063	1.22	0.033	0.000	0.85	3.00	0.122
	4	2.93	0.006	0.053	0.81	0.050	0.000	1.22	3.00	0.149
	5	2.94	0.006	0.056	0.80	0.050	0.002	1.22	3.00	0.146
	6	2.97	0.006	0.037	0.82	0.053	0.000	1.20	3.00	0.145
	7	2.97	0.005	0.035	0.91	0.051	0.000	1.11	3.00	0.159
	8	2.81	0.006	0.166	1.04	0.088	0.002	1.04	3.00	0.239
	9	2.92	0.006	0.098	0.78	0.049	0.001	1.28	3.00	0.193
	10	2.96	0.011	0.044	0.79	0.069	0.002	1.24	3.00	0.178
	11	2.96	0.008	0.044	0.81	0.070	0.001	1.19	3.00	0.220
	12	2.87	0.007	0.131	0.90	0.066	0.000	1.15	3.00	0.254
	13	2.96	0.011	0.053	0.79	0.077	0.000	1.24	3.00	0.195
	14	2.98	0.008	0.038	0.95	0.052	0.000	1.10	3.00	0.149
	15	2.95	0.006	0.043	0.84	0.048	0.002	1.19	3.00	0.165
	16	2.95	0.006	0.050	0.76	0.048	0.000	1.24	3.00	0.152
	17	2.91	0.008	0.061	0.84	0.044	0.000	1.21	3.00	0.144
BC2B4	2	2.95	0.003	0.047	0.88	0.016	0.000	1.17	3.00	0.092
	4	2.93	0.009	0.048	0.85	0.053	0.002	1.22	3.00	0.150
	5	3.00	0.005	0.050	0.82	0.055	0.000	1.23	3.00	0.160
	6	2.97	0.005	0.032	0.97	0.057	0.000	1.06	3.00	0.159
	7	2.96	0.010	0.036	0.92	0.044	0.000	1.13	3.00	0.146
	8	2.96	0.010	0.032	0.99	0.049	0.000	1.06	3.00	0.154
	9	2.84	0.006	0.139	0.98	0.071	0.000	1.12	3.00	0.213
	10	2.91	0.005	0.099	0.76	0.077	0.000	1.28	3.00	0.232
	11	2.92	0.011	0.064	0.78	0.063	0.001	1.23	3.00	0.166
	12	2.99	0.009	0.043	0.82	0.078	0.001	1.21	3.00	0.226
	13	2.97	0.007	0.048	0.83	0.090	0.001	1.18	3.00	0.206
	14	2.95	0.011	0.048	0.81	0.053	0.000	1.22	3.00	0.194
	15	2.98	0.010	0.046	0.87	0.067	0.000	1.17	3.00	0.179

Table 7.3. IR band areas and OH concentrations of zoned and granular garnets in sample 94ADK12.

Description*	Grain or Spot #	IR Band Area per cm	[OH] wt% H_2O†
granular	1	1706	0.1341
granular	2	1372	0.1078
granular	3	1492	0.1173
granular	4	1764	0.1387
granular	5	1810	0.1422
granular	6	1526	0.1200
granular	7	1752	0.1377
granular	8	1678	0.1319
granular	9	1822	0.1432
granular	10	1497	0.1177
granular	11	1319	0.1036
granular	12	1642	0.1291
granular	13	1567	0.1231
granular	14	1608	0.1264
granular	15	1758	0.1382
granular	16	1693	0.1330
granular	17	1761	0.1384
granular	18	1567	0.1232
granular	19	1696	0.1333
granular	20	1797	0.1412

Description*	Grain or Spot #	IR Band Area per cm	[OH] wt% H_2O
zoned	1.1	1941	0.1525
zoned	1.2	1197	0.0941
zoned	1.3	1482	0.1165
zoned	1.4	1188	0.0933
zoned	1.5	918	0.0722
zoned	1.6	1837	0.1444
zoned	1.7	1507	0.1184
zoned	2.1	1541	0.1211
zoned	2.2	1636	0.1286
zoned	2.3	1704	0.1339
zoned	2.4	1808	0.1421
zoned	2.5	1884	0.1481
zoned	2.6	1519	0.1194
zoned	2.7	744	0.0585
zoned	2.8	1824	0.1434
zoned	3.1	990	0.0778
zoned	3.2	1873	0.1472
zoned	3.3	1856	0.1459

*Granular = fine-grain recrystallized region of garnetite. Zoned = large, cm- sized euhedral garnets with visible compositional banding in garnetite.
†OH concentration determined using calibration of Rossman and Aines (1991).

Table 7.4. Band areas and OH concentrations for transect analyses of sample 94ADK11.

Transect A-A'.

Position (mm)	IR band area per cm thickness	[OH]* wt% H_2O
0.25	1290	0.1014
0.29	1290	0.1014
0.61	1390	0.1093
0.72	1200	0.0943
0.79	1370	0.1077
1.59	1650	0.1297
1.98	1670	0.1313
2.52	1660	0.1305
3.10	2000	0.1572
3.35	2050	0.1611
3.71	2020	0.1588
4.07	1900	0.1493
4.29	1740	0.1368
4.47	1660	0.1305
5.23	1760	0.1383
6.31	1740	0.1368

Transect B-B'.

Position (mm)	IR band area per cm thickness	[OH]* wt% H_2O
0.25	1340	0.1053
1.15	1280	0.1006
1.33	1510	0.1187
2.63	1800	0.1415

*OH concentration determined using calibration of Rossman and Aines (1991).

Table 7.5. Core depths, IR band areas, and OH concentrations of Willsboro Mine and Oak Hill Mine grossular-andradite garnets.

Willsboro Mine

Sample Number and Core Depth (feet, inches)	Meters (core depth)	Rock Type*	IR band area per cm thickness	[OH]† (wt% H_2O)
W77-102		Garnetite layer	753	0.0592
W48 304'		Garnetite layer		
99W-2‡		Ore	2369	0.1862
99W-2‡		Ore	2343	0.1842
W50-419		Garnetite layer	352	0.0277
99W-1‡		Ore	593	0.0466
99W-4‡		Ore	435	0.0342
99W-4‡		Ore	269	0.0211
W81-15 148'2"	45.16	Garnetite layer	304	0.0239
W81-15 148'2"	45.16	Garnetite layer	359	0.0282
W81-15 149'9"	45.64	Garnetite layer	358	0.0281
W81-15 149'9"	45.64	Garnetite layer	314	0.0247
W81-15 150'9"	45.95	Ore	303	0.0238
W81-15 150'9"	45.95	Ore	217	0.0171
W81-15 150'9"	45.95	Ore	341	0.0268
W81-15 321'	97.84	Ore	666	0.0524
W81-15 321'	97.84	Ore	620	0.0487
W81-15 321'	97.84	Ore	462	0.0363
W81-15 269'4"	82.09	Ore	124	0.0097
W81-15 269'10"	82.25	Ore	205	0.0161
W81-15 269'10"	82.25	Ore	209	0.0164
W81-15 270'5"	82.42	Garnetite layer	628	0.0494
W81-15 273'	83.21	Garnetite layer	622	0.0489
W81-15 276'2"	84.18	Garnetite layer	1608	0.1264
W81-15 276'2"	84.18	Garnetite layer	2060	0.1619
W81-15 276'5"	84.25	Garnetite layer	1422	0.1117
W81-15 278'5"	84.86	Garnetite layer	1136	0.0893
W81-15 282'5"	86.08	Ore	1100	0.0865
W81-15 282'5"	86.08	Ore	1067	0.0839
W81-15 285'	86.87	Ore	226	0.0177
W81-15 285'	86.87	Ore	325	0.0255

‡Samples from outcrop; all others from drill core.

Table 7.5 continued.

Willsboro Mine drill core W81-15

Sample Number and Core Depth (feet, inches)	Meters (core depth)	Rock Type*	IR band area per cm thickness	[OH]† (wt% H_2O)
W81-15 299'6"	91.29	Garnetite layer	1172	0.0922
W81-15 299'6"	91.29	Garnetite layer	1319	0.1037
W81-15 301'8"	91.95	Garnetite layer	956	0.0751
W81-15 301'8"	91.95	Garnetite layer	1019	0.0801
W81-15 304'	92.66	Ore	1849	0.1453
W81-15 304'	92.66	Ore	1480	0.1163
W81-15 307'	93.57	Garnetite layer	1482	0.1165
W81-15 311'	94.79	Ore	345	0.0271
W81-15 313'6"	95.55	Ore	423	0.0333
W81-15 313'6"	95.55	Ore	428	0.0336
W81-15 313'6"	95.55	Ore	387	0.0304
W81-15 314'	95.71	Ore	42	0.0033
W81-15 314'	95.71	Ore	51	0.0040
W81-15 318'7"	97.10	Ore	485	0.0381
W81-15 318'7"	97.10	Ore	530	0.0417
W81-15 328'6"	100.13	Ore	49	0.0039
W81-15 347'7"	105.94	Anorthosite	0	0.0000
W81-15 347'7"	105.94	Anorthosite	0	0.0000
W81-15 370'	112.78	Anorthosite	50	0.0039
W81-15 396'8"	120.90	Ore	374	0.0294
W81-15 396'8"	120.90	Ore	521	0.0410
W81-15 404'3"	123.22	Ore	1696	0.1333
W81-15 404'3"	123.22	Ore	1722	0.1353
W81-15 407'2"	124.10	Ore	2103	0.1653
W81-15 407'2"	124.10	Ore	2111	0.1659
W81-15 411'	125.27	Ore	487	0.0383
W81-15 411'	125.27	Ore	759	0.0597
W81-15 33_'0"	100.58	Ore	603	0.0474
W81-15 33_'0"	100.58	Ore	906	0.0712

*Ore = wo + gt + cpx; wo > (gt + cpx)
Garnetite layer = gt + cpx + wo; gt > (cpx + wo)
Anorthosite = plag + pyx + ilm + gt
gt = garnet; cpx = clinopyroxene; wo = wollastonite;
plag = plagioclase; scap = scapolite; qtz = quartz;
pyx = pyroxene; ilm = ilmenite
†OH concentration determined using Rossman and Aines (1991).

Table 7.5 continued.

Oak Hill Mine drill core OH98-16

Sample Number and Core Depth (feet, inches)	Meters (core depth)	Rock Type*	IR band area per cm thickness	[OH]† (wt% H_2O)
103'3"	31.47	Ore	617	0.0485
103'3"	31.47	Ore	895	0.0703
109'8"	33.43	Ore		
113'6"	34.59	Ore	203	0.0159
113'6"	34.59	Ore	229	0.0180
134'4"	40.94	Ore	851	0.0669
136'8" And.	41.66	Ore	990	0.0778
136'8" Gros.	41.66	Ore	788	0.0619
136'8" Gros.	41.66	Ore	1036	0.0814
138'10"	42.32	Ore	956	0.0751
139'9" gt	42.60	Garnetite layer	1016	0.0798
139'9" gt	42.60	Garnetite layer	1116	0.0877
139'9"	42.60	Ore	899	0.0707
139'9"	42.60	Ore	992	0.0780
140'7"	42.85	Garnetite layer	559	0.0439
140'7"	42.85	Garnetite layer	916	0.0720
140'7"	42.85	Garnetite layer	996	0.0783
144'2"	43.94	Garnetite layer	1784	0.1402
144'2"	43.94	Garnetite layer	1883	0.1480
144'6" And.	44.04	Ore	1495	0.1175
144'6" Gros.	44.04	Ore		
148'3"	45.19	Ore	1375	0.1081
148'3"	45.19	Ore	1368	0.1075
154'5"	47.07	Ore	90	0.0070
154'5"	47.07	Ore	143	0.0112
154'5"	47.07	Ore	138	0.0108
158'2"	48.21	Ore	150	0.0118
158'5"	48.29	Ore	300	0.0236
162'6"	49.53	Ore	592	0.0466
162'6"	49.53	Ore	1046	0.0822
167'8"	51.10	Ore	373	0.0293

Table 7.5 continued.

Oak Hill Mine drill core OH98-16

Sample Number and Core Depth (feet, inches)	Meters (core depth)	Rock Type*	IR band area per cm thickness	[OH]† (wt% H_2O)
167'8"	51.10	Ore	363	0.0285
171'6"	52.27	Garnetite layer	922	0.0725
174'9"	53.26	Ore	956	0.0751
174'9"	53.26	Ore	1011	0.0795
177'	53.95	Ore	197	0.0155
177'	53.95	Ore	181	0.0142
185'2"	56.44	Ore		
190	57.91	Ore	719	0.0565
194'6"	59.28	Ore	411	0.0323
194'6"	59.28	Ore	444	0.0349
200'3"	61.04	Ore	667	0.0524
205'9"	62.71	Garnetite layer	1054	0.0829
206'2"	62.84	Ore	1293	0.1016
210'6"	64.16	Ore	1059	0.0832
215'8"	65.74	Ore	1383	0.1087
218'8"	66.65	Massive garnetite	1160	0.0912
219'8"	66.95	Massive garnetite	1371	0.1077
219'8"	66.95	Massive garnetite	1234	0.0970
221'	67.36	Massive garnetite	1003	0.0789
226'	68.88	Massive garnetite	1090	0.0857
226'	68.88	Massive garnetite	1480	0.1163
230'6"	70.26	Ore		
238'3"	72.62	Massive garnetite	1846	0.1451
238'3"	72.62	Massive garnetite	1762	0.1385
238'8"	72.75	Massive garnetite	1508	0.1185
239'10"	73.10	Ore	281	0.0221
239'10"	73.10	Ore	450	0.0354
245'6"	74.83	Massive garnetite	1540	0.1210
245'6"	74.83	Massive garnetite	1548	0.1217
247'10"	75.54	Massive garnetite	1208	0.0950
247'10"	75.54	Massive garnetite	1455	0.1144
248'2"	75.64	Massive garnetite	643	0.0505
248'2"	75.64	Massive garnetite	1414	0.1111
248'2"	75.64	Massive garnetite	1454	0.1143
251'	76.50	Ore	776	0.0610
253'	77.11	Massive garnetite	880	0.0692

Table 7.5 continued.

Oak Hill Mine drill core OH98-16

Sample Number and Core Depth (feet, inches)	Meters (core depth)	Rock Type*	IR band area per cm thickness	[OH]† (wt% H_2O)
254'6"	77.57	Massive garnetite	1290	0.1014
254'6"	77.57	Massive garnetite	1426	0.1121
259'8"	79.15	Massive garnetite	1299	0.1021
259'11"	79.22	Massive garnetite	1405	0.1105
259'11"	79.22	Massive garnetite	1554	0.1221
261'1"	79.58	Massive garnetite	1163	0.0914
261'1"	79.58	Massive garnetite	1439	0.1131
267'	81.38	Massive garnetite	797	0.0626
267'	81.38	Massive garnetite	1384	0.1088
271'9"	82.83	Massive garnetite	1887	0.1483
271'9"	82.83	Massive garnetite	1896	0.1490
278'6"	84.89	Ore	1026	0.0806
278'6"	84.89	Ore	1243	0.0977
282'3"	86.03	Massive garnetite	1112	0.0874
282'3"	86.03	Massive garnetite	1156	0.0909
283'4"	86.36	Massive garnetite	1075	0.0845
285'6"	87.02	Massive garnetite	1001	0.0787
285'6"	87.02	Massive garnetite	1300	0.1022
287'2"	87.53	gt + plag/scap + cpx	499	0.0393
289'3"	88.16	plag/scap + gt + cpx	318	0.0250
289'3"	88.16	plag/scap + gt + cpx	585	0.0460

*Ore = wo + gt + cpx; wo > (gt + cpx)

Garnetite layer = gt + cpx + wo; gt > (cpx + wo)

Massive garnetite = gt +/- cpx, scap, plag, and qtz

gt = garnet; cpx = clinopyroxene; wo = wollastonite;

plag = plagioclase; scap = scapolite; qtz = quartz

†OH concentration determined using Rossman and Aines (1991).

Table 7.6. Electron microprobe analyses of Willsboro and Oak Hill garnets normalized to eight cations. Charge balance with oxygen was used to calculate Fe^{3+}/Fe^{2+}.

Willsboro Mine core W81-15 and additional samples

Sample	Ca	Mg	Mn	Ti	Fe^{2+}	Fe^{3+}	Cr	Al	Si	O
W77-102	2.86	0.03	0.02	0.03	0.08	0.4	0	1.61	2.96	12.04
W48-304'	2.82	0.02	0.02	0.03	0.14	0.38	0	1.64	2.96	12.07
99W-2	2.93	0.03	0.01	0.05	0.04	0.67	0	1.31	2.95	12.02
W50-419'	2.8	0.02	0.02	0.03	0.14	0.39	0	1.63	2.96	12.07
99W-1	2.87	0.02	0.01	0.03	0.1	0.59	0	1.41	2.97	12.05
99W-4	2.2	0.02	0	0.02	0.74	0.4	0	1.68	2.94	12.37
W81-15 149'9'	2.87	0.03	0	0.02	0.07	0.29	0	1.76	2.95	12.04
W81-15 150'9'	2.78	0.01	0.02	0.03	0.16	0.66	0	1.39	2.94	12.08
W81-15 221'	2.93	0.03	0.01	0.05	0.03	0.82	0	1.17	2.95	12.02
W81-15 269'4'	2.93	0.02	0.01	0.03	0.03	1.18	0	0.82	2.97	12.02
W81-15 269'10'	2.92	0.02	0.01	0.04	0.05	0.97	0	1.03	2.96	12.02
W81-15 270'5'	2.84	0.02	0.03	0.02	0.09	0.37	0	1.67	2.96	12.05
W81-15 273'	2.83	0.03	0.03	0.03	0.07	0.4	0	1.68	2.93	12.04
W81-15 276'2'	2.9	0.02	0.02	0.04	0.03	0.47	0	1.6	2.93	12.01
W81-15 276'5'	2.92	0.03	0.02	0.06	0.03	0.66	0	1.36	2.93	12.01
W81-15 282'5'	2.9	0.02	0.02	0.04	0.04	0.82	0	1.23	2.94	12.02

* Unpublished data from Cory Clechenko and John Valley, University of Wisconsin, Madison.

Table 7.6 continued.

Willsboro Mine core W81-15 and additional samples

Sample	Ca	Mg	Mn	Ti	Fe^{2+}	Fe^{3+}	Cr	Al	Si	O
W81-15 285'	2.98	0.02	0.01	0.03	0	1.54	0	0.54	2.95	11.99
W81-15 299'6'	2.83	0.02	0.02	0.02	0.12	0.39	0	1.62	2.97	12.06
W81-15 148'2'	2.86	0.02	0.01	0.03	0.09	0.56	0	1.48	2.95	12.04
W81-15 307'	2.9	0.03	0.02	0.03	0.02	0.56	0	1.49	2.94	12.01
W81-15 301'8'	2.93	0.02	0.01	0.04	0.03	1.07	0	0.93	2.96	12.02
W81-15 311'8'	2.97	0.01	0.01	0.02	0	1.42	0	0.63	2.96	12.01
W81-15 304'	2.93	0.03	0.01	0.05	0.05	0.74	0	1.23	2.96	12.02
W81-15 313'6'	2.95	0.02	0.01	0.03	0.02	1.34	0	0.67	2.96	12.01
W81-15 318'7'	2.95	0.02	0.01	0.06	0.02	1.13	0	0.86	2.94	12.01
W81-15 314'	2.96	0.01	0.01	0.01	0.02	1.53	0	0.48	2.98	12.01
W81-15 328'6'	2.97	0.01	0.01	0.02	0.02	1.51	0	0.48	2.99	12.01
W81-15 33_'0'	2.93	0.03	0.01	0.06	0.04	0.86	0	1.11	2.96	12.02
W81-15 347'7'	0.68	0.34	0.07	0	1.82	0.19	0	1.99	2.91	12.91
W81-15 370'	0.81	0.28	0.08	0.01	1.77	0.15	0	1.96	2.94	12.89
W81-15 396'8'	2.92	0.03	0.01	0.04	0.05	0.9	0	1.08	2.97	12.02
W81-15 404'3'	2.92	0.02	0.01	0.04	0.03	0.74	0	1.29	2.94	12.02
W81-15 407'2'	2.93	0.03	0.01	0.05	0.02	0.73	0	1.3	2.94	12.01

* Unpublished data from Cory Clechenko and John Valley, University of Wisconsin, Madison.

Table 7.6 continued.

Oak Hill Mine core 98-16

Sample	Ca	Mg	Mn	Ti	Fe^{2+}	Fe^{3+}	Cr	Al	Si	O
98-16 103'3'	2.84	0.03	0.03	0.05	0.13	0.39	0	1.56	2.98	12.00
98-16 109'8'	2.93	0.02	0.01	0.02	0.05	1.40	0.001	0.60	2.98	12.00
98-16 134'4'	2.91	0.02	0.01	0.05	0.08	0.84	0.002	1.12	2.97	12.00
98-16 136'8' Andr.	2.91	0.02	0.01	0.05	0.09	0.90	0	1.04	2.98	12.00
98-16 136'8' Gros.	2.86	0.01	0.02	0.04	0.12	0.61	0	1.38	2.97	12.00
98-16 138'10'	2.86	0.02	0.02	0.03	0.12	0.43	0.001	1.55	2.98	12.00
98-16 139'9' gt+cpx	2.82	0.02	0.02	0.03	0.15	0.49	0.001	1.50	2.98	12.00
98-16 139'9' ore	2.85	0.02	0.02	0.03	0.13	0.49	0.001	1.49	2.98	12.00
98-16 140'7'	2.86	0.02	0.02	0.02	0.12	0.44	0.001	1.55	2.99	12.00
98-16 144'2'	2.84	0.02	0.02	0.04	0.14	0.53	0.001	1.43	2.99	12.00
98-16 144'6' Andr.	2.89	0.02	0.01	0.04	0.09	0.79	0.002	1.18	2.98	12.00
98-16 144'6' Gros.	2.87	0.02	0.01	0.05	0.11	0.60	0.001	1.36	2.97	12.00
98-16 148'3'	2.90	0.03	0.01	0.04	0.07	0.85	0.001	1.12	2.97	12.00
98-16 154'5'	2.95	0.01	0.01	0.00	0.03	1.80	0.001	0.23	2.98	12.00
98-16 158'3'	2.95	0.01	0.01	0.02	0.03	1.59	0.001	0.42	2.98	12.00
98-16 162'6'	2.93	0.03	0.01	0.03	0.04	1.26	0.001	0.74	2.98	12.00
98-16 167'8'	2.95	0.02	0.01	0.03	0.03	1.50	0.002	0.49	2.98	12.00
98-16 171'6'	2.85	0.02	0.02	0.03	0.10	0.40	0.001	1.61	2.97	12.00
98-16 174'9'	2.78	0.02	0.03	0.02	0.17	0.45	0	1.54	2.98	12.00

* Unpublished data from Cory Clechenko and John Valley, University of Wisconsin, Madison.

Table 7.6 continued.

Oak Hill Mine core 98-16

Sample	Ca	Mg	Mn	Ti	Fe^{2+}	Fe^{3+}	Cr	Al	Si	O
98-16 177'0'	2.98	0.01	0.01	0.02	0.00	1.68	0.001	0.40	2.96	12.01
98-16 185'2'	2.94	0.01	0.01	0.01	0.04	1.68	0.002	0.33	2.99	12.00
98-16 190'0'	2.93	0.02	0.01	0.04	0.05	1.20	0.001	0.78	2.97	12.00
98-16 194'6'	2.94	0.03	0.01	0.03	0.02	1.18	0.001	0.82	2.97	12.00
98-16 200'3'	2.88	0.02	0.02	0.04	0.11	0.79	0.001	1.17	2.98	12.00
98-16 205'9'	2.90	0.02	0.02	0.06	0.08	0.72	0.002	1.24	2.97	12.00
98-16 206'2'	2.85	0.03	0.02	0.05	0.13	0.63	0	1.31	2.98	12.00
98-16 210'6'	2.87	0.03	0.02	0.05	0.11	0.69	0.002	1.27	2.97	12.00
98-16 215'8'	2.82	0.03	0.02	0.04	0.14	0.51	0	1.49	2.96	12.00
98-16 218'8'	2.84	0.02	0.03	0.03	0.12	0.49	0.001	1.50	2.97	12.00
98-16 219'4'	2.82	0.03	0.03	0.03	0.13	0.49	0.001	1.51	2.97	12.00
98-16 221'0'	2.88	0.02	0.02	0.03	0.07	0.47	0	1.53	2.97	12.00
98-16 226'0'	2.82	0.03	0.03	0.03	0.13	0.46	0.001	1.52	2.98	12.00
98-16 230'6'	2.82	0.02	0.02	0.03	0.16	0.40	0.001	1.56	2.99	12.00
98-16 238'3'	2.85	0.02	0.02	0.03	0.12	0.49	0.001	1.49	2.98	12.00
98-16 238'8'	2.83	0.03	0.02	0.03	0.12	0.50	0.002	1.50	2.97	12.00
98-16 239'10'	2.89	0.01	0.02	0.01	0.07	0.39	0	1.63	2.99	12.00
98-16 245'6'	2.84	0.03	0.02	0.03	0.12	0.52	0	1.47	2.98	12.00

* Unpublished data from Cory Clechenko and John Valley, University of Wisconsin, Madison.

Table 7.6 continued.

Oak Hill Mine core 98-16

Sample	Ca	Mg	Mn	Ti	Fe^{2+}	Fe^{3+}	Cr	Al	Si	O
98-16 247'10'	2.85	0.03	0.02	0.03	0.11	0.44	0.001	1.56	2.98	12.00
98-16 248'2'	2.85	0.02	0.02	0.03	0.12	0.44	0	1.55	2.98	12.00
98-16 251'0'	2.86	0.02	0.02	0.03	0.11	0.40	0	1.58	2.98	12.00
98-16 253'0'	2.83	0.03	0.02	0.03	0.12	0.39	0.001	1.61	2.97	12.00
98-16 254'6'	2.86	0.02	0.02	0.02	0.09	0.46	0.002	1.56	2.97	12.00
98-16 259'8'	2.81	0.02	0.03	0.03	0.16	0.41	0.001	1.56	2.98	12.00
98-16 259'11'	2.82	0.02	0.03	0.03	0.15	0.40	0.001	1.58	2.99	12.00
98-16 261'1'	2.83	0.03	0.03	0.03	0.13	0.41	0.001	1.57	2.98	12.00
98-16 267'0'	2.83	0.03	0.03	0.03	0.13	0.42	0.001	1.56	2.98	12.00
98-16 271'9'	2.81	0.02	0.03	0.03	0.16	0.39	0	1.57	2.99	12.00
98-16 278'6'	2.86	0.03	0.02	0.03	0.08	0.52	0.001	1.49	2.97	12.00
98-16 282'3'	2.86	0.02	0.03	0.02	0.09	0.44	0.002	1.58	2.97	12.00
98-16 283'4'	2.82	0.02	0.02	0.03	0.13	0.40	0.001	1.61	2.97	12.00
98-16 285'6'	2.84	0.02	0.02	0.03	0.11	0.41	0.001	1.60	2.97	12.00
98-16 287'2'	2.85	0.04	0.02	0.02	0.09	0.27	0.001	1.73	2.98	12.00

* Unpublished data from Cory Clechenko and John Valley, University of Wisconsin, Madison.

Figure 7.1. Transects of OH, Ti, and Fe^{3+} concentrations from core to rim of grossular-andradite crystal BC2B1.

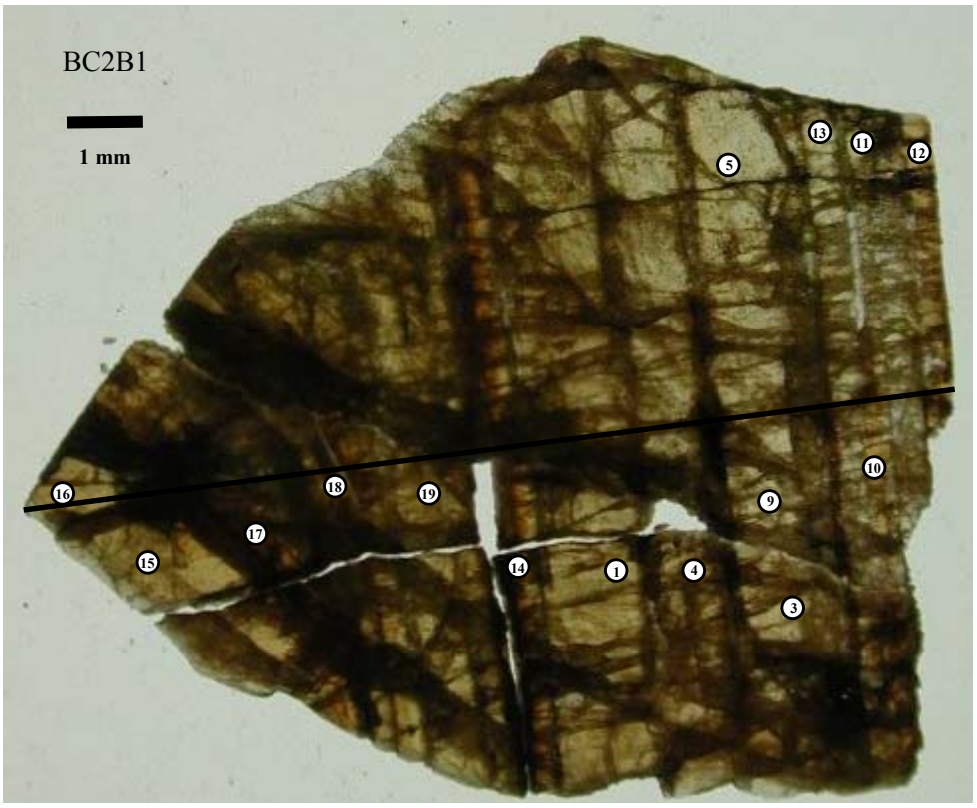

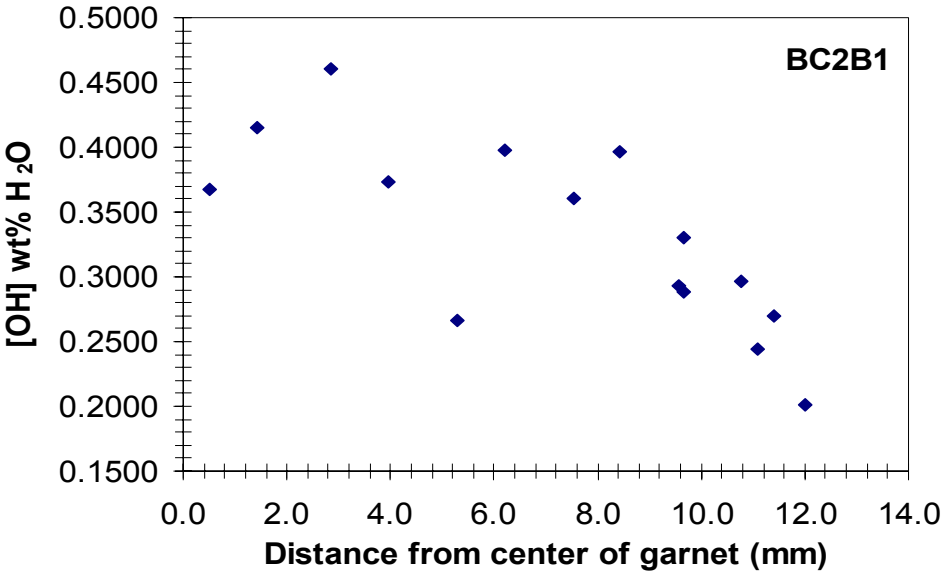

Figure 7.1 continued.

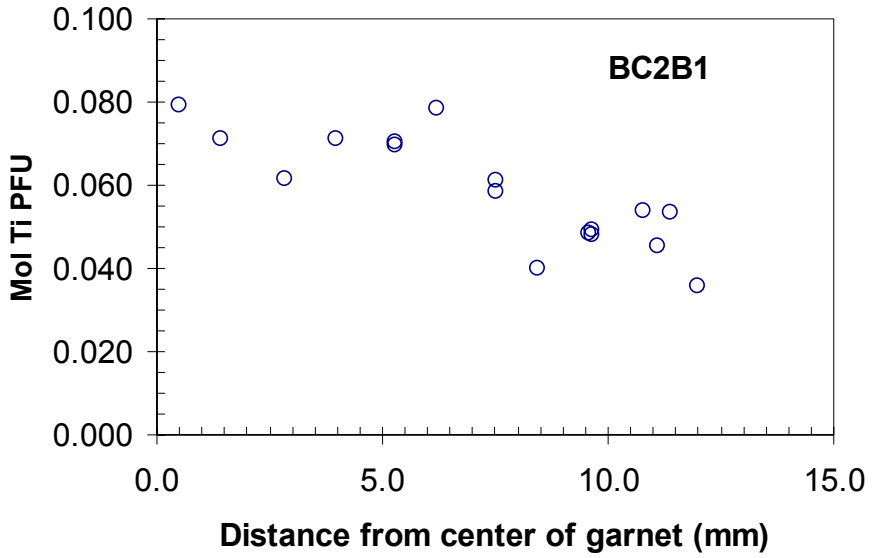

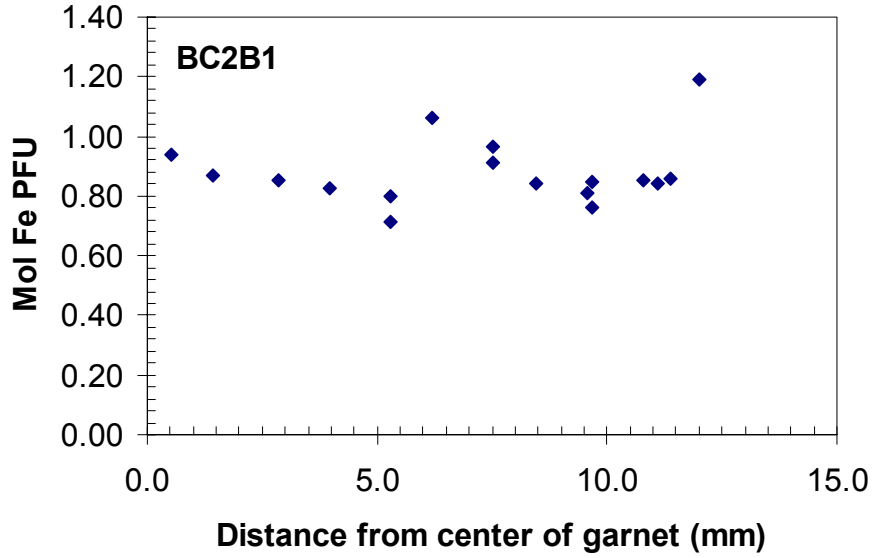

Figure 7.2. Transect of OH, Ti, and Fe^{3+} concentrations from core to rim of grossular-andradite crystal BC2B3.

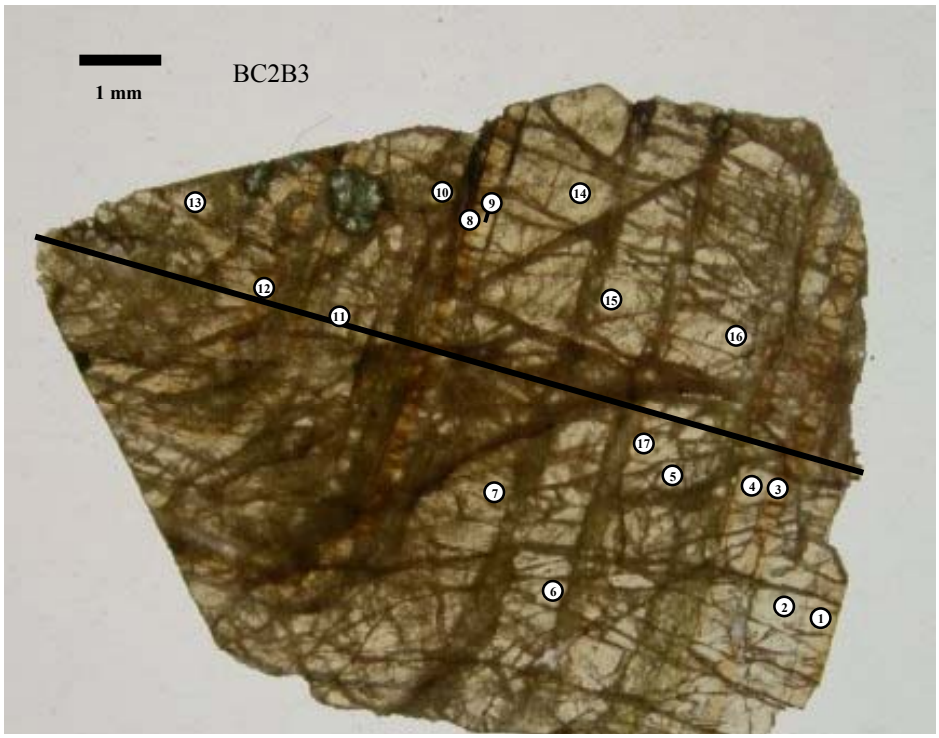

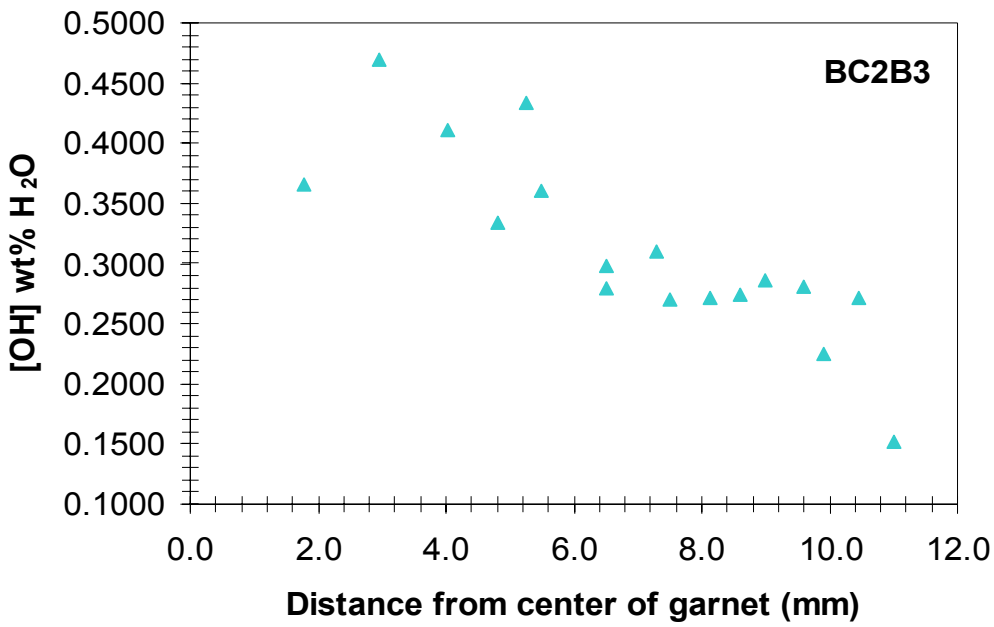

Figure 7.2 continued.

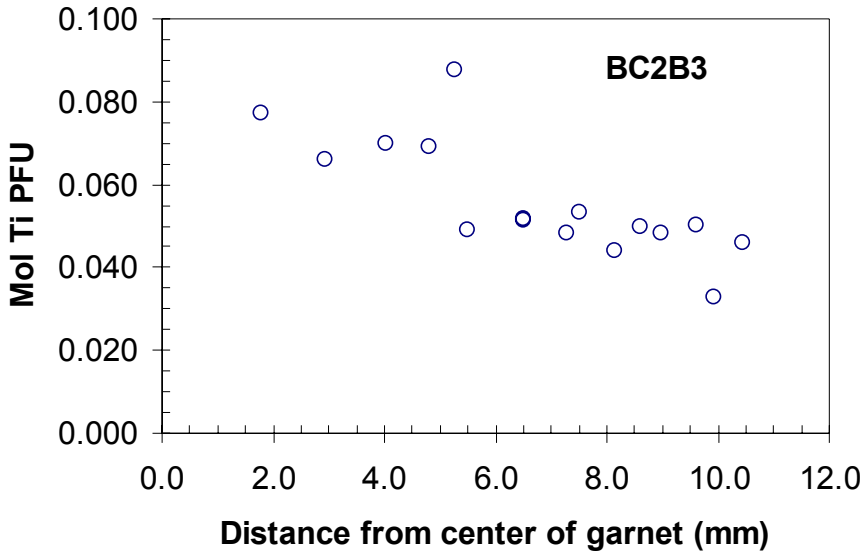

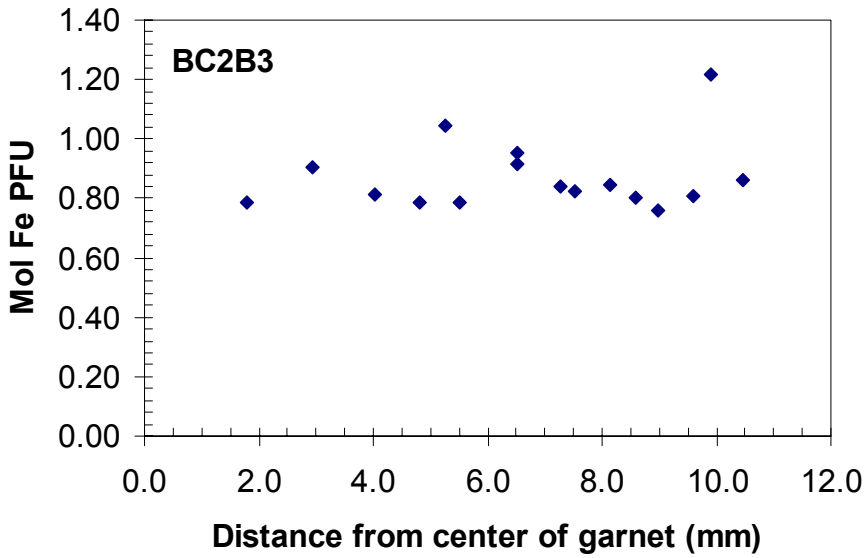

Figure 7.3. Transect of OH, Ti, and Fe^{3+} concentrations from core to rim of grossular-andradite crystal BC2B4.

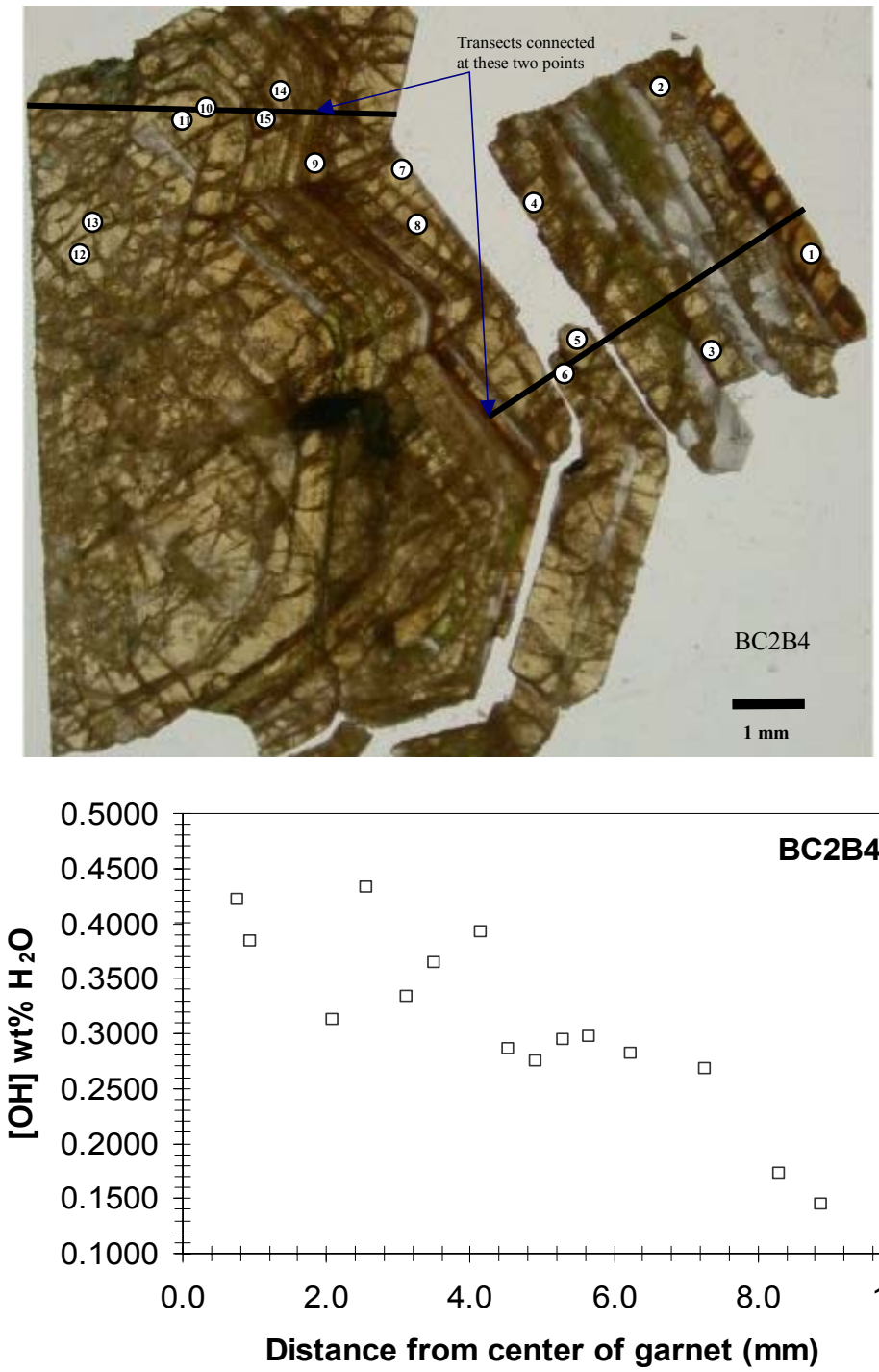

Figure 7.3 continued.

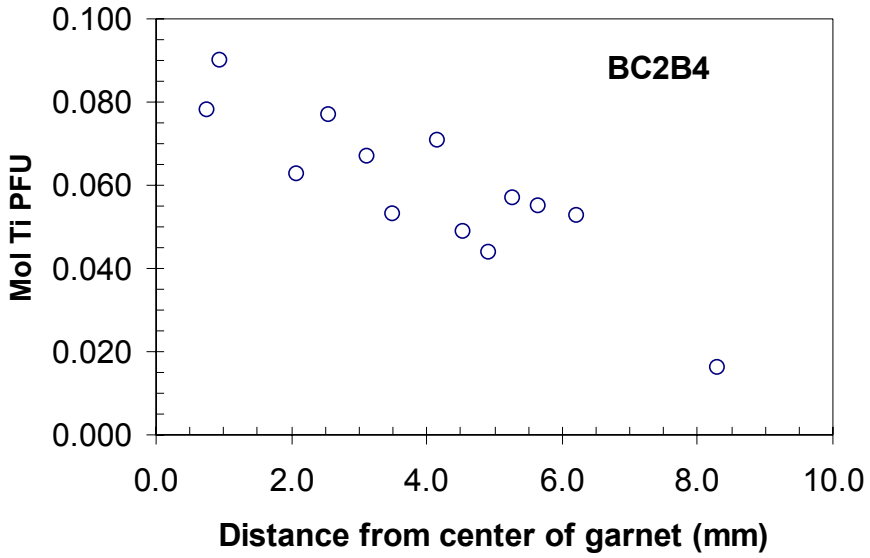

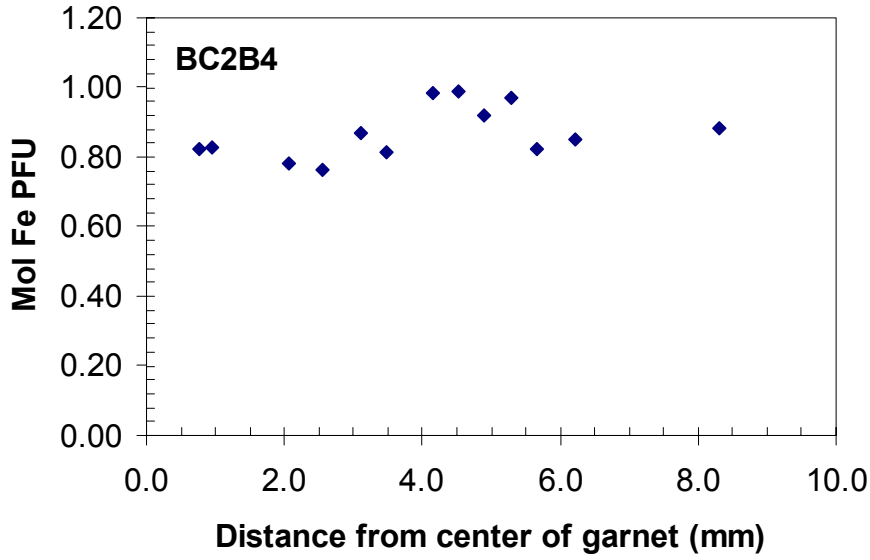

Figure 7.4. Representative mid-IR spectra of OH in sample BC2B3.

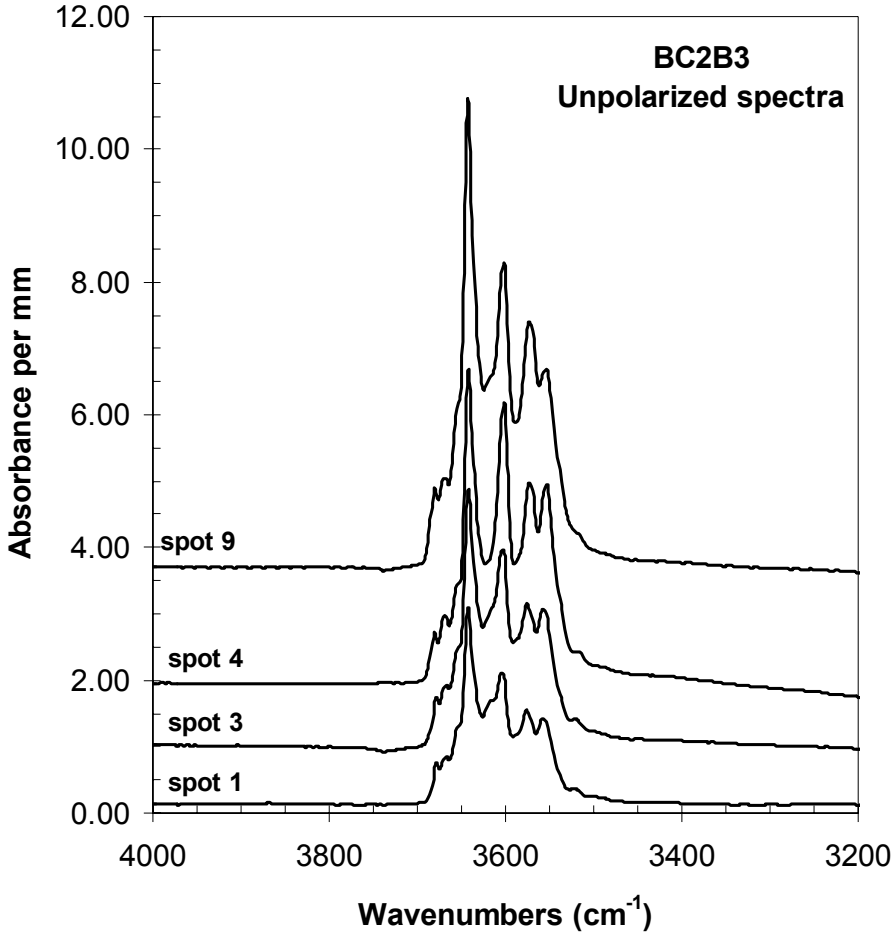

Figure 7.5. Moles of OH per formula unit garnet versus moles of a) Ti, b) Fe^{3+}, c) Mn, d) Mg, and e) Al per formula unit of garnet.

Figure 7.5A.

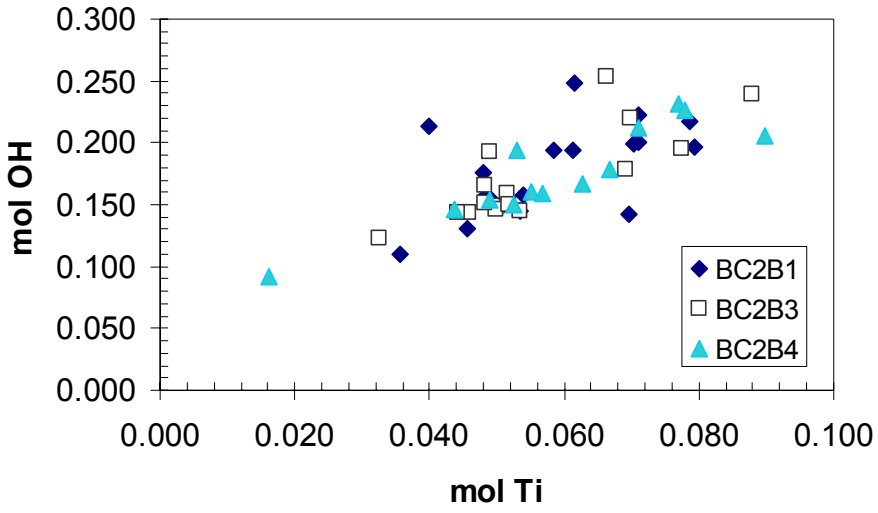

Figure 7.5B.

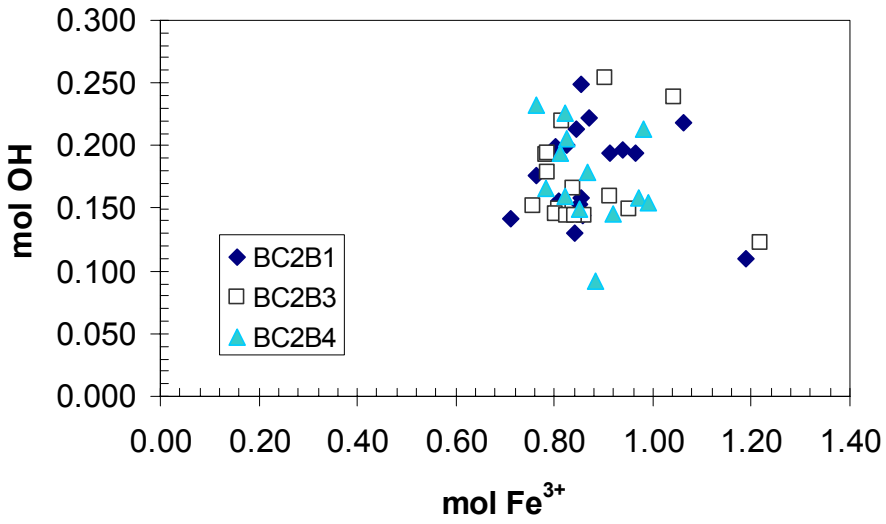

Figure 7.5C.

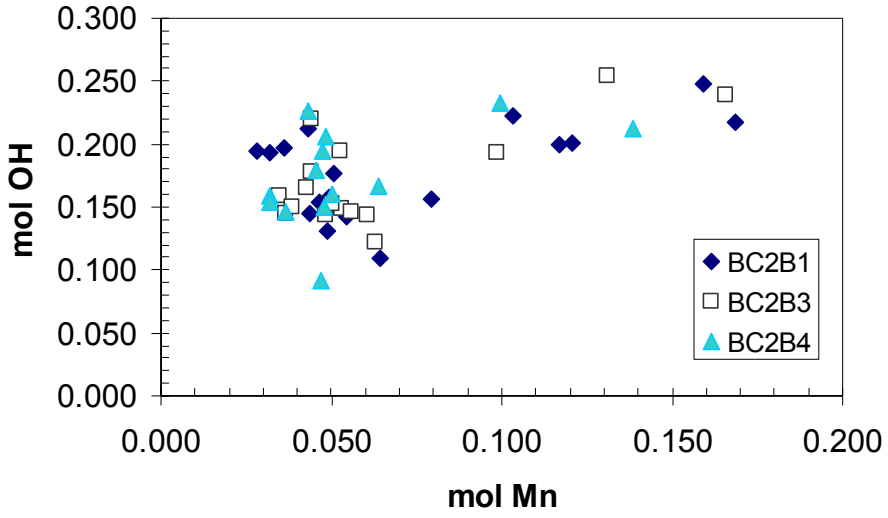

Figure 7.5D.

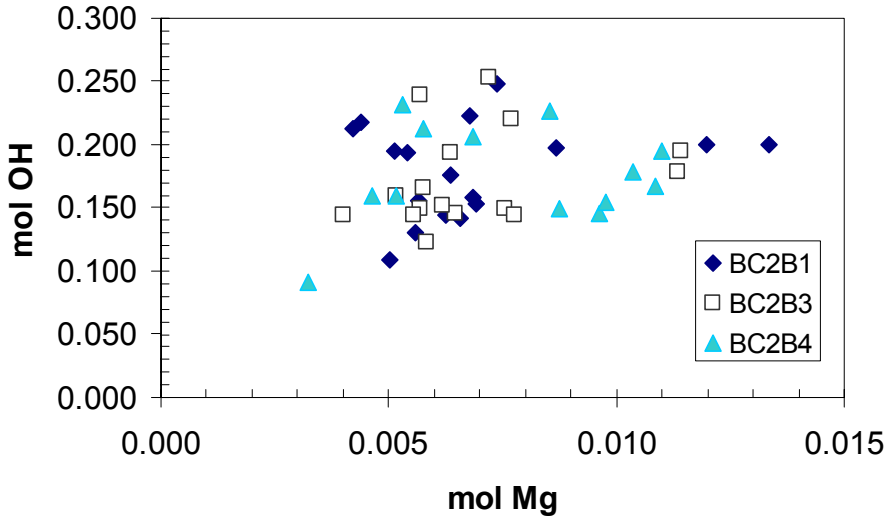

Figure 7.5E.

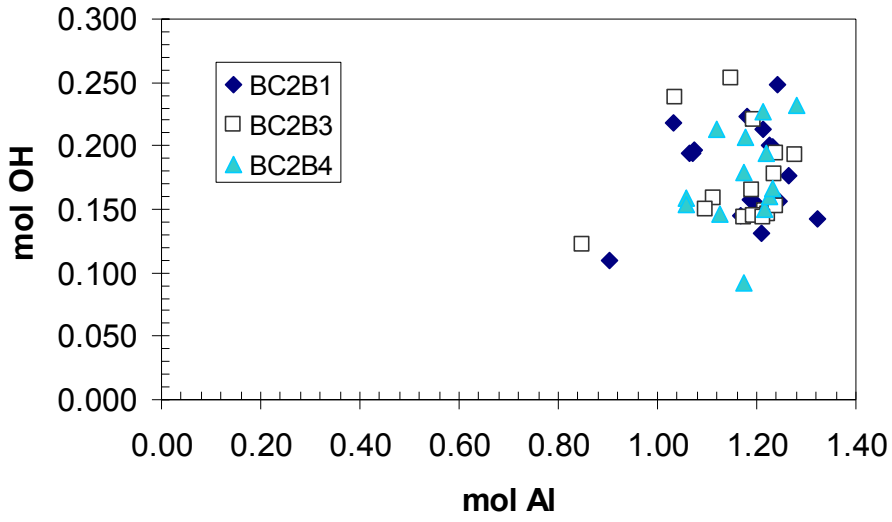
0.300
0.250
0.200
0.150
0.100
0.050
0.000
mol OH
BC2B1
BC2B3
BC2B4
0.00
0.20
0.40
0.60
0.80
1.00
1.20
1.40
mol Al

Figure 7.6. OH concentrations of zoned garnets and granular garnets from garnetite sample 94ADK12.

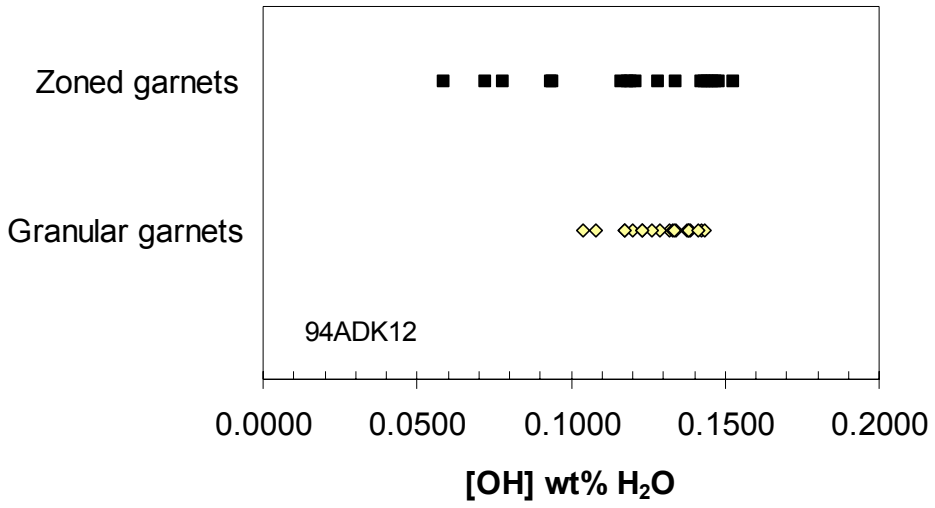

Figure 7.7. Transects of OH concentration across a zoned garnet and a fracture zone in garnetite sample 94ADK11.

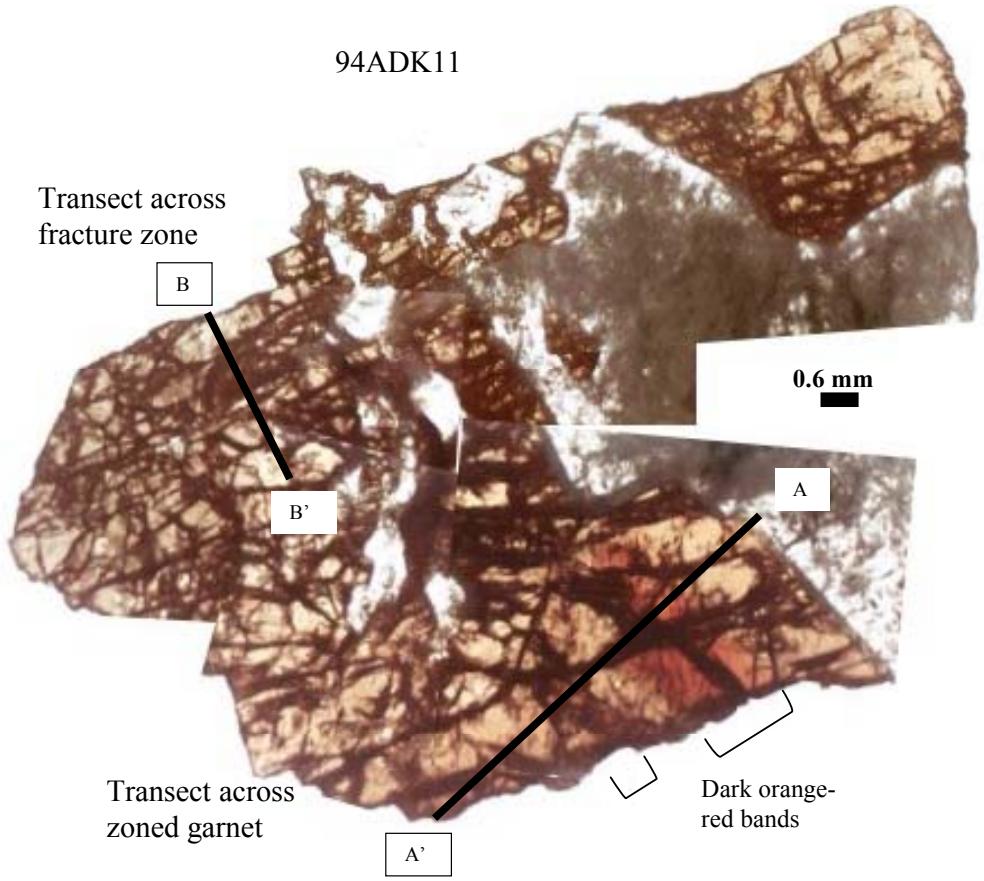

Figure 7.7 continued.

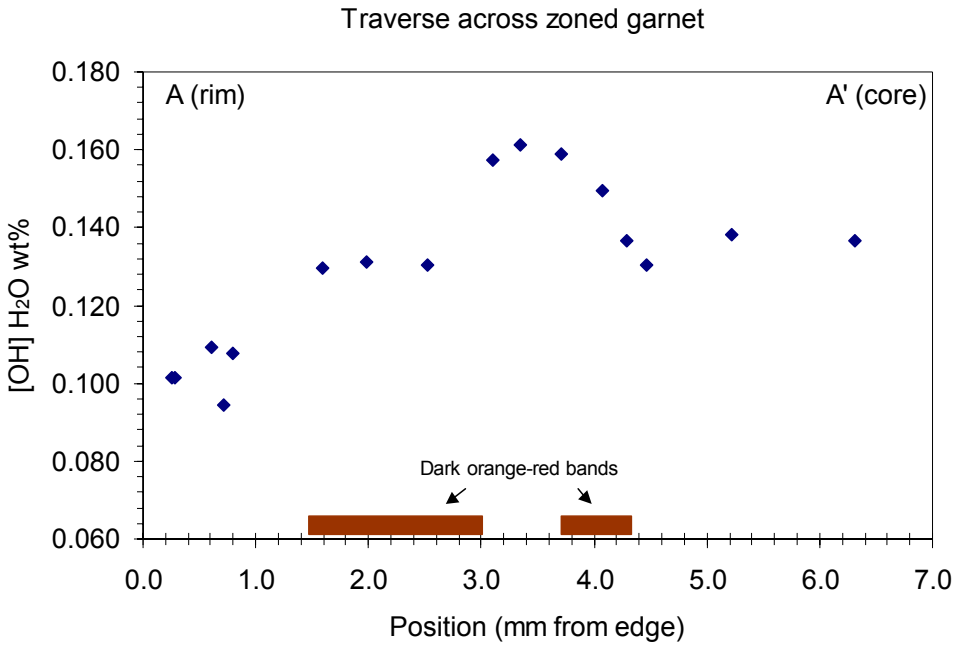

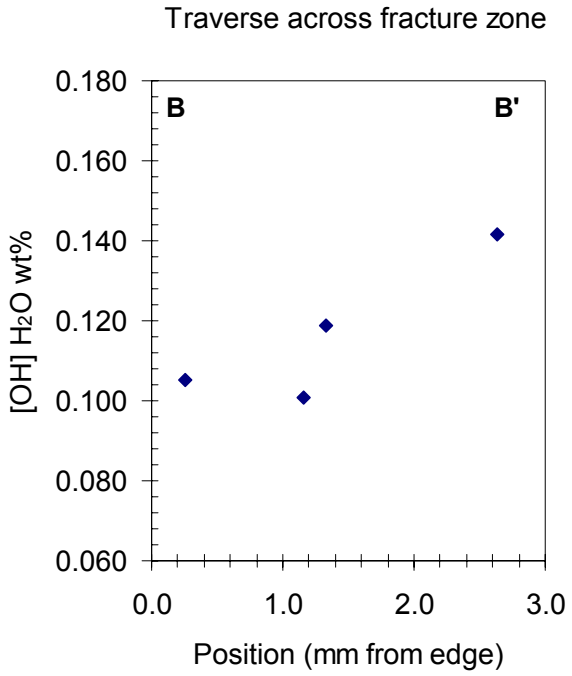

Figure 7.8. Representative mid-IR spectra of grossular andradite garnets from the Oak Hill Mine, Adirondack Mountains, New York.

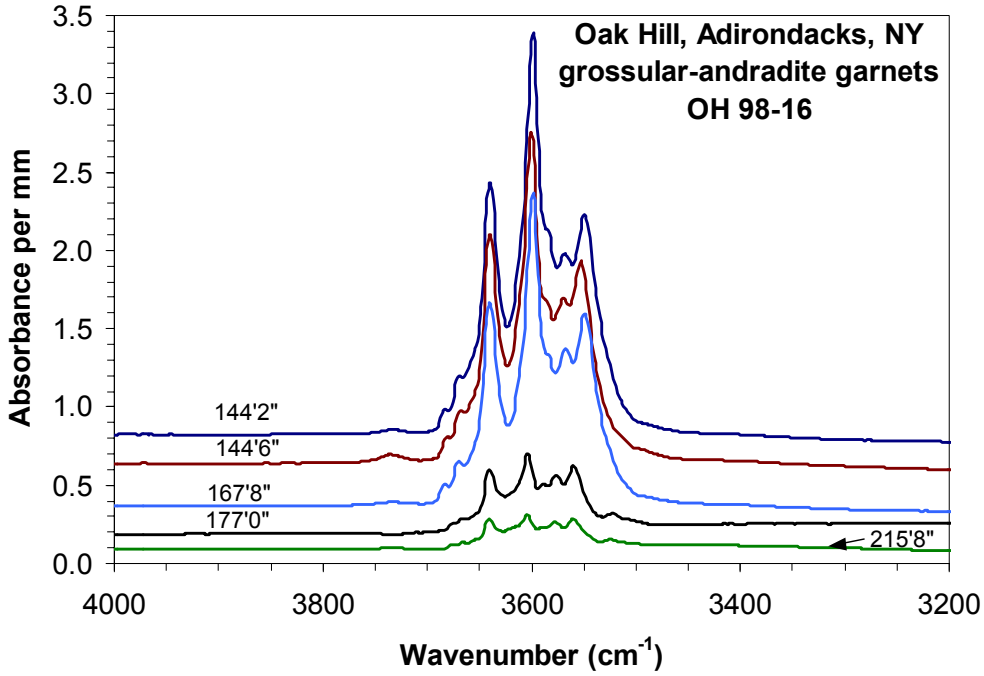

Figure 7.9. Garnet OH concentration versus depth for the Willsboro Mine drill core 81-15. The main anorthosite contact is located at approximately 130 meters depth.

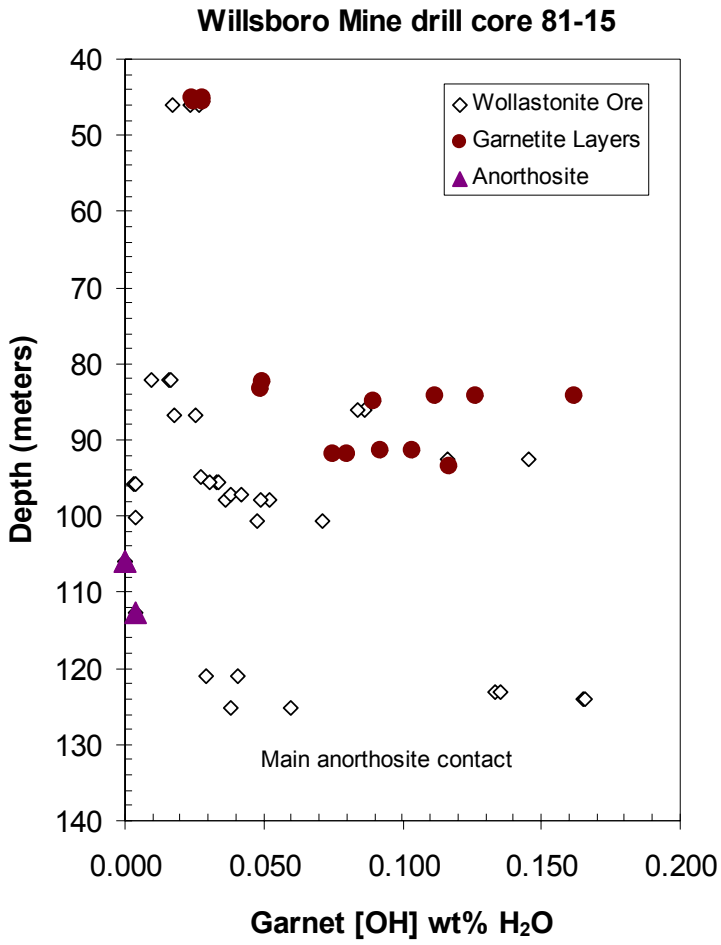

Figure 7.10. Garnet OH concentration versus depth for the Oak Hill Mine drill core 98-16. The main anorthosite contact is located at approximately 90 meters depth.

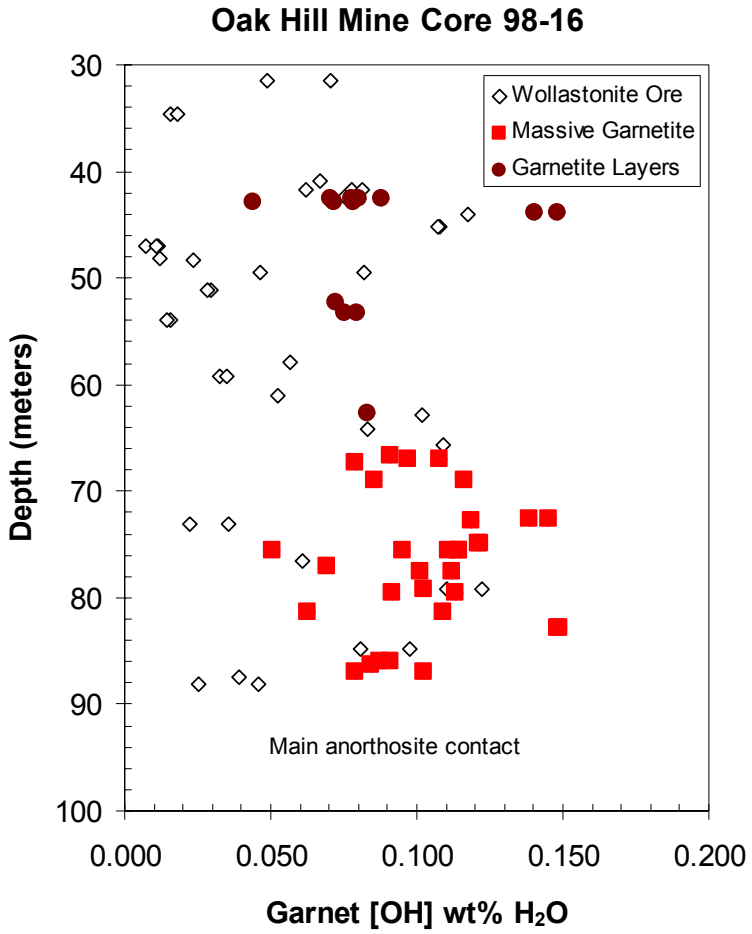

Figure 7.11. Garnet OH concentration versus moles of a) Fe^{2+}, b) Fe^{3+}, c) Ti, and d) Mn per formula unit for samples from the Willsboro Mine, New York.

Figure 7.11A.

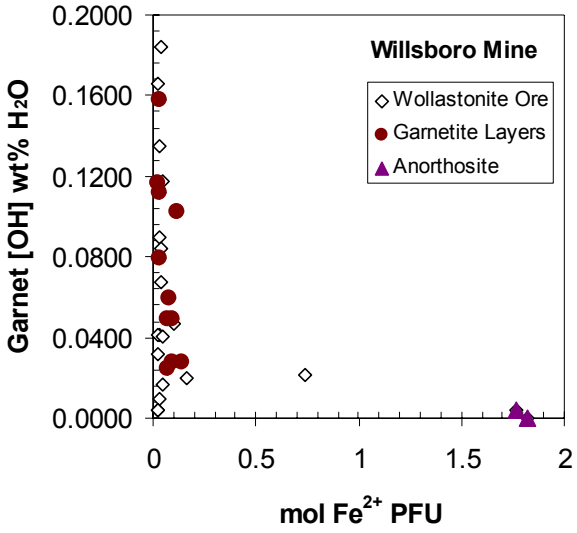

Figure 7.11B.

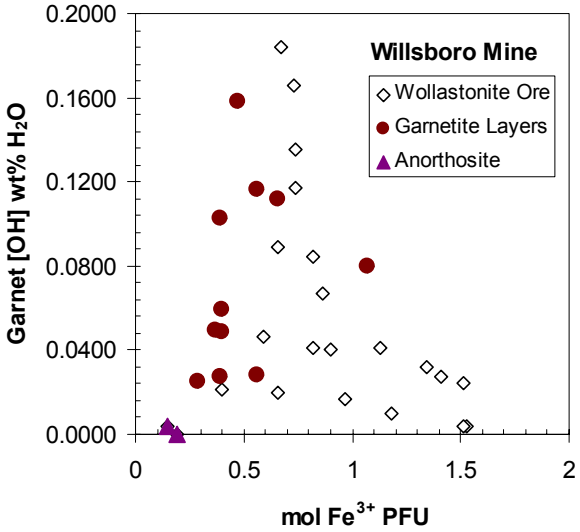

Figure 7.11C.

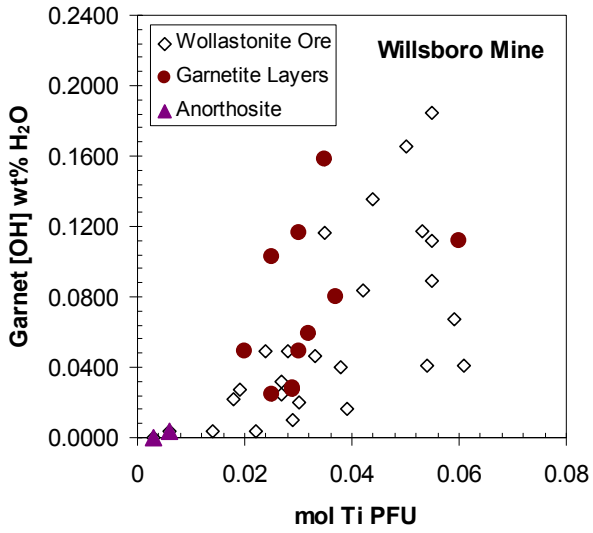

Figure 7.11D.

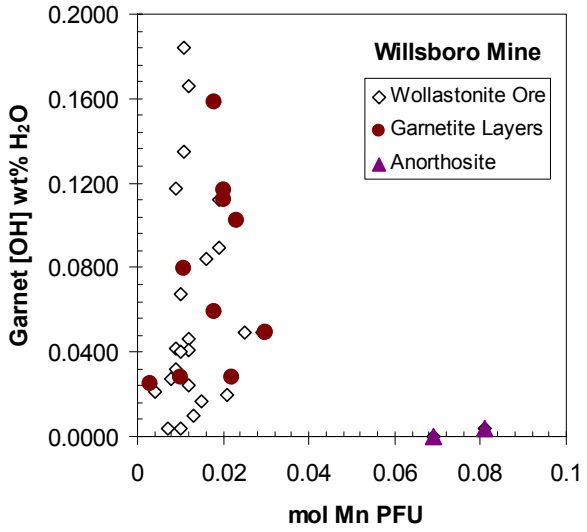

Figure 7.12. Garnet OH concentration versus moles of a) Fe^{2+}, b) Fe^{3+}, c) Ti, and d) Mn per formula unit for samples from the Oak Hill Mine, New York.

Figure 7.12A.

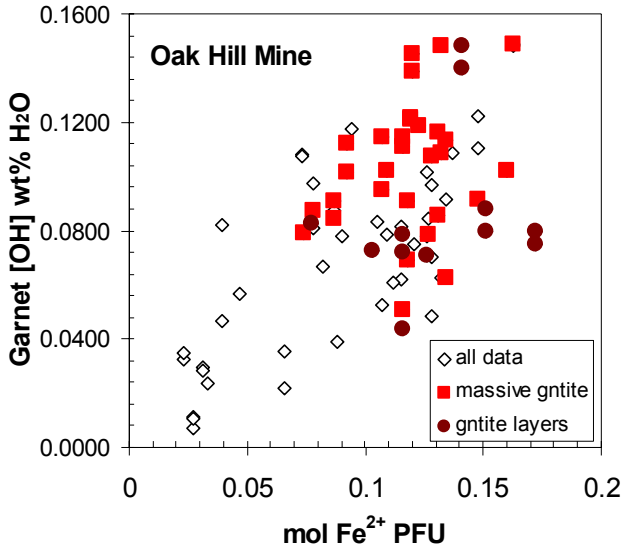

Figure 7.12B.

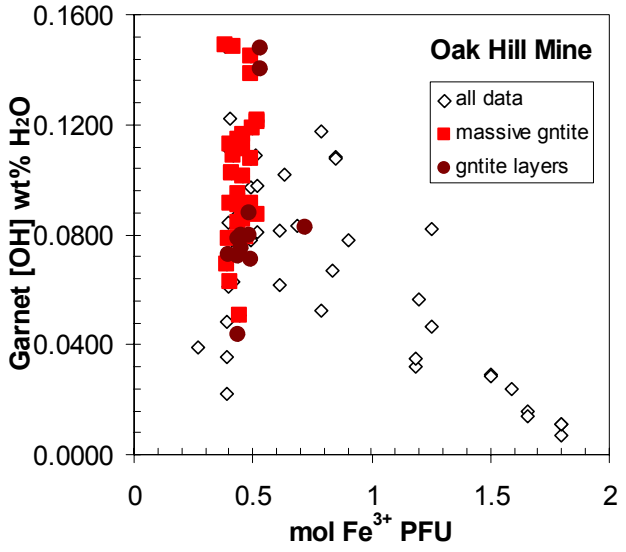

Figure 7.12C.

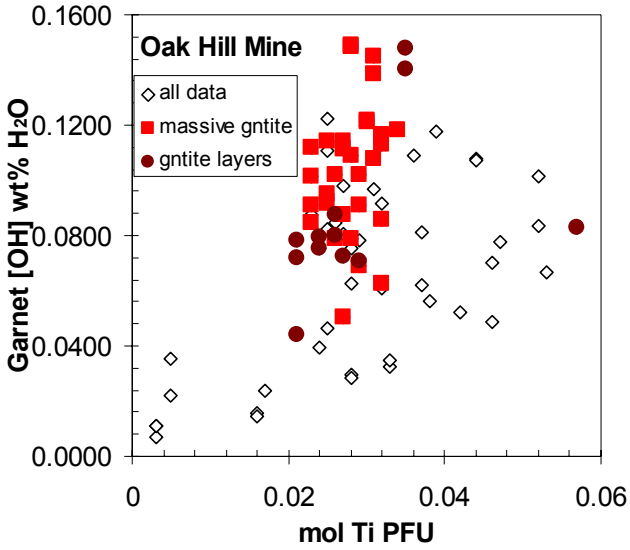

Figure 7.12D.

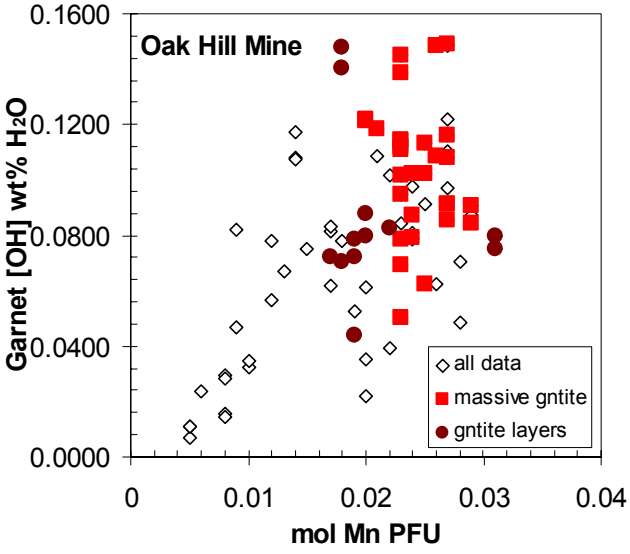

Appendix 1

A COMPARISON OF THE INFRARED SPECTRA OF OH IN LOW ALBITE AND REEDMERGNERITE, $NaBSi_3O_8$

Introduction

The mineral reedmergnerite was discovered in drill cores of the dolomitic oil shales of the Green River formation, Utah (Milton et al. 1960). Reedmergnerite is also found in pegmatites associated with subalkaline granitioids in the Dara-I-Pioz basin, Tien Shan Mountains, Tajikistan (Grew et al. 1993).

Reedmergnerite is triclinic, and it is isostructural with low albite (Milton et al. 1960; Appleman and Clark 1965). The B in reedmergnerite, and the Al in low albite, are completely ordered into the $T_1(0)$ tetrahedral site (Appleman and Clark 1965). The Na in reedmergnerite is bonded to the same five oxygen atoms as in low albite (Downs et al. 1996; Downs et al. 1999). The O_{co} oxygen is the most underbonded oxygen in the reedmergnerite and low albite structures, since it is a bridging oxygen between the $T_1(0)$ (Al) and T_{2m} (Si) tetrahedra, and, of the four Al-coordinating oxygens, it is the farthest distance

away from the Na (Downs et al. 1994). Therefore, the O_{co} oxygen is the most likely place for protonation in low albite and reedmergnerite (Downs et al. 1994). The OH spectra of low albite and reedmergnerite should be very similar if this line of reasoning is correct. Since the location of OH substitution into the low albite structure is unknown, the IR spectra of reedmergnerite provide a basis for comparison of the structural OH in these minerals.

Methods

A single, euhedral crystal of reedmergnerite from Utah (GRR188), approximately 0.5 mm × 0.5 mm × 2 mm, was removed from the oil shale host rock and cleaned in ethanol. The reedmergnerite crystals from Utah have several well-developed faces, including (001) and (110) (Milton et al. 1960). Polarized infrared spectra with E||**X'** and E||**Y'** (**X'** and **Y'** are the projections of two principal optical directions onto (001); in reedmergnerite these are only a few degrees away from **X** and **Y**) were obtained on {001} (Milton et al. 1960). The reedmergnerite from Tajikistan (GRR1761) is salmon-pink and forms aggregates of platy crystals up to several millimeters across with pronounced {001} cleavage. Infrared spectra with E||**X'** and E||**Y'** were obtained on a transparent crystal.

Polarized infrared spectra were obtained between 2300 and 4000 cm^{-1} on a Nicolet Magna 860 FTIR spectrometer at 4 cm^{-1} resolution, using a KBr beamsplitter, Au wire grid on AgBr polarizer, and MCT-A detector. Each spectrum was averaged over 512 scans. For sample GRR1761, spectra were taken in the main spectrometer compartment with a 1 mm circular aperture. Infrared spectra were also obtained at 77 K for this sample using a homebuilt vacuum chamber. Spectra of sample GRR188 were collected on a Spectra-Tech Continuμm® microscope accessory using a square aperture 100-50 μm in width.

Results and Discussion

The polarized IR spectra of the reedmergnerite from Utah are plotted in Figure 1A.1. Three main features are present in these spectra. There are two narrow bands at 3680 cm^{-1} and 3660 cm^{-1} that are essentially isotropic. These closely resemble the OH stretch bands of amphiboles (Ernst and Wai 1970). Magnesioriebeckite is commonly found in the host rock, and these infrared bands are likely due to inclusions of amphibole within the reedmergnerite. A second, broader band at 3140 cm^{-1} absorbs strongly with E||**Y'** but is considerably less intense with E||**X'**. Finally, there is a set of anisotropic bands in the 2800-3000 cm^{-1} region. The room-temperature and low-

temperature spectra of the sample from Tajikistan (Figure 1A.2) also contain a set of bands at 2800-3000 cm^{-1}. These are likely due to hydrocarbons present in inclusions within the mineral or as surface contamination. The broad, anisotropic band at 3450 cm^{-1} that shifts to two intense broad bands at 3100-3200 cm^{-1} (Figure 1A.2) is due to fluid inclusion water that freezes to ice upon cooling. There are also three narrow, anisotropic bands (the most prominent of which is at 3620 cm^{-1} in **X'**) that sharpen and intensify at 77 K in the Tajikistan spectra (Figure 1A.2).

Polarized spectra of a low albite from a Brazilian pegmatite are shown in Figure 1A.3. There is a broad, asymmetric band at 3060 cm^{-1} with **Y**>**X**, a narrow band at 3500 cm^{-1} with **X**>**Y**, and a large number of weak but narrow bands that appear only in the low-temperature spectra. The hydrous species responsible for these bands are not conclusively identified, but both the narrow and broad bands described here are assigned to OH groups, based on near-IR and ^{1}H NMR data (Chapter 2).

The interpretation of the infrared spectra of the two reedmergnerite samples is not straightforward. Disregarding the bands due to mineral inclusions, hydrocarbons, and fluid inclusions in Figures 1A.1 and 1A.2, only the broad band at 3140 cm^{-1} in GRR188 and the narrow bands (e.g., 3620 cm^{-1}) in GRR1766 remain unidentified. The first unidentified band is similar in width

and position to the albite OH band at 3060 cm^{-1}, and is also polarized with **Y'>X'**. The second set of unidentified bands have similar intensities and widths as the bands seen in the low-temperature spectra of low albite, and indeed there is a band at 3620 cm^{-1} in the **X** spectrum of low albite. The presence of multiple OH bands in the reedmergnerite and low albite spectra is not consistent with the theory that there is a single possible site for protonation in low albite and reedmergnerite. It is possible that other underbonded oxygens in these structures may also be protonated, producing multiple OH bands. The difference between spectra of the two reedmergnerite samples may be due to the differences in the environment in which the two samples formed.

The average B-O bond distance in reedmergnerite (1.465 Å) is much shorter than the average Al-O distance in low albite (1.744 Å) (Ribbe et al. 1962; Appleman and Clark 1965). Replacing the Al with B in the $T_1(0)$ site while holding the rest of the structure constant would lengthen the O-H···O distance of a hydroxyl bonded to that tetrahedra and increase the OH stretch frequency. Using the correlations of Nakamoto et al. (1955) and Libowitzky and Rossman (1997), the difference between the 3060 cm^{-1} low albite band and the 3140 cm^{-1} reedmergnerite band corresponds to a change in O-H···O distance of 0.022 Å. The energy difference between the 3500 cm^{-1} low albite band and the band at 3620 cm^{-1} corresponds to a lengthening of O-H···O by at least

0.205 Å. This is close to the difference between Al-O and B-O bond lengths (0.279 Å). The bands at 3500 cm^{-1} and 3620 cm^{-1} in the Tajikistan reedmergnerite and low albite spectra are therefore the best candidates for OH bands that are due to protonation of an oxygen (presumably O_{co}) that is bonded to Al and B, respectively. The 3620 cm^{-1} band may be present in the low albite spectra because minor amounts of B were incorporated into the structure during growth in the volatile-rich pegmatite environment.

Figure 1A.1. Polarized infrared spectra of reedmergnerite from the Green River formation oil shale, Utah.

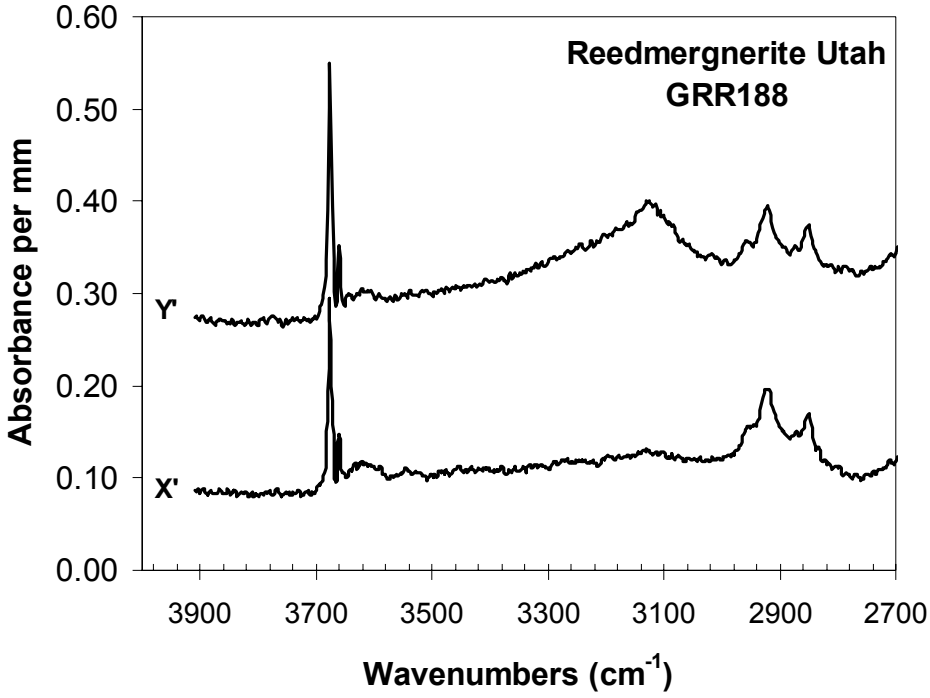

Figure 1A.2. Polarized infrared spectra of reedmergnerite (298K and 77K) from a pegmatite, Dara-I-Pioz, Tajikistan.

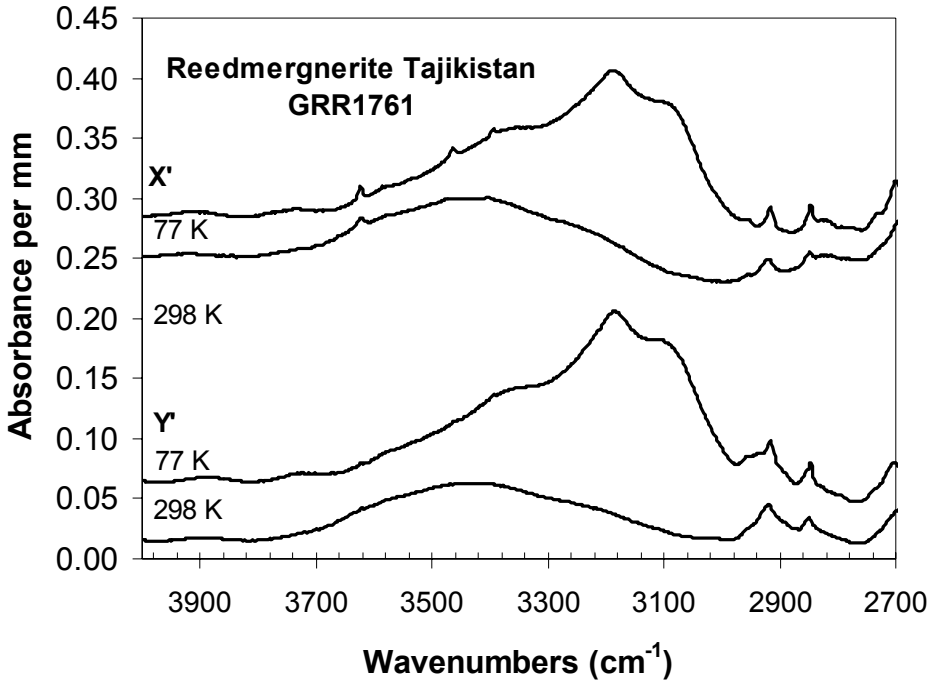

Figure 1A.3. Polarized infrared spectra of low albite from a pegmatite, Brazil (298 K and 77 K).

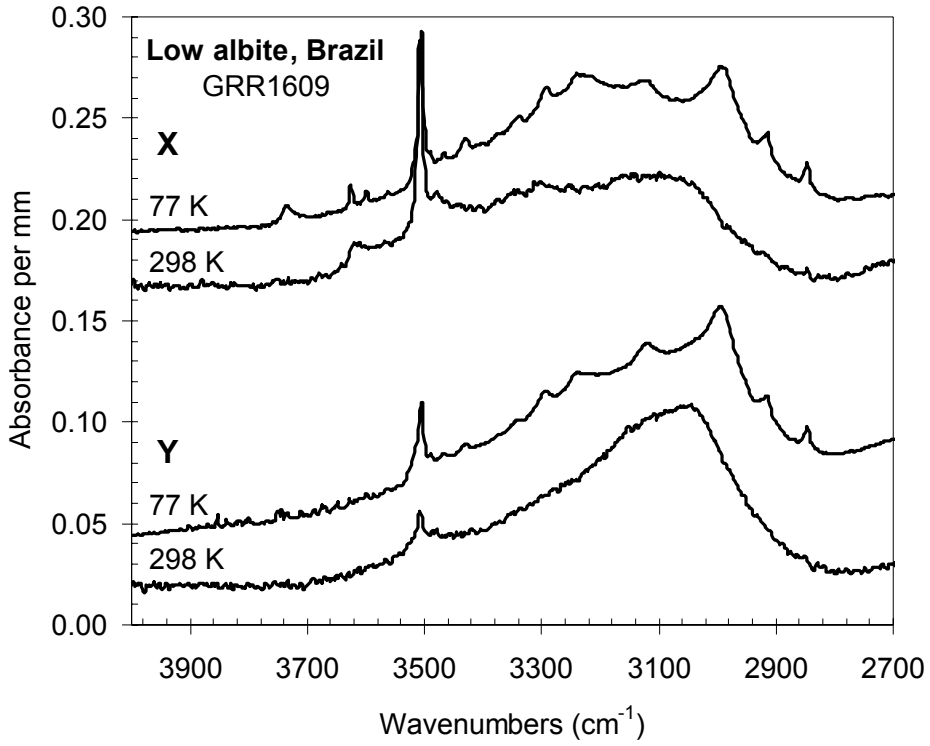

BIBLIOGRAPHY

Addison, C.C., Addison, W.E., Neal, G.H., and Sharp, J.H. (1962) Amphiboles: Part I. The oxidation of crocidolite. Journal of the Chemical Society, 1962, 1468-1471.

Aines, R.D., and Rossman, G.R. (1984) Water in minerals? A peak in the infrared. Journal of Geophysical Research, 89(B6), 4059-4071.

Aines, R.D., and Rossman, G.R. (1984) The hydrous component in garnets: pyralspites. American Mineralogist, 69, 1116-1126.

Aines, R.D., and Rossman, G.R. (1985) The high temperature behavior of trace hydrous components in silicate minerals. American Mineralogist, 70, 1169-1179.

Alcock, J., and Muller, P. (1999) Very high temperature, moderate pressure metamorphism in the New Russia gneiss complex, northeastern Adirondack Highlands, metamorphic aureole to the Marcy anothosite. Canadian Journal of Earth Sciences, 36, 1-13.

Amthauer, G., and Rossman, G.R. (1998) The hydrous component in andradite garnet. American Mineralogist, 83, 835-840.

Anderson, T.F. (1969) Self-diffusion of carbon and oxygen in calcite by isotope exchange with carbon dioxide. Journal of Geophysical Research, 74, 3918-3932.

Appleman, D.E., and Clark, J.R. (1965) Crystal structure of reedmergnerite, a boron albite, and its relation to feldspar crystal chemistry. American Mineralogist, 50, 1827-1850.

Armstrong, J.T. (1988) Quantitative analysis of silicate and oxide minerals: comparison of Monte Carlo, ZAF, and phi-ro-z procedures. In D.E. Newbury, Ed. Microbeam Analysis, p. 239-246. San Francisco Press, San Francisco.

Armstrong, J.T. (1995) CITZAF: A package of correction programs for the quantitative electron microbeam X-ray analysis of thick polished materials, thin films, and particles. Microbeam Analysis, 4, 177-200.

Arredondo, E.H., Rossman, G.R., and Lumpkin, G.R. (2001) Hydrogen in spessartine-almandine garnets as a tracer of granitic pegmatite evolution. American Mineralogist, 86, 485-490.

Bailey, A. (1971) Comparison of low-temperature with high-temperature diffusion of sodium in albite. Geochimica et Cosmochimica Acta, 35, 1073-1081.

Bakhtin, A.I., and Manapov, R.A. (1976a) Crystal chemistry of iron in alkali pyroxenes according to the data of optical and Mössbauer spectroscopy. Geochemistry International, 13(4), 72-76.

Bakhtin, A.I., and Manapov, R.A. (1976b) Investigation of clinopyroxenes by optical and Mössbauer spectroscopy. Geochemistry International, 13(2), 81-88.

Behrens, H., Johannes, W., and Schmalzried, H. (1990) On the mechanisms of cation diffusion processes in ternary feldspars. Physics and Chemistry of Minerals, 17, 62-78.

Behrens, H., and Müller, G. (1995) An infrared spectroscopic study of hydrogen feldspar ($HAlSi_3O_8$). Mineralogical Magazine, 59, 15-24.

Bell, D.R. (1992) Earth sciences; water in mantle minerals. Nature, 357(6380), 646-647.

Bell, D.R., and Rossman, G.R. (1992a) The distribution of hydroxyl in garnets from the subcontinental mantle of Southern Africa. Contributions to Mineralogy and Petrology, 111(2), 161-178.

Bell, D.R., and Rossman, G.R. (1992b) Water in Earth's mantle; the role of nominally anhydrous minerals. Science, 255(5050), 1391-1397.

Bell, D.R. (1993) Hydroxyl in mantle minerals. 389 p. California Institute of Technology, Pasadena, CA, United States, Ph.D. thesis.

Bell, D.R., Ihinger, P.D., and Rossman, G.R. (1995) Quantitative analysis of trace OH in garnet and pyroxenes. American Mineralogist, 80(5-6), 465-474.

Beran, A. (1986) A model of water allocation in alkali feldspar, derived from infrared-spectroscopic investigations. Physics and Chemistry of Minerals, 13, 306-310.

Beran, A., Armstrong, J., and Rossman, G.R. (1992) Infrared and electron microprobe analysis of ammonium ions in hyalophane feldspar. European Journal of Mineralogy, 4, 847-850.

Beran, A., and Libowitzky, E. (1999) IR spectroscopy and hydrogen bonding in minerals. In K. Wright and R. Catlow, Eds. Microscopic Properties and Processes in Minerals, p. 493-508. Kluwer Academic Publishers, the Netherlands.

Bethell, D.E., and Sheppard, N. (1953) The infrared spectrum of the H_3O^+ ion in acid hydrates. Journal of Chemical Physics, 21, 1421.

Böggild, O.B. (1914) Ussingit, ein neues mineral von Kangerdluarsuk. Zeitschrift für Kristallographie, 54, 120-126.

Bohlen, S.R., Valley, J.W., and Essene, E.J. (1985) Metamorphism in the Adirondacks I. Petrology, pressure and temperature. Journal of Petrology, 26(4), 971-992.

Brown, W.L. (1983) Feldspars and Feldspathoids; Structures, Properties and Occurrences, p. 541. D. Reidel Publishing Company, Dordrecht, Holland.

Busenberg, E., and Clemency, C.V. (1976) The dissolution kinetics of feldspars at 25°C and 1 atm CO_2 partial pressure. Geochimica et Cosmochimica Acta, 40, 41-49.

Cho, H., and Rossman, G.R. (1993) Single-crystal NMR studies of low-concentration hydrous species in minerals: Grossular garnet. American Mineralogist, 78, 1149-1164.

Clechenko, C.C., Valley, J.W., and McLelland, J. (2002) Timing and depth of intrusion of the Marcy anorthosite massif: Implications from field relations, geochronology, and geochemistry at Woolen Mill, Jay covered bridge, Split Rock Falls, and the Oak Hill wollastonite mine. In J. McLelland and P. Karabinos, Eds. Guidebook for Field Trips in New York and Vermont, New England Intercollegiate Geological Conference, 94th Annual Meeting, and New York State Geological Association, 74th Annual Meeting, p.C1-1-C1-17.

Clechenko, C.C., and Valley, J.W. (In press) Oscillatory zonation in garnet from skarn adjacent to massif anorthosite, WIllsboro Wollastonite Mine, northeastern Adirondacks Mts., New York. Journal of Metamorphic Geology.

Clunie, J.S., Goodman, J.F., and Ogden, C.P. (1966) Extinction coefficient of water at 2.93μ and water content of black foam films. Nature, 209, 1192-1193.

Colville, A.A., and Novak, G.A. (1991) Kaersutite megacrysts and associated crystal inclusions from the Cima volcanic field, San Bernardino County, California. Lithos, 27, 107-114.

Cory, D.G., and Ritchey, W.M. (1988) Suppression of signals from the probe in Bloch decay spectra. Journal of Magnetic Resonance, 80, 128-132.

Crank, J. (1970) The Mathematics of Diffusion. 347 p. Oxford University Press, London.

Criss, R.E. (1981) An $^{16}O/^{18}O$, D/H, and K-Ar study of the southern half of the Idaho batholith. Division of Geological and Planetary Sciences, p. 401. California Institute of Technology, Pasadena, CA.

Criss, R.E., and Taylor, H.P. Jr. (1983) An $^{18}O/^{16}O$ and D/H study of Tertiary hydrothermal systems in the southern half of the Idaho Batholith. Geological Society of America Bulletin, 94, 640-663.

Crowe, D.E., Riciputi, L.R., Bezenek, S., and Ignatiev, A. (2001) Oxygen isotope and trace element zoning in hydrothermal garnets: windows into large-scale fluid-flow behavior. Geology, 29, 479-482.

David, F.W.L. (1990) Ion microprobe study of intragrain micropermeability in alkali feldspars. Contributions to Mineralogy and Petrology, 106, 124-128.

David, F.W.L., Lee, M.R., and Parsons, I. (1995) Micropores and micropermeable texture in alkali feldspars: geochemical and geophysical implications. Mineralogical Magazine, 59, 505-534.

Deer, W.A., Howie, R.A., and Zussman, J. (1992) An introduction to the rock-forming minerals. 696 p. John Wiley & Sons, New York.

De Grave, E., and Van Alboom, A. (1991) Evaluation of ferrous and ferric Mössbauer fractions. Physics and Chemistry of Minerals, 18, 337-342.

Donnay, G., Wyart, J., and Sabatier, G. (1960) The catalytic nature of high-low feldspar transformations. Year Book - Carnegie Institution of Washington, 173-174.

Downs, R.T., Hazen, R.M., and Finger, L.W. (1994) The high-pressure crystal chemistry of low albite and the origin of the pressure dependency of Al-Si ordering. American Mineralogist, 79, 1042-1052.

Downs, R.T., Andalman, A., and Hudacsko, M. (1996) The coordination numbers of Na and K atoms in low albite and microcline as determined from a procrystal electron-density distribution. American Mineralogist, 81, 1344-1349.

Downs, R.T., Yang, H., Hazen, R.M., Finger, L.W., and Prewitt, C.T. (1999) Compressibility mechanisms of alkali feldspars: new data from reedmergnerite. American Mineralogist, 84, 333-340.

Dowty, E. (1978) Absorption optics of low-symmetry crystals — application to titanian clinopyroxene spectra. Physics and Chemistry of Minerals, 3, 173-181.

Edwards, K.J., and Valley, J.W. (1998) Oxygen isotope diffusion and zoning in diopside: The importance of water fugacity during cooling. Geochimica et Cosmochimica Acta, 62(13), 2265-2277.

Eeckhout, S.G., De Grave, E., McCammon, C.A., and Vochten, R. (2000) Temperature dependence of the hyperfine parameters of synthetic $P2_1/c$ Mg-Fe clinopyroxenes along the $MgSiO_3$-$FeSiO_3$ join. American Mineralogist, 85, 943-952.

Eiler, J.M., Baumgartner, L.P., and Valley, J.W. (1992) Intercrystalline stable isotope diffusion: a fast grain boundary model. Contributions to Mineralogy and Petrology, 112, 543-557.

Eiler, J.M., Baumgartner, L.P., and Valley, J.W. (1994) Fast grain boundary: A Fortran-77 program for calculating the effects of retrograde interdiffusion of stable isotopes. Computers & Geosciences, 20, 1415-1434.

Eiler, J.M., Valley, J.W., and Baumgartner, L.P. (1993) A new look at stable isotope thermometry. Geochimica et Cosmochimica Acta, 57, 2571-2583.

Emsley, J. (1981) Very strong hydrogen bonding. Chemical Society Reviews, 9, 91-124.

Engell, J., Hansen, J., Jensen, M., Kunzendorf, H., and Lovborg, L. (1971) Beryllium mineralization in the Ilímaussaq intrusion, South Greenland, with description of a field beryllometer and chemical methods. Grønlands Geologiske Undersøgelse Rapport, 33, 1-40.

Ernst, W.G., and Wai, C.M. (1970) Mössbauer, infrared, X-ray and optical study of cation ordering and dehydrogenation in natural and heat-treated sodic amphiboles. American Mineralogist, 55, 1226-1258.

Farmer, G.L., Glazner, A.F., Wilshire, H.G., Wooden, J.L., Pickthorn, W.J., and Katz, M. (1995) Origin of late Cenozoic basalts at the Cima volcanic field, Mojave Desert, California. Journal of Geophysical Research, 100(B5), 8399-8415.

Farver, J.R. (1989) Oxygen self-diffusion in diopside with application to cooling rate determinations. Earth and Planetary Science Letters, 92, 386-396.

Farver, J.R. (1994) Oxygen self-diffusion in calcite: Dependence on temperature and water fugacity. Earth and Planetary Science Letters, 121, 575-587.

Farver, J.R., and Yund, R.A. (1990) The effect of hydrogen, oxygen, and water fugacity on oxygen diffusion in alkali feldspar. Geochimica et Cosmochimica Acta, 54, 2953-2964.

Farver, J.R., and Yund, R.A. (1991) Oxygen diffusion in quartz: Dependence on temperature and water fugacity. Chemical Geology, 90, 55-70.

Ferriso, C.C., and Hornig, D.F. (1955) Infrared spectra of oxonium halides and the structure of the oxonium ion. Journal of Chemical Physics, 23, 1464-1468.

Foord, E.E., London, D., Kampf, A.R., Shigley, J.E., and Snee, L.W. (1991) Gem-bearing pegmatites of San Diego County, California. In M.J. Walawender and B.B. Hanan, Eds. Geological Excursions in Southern California and Mexico, Guidebook, 1991 Annual Meeting, Geological Society of America, p. 128-146.

Garrels, R.M., and Mackenzie, F.T. (1971) Evolution of Sedimentary Rocks. 397 p. W. W. Norton, New York.

Giletti, B.J., Semet, M.P., and Yund, R.A. (1978) Studies in diffusion III. Oxygen in feldspars: an ion microprobe determination. Geochimica et Cosmochimica Acta, 42, 45-57.

Goldsmith, J.R. (1986) The role of hydrogen in promoting Al-Si interdiffusion in albite ($NaAlSi_3O_8$) at high pressures. Earth and Planetary Science Letters, 80, 135-138.

Goldsmith, J.R. (1987) Al/Si interdiffusion in albite: effect of pressure and the role of hydrogen. Contributions to Mineralogy and Petrology, 95, 311-321.

Goldsmith, J.R. (1988) Enhanced Al/Si diffusion in $KAlSi_3O_8$ at high pressures: the effect of hydrogen. Journal of Geology, 96, 109-124.

Grew, E.S., Belakovskiy, D.I., Fleet, M.E., Yates, M.G., McGee, J.J., and Marquez, N. (1993) Reedmergnerite and associated minerals from peralkaline pegmatite, Dara-i-Pioz, southern Tien Shan, Tajikistan. European Journal of Mineralogy, 5, 971-984.

Hafner, S.S., and Huckenholz, H.G. (1971) Mössbauer spectrum of synthetic ferri-diopside. Nature, 233, 9-10.

Hadži, D., and Bratos, S. (1976) Vibrational spectroscopy of the hydrogen bond. In P. Schuster et al., Eds. The Hydrogen Bond— Recent Developments in Theory and Experiments, p. 567-611. North Holland Publishing Company, Amsterdam.

Hamilton, M.A., McLelland, J.M., Bickford, M.E., Clechenko, Cory C., and Valley, J.W. (2002) SHRIMP II geochronology of the Adirondack

AMCG suite, I: Emplacement chronology of anorthosites and gabbros. Abstracts with Programs - Geological Society of America , 34, 365.

Hammer, V.M.F., Libowitzky, E., and Rossman, G.R. (1998) Single-crystal IR spectroscopy of very strong hydrogen bonds in pectolite, $NaCa_2[Si_3O_8(OH)]$, and serandite, $NaMn_2[Si_3O_8(OH)]$. American Mineralogist, 83, 569-576.

Hayashi, S., and Hayamizu, K. (1991) Chemical shift standards in high-resolution solid-state NMR (I) ^{13}C, ^{29}Si, and ^{1}H nuclei. Bulletin of the Chemical Society of Japan, 64, 685-687.

Hercule, S., and Ingrin, J. (1999) Hydrogen in diopside: diffusion, kinetics of extraction-incorporation, and solubility. American Mineralogist, 84(10), 1577-1587.

Hofmeister, A.M., and Rossman, G.R. (1985a) A model for the irradiative coloration of smoky feldspar and the inhibiting influence of water. Physics and Chemistry of Minerals, 12, 324-332.

Hofmeister, A.M., and Rossman, G.R. (1985b) A spectroscopic study of irradiation coloring of amazonite: structurally hydrous, Pb-bearing feldspar. American Mineralogist, 70, 794-804.

Hofmeister, A.M., and Rossman, G.R. (1985c) Exsolution of metallic copper from Lake County labradorite. Geology, 13, 644-647.

Hofmeister, A.M., and Rossman, G.R. (1986) A spectroscopic study of blue radiation coloring in plagioclase. American Mineralogist, 71, 95-98.

Ilyukhin, V.V., and Semenov, Y.I. (1959) New data on ussingite. Doklady Akademii Nauk SSSR, 129, 1176-1178.

Ingrin, J., Latrous, K., Doukhan, J.C., and Doukhan, N. (1989) Water in diopside: An electron microscopy and infrared spectroscopy study. European Journal of Mineralogy, 1(3), 327-341.

Ingrin, J., Pacaud, L., and Jaoul, O. (2001) Anisotropy of oxygen diffusion in diopside. Earth and Planetary Science Letters, 192, 347-361.

Ingrin, J., and Skogby, H. (2000) Hydrogen in nominally anhydrous upper-mantle minerals: Concentration levels and implications. European Journal of Mineralogy, 12, 543-570.

Irvine, T.N. (1967) The Duke Island ultramafic complex, southeastern Alaska. In P.J. Wyllie, Ed. Ultramafic and Related Rocks, p. 84-97. John Wiley and Sons, Inc., New York.

Jahns, R.H., and Burnham, C.W. (1969) Experimental studies of pegmatite genesis: I. A model for the derivation and crystallization of granitic pegmatites. Economic Geology and the Bulletin of the Society of Economic Geologists, 64(8), 843-864.

Jamtveit, B., and Hervig, R.L. (1994) Constraints on transport and kinetics in hydrothermal systems from zoned garnet crystals. Science, 263, 505-508.

Jeffrey, G.A., and Yeon, Y. (1986) The correlation between hydrogen-bond lengths and proton chemical shifts in crystals. Acta Crystallographica, B42, 410-413.

Johnson, E.A., Rossman, G.R., Dyar, M.D., and Valley, J.W. (2002) Correlation between OH concentration and oxygen isotope diffusion rate in diopsides from the Adirondack Mountains, New York. American Mineralogist, 87, 899-908.

Johnson, E.A., and Rossman, G.R. (2003) The concentration and speciation of hydrogen in feldspars using FTIR and ^{1}H MAS NMR spectroscopy. American Mineralogist, 88, 901-911.

Karato, S. (1990) The role of hydrogen in the electrical conductivity of the upper mantle. Nature, 347, 272-273.

Kats, A. (1962) Hydrogen in alpha quartz. Phillips Research Report, 17, 133-195, 133-279.

Kats, A., Haven, Y., and Stevels, J.M. (1962) Hydroxyl groups in β-quartz. Physics and Chemistry of Glasses, 3, 69-75.

Keppler, H., and Rauch, M. (2000) Water solubility in nominally anhydrous minerals measured by FTIR and ^{1}H MAS NMR: the effect of sample preparation. Physics and Chemistry of Minerals, 27, 371-376.

Kimata, M., Nishida, N., Shimizu, M., Saito, S., Matsui, T., and Arakawa, Y. (1995) Anorthite megacrysts from island arc basalts. Mineralogical Magazine, 59, 1-14.

Kohlstedt, D.L., and Mackwell, S.J. (1998) Diffusion of hydrogen and intrinsic point defects in olivine. Zeitschrift für Physikalische Chemie, 207, 147-162.

Kohn, M.J., and Valley, J.W. (1998) Obtaining equilibrium oxygen isotope fractionations from rocks: theory and examples. Contributions to Mineralogy and Petrology, 132, 209-224.

Kohn, S.C. (1996) Solubility of H_2O in nominally anhydrous mantle minerals using ^{1}H MAS NMR. American Mineralogist, 81, 1523-1526.

Kracek, F.C., and Neuvonen, K.J. (1952) Thermochemistry of plagioclase and alkali feldspars. American Journal of Science, Bowen Volume 1952A, 293-318.

Kronenberg, A.K., and Wolf, G.H. (1990) Fourier transform infrared spectroscopy determinations of intragranular water content in quartz-bearing rocks: implications for hydrolytic weakening in the laboratory and within the earth. Tectonophysics, 172, 255-271.

Kronenberg, A.K., Yund, R.A., and Rossman, G.R. (1996) Stationary and mobile hydrogen defects in potassium feldspar. Geochimica et Cosmochimica Acta, 60(21), 4075-4094.

Lager, G.A., Rossman, G.R., Rotella, F.J., and Schultz, A.J. (1987) Neutron-diffraction structure of a low-water grossular at 20 K. American Mineralogist, 72, 766-768.

Lager, G.A., Armbruster, T., Rotella, F.J., and Rossman, G.R. (1989) OH substitution in garnets: X-ray and neutron diffraction, infrared, and geometric-modeling studies. American Mineralogist, 74, 840-851.

Lamb, W.M., and Valley, J.W. (1988) Granulite facies amphibole and biotite equilibria, and calculated peak-metamorphic water activities. Contributions to Mineralogy and Petrology, 100, 349-360.

Libowitzky, E., and Rossman, G.R. (1997) An IR absorption calibration for water in minerals. American Mineralogist, 82(11-12), 1111-1115.

Libowitzky, E. (1999) Correlation of O-H stretching frequencies and O-H···O hydrogen bond lengths in minerals. Monatshefte für Chemie, 130, 1047-1059.

Lutz, H.D. (1988) Bonding and structure of water molecules in solid hydrates-correlation of spectroscopic and structural data. Structure and Bonding, 69, 97-125.

Mackwell, S.J., and Kohlstedt, D.L. (1990) Diffusion of hydrogen in olivine: implications for water in the mantle. Journal of Geophysical Research, 95(B4), 5079-5088.

Mandarino, J.A., and Anderson, V. (1989) Monteregian Treasures: The Minerals of Mont Saint-Hilaire, Quebec, p. 207. Cambridge University Press, Cambridge.

McConnell, J.D.C. (1995) The role of water in oxygen isotope exchange in quartz. Earth and Planetary Science Letters, 136, 97-107.

McKee, E.H., and Nash, D.B. (1967) Potassium-argon ages of granitic rocks in the Inyo Batholith, east-central California. Geological Society of America Bulletin, 78, 669-680.

McLelland, J., Daly, J.S., and McLelland J.M. (1996) The Grenville Orogenic Cycle (ca. 1350–1000 Ma): an Adirondack perspective. Tectonophysics, 265, 1-28.

McLennan, S.M., and Taylor, S.R. (1999) Earth's Continental Crust. In C.P. Marshall, and R.W. Fairbridge, Eds. Encyclopedia of Geochemistry, p. 712. Kluwer Academic Publishers, Dordrecht.

Mezger, K., Rawnsley, C.M., Bohlen, S.R., and Hanson, G.N. (1991) U-Pb garnet, sphene, monazite, and rutile ages: Implications for the duration of high-grade metamorphism and cooling histories, Adirondack Mts., New York. Journal of Geology, 99, 415-428.

Miller, G.H., Rossman, G.R., and Harlow, G.E. (1987) The natural occurrence of hydroxide in olivine. Physics and Chemistry of Minerals, 14(5), 461-472.

Milton, C., Chao, E.C.T., Axelrod, J.M., and Grimaldi, F.S. (1960) Reedmergnerite, $NaBSi_3O_8$, the boron analogue of albite, from the Green River formation, Utah. American Mineralogist, 45, 188-199.

Morrison, J., and Valley, J.W. (1988) Contamination of the Marcy Anorthosite Massif, Adirondack Mountains, NY: petrologic and isotopic evidence. Contributions to Mineralogy and Petrology, 98, 97-108.

Muehlenbachs, K., and Kushiro, I. (1974) Oxygen isotope exchange and equilibrium of silicates with CO_2 or O_2. Year Book — Carnegie Institution of Washington, 73, 232-236.

Müller, G. (1988) Preparation of hydrogen and lithium feldspars by ion exchange. Nature, 332, 435-436.

Nakajima, Y., Morimoto, N., and Kitamura, M. (1977) The superstructure of plagioclase feldspars. Physics and Chemistry of Minerals, 1, 213-225.

Nakamoto, K., Margoshes, M., and Rundle, R.E. (1955) Stretching frequencies as a function of distances in hydrogen bonds. Journal of the American Chemical Society, 77, 6480-6486.

Nash, D.B. (1962) Contact metamorphism at Birch Creek, Blanco Mountain Quadrangle, Inyo County, California, p. 53. University of California, Berkeley.

Nesse, W.D. (1991) Introduction to Optical Mineralogy. Oxford University Press, New York, p.270.

Nyfeler, D., Hoffmann, C., Armbruster, T., Kunz, M., and Libowitzky, E. (1997) Orthorhombic Jahn-Teller distortion and Si-OH in mozartite, $CaMn^{3+}O[SiO_3OH]$: A single-crystal X-ray, FTIR, and structure modeling study. American Mineralogist, 82, 841-848.

Oglesby, J.V., and Stebbins, J.F. (2000) ^{29}Si CPMAS NMR investigations of silanol-group minerals and hydrous aluminosilicate glasses. American Mineralogist, 85, 722-731.

O'Neil, J.R., and Taylor, H.P. Jr. (1967) The oxygen isotope and cation exchange chemistry of feldspars. American Mineralogist, 52, 1414-1437.

Pacaud, L., Ingrin, J., and Jaoul, O. (1999) High-temperature diffusion of oxygen in synthetic diopside measured by nuclear reaction analysis. Mineralogical Magazine, 63(5), 673-686.

Parsons, I., and Boyd, R. (1971) Distribution of potassium feldspar polymorphs in intrusive sequences. Mineralogical Magazine, 38, 295-311.

Parsons, I. (1978) Feldspars and fluids in cooling plutons. Mineralogical Magazine, 42, 1-17.

Paterson, M.S. (1982) The determination of hydroxyl by infrared absorption in quartz, silicate glasses and similar materials. Bulletin de Minéralogie, 105, 20-29.

Pegau, A.A. (1929) The pegmatites of the Amelia, Goochland, and Ridgeway areas, Virginia. American Journal of Science, 17, 543-547.

Peslier, A.H., Luhr, J., and Post, J. (2000) Water in mantle xenolith pyroxenes from Mexico and Simcoe (WA, USA): The role of water in nominally anhydrous minerals from the mantle wedge. Geological Society of America- Abstracts with Programs, 7, p. 387.

Petrović, R. (1972a) Diffusion of alkali ions in alkali feldspars. In W.S. MacKenzie, and J. Zussman, Eds. The feldspars, p. 174-182. Manchester University Press, New York.

Petrović, R. (1972b) Alkali ion diffusion in alkali feldspars, p. 131. Yale University, New Haven, Connecticut, Ph.D. thesis.

Pohl, D., Guillemette, R., Shigley, J., and Dunning, G. (1982) Ferroaxinite from New Melones Lake, Calaveras County, California, a remarkable new locality. The Mineralogical Record, 13(5), 293-302.

Potter, R.M., and Rossman, G.R. (1977) Desert varnish: the importance of clay minerals. Science, 196, 1446-1448.

Povarennykh, A.S., Platonov, A.N., and Belichenko, V.P. (1970) On the colour of ussingite from the Ilímaussaq (South Greenland) and Lovozero (Kola Peninsula) alkaline intrusions. Bulletin of the Geological Society of Denmark, 20, 20-26.

Proctor, K. (1984) Gem pegmatites of Minas Gerais, Brazil: exploration, occurrence, and aquamarine deposits. Gems and Gemology, 20(2), 78-100.

Ragland, P.C. (1970) Composition and structural state of the potassic phase in perthites as related to petrogenesis of a granitic pluton. Lithos, 3, 167-189.

Rancourt, D.G. (1994a) Mössbauer spectroscopy of minerals I. Inadequacy of Lorentzian-line doublets in fitting spectra arising from quadrupole splitting distributions. Physics and Chemistry of Minerals, 21, 244-249.

Rancourt, D.G. (1994b) Mössbauer spectroscopy of minerals II. Problem of resolving cis and trans octahedral Fe^{2+} sites. Physics and Chemistry of Minerals, 21, 250-257.

Rancourt, D.G., Christie, I.A.D., Royer, M., Kodama, H., Robert, J.-L., Lalonde, A.E., and Murad, E. (1994a) Determination of accurate $^{[4]}Fe^{3+}$, $^{[6]}Fe^{3+}$, and $^{[6]}Fe^{2+}$ site populations in synthetic annite by Mössbauer spectroscopy. American Mineralogist, 79, 51-62.

Rancourt, D.G., Ping, J.Y., and Berman, R.G. (1994b) Mössbauer spectroscopy of minerals III. Octahedral-site Fe^{2+} quadrupole splitting distributions in the phlogopite-annite series. Physics and Chemistry of Minerals, 21, 258-267.

Ribbe, P.H. (1974) A comparison of bonding effects in ussingite and low albite. American Mineralogist, 59, 341-344.

Ribbe, P.H., Ferguson, R.B., and Taylor, W.H. (1962) A three-dimensional refinement of the structure of low albite. Norsk Geologisk Tidsskrift, 42, 152-157.

Ripmeester, J.A., Ratcliffe, C.I., Dutrizac, J.E., and Jambor, J.L. (1986) Hydronium ion in the alunite-jarosite group. Canadian Mineralogist, 24, 435-447.

Robinson, P. (1980) The composition space of terrestrial pyroxenes— internal and external limits. In C.T. Prewitt, Ed. Pyroxenes, 7, p. 419-490. Mineralogical Society of America, Washington, D.C.

Rossi, G., Tazzoli, V., and Ungaretti, L. (1974) The crystal structure of ussingite. American Mineralogist, 59, 335-340.

Rossman, G.R. (1980) Pyroxene spectroscopy. In C.T. Prewitt, Ed. Pyroxenes, 7, p. 93-116. Mineralogical Society of America, Washington, D.C.

Rossman, G.R. (1996) Studies of OH in nominally anhydrous minerals. Physics and Chemistry of Minerals, 23, 299-304.

Rossman, G.R., and Aines, R.D. (1986) Spectroscopy of a birefringent grossular from Asbestos, Quebec, Canada. American Mineralogist, 71, 779-780.

Rossman, G.R., and Aines, R.D. (1991) The hydrous components in garnets: Grossular-hydrogrossular. American Mineralogist, 76, 1153-1164.

Ryerson, F.J., and McKeegan, K.D. (1994) Determination of oxygen self-diffusion in åkermanite, anorthite, diopside, and spinel: Implications for oxygen isotopic anomalies and thermal histories of Ca-Al rich inclusions. Geochimica et Cosmochimica Acta, 58, 3713-3734.

Shannon, R.D., Dickinson, J.E., and Rossman, G.R. (1992) Dielectric constants of crystalline and amorphous spodumene, anorthite, and diopside and the oxide additivity rule. Physics and Chemistry of Minerals, 19, 148-156.

Shieh, Y.N., and Taylor, H.P., Jr. (1969) Oxygen and carbon isotope studies of contact metamorphism of carbonate rocks. Journal of Petrology, 10, 307-331.

Shoval, S., Yariv, S., Michaelian, K.H., Boudeulle, M., and Panczer, G. (2002) Hydroxyl-stretching bands in polarized micro-Raman spectra of oriented single-crystal Keokuk kaolinite. Clays and Clay Minerals, 50, 56-62.

Sinkankas, J. (1968) Classic mineral occurrences: I. Geology and mineralogy of the Rutherford pegmatites, Amelia, Virginia. American Mineralogist, 53, 373-405.

Skelton, A., Annersten, H., and Valley, J. (2002) $\delta^{18}O$ and yttrium zoning in garnet: time markers for fluid flow? Journal of Metamorphic Geology, 20, 457-466.

Skogby, H., Bell, D.R., and Rossman, G.R. (1990) Hydroxide in pyroxene: Variations in the natural environment. American Mineralogist, 75, 764-774.

Skogby, H., and Rossman, G.R. (1989) OH^- in pyroxene: An experimental study of incorporation mechanisms and stability. American Mineralogist, 74, 1059-1069.

Smith, J.V., and Brown, W.L. (1988) Spectroscopy- IR, Raman, NMR, NQR, EPR, NGR (Mössbauer), XAS, EXAFS, ESCA, XPS. Feldspar Minerals: Crystal Structures, Physical, Chemical, and Microtextural Properties, 1, p. 244-267, Springer-Verlag, Berlin.

Solomon, G.C., and Rossman, G.R. (1979) The role of water in structural states of K-feldspar as studied by infrared spectroscopy. Abstracts with programs - Geological Society of America, 11(7), 521.

Solomon, G.C., and Rossman, G.R. (1988) NH_4^+ in pegmatitic feldspars from the southern Black Hills, South Dakota. American Mineralogist, 73, 818-821.

Solomon, G.C., and Taylor, J., H.P. (1991) Oxygen isotope studies of Jurassic fossil hydrothermal systems, Mojave Desert, southeastern California. In J. Taylor, H.P., J.R. O'Neil, and I.R. Kaplan, Eds. Stable Isotope Geochemistry: A Tribute to Samuel Epstein, 3, p. 449-462.

Sørenson, H. (1997) The agpaitic rocks— an overview. Mineralogical Magazine, 61, 485-498.

Stakes, D.S., and Taylor, H.P. Jr. (1992) The northern Samail ophiolite: an oxygen isotope, microprobe and field study. Journal of Geophysical Research, 97(B5), 7043-7080.

Sternberg, U., and Brunner, E. (1994) The influence of short-range geometry on the chemical shift of protons in hydrogen bonds. Journal of Magnetic Resonance, Series A, 108, 142-150.

Stolper, E. (1982a) Water in silicate glasses: an infrared spectroscopic study. Contributions to Mineralogy and Petrology, 81, 1-17.

Stolper, E. (1982b) The speciation of water in silicate melts. Geochimica et Cosmochimica Acta, 46, 2609-2620.

Struzhkin, V.V., Goncharov, A.F., Hemley, R.J., and Mao, H.K. (1997) Cascading Fermi resonances and the soft mode in dense ice. Physical Review Letters, 78(23), 4446-4449.

Taylor, B.E., and O'Neil, J.R. (1977) Stable isotope studies of metasomatic Ca-Fe-Al-Si skarns and associated metamorphic and igneous rocks, Osgood Mountains, Nevada. Contributions to Mineralogy and Petrology, 63, 1-49.

Taylor, H.P. Jr., and Forester, R.W. (1979) An oxygen and hydrogen isotope study of the Skaergaard Intrusion and its country rocks: a description of a 55-m.y. old fossil hydrothermal system. Journal of Petrology, 20(3), 355-419.

Taylor, H.P. Jr., and Forester, R.W. (1971) Low-O^{18} igneous rocks from the intrusive complexes of Skye, Mull, and Ardnamurchan, western Scotland. Journal of Petrology, 12, 465-497.

Thompson, W.K. (1965) Infrared spectroscopic studies of aqueous systems Part I. Molar extinction coefficients of water, deuterium oxide, deuterium hydrogen oxide, aqueous sodium chloride and carbon disulphide. Transactions of the Faraday Society, 61, 2635-2640.

Tullis, J., and Yund, R.A. (1980) Hydrolytic weakening of experimentally deformed Westerly granite and Hale albite rock. Journal of Structual Geology, 2(4), 439-451.

Valley, J.W. (1985) Polymetamorphism in the Adirondacks: wollastonite at contacts of shallowly intruded anorthosite. In A.C. Tobi, and J.L.R. Touret, Eds. The Deep Proterozoic Crust in the North Atlantic Provinces, p. 217-236. D. Reidel Publishing Company, Dordrecht.

Valley, J.W., Bohlen, S.R., Essene, E.J., and Lamb, W. (1990) Metamorphism in the Adirondacks: II. The role of fluids. Journal of Petrology, 31(3), 555-596.

Valley, J.W., Essene, E.J., and Peacor, D.R. (1983) Fluorine-bearing garnets in Adirondack calc-silicates. American Mineralogist, 68, 444-448.

Valley, J.W., and O'Neil, J.R. (1982) Oxygen isotope evidence for shallow emplacement of Adirondack anorthosite. Nature, 300, 497-500.

Valley, J.W., and O'Neil, J.R. (1984) Fluid heterogeneity during granulite facies metamorphism in the Adirondacks: Stable isotope evidence. Contributions to Mineralogy and Petrology, 85, 158-173.

Van Baalen, M.R. (1993) Titanium mobility in metamorphic systems: a review. Chemical Geology, 110, 233-249.

Vedder, W., and Wilkins, R.W.T. (1969) Dehydroxylation and rehydroxylation, oxidation and reduction of micas. American Mineralogist, 54, 482-509.

Wang, L., Zhang, Y., and Essene, E.J. (1996) Diffusion of the hydrous component in pyrope. American Mineralogist, 81, 706-718.

Wenner, D.B. (1979) Hydrogen, oxygen and carbon isotopic evidence for the origin of rodingites in serpentinized ultramafic rocks. Geochimica et Cosmochimica Acta, 43, 603-614.

Wilkins, R.W.T., and Sabine, W. (1973) Water content of some nominally anhydrous silicates. American Mineralogist, 58, 508-516.

Wise, W.S. (1982) New occurrence of faujasite in southeastern California. American Mineralogist, 67, 794-798.

Wondratschek, H. (1985) Sanidine megacrysts from the Eifel, Germany: the ideal feldspar? Geological Society of America- Abstracts with Programs, 17(7), 754.

Wood, B.J., and Fraser, D.G. (1976) Elementary thermodynamics for geologists. 303 p. Oxford University Press, Oxford.

Woods, S.C., Mackwell, S., and Dyar, D. (2000) Hydrogen in diopside: diffusion profiles. American Mineralogist, 85, 480-487.

Xia, Q., Pan, Y., Chen, D., Kohn, S., Zhi, X., Guo, L., Cheng, H., and Wu, Y. (2000) Structural water in anorthoclase megacrysts from alkalic basalts: FTIR and NMR study. Acta Petrologica Sinica, 16(4), 485-491.

Yesinowski, J.P., Eckert, H., and Rossman, G.R. (1988) Characterization of hydrous species in minerals by high-speed ^{1}H MAS-NMR. Journal of the American Chemical Society, 110, 1367-1375.

Yund, R.A., and Anderson, T.F. (1974) Oxygen isotope exchange between potassium feldspar and KCl solution. In Hofmann et al., Eds. Geochemical Transport and Kinetics, p. 99-105, Carnegie Institution of Washington.

Yund, R.A., and Anderson, T.F. (1978) The effect of fluid pressure on oxygen isotope exchange between feldspar and water. Geochimica et Cosmochimica Acta, 42, 235-239.

Yund, R.A., and Ackermand, D. (1979) Development of perthite microstructures in the Storm King Granite, N.Y. Contributions to Mineralogy and Petrology, 70, 273-280.

Yund, R.A., and Tullis, J. (1980) The effect of water, pressure, and strain on Al/Si order-disorder kinetics in feldspar. Contributions to Mineralogy and Petrology, 72, 297-302.

Yund, R.A. (1983) Diffusion in feldspars. In P.H. Ribbe, Ed. Feldspar Mineralogy, 2, p. 203-222. Mineralogical Society of America, Washington, D.C.

Zhang, S., and Karato, S. (1995) Lattice preferred orientation of olivine aggregates deformed in simple shear. Nature, 375, 774-777.

Zhang, Y., Stolper, E.M., and Wasserburg, G.J. (1991a) Diffusion of a multi-species component and its role in oxygen and water transport in silicates. Earth and Planetary Science Letters, 103, 228-240.

Zhang, Y., Stolper, E.M., and Wasserburg, G.J. (1991b) Diffusion of water in rhyolitic glasses. Geochimica et Cosmochimica Acta, 55, 441-456.